MONTANUNIVERSITÄT LEOBEN

PhD Thesis

The Role of Interfaces in BCC Metal Plasticity across Length-Scales and Temperatures

Reinhard FRITZ

This work was financially supported by the
Austrian Science Fund (FWF) through project P25325-N20

Department Materials Physics
Montanuniversität Leoben
Jahnstraße 12
8700 Leoben, Austria

Affidavit

I declare in lieu of oath, that I wrote this thesis and performed the associated research myself, using only literature cited in this volume.

Leoben, August 2017 Reinhard FRITZ

Danksagung

Eine Dissertation zu verfassen bedeutet Zeit und steht für Veränderung. Zeit, in der man sich mit der gewählten Aufgabenstellung auseinandersetzt und in der man viele Höhen und Tiefen durchlebt. Zeit, in der man einen tiefen Einblick in die Welt der Werkstoffe erhält und mit der sich Ansichts- und/oder Denkweisen über gewisse Dinge ändern.

Die letzten Jahre haben mich nicht nur persönlich geprägt, ich konnte mein Wissen in meinem Fachgebiet wesentlich erweitern. Deshalb bin ich meinem Doktorvater Assoz. Prof. Dr. Daniel Kiener zu großem Dank verpflichtet. Die Arbeit mit ihm war immer herausfordernd sowie lehr- und abwechslungsreich, so wie ich es mir zu Beginn meiner Dissertation erhofft hatte.

Ebenso möchte ich mich bei Dr.-Ing.in Verena Maier-Kiener, Dr.in Ruth Konetschnik und DI Alexander Leitner bedanken. Ohne ihren Input bezüglich Nanoindentation, thermisch aktivierten Verformungsmechanismen, Hilfestellung bei FIB, REM und in-situ Versuchen sowie vielen Diskussionen wäre die Arbeit in diesem Umfang nicht möglich gewesen.

Weiters möchte ich mich bei Silke, Gabi, Peter, Franz und Robin bedanken. Sie standen mir bei der Probenpräparation stets zur Seite. Großer Dank gebührt auch Thomas, Gerald und Gerhard. Sie waren immer mit Rat und Tat zur Stelle wenn die Technik an REM, FIB oder am Laptop streikte. Eine Dissertation zu erarbeiten bedeutet natürlich auch organisatorischen Aufwand, bei dem mir Sabine und Daniela immer zur Seite standen. Danke dafür! All meinen Büro- und Arbeitskollegen sei gedankt. Sie waren immer da, sei es um mit mir am Mittagstisch zu sitzen, Kuchen zu essen, Kaffee zu trinken oder einfach nur um über alltägliche Dinge zu sprechen.

Um eine durchgehend gute Leistung zu erbringen ist ebenso ein großer Rückhalt in der Familie erforderlich. Deshalb bin ich meiner Freundin Kerstin, meinen Eltern Christa und Siegfried, meinem Bruder Siegi und seiner Frau Rrezarta, sowie meinen Schwiegereltern Markus und Sabine zu Dank verpflichtet. Vor allem Kerstin ist mir immer beigestanden und hat unzählige Wochenenden mit mir am FIB verbracht, damit ich meine Vielzahl an Proben in kurzer Zeit präparieren und testen konnte.

Zu guter Letzt fühle ich mich noch verpflichtet meiner Großmutter, Anna Fritz, zu danken. Immer wieder konnte ich aus ihren Worten, die sie vor mehr als 10 Jahren zu mir sagte, Motivation schöpfen!

Kurzfassung

Das umfangreiche Verständnis von Größeneffekten in der Kristallplastizität ist heutzutage noch immer eine Herausforderung, obwohl man sich in der Literatur zumindest über Größeneffekte in dem relativ einfachen, kubisch-flächenzentrierten Kristallsystem einig ist. Für Metalle mit kubisch-raumzentrierter Gitterstruktur hingegen werden immer wieder kontroverse Daten publiziert. Diese stammen meist von dem temperaturabhängigen, thermischen Spannungsanteil, der das Skalierungsverhalten der Festigkeit wesentlich beeinflusst. Eine noch viel komplexere Situation ergibt sich, wenn zusätzliche Grenzflächen in das Material eingebracht werden und die Plastizität eines Kristalls beeinflussen. Für technische Anwendungen auf Mikrometerebene ist die Plastizität von Strukturen mit Grenzflächen von enormer Bedeutung. Durch Designoptimierungen erfolgt ein weiterer Schritt Richtung Bauteilminiaturisierung welche zur Verlängerung der Zuverlässigkeit und der Lebensdauer beitragen kann.

In der vorliegenden Dissertation wird der mögliche Einfluss von internen Grenzflächen auf Größeneffekte in zwei kubisch-raumzentrierten Metallen (Chrom und Wolfram) untersucht. Durch makroskopische Druckversuche, Nanoindentierung und mikroskopische in-situ Druckversuche werden Experimente über mehrere Längenskalen abgedeckt. Weiters wurden Versuchstemperaturen von Raumtemperatur bis ~600°C realisiert.

Um Versuche bei erhöhter Temperatur im Rasterelektronenmikroskop an mikroskopisch kleinen Proben durchzuführen, wurde ein bereits existierender Mikroindenter mit einer selbstentwickelten Heizung ausgestattet. Zum ersten Mal konnte gezeigt werden, dass eine Kalibrierung der Kontakttemperatur durch eine Finite Elemente Simulation möglich ist. Des Weiteren konnten in-situ Versuche bis 300°C durchgeführt werden. Vorherrschende thermisch aktivierte Verformungsmechanismen wurden in den Modellmaterialien durch Bestimmung der Dehnratenabhängigkeit und der dazugehörigen Aktivierungsvolumina bestimmt. Weiters wurde das plastisch verformte Probenvolumen sorgfältig reduziert, um den Einfluss freier Oberflächen zu prüfen, bis ein Übergang von makroskopischem zu einkristallinem Verformungs-verhalten beobachtet wurde.

Die vorliegende Arbeit identifiziert mikrostrukturelle Mechanismen, die zu Größeneffekten in kubisch-raumzentrierten Metallen beitragen sowie Anteile, welche durch freie Oberflächen entstehen. Vorherrschende Verformungsmechanismen in

ultrafeinkörnigem Chrom und Wolfram werden untersucht und mit dem Verformungsverhalten von Einkristallen verglichen. Bei niedrigen Temperaturen verformen einkristalline sowie ultrafeinkörnige Proben durch thermisch aktivierte Bewegung von Schraubenversetzungen, wohingegen bei erhöhten Temperaturen ein konstantes Aktivierungsvolumen auf Interaktionen von Versetzungen mit Korngrenzen schließen lässt.

Abstract

The thorough understanding of size effects in crystal plasticity is still a challenging task even though consent is reached in literature on the strength scaling behaviour in single crystalline face-centred cubic structures. However, for body-centred cubic metals, controversial results have been reported, which is mainly attributed to a temperature-dependent thermal stress component that significantly alters the strength scaling behaviour. An even more complicated situation is expected if additional interfaces, such as grain boundaries, affect the crystal plasticity at small scales. For technical applications, the understanding of small-scale plasticity of structures containing interfaces is crucial, as design optimizations may lead to further miniaturization of devices and lifetime and reliability issues might be enhanced.

In this PhD thesis a possible influence of interfaces on the strength scaling behaviour of two body-centred cubic model metals, namely chromium and tungsten, is investigated. Macroscopic compression, nanoindentation and in-situ scanning electron microscope micro-compression experiments, spanning several length-scales and ranging from the (sub-)micron to the macroscopic regime, were performed. Furthermore, temperatures ranging from room temperature up to ~600°C were applied. To conduct experiments at small scale and elevated temperature, an existing micro-indenter was equipped with a custom-built heating device. For the first time, temperature calibration was performed by conducting a simulation approach to perform micromechanical tests up to 300°C. The apparent thermally activated deformation behaviour was addressed in terms of strain-rate sensitivity and activation volume. The influence of free surfaces was examined by thoroughly reducing the plastically deformed volume until a transition from bulk-like to single crystalline deformation behaviour was observed.

The present work identifies contributions of microstructure and free surfaces to the strength scaling behaviour in body-centred cubic structures. Underlying deformation mechanisms in ultrafine-grained chromium and tungsten are examined and related to the single crystal situation. At low temperatures single crystalline and ultrafine-grained samples deform by the thermally activated motion of screw dislocations. At elevated temperature, the constant activation volume indicates dislocation-grain boundary interactions.

Content

Chapter 1

Chapter 2

Appendix

Abbreviations

a	lattice constant
b	Burgers vector
bcc	body-centered cubic
BSE	backscattered electrons
cg	coarse grained
Cr	chromium
D	sample diameter
d	grain size
DBTT	ductile-to-brittle transition temperature
E	Young's modulus
EBSD	electron backscattered diffraction
EDM	electron discharge machining
fcc	face-centered cubic
FIB	focused ion beam
G	shear modulus
GB	grain boundary
HPT	high pressure torsion
m	strain-rate sensitivity
nc	nanocrystalline
ν	activation volume
RT	room temperature
SEM	scanning electron microscope
SPD	severe plastic deformation
sxx	single crystalline
TEM	transmission electron microscope
ufg	ultrafine-grained
W	tungsten

Chapter 1

1. Motivation

Since technical devices are getting ever smaller, the material requirements, especially regarding the mechanical response at small-scale and non-ambient conditions, are generally increasing. Therefore, it is of key importance to further improve and tailor mechanical properties, for example, in thin film technology, microelectronics, or structural applications. In recent years, effort was made to establish small-scale testing techniques such as nanoindentation [1] and micropillar compression [2] to understand the deformation behaviour from macroscopic scale down to small volumes. Those techniques are beneficial, as they offer the premise to assess specific intrinsic material behaviour such as plasticity mechanisms in single crystals or the interaction of dislocations in samples containing interfaces [3–6].

Small-scale testing techniques were recently applied to several metals and a general trend of increasing strength with reduced sample size was reported [7–12]. Nowadays, it is established that the strength in such confined volumes scales according to a power-law with the sample dimension d as the base and n as the strength scaling exponent ($\sim d^{-n}$) [7–12]. A lot of extrinsic and intrinsic sample parameters might alter this strengthening behaviour individually. Consequently, there is still an ongoing debate on the governing deformation mechanisms, especially for the less understood body-centred cubic (bcc) structures [13–20].

Bcc metals are of particular interest to be integrated in small-scale devices and structural applications which operate at elevated temperatures, as they offer high strength and thermal stability due to their high melting temperatures. Thus, to make high strength bcc metals suitable for technical applications it is important to derive a thorough mechanism-based understanding of:

- size-dependent plastic deformation,
- the influence of microstructure on strength scaling mechanisms, and
- microstructure-related effects on the thermally activated deformation behaviour of bcc metals.

2. Aim of the work

This thesis should help to extend the knowledge about mechanical properties of single- and polycrystalline bcc metals across several length-scales and stress-states at RT as well as non-ambient conditions. Especially surface contributions, enhanced at small-scales by an increase in surface-to-volume fraction [21–24], are of vital interest as they might cause differences in apparent deformation behaviour. Therefore, an existing in-situ micro-testing device operating inside a scanning electron microscope (SEM), was equipped with a custom-built heating device to perform in-situ experiments and to investigate specific deformation mechanisms of bcc metals. In particular, the role of the microstructure and the temperature-dependent friction stress in bcc metals are related to the size-affected strength scaling behaviour in two bcc model materials, namely Cr and W, and apparent deformation mechanisms will be examined.

3. State of the art

Bcc metals such as the investigated model materials in this thesis are widely used for applications in the electronics-, coating-, lighting- and high temperature industry. Especially Cr and W are established for coatings to shield load-bearing structures from acids or heat. In thin film technology, they are often used as thermal barrier coatings as they offer low coefficients of thermal expansion paired with pronounced electrical conductivity and low diffusivity coefficients. However, coatings and thin films are dimensionally constrained, which leads to a pronounced strength scaling behaviour and size effects due to the constraint sample dimension [12,25].

3.1 Plasticity in miniaturized metallic structures

Among the large variety of measurement techniques to obtain mechanical properties of thin films, pillar compression and nanoindentation methods are the most prominent ones capable of probing the mechanical response of small volumes. Especially pillar compression is a prominent, straight forward testing technique which offers the advantage of a nominally uniaxial stress state [2].

Pillar compression experiments to study the strength scaling behaviour of fcc and bcc metals have been performed widely by several groups in the past years. Greer *et al.* [10], for example, investigated the stress-strain behaviour of Au and Mo pillars, where differences in the strength scaling behaviour were attributed to varying

dislocation mechanisms. Typical *n*-values for fcc metals are in the order of 0.6 [2]. The mechanisms responsible for such a scaling behaviour are interpreted based on a single-armed source model by Parthasarathy *et al.* [26]. Detailed mechanisms are discussed by El-Awady [27]. Notably, the crystal orientation, or more precisely the number of active slip systems [14,28,29], as well as dislocation density [27,30–32] affect the scaling exponent *n*.

Several attempts have been made to analyse pillars containing different defect densities. Bei *et al.* [30] compared dislocation free to pre-strained Mo whiskers. While it is well-known that defect-free whiskers reveal theoretical strength values, testing pillars which contain defects leads to the afore mentioned size effects [30]. Their findings reveal no size effect for pillars with more than 11% pre-strain. Schneider *et al.* [31] and El-Awady *et al.* [32] pre-strained Ni pillars and found a decreasing strength scaling exponent with increasing pre-strain. This was related to cell structures that formed during straining and an increase in dislocation density in the cell walls with increasing pre-strain. For the sake of completeness, the influence of dislocation density on the strength scaling behaviour was additionally estimated by simulation approaches, for example by El-Awady [27]. Results are presented in Figure 1a, demonstrating that an increase in dislocation density goes along with a reduction of the strength scaling exponent *n*, in good agreement with experimental results [30,31].

While fcc metals can be regarded as athermal [33], in bcc structures the strength scaling exponent is additionally dependent on a thermal stress component (σ^*). σ^* limits the movement of elongated screw dislocations via the kink-pair mechanism [13,34,35]. Here, the thermal stress component is related to an absence of closest packed planes and complicated dislocation core spreading in the bcc structure [36,37].

Schneider *et al.* [13] tested various bcc metals with different critical temperatures (T_c) via pillar compression experiments. Hereby, the T_{test}/T_c ratio refers to the individual thermal contributions to the Peierls stress of the various metals. As illustrated in Figure 1b, metals such as W exhibit a high thermal stress component at RT, evidenced by *n*-values of ~0.2 - 0.4 [13,15,20,28,38,39]. Contrarily, bcc metals with rather low melting points (T_m) such as Nb or Fe show reduced thermal stress components resulting in strength scaling exponents of 0.48 [13] and 0.59 [29,40], respectively. If thermal activation reaches ~$0.2 \cdot T_m$ [35] (equals $T_{test} = T_c$), screw dislocations are not hindered by the Peierls potential anymore and propagate with the same velocity as

edge dislocations. At this critical temperature, the strength scaling behaviour in bcc metals approaches towards the fcc value, as demonstrated in Figure 1b.

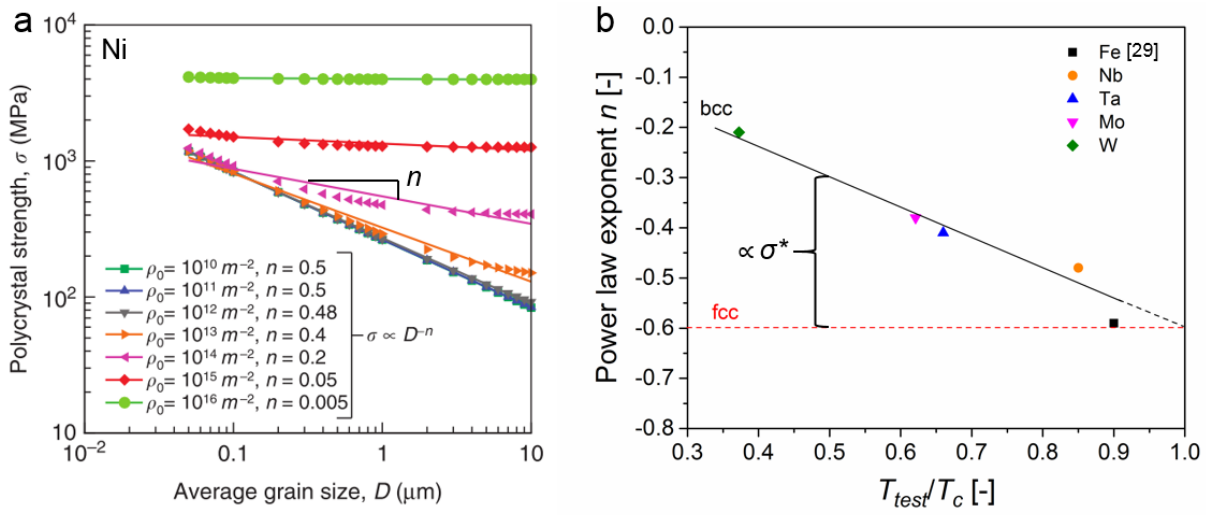

Figure 1: The strength scaling behaviour of fcc and bcc metals is shown to scale with an increasing number of intrinsic obstacles such as (a) dislocation density [27] and (b) a thermal stress component [13]. (a) An increase in dislocation density leads to a distinct decrease of the power-law exponent (n). (b) A comparison of individual bcc metals with varying thermal stress contribution tested at T_{test} = RT leads to distinct strength scaling behaviour.

Those findings were confirmed by Maier *et al.* [41] using advanced nanoindentation techniques. Also more recently, compression tests on sxx W and Ta were carried out at elevated temperatures by Torrents Abad *et al.* [15]. They observed increasing strength scaling exponents with increasing test temperature, which confirms the results presented in Figure 1b.

3.2 Interface dominated plasticity

To attribute variations in the strength scaling behaviour, especially when interfaces are present which modify apparent deformation mechanisms, rate-dependent experiments offer valuable information. A common approach to gain insight into the thermally activated deformation behaviour of fcc and bcc metals is to determine their strain-rate sensitivity [42]:

$$m = \frac{\partial \ln \sigma}{\partial \ln \dot{\varepsilon}} \tag{1}$$

where σ is the flow stress at a certain strain value and $\dot{\varepsilon}$ is the corresponding strain-rate. To relate a certain *m*-value to a corresponding deformation mechanism, an apparent activation volume (ν) [43] is calculated

$$\nu = \frac{C \cdot k_B \cdot T_{test}}{m \cdot \sigma}, \tag{2}$$

with *C* as a constant related to the microstructure and k_B the Boltzmann constant. To perform such experiments, multiple constant strain-rate tests [42] and/or strain-rate jump (SRJ) tests [44] are conducted. The rate-dependent stress response is used to determine *m*.

As illustrated in Figure 2, conventional coarse grained (cg) or sxx fcc metals exhibit *m*-values in the order of 10^{-3} [45–49]. If internal length-scales for dislocation interaction become smaller, for example by decreasing the grain size (*d*), *m* increases by about one order of magnitude [46,50]. The corresponding activation volume ν (indicated in multiples of the cubed Burger's vector b^3) decreases from values well above 100 b^3 (cg microstructure) to a couple of 10 b^3 in ultrafine-grained (ufg) fcc metals [47,50–54]. This indicates a transition from forest dislocation interactions to dislocation-grain boundary (GB) interactions. A further decrease of the grain size to the nanocrystalline (nc) regime leads to low ν of ~1 b^3 and *m*-values of ~0.1 [47,55–57]. These values are classically attributed to diffusion-driven processes, such as GB-sliding [50,58].

To further investigate the GB contribution in confined sample volumes, Zhang *et al.* [48,49] performed micro-compression tests on sxx and ufg Cu pillars and reported that *m* is strongly dependent on the sample diameter to grain diameter (*D/d*) ratio. While sxx and macroscopic polycrystalline Cu samples show low *m*-values of ~0.002, they reported ~0.10 - 0.15 for *D/d* ranging between 3 and 10. Thus, the high number of interfaces in the deformed volume strongly alters the deformation behaviour [45,50,59] and the yield stress [21–24] of pillars in the fcc case.

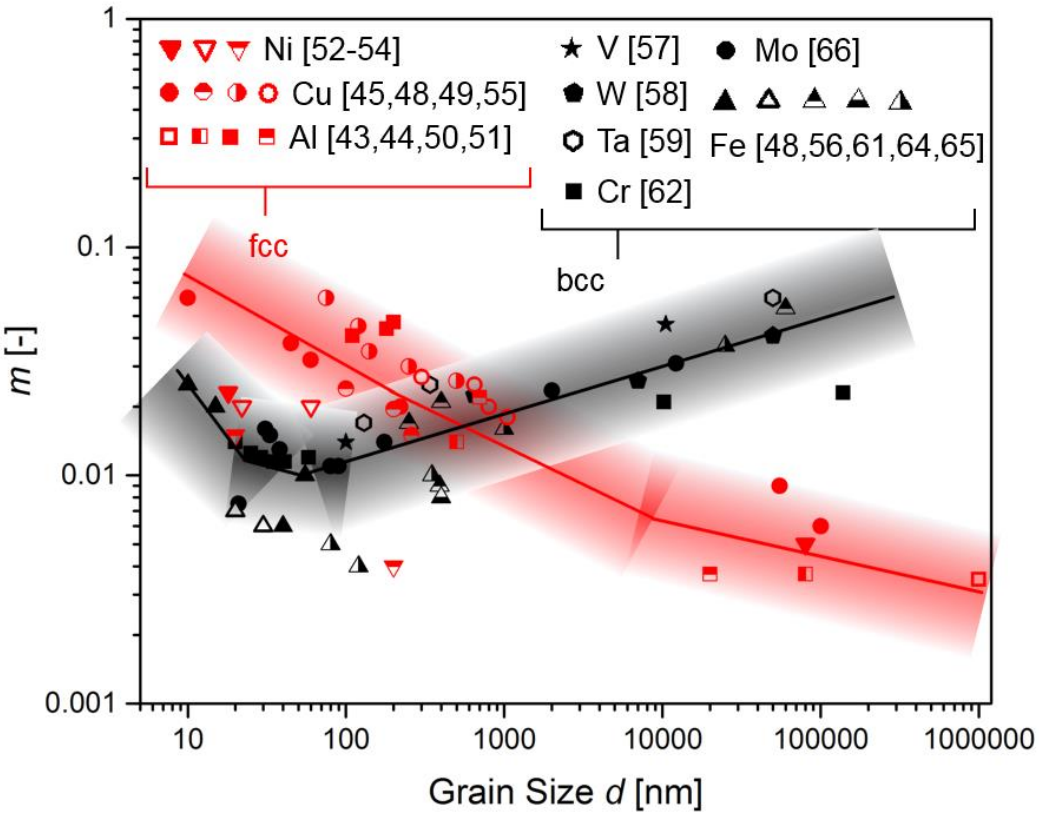

Figure 2: Rate dependence of various fcc and bcc metals. Increasing strain-rate sensitivity with decreasing grain size is observed for fcc metals (red). In bcc metals (black) *m*-values decrease with grain size until a minimum is reached. By overcoming this minimum, an increase in strain-rate sensitivity is observed.

While the situation in fcc metals is well understood, the situation is more difficult in bcc structures [17,18], as shown in Figure 2. In literature, rate-dependent investigations on bcc metals were conducted by Wei *et al.* [51,60–63], May *et al*. [59] and Jia *et al*. [64] performing macroscopic compression tests, as well as by Zhou *et al.* [65], Wu *et al.* [66], Jang *et al*. [67], Malow *et al.* [68] and Yoder et al. [69] performing nanoindentation tests. They addressed the rate-dependent deformation behaviour of V, W, Mo, Ta, Cr and Fe. Decreasing *m* with decreasing grain size was reported (see Figure 2), in contrast to reports on fcc metals [45,50,59]. Reducing the grain size to below ~100 nm, *m*-values were reported to increase again (Figure 2). One might conclude that those differences result from the application of different testing techniques over several length-scales. However, recent work on nc Ni, ufg Al and ufg Nb [44,70,71] revealed direct comparability of constant strain-rate tests and SRJ tests performed by nanoindentation, small-scale tension and compression experiments with macroscopic data.

3.3 Thermally activated deformation behaviour

More recently, Maier *et al.* [41,72] investigated deformation mechanisms in sxx and ufg bcc metals by means of advanced nanoindentation techniques at RT for Cr and W [41], and at elevated temperatures for Cr [72]. For Cr, *m*-values of ~0.07 at RT in sxx samples was attributed to a strong contribution of the Peierls potential (see Figure 3) and a low mobility of screw dislocations [35] which govern the deformation process at low homologous temperatures underneath T_c via the kink pair mechanism [35,73,74]. Increasing thermal activation leads to a decrease of the Peierls potential (σ^*, thermal stress contribution) until at ~$0.2 \cdot T_m$ the critical temperature is reached. Beyond this temperature which depends on strain-rate, impurity content and microstructure [72], screw- and edge dislocations propagate with equal speed. From this point on, typical fcc deformation mechanisms as indicated by the black horizontal line in Figure 3 have been observed.

Comparably lower *m*-values at RT of ~0.02 in ufg samples were referred to a prevailing contribution of the Peierls potential in combination with an increased athermal contribution σ_a due to athermal GB strengthening according to Hall and Petch [75,76], see Figure 3. Overcoming T_c in the ufg state, a further increase of *m* was related to a diminishing contribution of σ^* accompanied by an emerging dominant thermally activated dislocation-GB interaction (blue dotted line). Moreover, σ_a remained mostly constant with increasing temperature due to a thermally stable microstructure [72].

To make the apparent deformation behaviour visible, micro-mechanical experiments are conducted in-situ in an SEM. Thus it appears that site specific sample preparation is required.

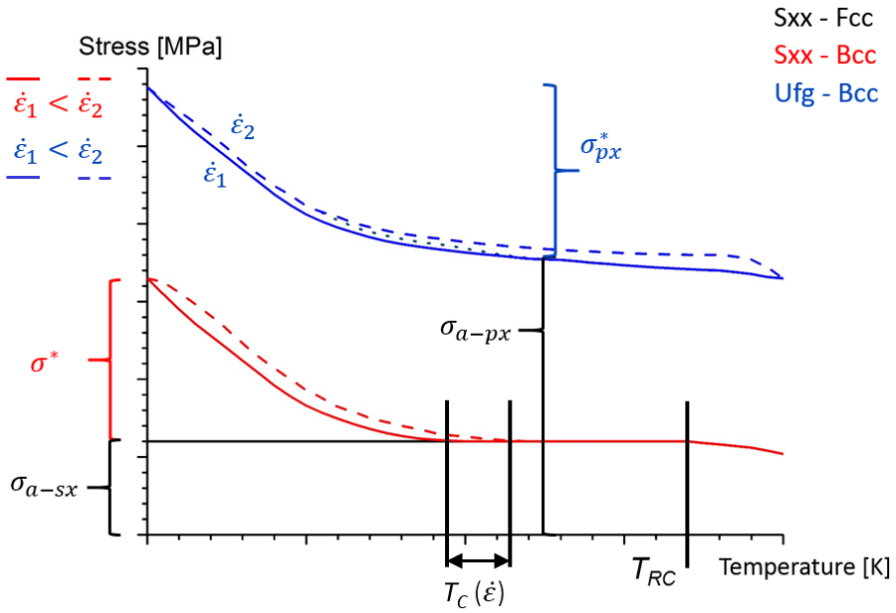

Figure 3: The thermally activated deformation behaviour of sxx (red) and polycrystalline bcc metals (blue). σ^* and σ_a indicate the thermal and the athermal stress contribution, respectively. Dashed lines refer to a stress response at higher strain-rates The image was modified and reprinted from [72].

3.4 Miniaturized sample fabrication using FIB

In order to obtain a free perpendicular view of the electron beam on the compression samples, pillars are placed on a thinned lamella [77]. The individual steps of the FIB fabrication of rectangular, taper-free pillars are illustrated in Figure 4. A rotation angle of 45° of the pillar with respect to the parallel lamella side offers the possibility to monitor the deformation simultaneously on two side faces of the sample (Figure 4). As a first step, coarse cuts are milled into the lamella to obtain rough compression samples, as shown in Figure 4b and c. Remnant tips are subsequently removed by a top down milling step, as demonstrated in Figure 4d and e. Finally, the lamella is put back in its original position and the two perpendicular sample sides and the final height of the pillars are obtained by applying finer polishing steps.

Beside the advantage of site specific sample preparation using FIB techniques as shown in Figure 4, FIB damage caused by the implantation of ions is intensively discussed in literature [78–80]. Preparation induced effects might alter the mechanical properties of millimetre-sized and even micron-sized samples [81]. In contrast to that, Jennings *et al.* [82] reported that size effects are independent of FIB damage. Samples tested within this thesis are large compared to a potentially affected surface depth (typically ~50 nm, [78]) and therefore only a minor influence of a processing induced

size effect is expected. Detailed information about the micromachining process utilizing a FIB is further discussed by Phaneuf [83] and Volkert and Minor [84].

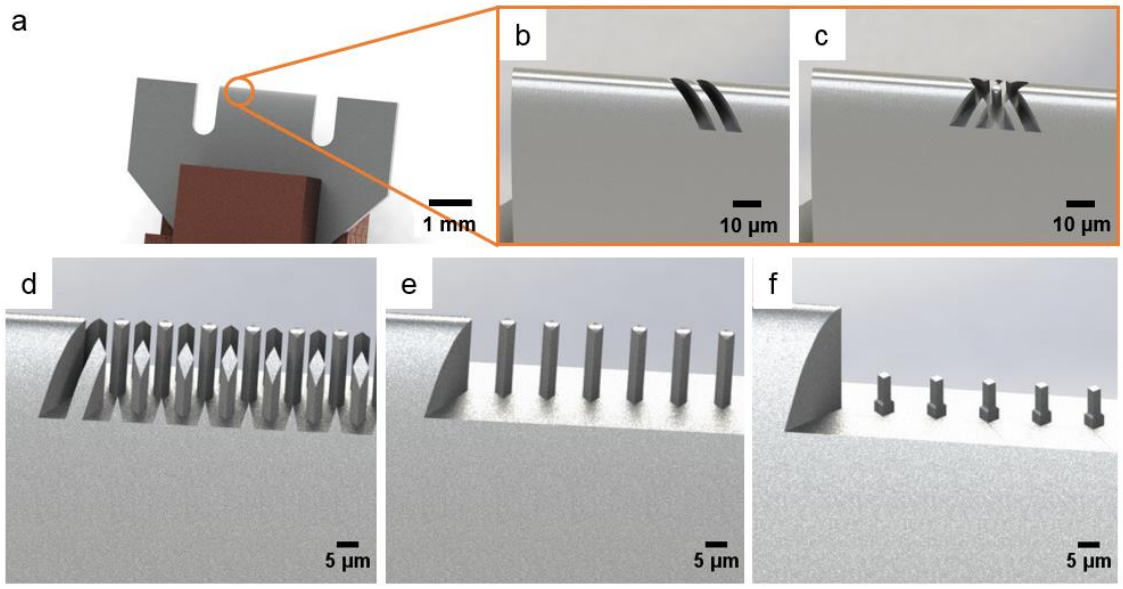

Figure 4: Individual steps necessary to prepare pillar compression samples on a lamella using FIB. The image was reprinted from [77].

3.5 Mechanical testing techniques at non-ambient conditions

3.5.1 Macroscopic compression testing

Macroscopic compression tests were performed ex-situ in air using a universal tensile testing unit (Zwick GmbH & Co. KG, Ulm, Germany) modified with a load reverse tool to a compression device to perform experiments at nominal uniaxial stress states. The samples were held between two WC-Co plates and sample-plate interface friction during deformation was neglected. In order to measure thermally activated processes, tests were conducted at constant strain-rates between 10^{-2} and 10^{-4} s^{-1} for temperatures ranging between RT and 610°C. Loads were measured utilizing calibrated 10 kN and 20 kN load cells (resolution limit < ± 0.5%) for ufg Cr and ufg W samples, respectively, and strains were calculated from recorded time and corresponding crosshead velocity data.

3.5.1 In-situ SEM pillar compression

Temperature dependent quantitative miniaturized in-situ micro-compression tests were carried out inside an SEM (Zeiss LEO 982, Oberkochen, Germany). Pillars smaller than 1 µm were tested with a Hysitron PI85 Picoindenter® using a feedback loop of 200 Hz, while for pillars larger than 1 µm, an UNAT-SEM indenter (Zwick GmbH & Co. KG, Ulm, Germany) with a feedback loop of 64 Hz was utilized, as this device offers the required higher loads. For RT, the indenters were equipped with conductive diamond flat punches (Synton-MDP AG, Nidau, Switzerland) with diameters of ~6 µm and ~8 µm, respectively.

To perform experiments at elevated temperature, a custom-built heating equipment was installed on the existing UNAT-SEM indenter (see **Publication C**). Indenter tips suitable for the heating device were equipped with thermocouples and a rectangular-shaped ~10 · 6 µm² flat punch, as well as a wedge with a length of 120 µm, were subsequently FIB milled.

Stress-strain curves were recorded at strain-rates ranging from 10^{-2} s^{-1} - 10^{-4} s^{-1} and further calculated from the recorded force-displacement data after taking into account corrections for the sample sink-in [85] and the machine stiffness [86]. The top pillar area was used for stress calculations, and the strain refers to initial height of the non-tapered samples [87].

Based on the law of error propagation by Gauss, taking into account multiple independent defective inputs, additional errors in determining engineering stresses were calculated using

$$\Delta\sigma = \sqrt{\left(\left|\frac{\partial\sigma}{\partial F}\right| \cdot \Delta F\right)^2 + \left(\left|\frac{\partial\sigma}{\partial A}\right| \cdot \Delta A\right)^2}, \tag{3}$$

and:

$$\Delta\sigma = \sqrt{\left(\frac{1}{A} \cdot \Delta F\right)^2 + \left(\frac{F}{A^2} \cdot \Delta A\right)^2}. \tag{4}$$

ΔA is given by the squared pixel size error which originates from inaccuracies of determining the sample area. ΔF is estimated by the noise in the data before approaching the contact as upper bound.

3.5.2 Nanoindentation

In order to measure thermally activated processes at various temperatures and multiaxial stress states, nanoindentation SRJ tests [44] were performed using a Nanoindenter G200 (Keysight Technologies, USA) [88]. The device is equipped with a continuous stiffness measurement (CSM) which was used to continuously record the contact stiffness to check the Young's modulus / displacement profile which is horizontal and independent on indentation depth for mechanically isotropic materials. Machine stiffness and tip shape calibrations were performed at RT according to the Oliver-Pharr method [89]. Strain-rate jumps for displacement segments of 500 nm each and strain-rate levels of $5 \cdot 10^{-2}$ s^{-1}, 10^{-2} s^{-1}, $5 \cdot 10^{-3}$ s^{-1} (high temperature) and $5 \cdot 10^{-2}$ s^{-1}, $5 \cdot 10^{-3}$ s^{-1} and 10^{-3} s^{-1} (RT), were performed, respectively. Furthermore, strain-rate controlled tests with a constant strain-rate of $5 \cdot 10^{-2}$ s^{-1} were conducted to compare to results from SRJ tests as well as uniaxial testing techniques. For all tests, the CSM frequency was set to 45 Hz and a harmonic displacement amplitude of 2 nm was superimposed.

For RT testing, a three-sided diamond Berkovich pyramid (imposing ~8% plastic strain, obtained from MicroStar Technologies, Huntsville, USA) as well as a diamond Cube Corner indenter (Synton-MDP AG, Nidau, Switzerland), which imposes ~20% plastic strain [90], were utilised. For high temperature measurements at 100°C, 150°C, 200°C, 250°C and 300°C a Berkovich pyramid tip made of sapphire (Synton-MDP AG, Nidau, Switzerland) was used. Independent heating of sample and indenter was achieved by a laser heating stage (SurfaceTec, Hückelhoven, Germany) and an active water-cooling system. Moreover, the maximum indentation depth for all indents was 2500 nm and tests under non-ambient conditions were performed in an inert gas environment (95% N_2 and 5% H_2) to exclude sampling issues and oxidation effects. Thermal drift was measured in post-test regimes at 10% of the maximum load. Tests for which drift exceeded 0.3 nm/s were not considered. Details of the nanoindentation equipment are found in **Publication B**, **Publication D** and [88].

To facilitate comparison of nanoindentation data obtained with self-similar indenters with uniaxial stress-strain data, following considerations are taken into account within this thesis: The choice of an appropriate value for the constraint factor C^*, which links the hardness to flow stresses, can validate the uniaxial test data. However, if C^* is considered to be in the range of 2.5 - 3, rather than 2.8 used in this

thesis, the change of stress values of ~10% would only insignificantly affect present results and not change any qualitative relations. Moreover, the Young's modulus to hardness (E/H) ratio [91] and the rate-dependence of the tested material [92] affect the load response of the indenter, and might result in additional error. The E/H ratio for the investigated ufg Cr and ufg W is ~70 and ~130, respectively, therefore a possible phase shift of the indenter signal should be only of minor influence.

Furthermore, the plastically deformed volumes vary with the indenter geometry and mechanical properties [93,94]. Lastly, it should be noted that in terms of nanoindentation the induced representative strain will depend on the apex angle of the used tip. Hence, varying capabilities of strain hardening are examined, which affects the stress level [95]. However, as long as the contact stiffness is properly accounted for (indicated by stable hardness and Young's modulus values with indentation depth) the tests can be considered valid and compared to uniaxial stress-strain data.

To conclude, main questions are derived from this short literature review and will be answered in the following chapter termed ‘summary of publications’:

1. There is high demand of micro-mechanical properties obtained by in-situ SEM testing at elevated temperatures. One main goal of the thesis was to develop a custom-built heating device which fits on an existing micro-indenter. In this course, if it is possible to implement a heating device to the existing indenter system, several questions arise. Is it possible to perform experiments at elevated temperatures with the aim to study thermally activated deformation mechanisms utilizing the existing indenter? Which temperatures are achievable? Is it possible to perform temperature calibration by using a finite element simulation approach?
2. The strength scaling behaviour in bcc metals is suspected to be related to a thermal stress component. If this is true, does the strength scaling behaviour of single crystalline chromium fit to literature data?
3. It is reported that the increasing surface-to-volume ratios in small scale plasticity alter the strength scaling behaviour. Do these findings hold true for ultrafine-grained pillars, where interfaces in terms of grain boundaries additionally affect the strength scaling behaviour? Which role is attributed to interface spacing and free surfaces?
4. In refined microstructures, deformation mechanisms are not necessarily controlled by dislocation mediated plasticity. Which mechanisms are present in the investigated model materials? Does thermal activation additionally alter apparent mechanisms?

4. List of publications

The following list of publications is split into two parts. First, main-author papers are presented where the majority of work (sample preparation, conducting and analysing experiments, composition of the text) was done by myself. Main author publications are additionally added in chapter 2 of the thesis. Co-author publications, where only parts of the work were contributed by myself, are listed afterwards and are separately added in the appendix. In addition to the publication list, a remark is given to underline the input of my contributors.

4.1 Contributions as main-author:

Publication A:

Interplay between Sample Size and Grain Size: Single Crystalline vs. Ultrafine-grained Chromium Micropillars

R. Fritz, V. Maier-Kiener, D. Lutz and D. Kiener in *Materials Science & Engineering A* 674 (2016) 626-633.

In this publication, the strength scaling behaviour of single crystalline and ultrafine-grained chromium (grain size ~160 nm) is analysed in terms of in-situ pillar compression experiments. For both microstructures, a strength scaling behaviour where ‘smaller is stronger’, was observed.

Publication B:

Dominating Deformation Mechanisms in Ultrafine-grained Chromium across Length-Scales and Temperatures

R. Fritz, D. Wimler, A. Leitner, V. Maier-Kiener and D. Kiener in *Acta Materialia* 140 (2017) 176-187.

Apparent deformation mechanisms in ultrafine-grained chromium are investigated in Publication B based on experiments spanning over several length-scales and temperatures. A comparison to single crystalline samples revealed a direct influence of dislocations interacting with grain boundaries.

Publication C:

Development and Application of a Heated In-situ SEM Micro-Testing Device

R. Fritz and D. Kiener in *Measurement* 110 (2017) 356-366.

In Publication C the development of a custom-built heating device is discussed, and a new finite element approach is presented to calibrate contact temperatures. Exemplary pillar compression and cantilever fracture experiments further demonstrate the functionality of the device.

Publication D:

Interface-dominated Strength Scaling Behaviour in Ultrafine-grained Tungsten Samples

R. Fritz, A. Leitner, V. Maier-Kiener, R. Pippan and D. Kiener, submitted (10.08.2017) submitted to a SCI Journal.

Based on Publication A, this work identifies the strength scaling behaviour of single crystalline and ultrafine-grained tungsten samples (grain size ~500 nm). The scaling behaviour is discussed in terms of a probable influence of free surfaces and strain hardening. Finally, deformation mechanisms are related to single crystalline and ultrafine-grained chromium.

4.2 Contributions as co-author:

Publication E:

Novel Methods for the Site Specific Preparation of Micromechanical Structures

S. Wurster, R. Treml, R. Fritz, M. W. Kapp, E. Langs, M. Alfreider, C. Ruhs, P. J. Imrich, G. Felber and D. Kiener in *Practical Metallography* 52 (2015) 3 131-146.

Publication F:

The influence of microstructure on the cyclic deformation and damage of copper and an oxide dispersion strengthened steel studied via in-situ micro-beam bending

C. Howard, R. Fritz, M. Alfreider, D. Kiener and P. Hosemann in *Materials Science and Engineering A* 687 (2017) 313-322.

4.3 Remarks

Beside the following remarks, all co-authors additionally contributed to the work by proof-reading the text. The main idea for all publications originates from my supervisor, D. Kiener.

Publication A

D. Lutz performed TEM investigations and V. Maier-Kiener supported the authors with her knowledge on bcc metals.

Publication B

Nanoindentation experiments were conducted by V. Maier-Kiener and A. Leitner. D. Wimler performed macroscopic compression experiments. V. Maier-Kiener further contributed with her profound knowledge on thermally activated deformation behaviour.

Publication D

Nanoindentation experiments were performed by A. Leitner. R. Pippan and V. Maier-Kiener contributed with their wide knowledge about fracture- and deformation behaviour of bcc metals.

5. Summary of publications

The following pages summarize the obtained mechanical properties of the metals investigated in this thesis, the development of the heatable in-situ micro-testing device, as well as main results and significant findings of the PhD thesis. The influence of grain boundaries and free surfaces on the strength scaling behaviour of miniaturized specimens is discussed by investigating the bcc model materials Cr and W. In the following subsections, light is shed on apparent deformation mechanisms responsible for the observed strength scaling behaviour. At the end of this chapter, the main findings will be summarized and suggestions how to further improve the heated in-situ micro-testing device will be given.

5.1 Materials

The bcc model materials examined in this thesis are Cr and W. Characteristic material properties are summarized in Table 1.

Table 1: Characteristic properties of Cr and W.

	Abbreviation	Cr	W	Ref.
Density	ρ^* [kg/m³]	7200	19300	[96,97]
Young's modulus	E [GPa]	294	380-420	[98,99]
Shear modulus	G [GPa]	115	160	[100,101]
Friction stress at RT	τ^* [MPa]	~50	~345	[38,102]
Poisson ratio	ν [-]	0.21	0.28-0.3	[98,99]
Melting temperature	T_m [°C]	1890	3410	[101]
Critical temperature	T_c [°C]	~160	~530	[35]
Ductile-to-brittle-transition temperature	DBTT [°C]	~320-390	~675	[103,104]
Lattice constant	a [m]	$2.885 \cdot 10^{-10}$	$3.165 \cdot 10^{-10}$	[97,98]
Burger's vector	b [m]	$2.50 \cdot 10^{-10}$	$2.74 \cdot 10^{-10}$	[101]
Hall-Petch constant	$k_{H\text{-}P}$ [MPam$^{1/2}$]	1.38	1.86	[95,100]

Both metals are non-ferromagnetic and show semi-brittle deformation behaviour in the recrystallized states. They vary in density, Young's modulus and melting temperature, and therefore the critical temperature and their friction stress at RT are

different. This situation is particularly of interest to study the deformation behaviour of bcc metals over a wide range of relative temperatures [13]. Besides investigations of intrinsic material properties [11] and their influence on the strength scaling [13] and deformation behaviour [41,66,72], interfaces in terms of GBs were integrated into the microstructure in this thesis. To reach an ufg state, microstructural refinement processes such as severe plastic deformation (SPD) are commonly applied. Here, the high pressure torsion (HPT) deformation process [105–110] was utilized to break down the materials initial interface spacing from several microns to a few hundreds of nm. The refinement process happens under high hydrostatic pressure (~4 GPa) and elevated deformation temperature (200°C for Cr, 600°C for W). Samples were deformed in a quasi-constrained setup [105] between two anvils to prevent crack formation, especially for semi-brittle materials such as Cr and W. After HPT processing, a deformed disk as shown in Figure 5 was obtained, featuring a diameter of 30 mm and a thickness of 7 mm. An equivalent strain at a disk radius of 14 mm of 36000% (50 rotations, 0.4 rpm) and 7500% (5 rotations, 0.2 rpm) was achieved for Cr and W, respectively.

On top of the HPT cross-section, the radius-dependent hardness is shown, exemplarily for ufg W (Figure 5). To achieve gradient-free sample volumes in macroscopic samples for testing ($2 \cdot 2 \cdot 3$ mm³ in size), specimens were cut out from a constant disk radius of 12-14 mm using electron discharge machining (EDM), as shown in Figure 5. Furthermore, a lamella-shaped sample was cut out of the disc to fabricate micromechanical test samples by subsequently using the FIB [77].

The grain size of the HPT deformed samples was determined using backscattered electrons (BSE) and electron backscattered diffraction (EBSD) imaging, as well as transmission electron microscopy (TEM) investigations (for Cr). The microstructures obtained by EBSD are shown in Figure 6a and b for ufg Cr and in Figure 6c and d for ufg W. The corresponding GB maps reveal a majority of large angle GBs (~87%) within the investigated metals. The average grain sizes were determined using area equivalent circle diameters resulting in 160 ± 51 nm and 480 ± 230 nm for Cr and W, respectively. For details see **Publication A** and **Publication D**. In both cases, grains are slightly elongated but no pronounced texture was observed.

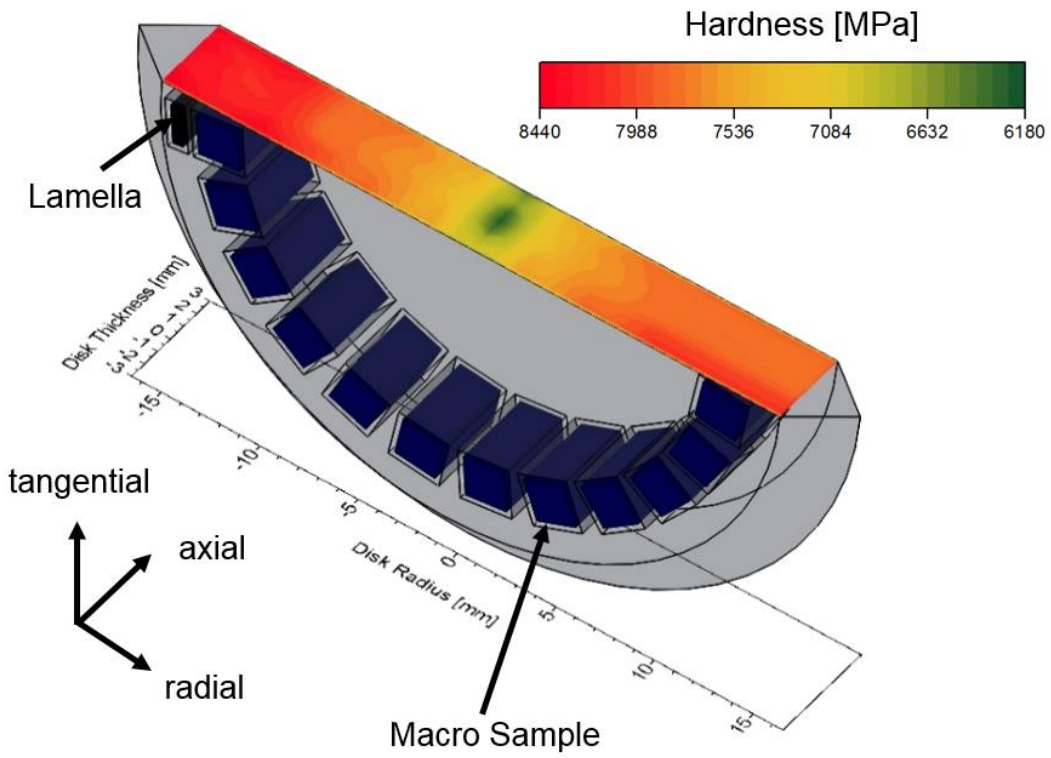

Figure 5: Half of a HPT-deformed W disk with corresponding hardness map. EDM was used to cut a lamella (black – left side) from the HPT disk for FIB pillar preparation from a disk radius of 14 mm and several macroscopic compression samples from a radius range between 12 mm and 14 mm. The compression axis is the axial direction of the HPT sample.

To facilitate comparison of macroscopic compression samples and the influence of interfaces in ufg samples, nanoindentation and pillar compression tests were performed and compared to the deformation behaviour of the single crystal situation. Therefore, sxx samples of Cr and W were aligned in either (100) or (110) crystal orientation to test multiple slip orientations. The hardness of the initial and the HPT deformed microstructures were analysed using nanoindentation and Vickers micro-hardness testing. Results are summarized in Table 2.

To further correlate and separate deformation mechanisms to contributions of a thermal stress component, dislocation mediated plasticity, crack nucleation and propagation, or diffusional processes, experiments were conducted over a wide range of relative temperatures. Therefore, the existing in-situ micro-testing device was equipped with a custom-built heating device to enlarge present temperature ranges and to perform micromechanical experiments at elevated temperature.

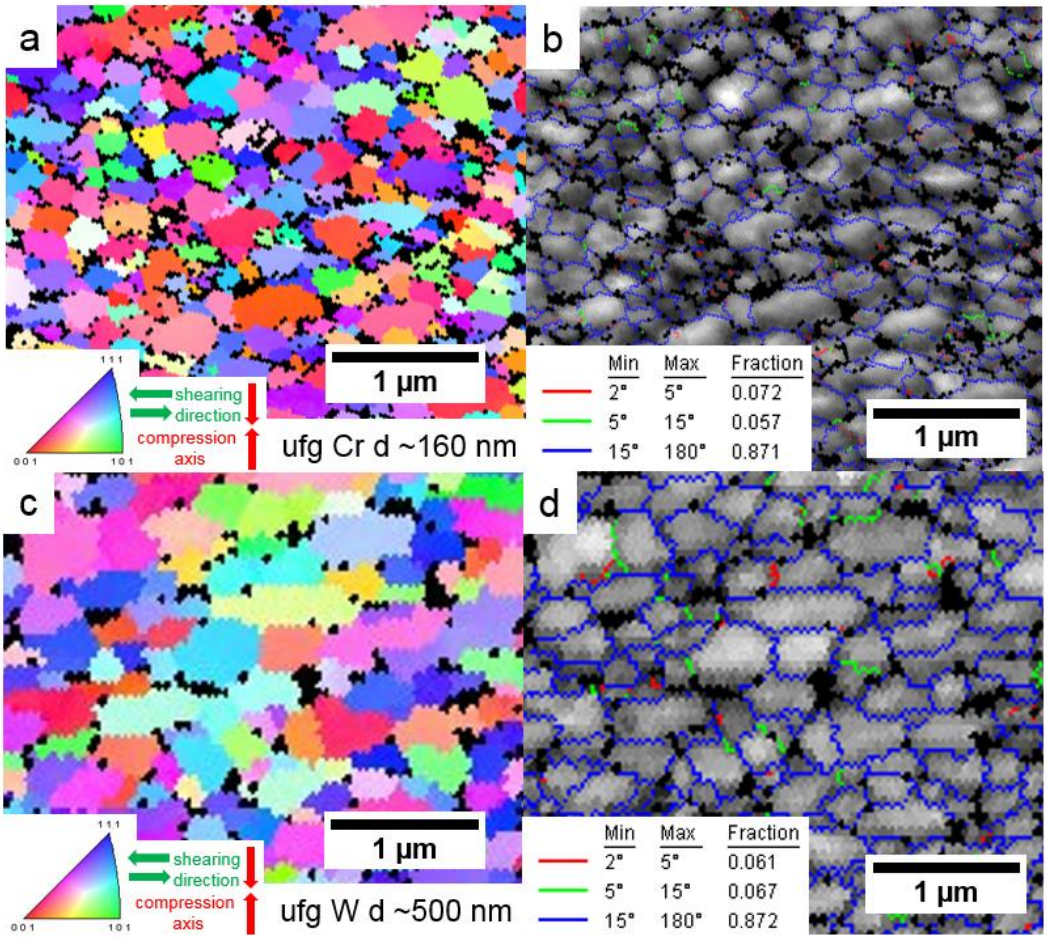

Figure 6: The microstructure of the investigated ufg material. EBSD images and corresponding grain boundary maps for ufg Cr (a, b) and ufg W (c, d). The average grain sizes were ~160 nm ± 51 nm and 480 nm ± 230 nm for ufg Cr and W, respectively. In both cases, ~87% of grain boundaries are large angle grain boundaries.

Table 2: Bulk hardness values of Cr and W obtained by nanoindentation and Vickers micro-hardness testing.

Sample	Method	Hardness [GPa]
sxx Cr (100)	Nanoindentation	1.6 [72]
as-received polycrystalline Cr (d~200 µm)	Vickers	1.2 ± 0.04
ufg Cr, r ~14 mm	Vickers	4.4 ± 0.10
ufg Cr, r ~12 mm	Vickers	4.2 ± 0.10
sxx W (110)	Nanoindentation	5.0 ± 0.12
as-received polycrystalline W (d~5 µm)	Vickers	4.3 ± 0.18
ufg W, r ~14 mm	Nanoindentation	8.5± 0.36

5.2 Development of the heated in-situ micro-testing device

One of the main goals of the thesis was to develop a custom-built heating equipment to fit on an existing in-situ micro-testing device which is located in an additional cap inside an SEM (Figure 7a). The present situation is as follows: The sample is mounted on a separately controlled stage (Figure 7b). The UNAT-SEM micro-indenter used for testing is shown in Figure 7c, already equipped with the heating device. Figure 7d displays details of heated parts in the SEM chamber.

The development process of the heating device is described in detail in **Publication C**. The three main parts regarding development, namely material selection, temperature control and numerical simulation, and of course, in-situ testing at elevated temperature, are summarized below.

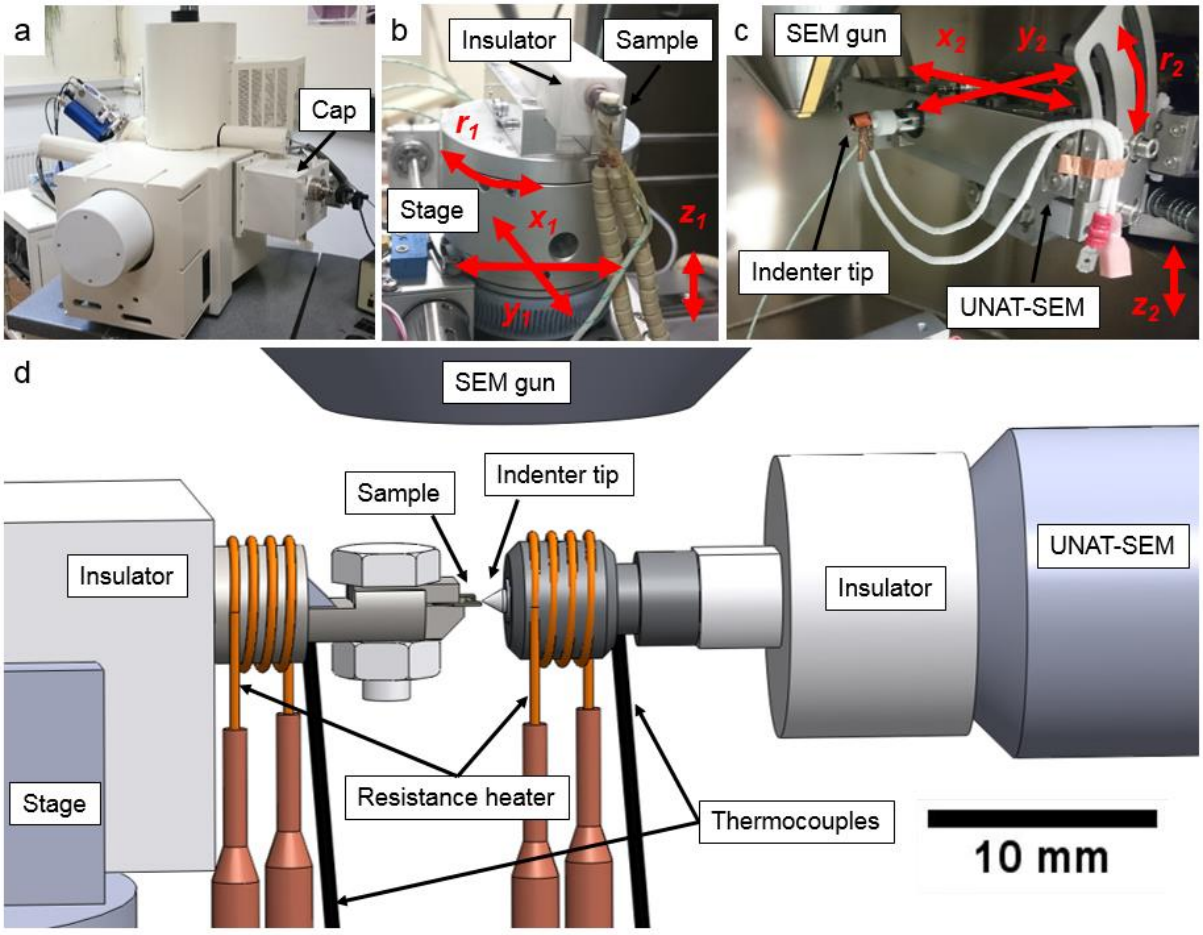

Figure 7: Schematic of the present high temperature in-situ SEM testing setup. (a) Adapted SEM with cap (right) containing the micro-indenter and positioning stage. SEM stage (b) and micro-indenter (c), adapted with custom-built heating devices. Red arrows demonstrate available positioning axes. (d) Detailed schematic of heated parts inside the SEM chamber. The figure was reprinted from **Publication C**.

5.2.1 Material selection

The heating device operates in vacuum atmosphere inside the SEM, hence material restrictions in terms of vapour pressure and magnetic properties need to be considered. Furthermore, if two individual materials get into contact at elevated temperatures, their service temperature, oxidation issues, chemical reactions, diffusional processes, and loss of strength and creep have to be carefully taken into account. The main advantage of performing micro-mechanical experiments in-situ in the SEM is the observation of detailed deformation mechanisms in confined test volumes. Therefore, focussing the electron beam on the sample is of major importance and issues regarding drift induced by electrical charging and/or thermal mismatches must be avoided. Additionally, high demand for minimized material volumes to enable localized heating to permit fast heating rates, as well as requirements regarding operational space inside the SEM have to be met. Once material properties of the indenter tip and the sample are balanced, issues in terms of an appropriate joining technology need to be examined. In the present case, indenter tips were glued to their holders by utilizing a ceramic adhesive. Thermocouples were brazed on the respective holders utilizing tin-free brazes and the lamella-shaped samples were clamped to the holder with Macor® ceramic screws (see Figure 7d and **Publication C**).

Heating the sample and the indenter was achieved by forming Konstantan© filaments to coils which were looped around the holders to stay in contact with them. A dual-output DC power supply was connected with copper cables via signal-feedthroughs to the vacuum chamber. The insulated cables transferred electrical energy to the resistively-heated coils that further transported heat to the sample and the indenter.

5.2.2 Temperature control and numerical simulation

Thermocouples were connected to a data logger that converted voltage into temperature. The data of the power supply and the recorded temperatures were controlled by a custom-coded LabVIEW® program which stores all datasets in a convertible text file. The LabVIEW® code is included digitally on the storage medium located at the end of the thesis. Temperature control was achieved using a PID feedback loop and desired temperatures up to 300°C were reached within 30 min. Once a stable temperature is reached, temperature matching is achieved by bringing

sample and indenter into contact and subsequently examining temperature shifts. By minimizing those temperature shifts, displacement drifts are corrected. Brazing thermocouples on micron-sized samples is challenging, and the real temperature at the contact will remain unknown. To avoid such inaccuracies, individual temperature calibration techniques are inevitable to determine and match contact temperatures [111].

For the first time, temperature calibration by using a finite element simulation approach was conducted in this thesis. 3D data which was recreated after the original parts was loaded into the finite element program Abaqus to conduct heat flow calculations. Convection within the vacuum chamber was neglected and characteristic radiation properties of each material as suggested in [112] were chosen. A constant direct current at the sample and the indenter side were used to reach constant temperatures at the thermocouples after heating times of 3600s. Beside separately heating sample and indenter in out-of-contact mode, simulations were conducted where sample and indenter were brought into contact (Figure 8), displaying equilibrated thermocouple temperatures (T_1^I equals T_1^S). At the contact point shown in detail in Figure 8b, large temperature gradients arose. They introduced displacement drifts that need to be minimized before conducting an experiment.

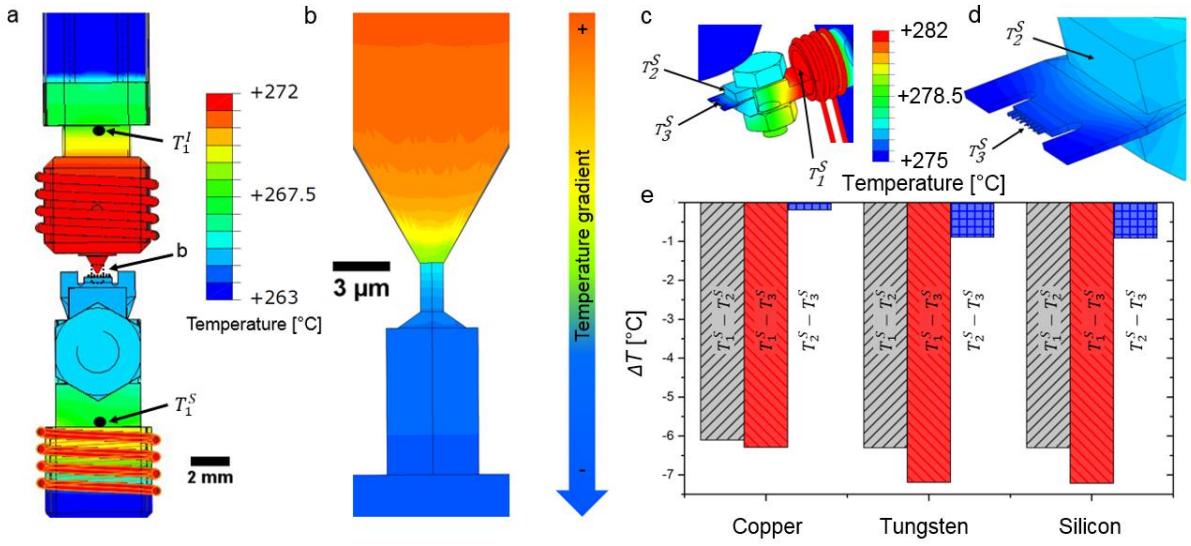

Figure 8: Although the thermocouples T_1^S and T_1^I are at the same temperature (a), a large temperature gradient resulting in thermal drift occurs when bringing sample and indenter in contact. (b) Detailed view of the contact situation revealing a large temperature gradient. (c) and (d) indicate local temperature distribution and positions of the temperature measurement. The influence of varying specimen material on temperature gradients is shown in (e).

To underline the importance of temperature calibration, the tested specimen material was varied and temperature gradients were analysed as demonstrated in Figure 8c. T_2^S and T_3^S indicate individual positions of temperature measurement on the specimen fixation and directly at the pillar.

By heating different specimens with different thermal conductivity such as Cu, W or Si, it became evident that samples with high thermal conductivity alike Cu allow lower temperature gradients compared to W or Si (Figure 8d). Finally, the simulated temperature mismatch between thermocouple and sample is balanced in terms of heating atop the thermocouple temperature to achieve the desired sample temperatures. Nonetheless, it is concluded that beside geometrical issues regarding sample and holders, thermal properties strongly influence the temperature distribution. It is noteworthy that for different materials unique temperature gradients arise. Therefore, new simulation approaches are necessary to predict individual temperature gradients. Further details of temperature calibration are discussed in **Publication C**.

5.2.3 Conducting experiments at elevated temperature

Beside numerous in-situ and ex-situ experiments at RT on Cr and W, micro-pillar compression tests and notched cantilever fracture experiments were conducted on sxx and ufg Cr at elevated temperature (see Figure 9) by utilizing the heating device to demonstrate its functionality and to further investigate thermally activated deformation behaviour.

Figure 9a shows engineering stress-strain curves of 2 µm sized sxx and ufg Cr pillars obtained at various strain-rates at RT, while Figure 9b shows engineering stress-strain curves of 4 µm sized pillars recorded at 230°C. Related nanoindentation hardness data obtained using a Berkovich indenter (imposes ~8% plastic strain) are included as horizontal lines at the respective temperatures. Comparison of stress-strain data between RT and 230°C reveals decreased flow stresses for sxx and ufg pillars, and a diminishing work hardening for the pillars at elevated temperature. Figure 9c displays the stress-strain response of macroscopic ufg samples tested at a constant strain-rate of $3 \cdot 10^{-3}$ s^{-1} at different temperatures. The flow stress decreases with increasing temperature, and the strain hardening behaviour is less pronounced at elevated temperatures, in accordance with the micro-pillar data. Figure 9d presents bending stress vs. displacement curves of cantilever fracture experiments performed

on ufg Cr at RT (black) and 230°C (red). Yield stresses of uniaxial deformed samples (1100 MPa at RT and 950 MPa at 230°C) and cantilever fracture experiments (1130 MPa at RT and 910 MPa at 230°C) indicate comparable plastic limits obtained by different testing techniques on ufg Cr.

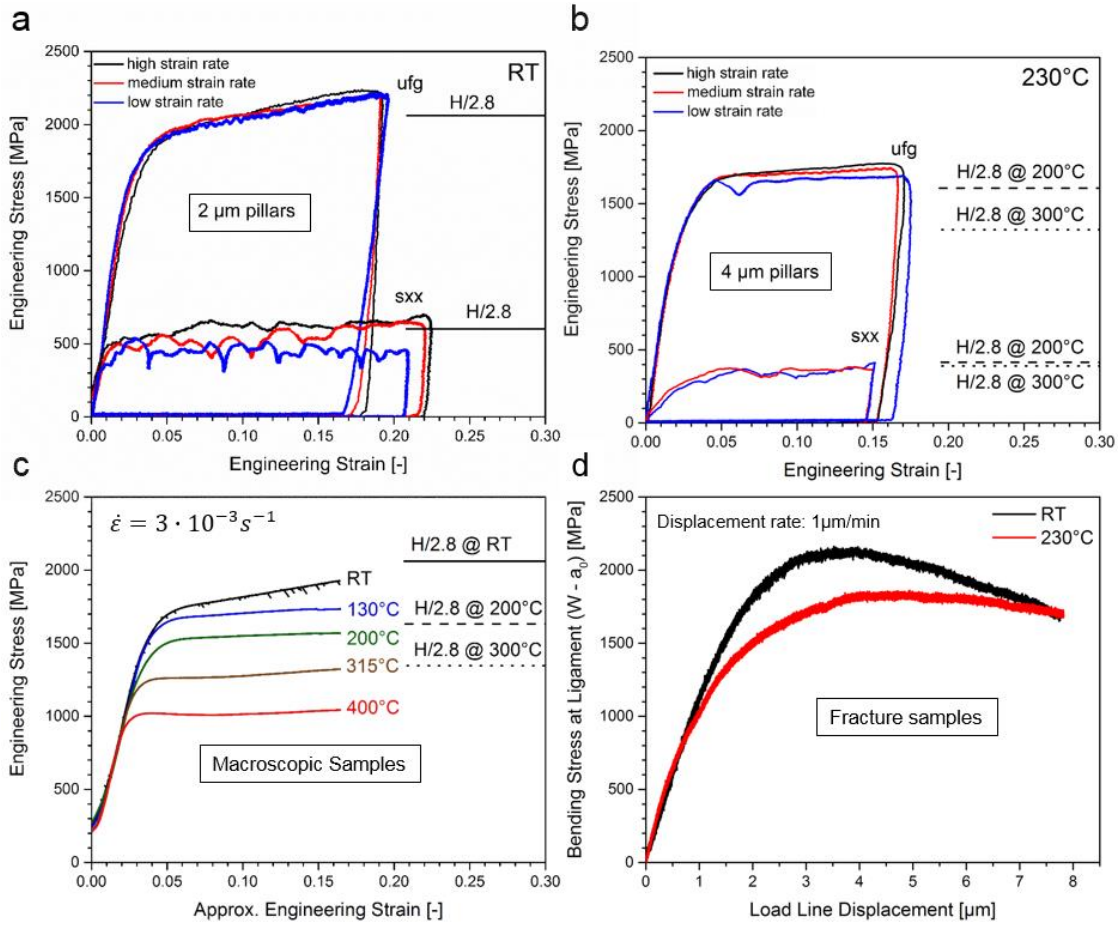

Figure 9: Engineering stress-strain curves obtained by (a, b) in-situ micro-pillar compression, (c) ex-situ macroscopic compression experiments and (d) in-situ cantilever fracture experiments of sxx and ufg Cr compared at RT and elevated temperature.

Elevated temperature data obtained on sxx and ufg Cr were used to study apparent deformation mechanisms. Additionally, the contribution of GB's and the material dependent friction stress was examined. Moreover, the specimen size was varied over several length-scales to investigate a possible interplay of sample size and grain size. Thus, the contribution of the present interface spacing and free surfaces to specific strength scaling behaviour in ufg Cr and W were discussed in detail in **Publication A** and **Publication D**. Results and a material independent mechanistic description of the strength scaling behaviour incorporating the lattice friction stress,

strain hardening, Hall-Petch strengthening and a source-controlled strength are summarized below.

5.3 How grain boundaries and free surfaces alter the strength of miniaturized specimens

Besides performing macroscopic compression experiments and nanoindentation tests utilizing a Cube Corner and a Berkovich indenter, non-tapered rectangular pillars in the size range between ~150 nm and ~5 µm and an aspect ratio of 3:1 were milled for sxx and ufg Cr and W utilizing a dual-beam SEM-FIB workstation. Displacement-controlled tests were conducted at constant displacement rates that were adapted to the pillar geometry in order to reach a constant nominal strain rate of $3 \cdot 10^{-3}\ s^{-1}$, thereby excluding strain rate influences.

Figure 10a and b display engineering stress-strain curves of sxx and ufg Cr, respectively. The data for the bulk yield stress (0.02% plastic strain) of sxx Cr in (100) orientation is reported from tensile tests by Sameljuk *et al*. [113] as ~290 MPa, a much lower value as observed for present samples. This difference is attributed to incipient effects on sample size, as well as the large amount of strain hardening between the yield stress and an engineering strain of ~8%. For pillars larger than 2 µm, the stress-strain curves show reasonably continuous plastic deformation with occasional burst events, while for smaller samples pronounced load drops occur. At pillar sizes below ~1 µm serrated flow is evident and load drops are observed.

Nanoindentation tests on ufg Cr utilizing a Berkovich indenter resulted in a strength of ~2050 MPa. Bulk compression samples and pillars with diameters of 4 µm show comparable yield strengths of ~2000 MPa and continuous plastic deformation. However, alignment of bulk samples was hindered due to lower stiffness of the compression equipment, resulting in a sample misalignment of ~1°. Therefore, the elastic loading stiffness of bulk samples is reduced and not comparable with pillar compression experiments.

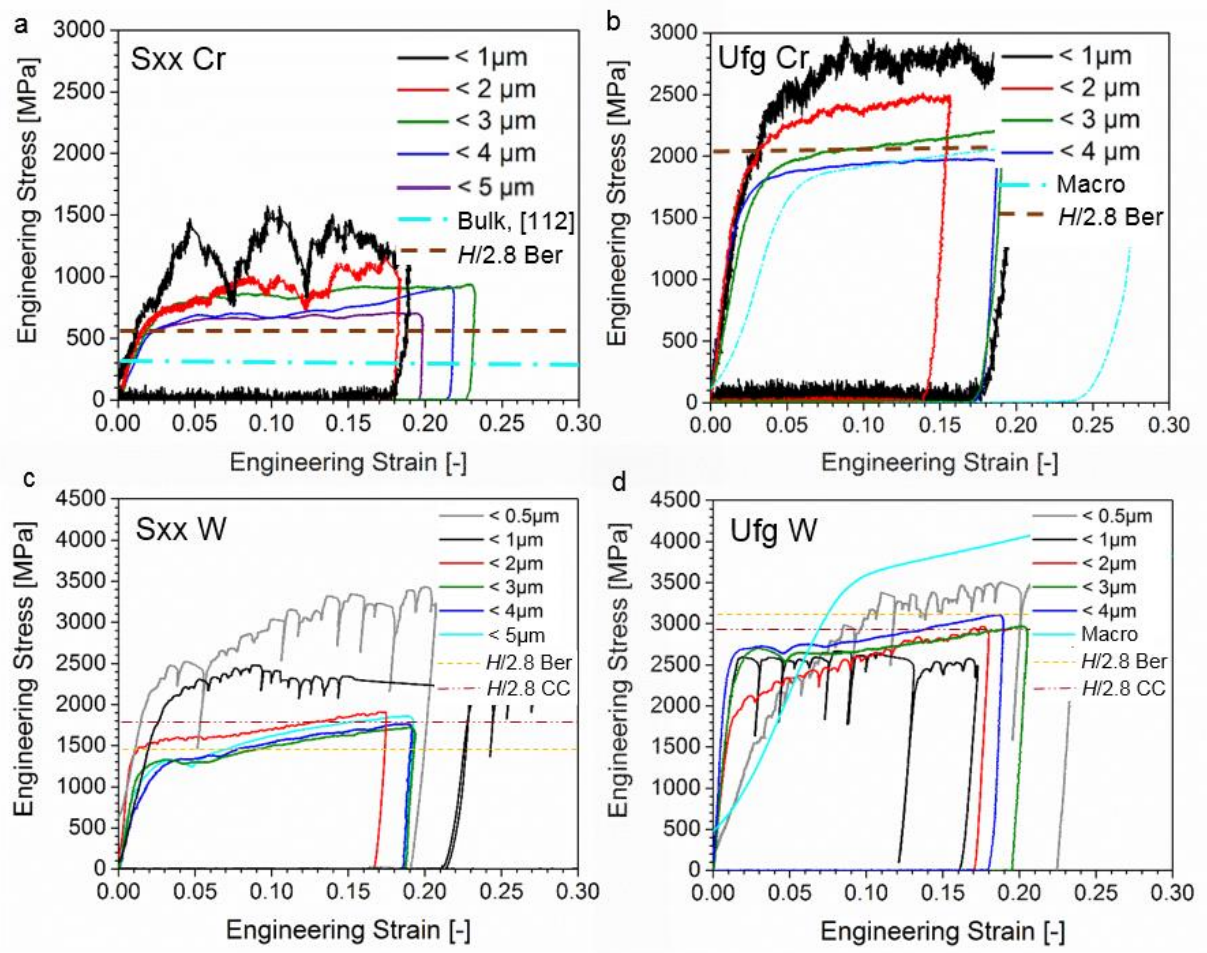

Figure 10: Representative engineering stress-strain curves of sxx Cr (a), ufg Cr (b), sxx W (c) and ufg W (d). While for the sxx case the strength generally increases with decreasing sample size, interfaces contribute to a somewhat controversial strength scaling behaviour in ufg Cr (b) and ufg W (d).

In the case of decreasing pillar diameters, the yield strength of ufg Cr pillars increase slightly. The stress-strain curves show features comparable to those in sxx samples, for instance, serrations and load drops for the same experimental setup.

Figure 10c and d show engineering stress-strain curves of (100) oriented sxx and ufg W, respectively. In both cases large samples show continuous flow curves. Generally, sxx W pillars deform comparably to sxx Cr pillars. A contrary behaviour was observed for ufg W samples (Figure 10d), where flow stresses decrease with decreasing sample sizes. At sample diameters of ~3 µm, first serrations in the stress-strain curves were observed. Further decreasing the sample size led to an apparent increase of flow stress values and pronounced load drops were detected, comparable to small sxx Cr and W samples. The gap in flow stress values between sxx and ufg Cr and W results from microstructural refinement according to Hall and Petch [75,76].

Estimation of a yield stress value, for example, for W using a friction stress of 345 MPa [38], a mean grain size of 480 nm and a Hall-Petch coefficient of 1.86 $MPam^{-1/2}$ [95] resulted in ~3000 MPa, in close agreement with ufg W bulk data obtained from macroscopic compression tests and nanoindentation data.

Individual stress values were obtained using different indenter tip geometries. The gap between stress values of Berkovich and cube corner indenters was explained by a varying apex angle of the used tip. Moreover, varying capabilities of strain hardening are examined which directly affect the stress level [95].

Figure 11 presents post deformation SEM images (a-e) and corresponding cross sections (f-j) of various ufg W samples. Here, the sample size decreases accordingly to the presented alphabetic order.

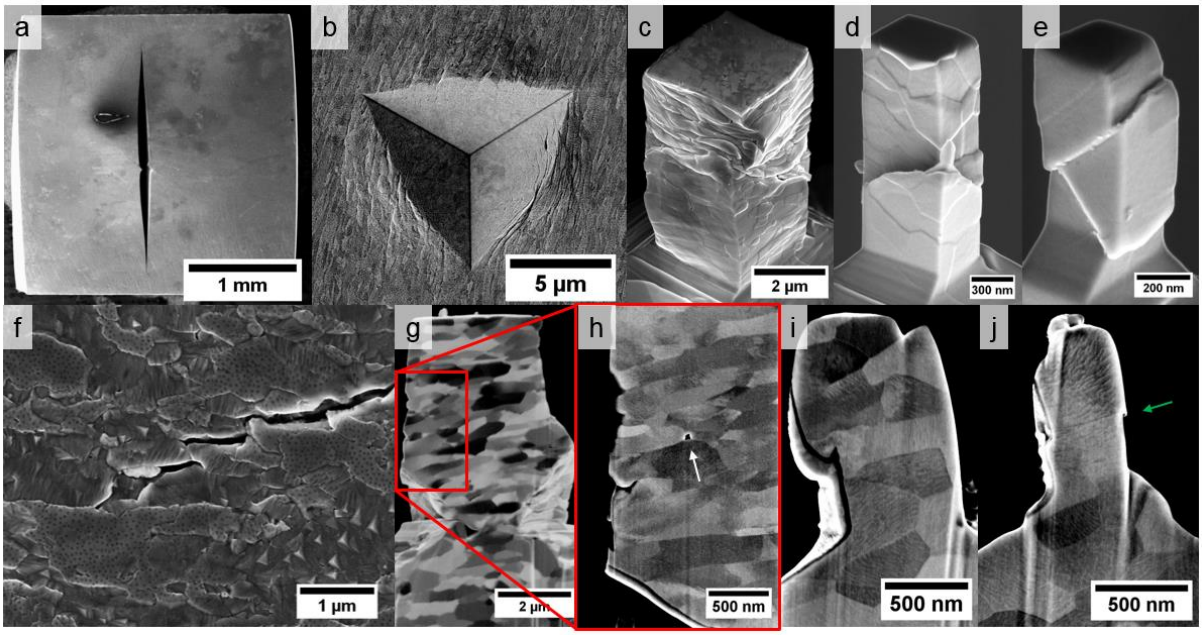

Figure 11: Post-compression SEM images (a-e) and corresponding cross sections (f-j) of various ufg W samples. The white arrow indicates decohesion at a grain boundary triple junction while the green arrow marks an observed slip step within the smallest pillar.

In macroscopic bulk samples, as exemplarily shown for a sample deformed at RT in Figure 11a, crack initiation and growth was observed up to 450°C. By overcoming that temperature, plastic deformation without crack initiation and propagation was noted. Figure 11b shows a residual Berkovich indent and Figure 11c-e display ufg pillars of various sizes, where in Figure 11c the sample size is larger than the grain size. In Figure 11d the sample size equals the grain size and Figure 11e demonstrates

sxx deformation in submicron-sized ufg pillars, where the sample size in the present case was smaller than the grain size. The cross section in Figure 11f reveals intercrystalline failure at GBs, which is commonly obserrved for ufg W [104,114]. Figure 11g and h display a cross section and a detailed view of the grain interior of the pillar shown in Figure 11c. The white arrow indicates decohesion and failure at GB triple points, which was observed through all ufg W samples at low temperatures. Figure 11i and j represent cross sections of pillars shown in Figure 11d and e. Once the sample size is reduced to the average grain size (Figure 11i) or below (Figure 11j) the probability for crack nucleation at GB junctions decreases. Pronounced plasticity is observed for the smallest pillar (300 nm, Figure 11j) and sxx-like slip steps, indicated by the green arrow are visible.

To discuss the observed deformation behaviour over several length-scales, flow stresses at 8% plastic strain are plotted either against the sample diameter (Figure 12a for Cr) or the plastically deformed volume of individual experiments in Figure 12b for W. 8% plastic strain were chosen to allow comparison with hardness tests performed utilizing a Berkovich indenter and to include the strain hardening behaviour within the first few percent of deformation to be comparable with previous bcc studies [13,14,28,31].

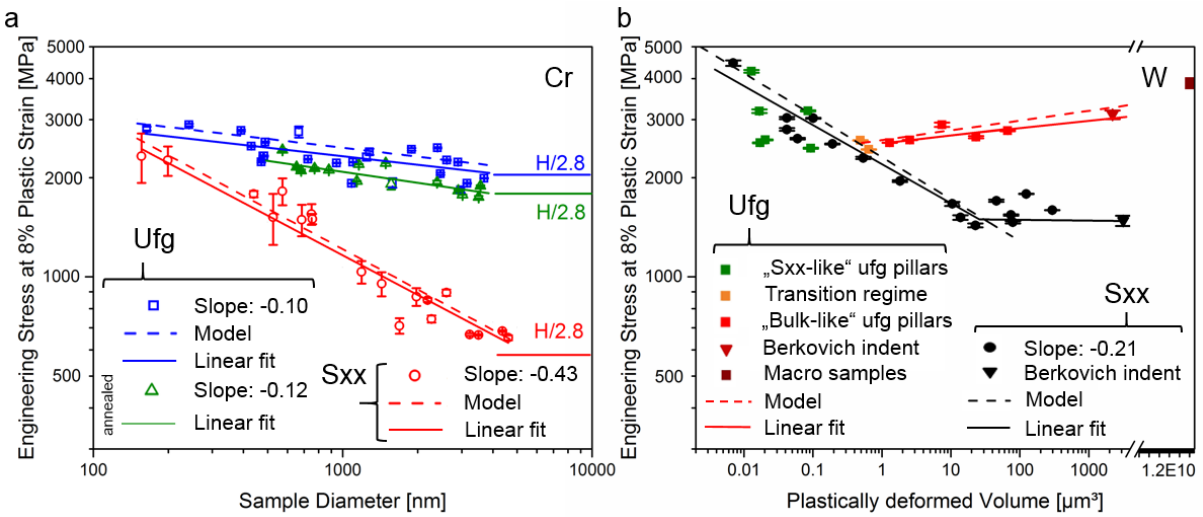

Figure 12: Schematic of the obtained strength scaling behaviour in Cr (a) and W (b). All data points display stress values at 8% plastic strain. (a) The red (sxx), green (annealed ufg) and blue (ufg) lines reproduce the observed trends in strength scaling behaviour. (b) The strength scaling behaviour of sxx W is plotted in black, while ufg data is marked by three different colours, indicating three different regimes. Dashed lines refer to the mechanistic description of the strength scaling behaviour.

In Figure 12a, horizontal lines represent bulk strengths obtained by nanoindentation. The slopes of linear fits give the power-law scaling exponents, which are 0.43 ± 0.03 and 0.10 ± 0.02 for sxx and ufg Cr, respectively. Even though the scaling behaviour of sxx bcc metals is well investigated, Cr has not been examined so far. Thus, it is interesting to note that this value fits well into the concept of Schneider *et. al*. [13], where the power-law exponent was plotted against the relative critical temperature (~0.68 · T_c for Cr) predicting a power-law scaling exponent of ~0.41.

In the case of ufg Cr pillars, the slope decreases due to the presence of GBs and higher dislocation densities which stem from HPT processing. Still, a slight scaling exponent is observed. The point of intersection of the two fit lines indicates the transition to sxx behaviour. It occurs at a pillar size of ~150 nm, which is in good agreement with the grain size of the material (~160 nm). Error bars in both diagrams result from uncertainties of determining the cross sections and the noise of the indenter load without contact as a worst case limit.

To test whether larger grain sizes would modify the observed scaling behaviour in ufg Cr, an annealing approach at 165°C (0.2 · T_m) was conducted for 1h utilizing the custom-built heating device past the sample fabrication but prior to testing. Results are shown as green data points in Figure 12a. Obviously, almost no change of the strength scaling exponent was observed, even though the strength of the tested material was slightly reduced. This was caused by a slightly larger average grain size due to thermally induced grain growth. In fact, extending the fit line to intersect with the sxx case would result in a grain size of ~220 nm. Moreover, the annealing approach might serves as a proof that a possible effect of FIB damage [78,80,115] did not affect the scaling behaviour, as FIB damage was shown to be minimized by an annealing treatment at 0.6 · T_m after sample preparation [79].

To discuss the strength scaling behaviour in terms of a plastically deformed sample volume of individual sample geometries as shown for W in Figure 12b, the calculation of sample volumes must be clarified. For uniaxial compression tests, the sample volume was considered by taking the sample's base area and its height into account. Considering the individual indents, a simplified hemispheric plastic zone after penetration to maximum displacement subtracted by the volume of the residual indent was calculated. The black guideline through sxx W data demonstrates its strength scaling behaviour, which is ~0.21 ± 0.02 for the (100) orientation, in agreement with

literature data [13,15,20,28,38,39]. Moreover, literature data as well as present results indicate that strain hardening does not affect the strength scaling behaviour (see **Publication D**).

The ufg W data in Figure 12b is separated into 3 different regimes. Red, orange and green symbols indicate bulk behaviour, a transition regime where the sample size is in the order of the grain size, and ufg W pillars that deform alike sxx W pillars, respectively. Ufg bulk W samples reveal the highest flow stress levels. By decreasing the plastically deformed volume, flow stresses begin to decrease until the transition regime in Figure 12b is reached (orange). Here, pillars deform without crack initiation, and upon further reducing the sample dimension, sxx deformation behaviour is evident. However, decreasing flow stress values are explained by an increasing importance of free surfaces in decreasing sample volumes. In ~500 nm sized grains, dislocation debris developed from the initial HPT deformation process, remain in the grain interior. During plastic deformation, dislocations pile-up at GBs within the sample volume [23,116]. In grains located at free surfaces, dislocation debris easily exit the pillar surface and therefore lower their flow stress . With decreasing sample size the relative fraction of surface grains notably rises, hence stress values decrease until the sample size approaches the grain size and source-controlled strengthening [26] dominates the deformation. Notably, the point of intersection of the drawn guidelines of sxx and ufg W in Figure 12b correlates well with the grain size of the present sample, as shown before for ufg Cr.

5.3.1 Mechanistic description of the strength scaling behaviour

To derive a thorough mechanism-based understanding of the observed strength scaling behaviour, all contributions to strengthening (thermal and athermal) such as intrinsic lattice friction (τ^*), Taylor-hardening (τ_G), a source-controlled strength (τ_S) and GB strengthening ($\tau_{H\text{-}P}$) were considered to reflect the resolved shear strength of pillars [26,38,117,118]:

$$\tau_{sum} = \sigma \cdot m_s = \tau^* + \tau_a = \tau^* + \tau_G + \tau_S + \tau_{h-p}. \quad (5)$$

Zou *et al.* [117] suggested the following terms to address those:

$$\tau_{sum} = \tau^* + \alpha \cdot b \cdot G \cdot \sqrt{\rho} + K \cdot G \cdot \frac{\ln\left(\frac{\bar{\lambda}}{b}\right)}{\frac{\bar{\lambda}}{b}} + m_s \cdot k_{H-P} \cdot d^{-\frac{1}{2}} \quad (6)$$

where α = 0.5 is a constant, ρ is the dislocation density, K = 0.5 is the source strengthening constant, $\bar{\lambda}$ is the average source length, m_s is the Schmid factor (0.47 for slip on (112) oriented planes) and d is the grain size. All other constants are described in Table 1. $\bar{\lambda}$ was chosen to be the half pillar diameter (D/2) in the sxx case [26]. Equation (6) describes the strength scaling behaviour for sxx samples in a sufficient manner, as shown in Figure 12a and b. By utilizing a dislocation density of $9 \cdot 10^{13}$ m^{-2} for sxx Cr and W, close agreement between experiments and the mechanistic model was found.

To describe the strength scaling behaviour of ufg samples, an adaption of equation (5) was necessary, as the contribution of the yield strength of surface grains to the overall yield strength varies with respect to the present grain size. In particular, grains located at the free-surface in ufg Cr pillars were determined to be stronger compared to the pillar interior. No substructure formation is possible due to the small grain size leading to a constraint for dislocations. Grain boundaries further act as sinks and sources for dislocations. To consider that case, the estimated grain size was taken into account for calculations for ufg Cr. To consider possible substructure formation in ~500 nm grained ufg W, one third of the grain size (d/3) was taken for ufg W pillars [119]. As described earlier by Yang *et al.* [23] equation (5) is rewritten as followed:

$$\sigma_{sum} = \sigma_s \cdot f_s + \sigma_i \cdot (1 - f_s), \quad (7)$$

where σ_s and σ_i are the flow stresses of surface and internal grains, respectively, and f_s is stated as the fraction of surface grains. f_s is approximated by

$$f_s = 4 \cdot \frac{\alpha}{r} \cdot \left(1 - \frac{\alpha}{r}\right), \quad (8)$$

with $\alpha = s/d$ and $r = D/d$. s describes the thickness of the surface zone affected by the free surface and D is the pillar diameter. The flow stress of near-surface grains is considered to be the flow stress of an sxx pillar, where D equals d, since in both cases it is thought that dislocations exit on free surfaces. The flow stress considered for internal grains was calculated using

$$\sigma_i = (\tau^* + \tau_G + \tau_{H-P}) \cdot \frac{1}{M}, \tag{9}$$

where $M = 2.9$ is the average Taylor factor for slip on (112) oriented slip planes [120]. Combining equations (6), (8) and (9) with equation (7) results in a mechanistic model which describes the strength scaling behaviour of sxx and ufg pillars in a sufficient manner:

$$\sigma_{sum} = \left[(\tau^* + \tau_G + \tau_S) \cdot \frac{1}{m_S}\right] \cdot f_s + \left[(\tau^* + \tau_G + \tau_{H-P}) \cdot \frac{1}{M}\right] \cdot (1 - f_s) \tag{10}$$

The dashed lines in Figure 12a and b reveal agreement with experimental results. However, such agreement is only achieved if a detailed knowledge of the microstructure is given.

Taking post compression SEM images (Figure 11) and mechanical data (Figure 12) into account, still, several mechanisms might have contributed to the overall deformation. However, the current mechanistic model was derived on the basis of dislocation-mediated plasticity, indicating that dislocation plasticity-based mechanisms instead of crack nucleation, decohesion processes or diffusion-based mechanisms such as GB sliding [121,122] mainly alter the deformation behaviour.

5.4 Thermally activated deformation processes in ufg Cr and W

To further justify apparent deformation mechanisms responsible for the individual strength scaling behaviour, thermally activated deformation mechanisms in Cr and W were identified and discussed in **Publication B** and **Publication D** based on rate- and temperature-dependent properties, such as strain-rate sensitivity (m) and activation volume (v). The obtained results are summarized below and 3D strain-rate sensitivity and activation volume maps are proposed.

To calculate *m*- and ν-values from present experimental data and to facilitate comparison between sxx and ufg Cr and W, equations (1) and (2) were utilized. Comparable experiments in terms of various length-scales and stress states were conducted on Cr and W, and the obtained *m*- and ν-values were plotted as function of a relative test temperature (T_{test}/T_c) to compare bcc metals exhibiting individual thermal stress components. Results are illustrated in Figure 13.

At low relative temperatures *m*-values for sxx Cr and W are ~0.02 and ~0.03, respectively, as shown in Figure 13a. First, an increase of *m* is notable until peak *m*-values of ~0.07 are reached at T_{test}/T_c = 0.65. Approaching and overcoming T_c, thermal activation eases the movement of kink pairs until *m*-values in the order of 10^{-3} are reached, as common for low Peierls potential materials such as fcc metals. Here, deformation is not governed by thermal activation of screw dislocations anymore. This behaviour is in good accordance with other studies [15,16,35], showing that overcoming T_c the thermally activated component diminishes.

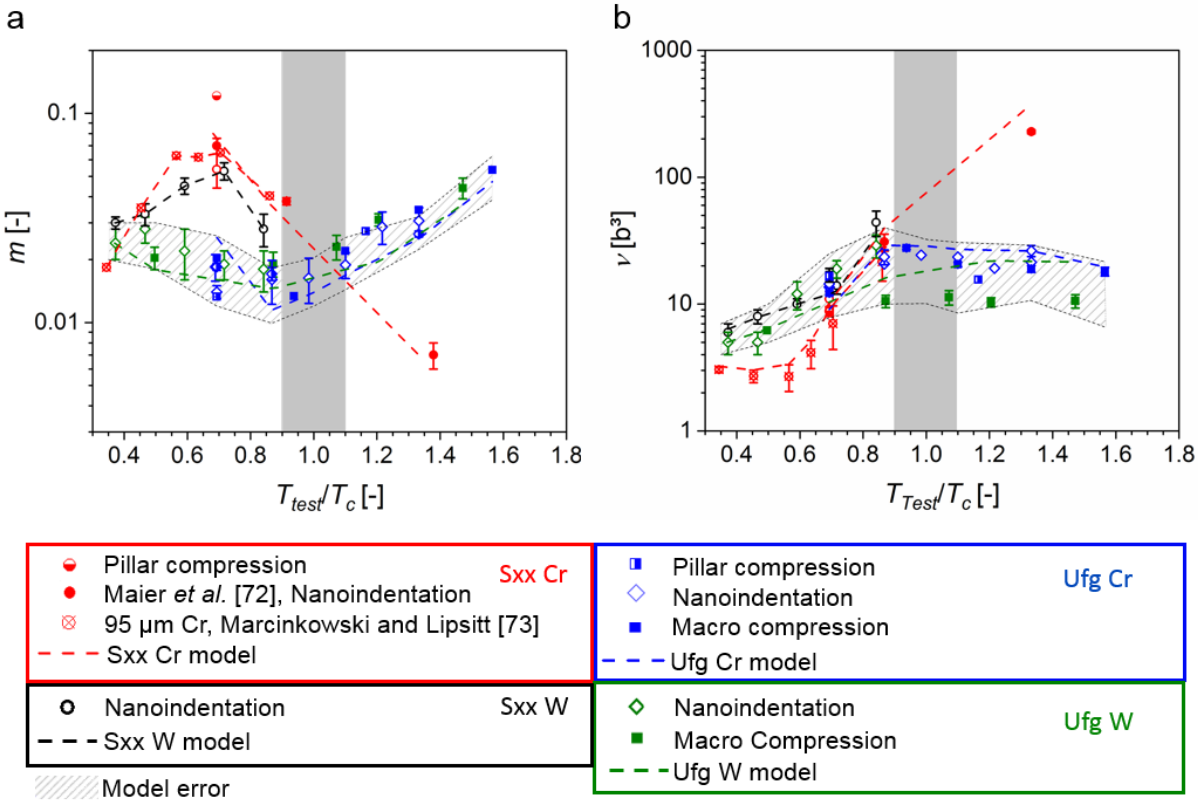

Figure 13: Evolution of strain-rate sensitivity *m* (a) and activation volume ν (b) with relative temperature to compare sxx and ufg Cr and W. The grey-shaded area indicates the range of the critical temperature T_c.

Contrarily to that, the general trend for ufg samples is significantly different from the sxx state. *m*-values for ufg counterparts are found to be ~0.025 at low temperatures. Upon thermal activation, *m*-values further decrease to ~0.015 before T_c is approached. This is attributed to increasing thermal activation, while dislocation interaction with GBs remains mostly unaffected at low temperatures. The generally reduced *m* for ufg samples compared to the sxx state at T_{test}/T_c = 0.65 is attributed to the higher athermal stress component in ufg states (see Figure 3). Overcoming T_c, *m* increases continuously with temperature. According to [41,72], this is mainly attributed to dislocation interactions with GBs, as described also for ufg fcc metals [47,123]. An additional contribution to the increase of *m* could stem from the reduction of the athermal stress contribution due to slight grain coarsening. Thus, the overall *m* is a mixture of both, thermally activated dislocation-GB interactions and thermally activated grain coarsening. Notably, while the first contribution leads to an increasing *m*, the second one acts against it. However, the obtained results are in good agreement with results on sxx [72] and cg Cr [73], hence no major impact of grain coarsening is expected.

The mechanisms based on the varying microstructures are shown in Figure 13b, where corresponding ν-values are plotted vs. T_{test}/T_c. To compare activation volumes, they are normalized by the Burgers vector (for values see Table 1) of the respective metal and expressed in multiples of b^3. At low temperatures, ν-values of 4-7 b^3 were calculated for sxx Cr and W. Those values are attributed to the kink pair mechanism [35], where dislocation segments involved in formation of a double kink need to overcome the next Peierls potential [14,66]. Comparable ν for uniaxial bulk data have been already reported by Glebovsky and Brunner [124], Wu *et al*. [66], Wei *et al*. [51], Kim *et al*. [20] and Schneider *et al*. [14] for sxx W, nc Cr, ufg Fe and sxx Mo, respectively. ν seems to remain constant in sxx Cr until T_{test}/T_c = 0.5. Here, thermal activation of kinks might be hindered by interstitial atoms. This idea is verified by a pronounced yield strength observed in tensile stress-strain data [73], which was the base for calculated activation volumes. At low temperatures, the impurity concentration seems to alter apparent deformation mechanisms. Additionally, *m*- and ν-values from [73] were calculated at the lower yield point, while nanoindentation data and test data obtained from compression experiments were evaluated at ~8% plastic strain. By further increasing the temperature, the movement of kink pairs is eased due to thermal

activation, indicated by an increase of the activation volume. Overcoming T_c gives ν-values of ~200 b^3 for sxx Cr, indicative for dislocation-dislocation interactions, a common mechanism observed in fcc metals [46].

In ufg Cr and W the activation volume increases at relative low temperatures comparably to the sxx states. However, upon passing T_c, ν-values remain rather constant at ~20 b^3 independent of testing technique and stress state. This behaviour is indicative for dislocation-GB interactions at elevated temperature in the ufg states.

Despite the vastly different surface-to-volume ratios probed by the different experiments, different length-scales and stress states, it can be concluded that the observed deformation mechanisms are governed mainly by dislocation-based plasticity. Moreover, the same mechanisms are present in Cr and W, as comparable *m*- and ν-values were determined.

To interpret the varying deformation mechanisms in fcc and bcc metals in terms of dislocation-mediated plasticity with respect to a varying microstructure, a basic fcc model established by Conrad [47] was considered:

$$\frac{1}{\nu} = \frac{1}{\nu^*} + \frac{M^2 \cdot G \cdot b}{\alpha \cdot 2 \cdot \pi \cdot K_{H-P} \cdot d^{1/2}} \cdot \frac{1}{\nu_{ath}}, \tag{11}$$

where the constant α = 0.36. ν^* is the activation volume related to thermal activation (see equation (2)) and ν_{ath} was set as a constant activation volume related to athermal dislocation emission from a GB at constant temperature. ν^* varies with temperature, as the lattice friction stress diminishes with increasing thermal activation. The Conrad model was extended by Wu *et al.* [66] to estimate apparent *m*- and ν-values for polycrystalline aggregates, using

$$\nu_{ath} = \xi \cdot d \cdot b^2, \tag{12}$$

where ξ is a grain shape coefficient which is constant for a certain temperature. Except equation (12), no further modifications of the fcc model were applied, as Conrad [47] already implemented a thermal stress component in the model to derive thermal activation volumes (ν^*). Results obtained by Wu *et al.* [66] show that *m*-values of Cr and Fe at RT can be correctly predicted over a wide range of varying grain sizes, as

both, the friction stress (thermal) and dislocation interaction with GB's (athermal) contribute to the overall deformation. In the present case, ξ is temperature-dependent, as the aspect ratio of initially elongated grains decreased with increasing temperature. Additionally, the grain size slightly increased as experiments were performed at elevated temperature. To verify microstructural changes during heating up the sample or compression experiments, an annealing approach was conducted on ufg Cr samples, which is discussed in detail in **Publication B**. In Figure 13, the dashed lines demonstrate the suitability of the modified equations. The grey dashed area gives the error resulting from the standard deviation of the grain size estimation. By taking into account grain shape coefficients ranging from 0.025 (equiaxed grain shape) to 0.003 (elongated grain structure) the model fits the increasing m- and υ-values at elevated temperatures well.

Beside the examination of deformation mechanisms in constant sample volumes, a variation of strain-rate sensitivity is expected in terms of variable interface fractions within the tested sample volumes, as already shown for fcc Cu pillars [49].

To identify a possible influence of interfaces, the number of grains across the plastic volume (magenta dashed line) and the fraction of grains which are affected by the sample surface (green dashed line) were calculated for different sample geometries during uniaxial and multiaxial testing. Therefore, grains were estimated to be of cylindrical shape with an aspect ratio of 3:1, typical for HPT deformation [105,125]. For rectangular-shaped samples an equivalent cylindrical sample diameter L was calculated (see Figure 14a). The number of grains contained in the plastic volume was estimated by calculating the sample volume and dividing by the before mentioned cylindrical-shaped grain volume. The fraction of grains affected by the sample surface was estimated using the specimen's surface area (red) subtracted by the top and bottom faces which are in direct contact with the flat punch indenter and the bulk material (grey). This lateral area was divided by the average cross-sectional area of a single grain. Considering the different indents illustrated in Figure 14b, a simplified hemispheric plastic zone [94] after penetration to 2500 nm was taken into account for estimating the number of deformed grains per volume. The volume of the residual imprint was therefore subtracted from the hemispheric plastic zone. The remaining volume was further divided by the volume of a single grain. To consider the surface connectivity of grains, the base area of the hemispheric plastic zone (red) was

subtracted by the triangle-shaped surface area of the residual imprints (grey) and divided by the average cross-sectional area of a single grain.

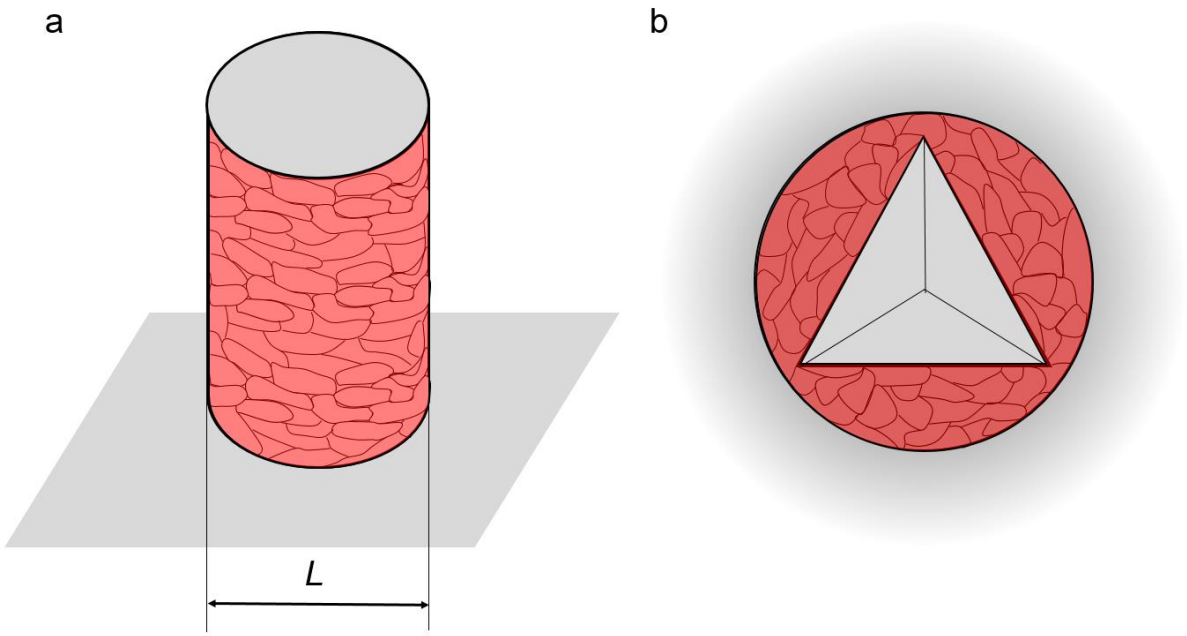

Figure 14: Schematic of (a) compression samples and (b) residual imprints to illustrate the calculated number of grains in the plastic volume and fraction of grains which are affected by the sample surface (red).

The impact of different surface-to-volume ratios and the number of involved interfaces on the determined *m*-values was examined in **Publication B** for Cr and is illustrated in Figure 15.

Based on this, a comparison of *m*-values (black), number of interfaces across the plastic volume (magenta), and fraction of surface-connected grains (green) is presented in Figure 15 as a function of the ratio between grain size vs. sample size *d*/*L*. Furthermore, the error bars indicate the resultant error which was derived by taking the standard deviation upon grain size estimation into account (d=160 ± 51 nm for ufg Cr). Also shown are representative stress-strain curves of micro-pillars with varying interface fractions (I-IV).

The grey area in Figure 15 indicates the macroscopic regime, where the sample size is much larger than the grain size. Only a diminishing fraction of grains is located directly at the sample surface, and no influence of near-surface grains is observed during deformation. Overcoming a *d/L* ratio of ~0.02, the amount of surface-affected grains increases drastically. In this regime, indicated by the red shaded area, grains

noticeably emerge from the sample surface and affect the deformation behaviour. Moreover, in this regime a varying interface fraction and an increasing contribution of free surfaces, as described in section 5.3, significantly alter the strength scaling behaviour. Overcoming *d/L* values of ~0.1, ~50% of the grains are connected with the surface, and the grain size approaches the size of the plastic zone. For these states, an sxx-like deformation behaviour is expected (cyan shaded area) and the thickness of the surface-affected zone (see equation (8)) approaches the sample size. Notably, due to pillar aspect ratios of 3:1 and the used representative grain diameter in this simplified model, a fully sxx sample volume is statistically reached for *d*/*L* ratios larger than 1.33. Below this, individual GBs might affect the plastic behaviour [3–6]. However, as long as crystallographic slip traces reveal no intersections with GBs or other internal obstacles [125], dislocations can glide through the crystal and exit on the pillar surface, corresponding to slip events in sxx pillars. Such characteristics are evident in representative engineering stress-strain curves of small ufg Cr pillars (Figure 15, II-IV), where serrations and load drops are commonly observed.

For macroscopic experiments, a smooth flow behaviour (Figure 15, I), due to the large number of grains in the sample volume, and *m*-values of ~0.02 are observed. By increasing the fraction of surface grains a slight decrease of *m* to ~0.014 is observed and serrated flow arises in the stress-strain curves (Figure 15, II and III). This is explained by slip events in individual grains. The scatter within evaluated *m*-values for such pillar sizes is quite large compared to bulk or sxx Cr samples, because deformation is strongly affected by the local microstructure and crystal orientation. Further increasing *d*/*L* ratios leads to a decreased scatter regarding *m*, as the probability for dislocations interacting with individual GBs is decreased, until *m* of sxx bulk Cr samples and corresponding stress-strain curves (Figure 15 IV) are obtained.

While *m*- and ν-values for fcc and bcc metals were intensively examined to correlate apparent deformation mechanisms with a varying microstructure (see Figure 2), it is now possible to correlate them to thermally activated deformation mechanisms. 3D surface contour plots of *m*- and ν-values were generated by processing the obtained data in this thesis from Figure 13 and Figure 15. They are plotted vs. a relative temperature (T_{test}/T_c) in Figure 16. Moreover, they were extended by the number of interfaces within the sample volumes.

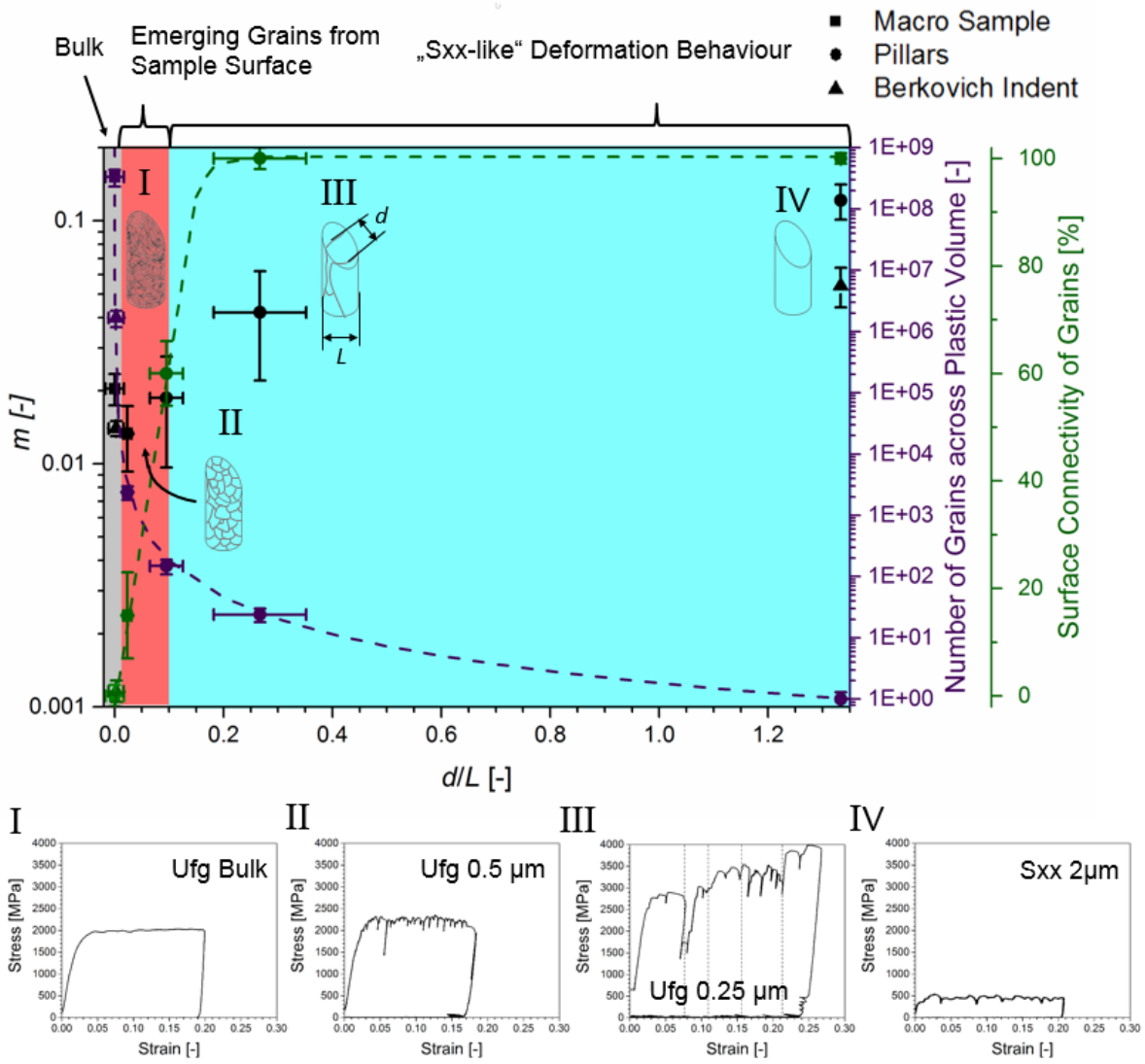

Figure 15: Strain-rate sensitivity *m* (black), number of grains in the plastic volume (magenta) and corresponding connectivity of surface grains (green), dependent on sample size-normalized characteristic dimension *d*/*L* for Cr samples. The red-shaded area shows a transition zone where the free surface alters the deformation process. I) – IV) Corresponding stress-strain curves of pillars indicated. The figure was modified and reprinted from **Publication B**.

Surface contour plots based on equations (11) and (12) and a corresponding colour code reveal apparent *m*- and ν-values for an individual number of interfaces within the sample. The indicated cuts at a constant number of interfaces (Cut 1 and Cut 2) refer to apparent deformation mechanisms for the sxx and the ufg state as demonstrated in Figure 13. Cut 3 in Figure 16a illustrates individual *m*-values obtained at a constant relative temperature, as comparatively shown in Figure 15. A maximum in *m* is either achieved by increasing the thermal stress contribution in the bcc single crystal state at rather low temperatures or by integrating a certain number of grain

boundaries at elevated temperatures. The lowest *m*-values and hence a maximum in activation volume might only be achieved above T_c, where *m*- and ν-values typical for fcc deformation behaviour are present.

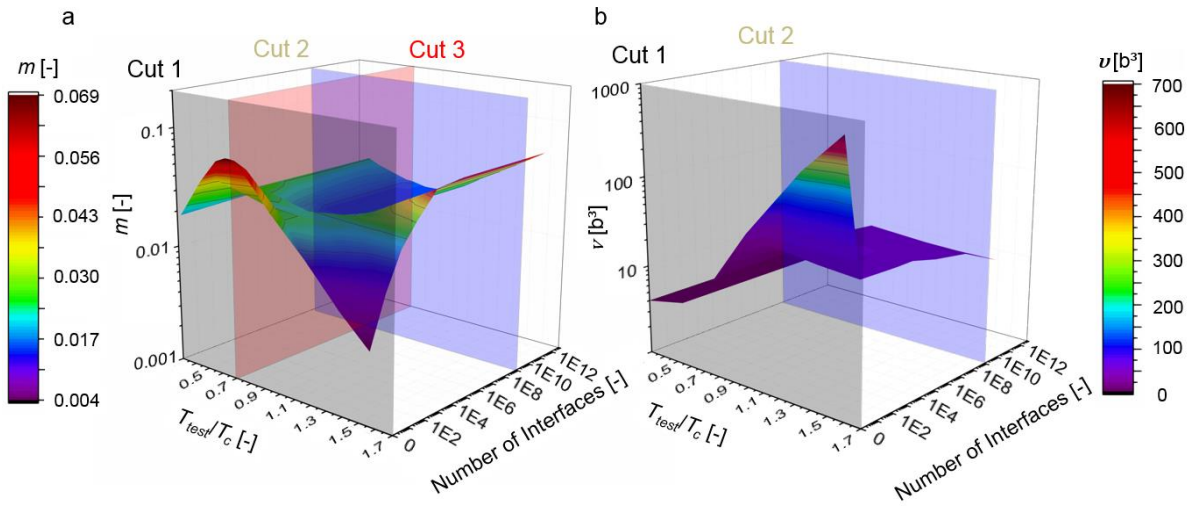

Figure 16: Surface contour plots and corresponding colour codes for obtained (a) strain-rate sensitivity and (b) activation volume values vs. a relative temperature and number of interfaces contained within a sample.

6. Conclusion

A custom-built heating device consisting of independently resistive-heated sample and indenter parts was developed to determine apparent deformation mechanisms in sxx and ufg bcc metals. Temperatures ranging from RT up to 300°C were achieved and, for the first time, comprehensive temperature calibration was obtained by applying a finite element simulation approach. Results underline the importance of temperature calibration and exact temperature matching to minimize thermal drift. Finally, pillar compression and cantilever fracture experiments were conducted at elevated temperature to show assets of the utilized heating tool.

Various experiments were conducted on sxx and ufg Cr and W samples, which served as bcc model materials. By varying the sample size over several length-scales, the interaction between internal microstructure and external sample dimension was investigated. A strength scaling exponent of 0.43 ± 0.03 for single crystalline chromium was obtained which fits to the model of Schneider *et al.* [13]. The strength scaling behaviour obtained for ufg Cr and W samples was compared. In all ufg samples investigated, interfaces were identified mainly as large angle grain boundaries. The interface-dominated strength scaling behaviour was attributed to an increasing influence of free surfaces at small-scales. The demonstrated interplay with the present grain size provided a novel view on the strength scaling behaviour in ufg bcc pillars, which was also successfully modelled based on dislocation-mediated plasticity within this work. Three main findings can be summarized:

- If the grain size is large enough to allow dislocation debris remaining in the grain interior, a reduced strength with decreasing sample dimension is expected. Then the grains influenced by free surfaces show reduced flow stress values compared to inner grains. The decrease in strength with decreasing sample size ends when approaching the single crystal state, as shown for ufg W samples.
- As the grain size approaches the substructure size no pronounced strength scaling behaviour is expected. Experiments conducted over several length-scales result in identical stress values until the single crystal state is realized.
- If the grain size is reduced and dislocation debris in the grain interior are not available, the grain boundaries remain as sinks and sources for dislocations.

Here, grains near free surfaces show enhanced strength compared to grains in the sample interior. Dislocation nucleation within the grain and subsequent escape on the free surface would require larger stresses. A strength scaling behaviour where smaller is stronger, as shown for ufg Cr will be observed upon approaching the single crystal state.

To allow a more detailed insight into apparent thermally activated deformation mechanisms, the mechanical behaviour of sxx and ufg bcc Cr and W was examined in terms of rate- and temperature-dependent experiments over several length-scales and stress states. Uniaxial pillar compression experiments, multiaxial advanced nanoindentation tests and macroscopic compression experiments were conducted and a model was successfully applied to predict strain-rate sensitivity and activation volume values. The main findings are the following:

- Different uniaxial and multiaxial testing techniques allow comparison of flow characteristics and thermally activated deformation mechanisms. In the investigated model materials Cr and W, the same deformation mechanisms are dominant.
- Deformation of single-crystalline samples is dominated by the Peierls potential and a potentially present impurity trace up to the critical temperature T_c. Overcoming this temperature, the thermally activated component of the flow stress diminishes and a strain-rate insensitive behaviour accompanied by further increasing activation volumes is observed.
- At low temperatures ufg samples deform by the thermally activated motion of screw dislocations. The thermal stress contribution decreases with increasing temperature and leads to a slight reduction of the strain-rate sensitivity. Exceeding T_c, constant activation volumes and increasing strain-rate sensitivity are indicative for dislocation-GB interactions as the dominant deformation mechanism. Grain coarsening due to annealing and a change in grain aspect ratio lead to a slight decrease of the activation volume, especially at elevated temperatures. Grain boundary sliding has not been observed.
- A transition in strain-rate sensitivity is observed from a polycrystalline behaviour to an sxx situation, which is controlled by the number of interfaces in the tested volume. The strength scaling behaviour of ufg samples is clearly

affected by free surfaces, which is also of concern for examining rate-dependent deformation behaviour.

Suggestions to further improve the heated in-situ micro-testing device:

To enhance the performance of the heating device, the number of turns of the filament coil could be increased and a filament material offering an enhanced melting point and heat capacity might be utilized. For sufficient insulation of the micro-tester hardware and to further reduce thermal drift, the volume of spacers and their design might be improved. Filament coils should be moulded, for example, in ceramic adhesives to ease their installation process. Once temperatures above 300°C are achieved, a cooling system to minimize the heated volume and to further reduce drift issues should be installed.

To conclude, the achieved results within this thesis vitally contribute to the knowledge on the less understood deformation behaviour of bcc metals. Improvements in terms of modelling the microstructure-dependent strength scaling behaviour and the apparent deformation mechanisms in ufg bcc structures will help to push the development of small-scale micro-mechanical devices to new limits.

7. References

[1] A.C. Fischer-Cripps, Nanoindentation, Springer, New York, 2004.

[2] M.D. Uchic, D.M. Dimiduk, J.N. Florando, W.D. Nix, Sample Dimensions Influence Strength and Crystal Plasticity, Science 305 (2004) 986–989.

[3] N. Kheradmand, H. Vehoff, A. Barnoush, An insight into the role of the grain boundary in plastic deformation by means of a bicrystalline pillar compression test and atomistic simulation, Acta Mater. 61 (2013) 7454–7465.

[4] N. V Malyar, G. Dehm, C. Kirchlechner, Strain rate dependence of the slip transfer through a penetrable high angle grain boundary in copper, Scr. Mater. 138 (2017) 88–91.

[5] N. V Malyar, J.S. Micha, G. Dehm, C. Kirchlechner, Size effect in bi-crystalline micropillars with a penetrable high angle grain boundary, Acta Mater. 129 (2017) 312–320.

[6] P.J. Imrich, C. Kirchlechner, D. Kiener, G. Dehm, In Situ TEM Microcompression of Single and Bicrystalline Samples: Insights and Limitations, Jom. 67 (2015) 1704–1712.

[7] D. Kiener, C. Motz, T. Schöberl, M. Jenko, G. Dehm, Determination of Mechanical Properties of Copper at the Micron Scale, Adv. Eng. Mater. 8 (2006) 1119–1125.

[8] D.M. Dimiduk, M.D. Uchic, T.A. Parthasarathy, Size-affected single-slip behavior of pure nickel microcrystals, Acta Mater. 53 (2005) 4065–4077.

[9] M.D. Uchic, P.A. Shade, D.M. Dimiduk, Plasticity of Micrometer-Scale Single Crystals in Compression, Annu. Rev. Mater. Res. 39 (2009) 361–386.

[10] J.R. Greer, C.R. Weinberger, W. Cai, Comparing the strength of f.c.c. and b.c.c. sub-micrometer pillars: Compression experiments and dislocation dynamics simulations, Mater. Sci. Eng. A. 493 (2008) 21–25.

[11] J.R. Greer, J.T.M. De Hosson, Plasticity in small-sized metallic systems: Intrinsic versus extrinsic size effect, Prog. Mater. Sci. 56 (2011) 654–724.

[12] O. Kraft, P.A. Gruber, R. Mönig, D. Weygand, Plasticity in Confined Dimensions, Annu. Rev. Mater. Res. 40 (2010) 293–317.

[13] A.S. Schneider, D. Kaufmann, B.G. Clark, C.P. Frick, P.A. Gruber, R. Mönig, O. Kraft, E. Arzt, Correlation between Critical Temperature and Strength of Small-Scale bcc Pillars, Phys. Rev. Lett. 103 (2009) 105501/1-4.

[14] A.S. Schneider, B.G. Clark, E. Arzt, C.P. Frick, P.A. Gruber, Effect of orientation and loading rate on compression behavior of small-scale Mo pillars, Mater. Sci. Eng. A. 508 (2009) 241–246.

[15] O. Torrents Abad, J.M. Wheeler, J. Michler, A.S. Schneider, E. Arzt, Temperature-dependent size effects on the strength of Ta and W micropillars, Acta Mater. 103 (2016) 483–494.

[16] A.S. Schneider, C.P. Frick, E. Arzt, W.J. Clegg, S. Korte, Influence of test temperature on the size effect in molybdenum small-scale compression pillars, Philos. Mag. Lett. 93 (2013) 331–338.

[17] Y. Cui, G. Po, N. Ghoniem, Temperature insensitivity of the flow stress in body-centered cubic micropillar crystals, Acta Mater. 108 (2016) 128–137.

[18] R. Huang, Q.-J. Li, Z.-J. Wang, L. Huang, J. Li, E. Ma, Z.-W. Shan, Flow Stress in Submicron BCC Iron Single Crystals: Sample-size-dependent Strain-rate Sensitivity and Rate-dependent Size Strengthening, Mater. Res. Lett. (2015) 1–7.

[19] G.M. Cheng, W.W. Jian, W.Z. Xu, H. Yuan, P.C. Millett, Y.T. Zhu, Grain Size

Effect on Deformation Mechanisms of Nanocrystalline bcc Metals, Mater. Res. Lett. 1 (2013) 26–31.
[20] J.-Y. Kim, D. Jang, J.R. Greer, Tensile and compressive behavior of tungsten, molybdenum, tantalum and niobium at the nanoscale, Acta Mater. 58 (2010) 2355–2363.
[21] C. Keller, E. Hug, X. Feaugas, Microstructural size effects on mechanical properties of high purity nickel, Int. J. Plast. 27 (2011) 635–654.
[22] X.X. Chen, A.H.W. Ngan, Specimen size and grain size effects on tensile strength of Ag microwires, Scr. Mater. 64 (2011) 717–720.
[23] B. Yang, C. Motz, M. Rester, G. Dehm, Yield stress influenced by the ratio of wire diameter to grain size - a competition between the effects of specimen microstructure and dimension in micro-sized polycrystalline copper wires, Philos. Mag. 92 (2012) 3243–3256.
[24] P. Ghosh, A.H. Chokshi, Size Effects on Strength in the Transition from Single- to-Polycrystalline Behavior, Metall. Mater. Trans. A. 46 (2015) 5671–5684.
[25] E. Arzt, Size effects in materials due to microstructural and dimensional constraints: a comparative review, Acta Mater. 46 (1998) 5611–5626.
[26] T.A. Parthasarathy, S.I. Rao, D.M. Dimiduk, M.D. Uchic, D.R. Trinkle, Contribution to size effect of yield strength from the stochastics of dislocation source lengths in finite samples, Scr. Mater. 56 (2007) 313–316.
[27] J.A. El-Awady, Unravelling the physics of size-dependent dislocation-mediated plasticity, Nat Comms. 6 (2015) 5926.
[28] A.S. Schneider, C.P. Frick, B.G. Clark, P.A. Gruber, E. Arzt, Influence of orientation on the size effect in bcc pillars with different critical temperatures, Mater. Sci. Eng. A. 528 (2011) 1540–1547.
[29] B.R.S. Rogne, C. Thaulow, Effect of crystal orientation on the strengthening of iron micro pillars, Mater. Sci. Eng. A. 621 (2015) 133–142.
[30] H. Bei, S. Shim, G.M. Pharr, E.P. George, Effects of pre-strain on the compressive stress-strain response of Mo-alloy single-crystal micropillars, Acta Mater. 56 (2008) 4762–4770.
[31] A.S. Schneider, D. Kiener, C.M. Yakacki, H.J. Maier, P.A. Gruber, N. Tamura, M. Kunz, A.M. Minor, C.P. Frick, Influence of bulk pre-straining on the size effect in nickel compression pillars, Mater. Sci. Eng. A. 559 (2013) 147–158.
[32] J.A. El-Awady, M.D. Uchic, P.A. Shade, S.-L. Kim, S.I. Rao, D.M. Dimiduk, C. Woodward, Pre-straining effects on the power-law scaling of size-dependent strengthening in Ni single crystals, Scr. Mater. 68 (2013) 207–210.
[33] J.M. Wheeler, C. Kirchlechner, J.S. Micha, J. Michler, D. Kiener, The effect of size on the strength of FCC metals at elevated temperatures: annealed copper, Philos. Mag. (2016) 1–17.
[34] H. Conrad, Thermally activated deformation of metals, J. Met. (1964) 582–588.
[35] B. Sestak, A. Seeger, Gleitung und Verfestigung in kubisch-raumzentrierten Metallen und Legierungen, Zeitschrift Für Met. 69 (1978) 195–202.
[36] D. Caillard, Kinetics of dislocations in pure Fe. Part I. In situ straining experiments at room temperature, Acta Mater. 58 (2010) 3493–3503.
[37] D. Caillard, Kinetics of dislocations in pure Fe. Part II. In situ straining experiments at low temperature, Acta Mater. 58 (2010) 3504–3515.
[38] S.-W. Lee, W.D. Nix, Size dependence of the yield strength of fcc and bcc metallic micropillars with diameters of a few micrometers, Philos. Mag. 92 (2012) 1238–1260.
[39] S.-W. Lee, Y. Cheng, I. Ryu, J.R. Greer, Cold-temperature deformation of nano-

sized tungsten and niobium as revealed by in-situ nano-mechanical experiments, Sci. China Technol. Sci. 57 (2014) 652–662.
[40] B.R.S. Rogne, C. Thaulow, Strengthening mechanisms of iron micropillars, Philos. Mag. (2014) 1–15.
[41] V. Maier, C. Schunk, M. Göken, K. Durst, Microstructure-dependent deformation behaviour of bcc-metals - indentation size effect and strain rate sensitivity, Philos. Mag. 95 (2015) 1766–1779.
[42] E.W. Hart, Theory of the tensile test, Acta Metall. 15 (1967) 351–355.
[43] M.F. Ashby, The deformation of plastically non-homogeneous materials, Philos. Mag. 21 (1970) 399–424.
[44] V. Maier, K. Durst, J. Mueller, B. Backes, H.W. Höppel, M. Göken, Nanoindentation strain-rate jump tests for determining the local strain-rate sensitivity in nanocrystalline Ni and ultrafine-grained Al, J. Mater. Res. 26 (2011) 1421–1430.
[45] H.W. Höppel, J. May, P. Eisenlohr, M. Göken, Strain rate sensitivity of ultrafine-grained materials, Z. Met. 96 (2005) 566–571.
[46] J. May, H.W. Höppel, M. Göken, Strain rate sensitivity of ultrafine-grained aluminium processed by severe plastic deformation, Scr. Mater. 53 (2005) 189–194.
[47] H. Conrad, Plastic deformation kinetics in nanocrystalline FCC metals based on the pile-up of dislocations, Nanotechnology. 18 (2007) 1–8.
[48] J.Y. Zhang, G. Liu, J. Sun, Strain rate effects on the mechanical response in multi- and single-crystalline Cu micropillars: Grain boundary effects, Int. J. Plast. 50 (2013) 1–17.
[49] J.Y. Zhang, X. Liang, P. Zhang, K. Wu, G. Liu, J. Sun, Emergence of external size effects in the bulk-scale polycrystal to small-scale single-crystal transition: A maximum in the strength and strain-rate sensitivity of multicrystalline Cu micropillars, Acta Mater. 66 (2014) 302–316.
[50] M.A. Meyers, A. Mishra, D.J. Benson, Mechanical properties of nanocrystalline materials, Prog. Mater. Sci. 51 (2006) 427–556.
[51] Q. Wei, S. Cheng, K.T. Ramesh, E. Ma, Effect of nanocrystalline and ultrafine grain sizes on the strain rate sensitivity and activation volume: fcc versus bcc metals, Mater. Sci. Eng. A. 381 (2004) 71–79.
[52] A.T. Jennings, J. Li, J.R. Greer, Emergence of strain-rate sensitivity in Cu nanopillars: Transition from dislocation multiplication to dislocation nucleation, Acta Mater. 59 (2011) 5627–5637.
[53] H. Miyamoto, K. Ota, T. Mimaki, Viscous nature of deformation of ultra-fine grain aluminum processed by equal-channel angular pressing, Scr. Mater. 54 (2006) 1721–1725.
[54] R.W. Hayes, D. Witkin, F. Zhou, E.J. Lavernia, Deformation and activation volumes of cryomilled ultrafine-grained aluminum, Acta Mater. 52 (2004) 4259–4271.
[55] R. Schwaiger, B. Moser, M. Dao, N. Chollacoop, S. Suresh, Some critical experiments on the strain-rate sensitivity of nanocrystalline nickel, Acta Mater. 51 (2003) 5159–5172.
[56] F.D. Torre, P. Spätig, R. Schaublin, M. Victoria, Deformation behaviour and microstructure of nanocrystalline electrodeposited and high pressure torsioned nickel, Acta Mater. 53 (2005) 2337–2349.
[57] D. Pan, T.G. Nieh, M.W. Chen, Strengthening and softening of nanocrystalline nickel during multistep nanoindentation, Appl. Phys. Lett. 88 (2006).

[58] J. Chen, L. Lu, K. Lu, Hardness and strain rate sensitivity of nanocrystalline Cu, Scr. Mater. 54 (2006) 1913–1918.
[59] J. May, H.W. Höppel, M. Göken, Strain Rate Sensitivity of Ultrafine Grained FCC- and BCC-Type Metals, Mater. Sci. Forum. 503–504 (2006) 781–786.
[60] Q. Wei, T. Jiao, K.T. Ramesh, E. Ma, Nano-structured vanadium: processing and mechanical properties under quasi-static and dynamic compression, Scr. Mater. 50 (2004) 359–364.
[61] Q. Wei, T. Jiao, K.T. Ramesh, E. Ma, L.J. Kecskes, L. Magness, R. Dowding, V. Kazykhanov, R.Z. Valiev, Mechanical behavior and dynamic failure of high-strength ultrafine grained tungsten under uniaxial compression, Acta Mater. 54 (2005) 77–87.
[62] Q. Wei, Z.L. Pan, X.L. Wu, B.E. Schuster, L.J. Kecskes, R.Z. Valiev, Microstructure and mechanical properties at different length scales and strain rates of nanocrystalline tantalum produced by high-pressure torsion, Acta Mater. 59 (2011) 2423–2436.
[63] Q. Wei, Strain rate effects in the ultrafine grain and nanocrystalline regimes - influence on some constitutive responses, J Mater Sci. 42 (2007) 1709–1727.
[64] D. Jia, K.T. Ramesh, E. Ma, Effects of nanocrystalline and ultrafine grain sizes on constitutive behavior and shear bands in iron, Acta Mater. 51 (2003) 3495–3509.
[65] Q. Zhou, J. Zhao, J.Y. Xie, F. Wang, P. Huang, T.J. Lu, K.W. Xu, Grain size dependent strain rate sensitivity in nanocrystalline body-centered cubic metal thin films, Mater. Sci. Eng. A. 608 (2014) 184–189.
[66] D. Wu, X.L. Wang, T.G. Nieh, Variation of strain rate sensitivity with grain size in Cr and other body-centred cubic metals, J. Phys. D. Appl. Phys. 47 (2014) 175303.
[67] D. Jang, M. Atzmon, Grain-size dependence of plastic deformation in nanocrystalline Fe, J. Appl. Phys. 93 (2003) 9282–9286.
[68] T.R. Malow, C.C. Koch, P.Q. Miraglia, K.L. Murty, Compressive mechanical behavior of nanocrystalline Fe investigated with an automated ball indentation technique, Mater. Sci. Eng. A. 252 (1998) 36–43.
[69] K.B. Yoder, A.A. Elmustafa, J.C. Lin, R.A. Hoffman, D.S. Stone, Activation analysis of deformation in evaporated molybdenum thin films, J. Phys. D Appl. Phys. 36 (2003) 884–895.
[70] J. Wehrs, G. Mohanty, G. Guillonneau, A. Taylor, X. Maeder, D. Frey, L. Philippe, S. Mischler, J.M. Wheeler, J. Michler, Comparison of In Situ Micromechanical Strain-Rate Sensitivity Measurement Techniques, JOM. 67 (2015) 1684–1693.
[71] J. Alkorta, J.M. Martínez-Esnaola, J.G. Sevillano, Critical examination of strain-rate sensitivity measurement by nanoindentation methods: Application to severely deformed niobium, Acta Mater. 56 (2008) 884–893.
[72] V. Maier, A. Hohenwarter, R. Pippan, D. Kiener, Thermally activated deformation processes in body-centered cubic Cr - How microstructure influences strain-rate sensitivity, Scr. Mater. 106 (2015) 42–45.
[73] M.J. Marcinkowski, H.A. Lipsitt, The plastic deformation of Chromium at low temperatures, Acta Metall. 10 (1962) 95–111.
[74] A. Seeger, The temperature and strain-rate dependence of the flow stress of bcc metals: A theory based on kink-kink interactions, Z. Met. 72 (1981) 369–380.
[75] E.O. Hall, The Deformation and Ageing of Mild and Steel: III and Discussion of Results, Proc. Phys. Soc. B. 64 (1951) 747–753.
[76] N.J. Petch, The cleavage strength of polycrystals, J. Iron Steel Inst. 174 (1953)

25–28.
[77] S. Wurster, R. Treml, R. Fritz, M.W. Kapp, E.-M. Langs, M. Alfreider, C. Ruhs, P.J. Imrich, G. Felber, D. Kiener, Novel methods for the site specific preparation of micromechanical structures, Prakt. Met. Sonderband. 46 (2014) 27–36.
[78] D. Kiener, C. Motz, M. Rester, M. Jenko, G. Dehm, FIB damage of Cu and possible consequences for miniaturized mechanical tests, Mater. Sci. Eng. A. 459 (2007) 262–272.
[79] M.B. Lowry, D. Kiener, M.M. Leblanc, C. Chisholm, J.N. Florando, J.W. Morris, A.M. Minor, Achieving the ideal strength in annealed molybdenum nanopillars, Acta Mater. 58 (2010) 5160–5167.
[80] Y. Xiao, J. Wehrs, H. Ma, T. Al-Samman, S. Korte-Kerzel, M. Göken, J. Michler, R. Spolenak, J.M. Wheeler, Investigation of the deformation behavior of aluminum micropillars produced by focused ion beam machining using Ga and Xe ions, Scr. Mater. 127 (2017).
[81] P.J.M. Janssen, J.P.M. Hoefnagels, T.H. de Keijser, M.G.D. Geers, Processing induced size effects in plastic yielding upon miniaturisation, J. Mech. Phys. Solids. 56 (2008) 2687–2706.
[82] A.T. Jennings, M.J. Burek, J.R. Greer, Microstructure versus Size and Mechanical Properties of Electroplated and Single Crystalline Cu Nanopillars, PRL. 104 (2010) 135503.
[83] M.W. Phaneuf, Application of focused ion beam microscopy to materials science specimens, Micron. 30 (1999) 277–288.
[84] C.A. Volkert, A.M. Minor, Focused ion beam microscopy and micromachining, MRS Bull. 32 (2007) 389–399.
[85] I. Sneddon, The relation between load and penetration in the axisymmetric Boussinesq Problem for a punch of arbitrary profile, Int. J. Engng Sci. 3 (1965) 47–57.
[86] D. Kiener, W. Grosinger, G. Dehm, On the importance of sample compliance in uniaxial microtesting, Scripta. 60 (2009) 148–151.
[87] D. Kiener, C. Motz, G. Dehm, Micro-compression testing: A critical discussion of experimental constraints, Mater. Sci. Eng. A. 505 (2009) 79–87.
[88] V. Maier, A. Leitner, R. Pippan, D. Kiener, Thermally Activated Deformation Behavior of ufg-Au: Environmental Issues During Long-Term and High-Temperature Nanoindentation Testing, JOM. 67 (2015) 2934–2944.
[89] W.C. Oliver, G.M. Pharr, An improved technique for determining hardness and elastic modulus using load and displacement sensing indentation experiments, J. Mater. Res. 7 (1992) 1564–1583.
[90] D. Tabor, The Hardness of Metals, OUP Oxford, Oxford UK, 1951.
[91] B. Merle, V. Maier-Kiener, G.M. Pharr, Influence of modulus-to-hardness ratio and harmonic parameters on continuous stiffness measurement during nanoindentation, Acta Mater. 134C (2017) 167–176.
[92] A. Leitner, V. Maier-Kiener, D. Kiener, Dynamic nanoindentation testing: Is there an influence on a material's hardness?, Mater. Res. Lett. (2017).
[93] K.L. Johnson, The correlation of indentation experiments, J. Mech. Phys. Solids. 18 (1970) 115–126.
[94] M. Mata, O. Casals, J. Alcala, The plastic zone size in indentation experiments: The analogy with the expansion of a spherical cavity, Int. J. Solids Struct. 43 (2006) 5994–6013.
[95] A. Leitner, V. Maier-Kiener, D. Kiener, Extraction of Flow Behavior and Hall-Petch Parameters Using a Nanoindentation Multiple Sharp Tip Approach, Adv.

Eng. Mater. (2016) 1–9.
[96] D.I. Bolef, J. De Klerk, Anomalies in the Elastic Constants and Thermal Expansion of Chromium Single Crystals, Phys. Rev. 129 (1963) 1063–1067.
[97] Tungsten properties, https://www.plansee.com/de/werkstoffe/wolfram.html (accessed July 14, 2017).
[98] Chromium properties, https://www.plansee.com/de/werkstoffe/chrom.html (accessed July 14, 2017).
[99] E. Grünwald, R. Nuster, R. Treml, D. Kiener, G. Paltauf, R. Brunner, Young ' s Modulus and Poisson ' s Ratio Characterization of Tungsten Thin Films via Laser Ultrasound, Mater. Today Proc. 2 (2015) 4289–4294.
[100] D. Wu, J. Zhang, J.C. Huang, H. Bei, T.G. Nieh, Grain-boundary strengthening in nanocrystalline chromium and the Hall-Petch coefficient of body-centered cubic metals, Scr. Mater. 68 (2013) 118–121.
[101] H.J. Frost, M.F. Ashby, Deformation mechanism maps: The plasticity and Creep of Metals and Ceramics, Pergamon Press, 1982.
[102] H. Conrad, W. Hayes, Correlation of the Thermal Component of the Yield Stress of Body Centered Cubic Metals, Aerosp. Corp. 4 (1963) 33.
[103] R. Wadsack, R. Pippan, B. Schedler, The effect of pre-deformation on the ductility of chromium, J. Nucl. Mater. 307–311 (2002) 701–704.
[104] J. Reiser, J. Hoffmann, U. Jäntsch, M. Klimenkov, S. Bonk, C. Bonnekoh, M. Rieth, A. Hoffmann, T. Mrotzek, Ductilisation of tungsten (W): On the shift of the brittle-to-ductile transition (BDT) to lower temperatures through cold rolling, Int. J. Refract. Met. Hard Mater. 54 (2016) 351–369.
[105] R. Pippan, S. Scheriau, A. Taylor, M. Hafok, A. Hohenwarter, A. Bachmaier, Saturation of Fragmentation During Severe Plastic Deformation, Annu. Rev. Mater. Res. 40 (2010) 319–343.
[106] R.Z. Valiev, R.K. Islamgaliev, I. V Alexandrov, Bulk nanostructured materials from severe and plastic deformation, Prog. Mater. Sci. 45 (2000) 103–189.
[107] Q. Wei, H. Zhang, B.E. Schuster, K.T. Ramesh, R.Z. Valiev, L.J. Kecskes, R. Dowding, L. Magness, K. Cho, Microstructure and mechanical properties of super-strong nanocrystalline tungsten processed by high-pressure torsion, Acta Mater. 54 (2006) 4079–4089.
[108] L.J. Kecskes, K.C. Cho, R.J. Dowding, B.E. Schuster, R.Z. Valiev, Q. Wei, Grain size engineering of bcc refractory metals: Top-down and bottom-up-Application to tungsten, Mater. Sci. Eng. A. 467 (2007) 33–43.
[109] A. V Ganeev, R.K. Islamgaliev, R.Z. Valiev, Refinement of tungsten microstructure upon severe plastic deformation, Phys. Met. Metallogr. 115 (2014) 139–145.
[110] R. Wadsack, R. Pippan, B. Schedler, Structural refinement of chromium by severe plastic deformation, Fusion Eng. Des. 66–68 (2003) 265–269.
[111] J.M. Wheeler, P. Brodard, J. Michler, Elevated temperature, in situ indentation with calibrated contact temperatures, Philos. Mag. 92 (2012) 3128–3141.
[112] Granta Design Limited, CES Edupack, (2016).
[113] A. V Sameljuk, A.D. Vasilev, S.A. Firstov, Low temperature deformation and fracture behaviour of [100] and [110] chromium single crystals, Int. J. Refract. Met. Hard Mater. 14 (1996) 249–255.
[114] M. Faleschini, H. Kreuzer, D. Kiener, R. Pippan, Fracture toughness investigations of tungsten alloys and SPD tungsten alloys, J. Nucl. Mater. 367–370 (2007) 800–805.
[115] S. Shim, H. Bei, M.K. Miller, G.M. Pharr, E.P. George, Effects of focused ion

beam milling on the compressive behavior of directionally solidified micropillars and the nanoindentation response of an electropolished surface, Acta Mater. 57 (2009) 503–510.
[116] B. Yang, C. Motz, W. Grosinger, G. Dehm, Cyclic loading behavior of micro-sized polycrystalline copper wires, Procedia Eng. 2 (2010) 925–930.
[117] Y. Zou, H. Ma, R. Spolenak, Ultrastrong ductile and stable high-entropy alloys at small scales, Nat Comms. 6 (2015) 7748–7756.
[118] S.I. Rao, D.M. Dimiduk, M. Tang, M.D. Uchic, T.A. Parthasarathy, C. Woodward, Estimating the strength of single-ended dislocation sources in micron-sized single crystals, Philos. Mag. 87 (2007) 4777–4794.
[119] B. von Blanckenhagen, E. Arzt, P. Gumbsch, Discrete dislocation simulation of plastic deformation in metal thin films, Acta Mater. 52 (2004) 773–784.
[120] J.M. Rosenberg, H.R. Piehler, Calculation of the Taylor Factor and Lattice Rotations for Bcc Metals Deforming by Pencil Glide, Metall. Trans. 2 (1971) 257–259.
[121] T.G. Langdon, Grain boundary sliding revisited: Developments in sliding over four decades, J. Mater. Sci. 41 (2006) 597–609.
[122] N.Q. Chinh, T. Csanadi, J. Gubicza, R.Z. Valiev, B.B. Straumal, T.G. Langdon, The Effect of Grain Boundary Sliding and Strain Rate Sensitivity on the Ductility of Ultrafine-Grained Materials, MSF. 667–669 (2010) 677–682.
[123] H. Conrad, Grain-size dependence of the flow stress of Cu from millimeters to nanometers, Metall. Mater. Trans. A. 35 (2004) 2681–2695.
[124] D. Brunner, V. Glebovsky, Analysis of flow-stress measurements of high purity tungsten single crystals, Mater. Lett. 44 (2000) 144–152.
[125] R. Fritz, D. Lutz, V. Maier-Kiener, D. Kiener, Interplay between Sample Size and Grain Size: Single Crystalline vs. Ultrafine-grained Chromium Micropillars, Mater. Sci. Eng. A. 674 (2016) 626–633.

Chapter 2

Publication A

Interplay between Sample Size and Grain Size: Single Crystalline vs. Ultrafine-grained Chromium Micropillars

R. Fritz[1], V. Maier-Kiener[2], D. Lutz[1], D. Kiener[1]

Materials Science & Engineering A 674 (2016) 626-633

[1] Department Materials Physics, Montanuniversität Leoben, Leoben, Austria
[2] Department Physical Metallurgy & Materials Testing, Montanuniversität Leoben, Leoben, Austria

A - Abstract

To gain insights into the influence of the microstructure on the strengthening behaviour in confined volumes, single crystalline (sxx) and ultrafine-grained (ufg) Cr micropillars were investigated using in-situ scanning electron microscope microcompression tests. Post-compression images of the sxx pillars indicate crystallographic slip, while the ufg pillars reveal a bulk-like deformation behaviour and an emergence of grains from the sample surface. Stress-strain curves of sxx samples show intermittent flow and a scaling behaviour agreeing well with other bcc metals investigated previously. Also for ufg samples a size-dependent strength with a reduced but non-negligible scaling exponent is determined. This latter ufg size effect contributes to an increasing influence of near-surface grains controlling plastic flow with decreasing pillar diameter. While for micron-sized pillars the strength differs between the two microstructures, the two scaling trends converge for sub-micron pillars with diameters close to the grain size, indicative of a transition from boundary-mediated to single crystal plasticity.

A1 - Introduction

Since technical devices are getting ever smaller, the requirements for materials performances are generally increasing. Experimental setups were developed to investigate confined volumes, and efforts were made to establish small scale testing techniques. Uchic *et al.* [1] were the first to report a size effect in pillar compression testing of single crystalline (sxx) Ni. It was observed that the yield stress scales inversely with some power to the pillar diameter *d*. Many subsequent investigations followed on sxx face-centred-cubic (fcc) and body-centred-cubic (bcc) metals, with power law scaling exponents being agreed to be ~0.6 for fcc [2,3], and 0.2 to 0.6 for bcc metals [3-5], respectively. The reason for this variation in bcc metals is still under debate [6].

Due to the absence of closest packed planes in the bcc crystal structure, deformation is rate limited by the movement of screw dislocations via the kink pair mechanism [7]. Thermal activation helps to move these kink pairs. Thermally activated processes seem to be the direct reason for an increasing power law scaling exponent towards the fcc value. If thermal activation reaches ~$0.2 \cdot T_m$, where T_m is the melting

temperature of the metal, the critical temperature (T_c) is typically reached [8]. At this point, screw dislocations propagate through the material with the same velocity as edge dislocations and the scaling exponent approaches 0.6 [2-4,9], the common value of fcc metals.

The scaling behaviour of fcc and bcc metals has been studied by several groups in the last few years. Greer *et al.* [10] investigated the stress-strain behaviour of Au and Mo pillars, and differences in the scaling behaviour were accounted to varying dislocation mechanisms. Schneider *et al.* [6] tested various bcc metals with different T_c at room temperature (*RT*). Hereby, the RT/T_c ratio refers to different thermal contributions to the Peierls stress of various metals. The received wide range in scaling exponents of the bcc metals (Nb, Ta, W, Mo) has been explained by the thermally activated component of the yield stress [7]. These findings were confirmed by Maier *et al.* [11] using advanced nanoindentation (NI) techniques. More recently, compression tests on sxx W and Ta were carried out at elevated temperature by Torrents Abad *et al.* [12]. They observed increasing strength scaling behaviour with increasing temperature. However, in the present case of polycrystalline pillars, the size effect is not only composed of a thermal stress contribution. It is also dependent of an intrinsic grain size [13-16].

It is well-known that defect-free whiskers reveal theoretical strength values, whereas pillars with defects lead to the investigated size effect [14]. In other words there could be a preparation induced size effect. For millimetre-sized and micron-sized samples, Janssen *et al.* [17] investigated Al and found a processing induced strength scaling behaviour. Samples used in our investigations are very large compared to a probably affected surface volume (typically ~50 nm, Kiener *et al.* [18]) and therefore no significant influence of a processing induced size effect is expected. In fact, Jennings *et al.* [19] compared Cu pillars produced with and without focused ion beam (FIB) milling and found that size effects are independent of FIB damage.

Attempts were made to analyse pillars containing different defect densities. Bei *et al.* [14] compared dislocation free and pre-strained Mo whiskers. Their findings reveal no size effect for pillars with more than 11% pre-strain. Schneider *et al.* [15] and El-Awady *et al.* [16] pre-strained Ni pillars and found a reduction of the scaling exponent with increasing pre-strain. This was related to cell structures that formed

during straining and the increase in dislocation density in the cell walls with increasing pre-strain.

In our work, the dislocation density was further increased by deforming Cr to far more than 100% representative strain. High pressure torsion (HPT) was used to form an ultrafine-grained (ufg) microstructure with mostly high angle grain boundaries [20,21]. FIB milled pillars were compressed in-situ in a scanning electron microscope and the occurring size effect and deformation behaviour of ufg samples were compared with sxx samples.

A2 - Materials and Methods

An sxx Cr rod with a purity of 99.999% was obtained from Mateck GmbH (Jülich, Germany) in (100) orientation. Slices of approximately 1 mm thickness were cut with a diamond wire saw and subsequently ground and polished to a lamella, on which non-tapered pillars in the size range between 200 nm to 4 µm and with an aspect ratio of 2.5 – 3 were milled with a dual-beam SEM-FIB workstation (Zeiss LEO 1540 XP, Oberkochen, Germany) [22].

The polycrystalline Cr with a purity of 99.9% was provided as sheets by Plansee SE (Reutte, Austria). To achieve an ufg microstructure, the as-received sample was cut via electron discharge machining (EDM, Brother HS-3100) to a cylinder with a diameter of 30 mm and a height of 7 mm and was subsequently deformed via HPT [20,21]. Due to the RT brittleness of Cr (the ductile to brittle transition temperature (DBTT) of the recrystallized microstructure is 320 – 390°C [23]), the deformation process was performed at 200°C. The sample was processed at a pressure of 4.2 GPa with a rotational speed of 0.5 rpm. After 50 rotations and an imposed equivalent strain of ~360, a saturated ufg microstructure was reached. Subsequently, a lamella with $3 \cdot 2 \cdot 1$ mm³ was cut by EDM, followed by thinning, polishing and FIB milling in a similar way as the sxx sample. Due to the radial strain gradient in HPT samples [20,21], the lamella was cut from a disk radius of 14 mm.

Vickers hardness measurements were performed on the as-received polycrystalline sample as well as on ufg samples using a Buehler MicroMet 5104 and a load of 500 gf.

The grain size was determined at the same disk radius of 14 mm using back-scattered electron (BSE) images (Figure 1a) and electron back scattered diffraction (EBSD)

grain orientation maps (Figure 1b) recorded in an SEM (Zeiss LEO 1525, Oberkochen, Germany). Additionally, a thin lamella was prepared from a disk radius of approximately 14 mm to investigate the microstructure via transmission electron microscopy (TEM, Philips CM 12), shown in Figure 1c. For interpretation, the arrangement of the HPT principal directions with respect to the compression axes of the pillars are included in Figure 1a, the inverse pole figure colour code map is shown in the bottom left corner of Figure 1b, and the diffraction pattern of the corresponding TEM image is presented in Figure 1c, revealing almost no texture but slightly elongated grains.

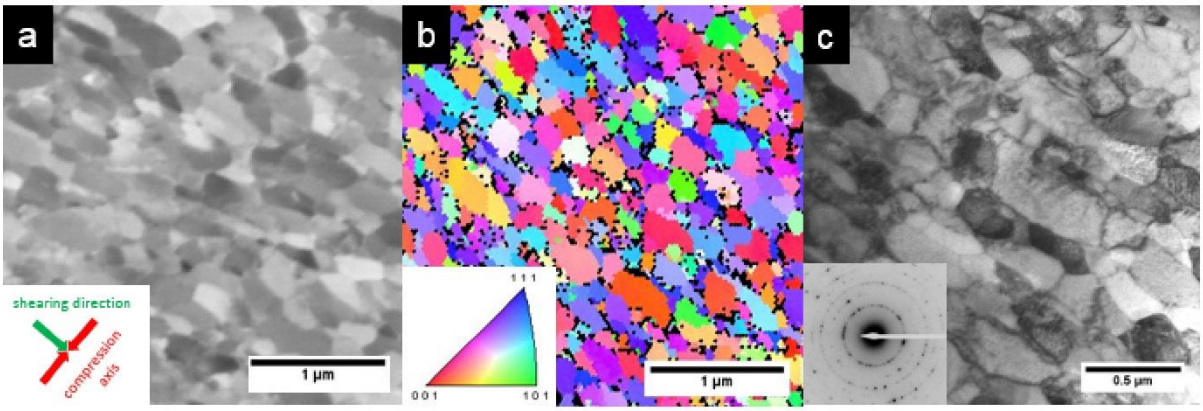

Figure 1: Microstructure of the HPT deformed Cr. a) BSE image, red arrows in the inset mark the compression axis regarding the direction of shear (green arrow) of the HPT sample, b) EBSD image and corresponding inverse pole figure, and c) bright field TEM image with corresponding diffraction pattern.

The pillar compression tests were carried out at RT in-situ in an SEM (Zeiss LEO 982, Oberkochen, Germany). Tests on samples smaller than 1 µm were performed utilizing a Hysitron PI 85 Picoindenter® using a feedback loop of 200 Hz, while pillars in the size range between 1 µm and 4 µm were tested with an UNAT-SEM indenter (Zwick GmbH & Co. KG, Ulm, Germany) with a feedback loop of 64 Hz, as this device offers higher loads [24] required to deform the large and strong ufg pillars. The indenters were equipped with conductive diamond flat punches with diameters of 6 µm and 8 µm, respectively (Synton-MDP AG, Nidau, Switzerland). Displacement-controlled tests were conducted at constant displacement rates that were adapted to the pillar geometry in order to reach a constant nominal strain rate of 10^{-3} s^{-1}, thereby excluding strain rate influences. The stress-strain curves were calculated from

recorded force-displacement data using the top pillar area and height from the untapered samples. The specimens were strained to ~20%, and corrections for sink-in [25] and machine stiffness [26] were taken into account. Furthermore, movies were captured from the compression tests with 1 frame per second to analyse the dynamics of the deformation processes, and high resolution SEM images were taken post-compression to relate them to the corresponding stress-strain curves.

To compare pillar compression with macroscopic results, ufg samples with dimensions of 2 · 2 · 3 mm³ were also cut by EDM from a disk radius of 14 mm. These samples were tested using a universal tensile testing unit (Zwick GmbH & Co. KG, Ulm, Germany) modified with a load reverse tool to a compression device. Tests were conducted in air at RT and loads were measured with a 10 kN load cell. Strains were calculated from the recorded time and corresponding crosshead velocity. The sample was held between two WC-Co plates and sample-plate interface friction was neglected.

A3 - Results

The bulk hardness of the sxx Cr samples is 1.6 GPa measured by NI [27] and results of Vickers microhardness testing are presented in Table 1. The corresponding indentation sizes for the as-received Cr and the HPT deformed Cr were ~7400 µm² and ~2025 µm², respectively. The initial grain size of the as-received polycrystalline Cr was ~200 µm. The mean grain sizes of the three images in Figure 1 were determined at a disk radius of ~14 mm using area-equivalent circle diameters, resulting in average grain sizes of 135 ± 34 nm, 170 ± 84 nm and 150 ± 36 nm for BSE, EBSD and TEM, respectively.

Table 1: Purity of the investigated materials and results of hardness testing.

Sample	Purity [%]	Hardness [GPa]
sxx Cr	99.999	1.6 [27]
as-received polycrystalline Cr	99.9	1.2 ± 0.04
ufg Cr	99.9	4.3 ± 0.10

Figure 2a depicts representative stress-strain curves of the sxx Cr pillars. While small samples show increasing flow stresses, pillar diameters larger than 4 µm reveal a strength of ~600 MPa. Converting the NI hardness (using a constraint factor of 2.8 and $H = \sigma \cdot C^*$ [28]), bulk strengths of ~570 MPa [27] are reached. The data for the bulk yield stress (0.02% plastic strain) of sxx Cr in (100) orientation is reported from tensile tests by Sameljuk *et al*. [29] as ~290 MPa, a much lower value as observed for present samples. This difference is explained by the large amount of strain hardening between the yield stress and a representative strain of ~8%. For pillars larger than 2 µm, the stress-strain curves show reasonably continuous plastic deformation with occasional burst events, while for smaller samples pronounced load drops occur. At pillar sizes below ~1 µm serrated flow is evident and load drops in the order of 700 MPa are observed. Notably, the number of load drops might also depend on the machine dynamics and whether displacement or load controlled mode is used [30].

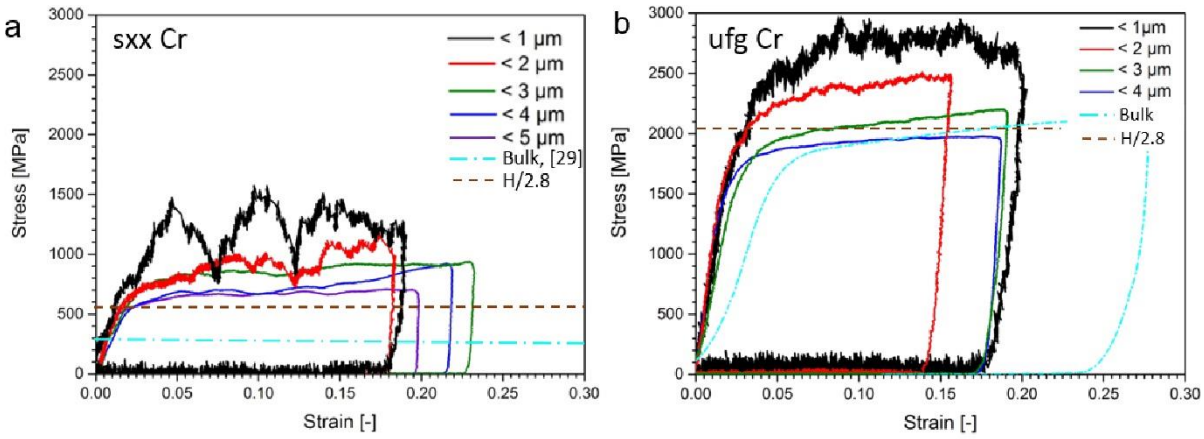

Figure 2: Representative micro compression stress-strain curves of a) sxx and b) ufg Cr pillars.

In the case of the ufg samples (Figure 2b), a higher yield stress is reached due to a refined microstructure. NI tests resulted in a strength of ~2050 MPa. Bulk compression samples and pillars with diameters of 4 µm show comparable yield strengths of ~2000 MPa and continuous plastic deformation. However, alignment was hindered due to lower stiffness of the bulk compression equipment, resulting in a sample misalignment of ~1°. Therefore, the elastic loading stiffness of bulk samples is reduced and not comparable with pillar compression experiments, where the determined Young's modulus of 250 GPa is reasonably close to the bulk value of 294 GPa [31].

In the case of decreasing pillar diameter, the yield strength of the ufg pillars also increases slightly. The stress-strain curves show features comparable with those in sxx samples, for instance, serrations and load drops in the order of 300 MPa for the same experimental setting. The plastic deformation behaviour can be seen in the supplementary videos, where video 1 depicts in-situ SEM pillar compression tests of two ~4 µm sized pillars, sxx and ufg, respectively. The insets show the corresponding stress-strain data. Video 2 depicts the same scheme for pillars with diameters of ~0.6 µm.

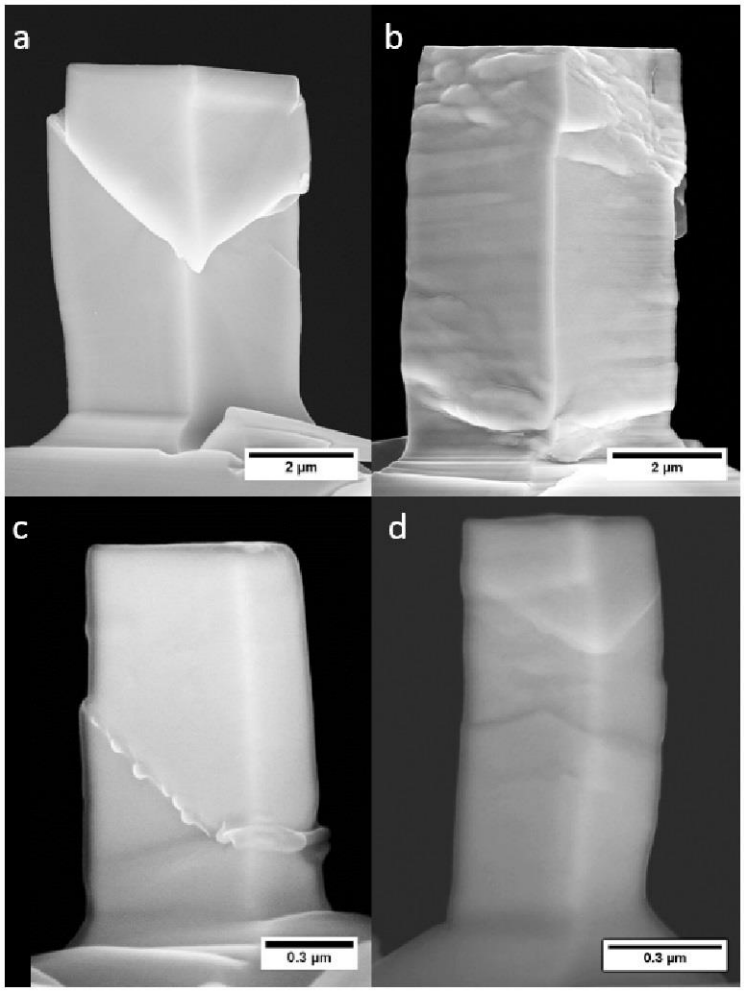

Figure 3: Post-deformation SEM images of compressed micropillars: a) 4 µm sxx, b) 3.8 µm ufg, c) 0.6 µm sxx and d) 0.4 µm ufg, respectively. All pillars were deformed to about 20% plastic strain.

Post-compression SEM images in Figure 3a and c represent deformed sxx pillars with diameters of ~4 µm and ~0.6 µm. Corresponding stress-strain curves are shown in Figure 2a where the dark blue curve describes the deformation of the 4 µm sxx pillar

and the black curve the deformation of the 0.6 µm sxx pillar, respectively. In case of the large sxx pillar (Figure 3a), deformation takes place on a preferred slip plane which has been estimated as the (110) plane typical for slip in bcc metals. Due to cross-slip of screw dislocations, deformation occurs on ill-defined crystallographic planes which intersect along the <111> direction [7]. In case of the small sxx pillar shown in Figure 3c, a similar deformation behaviour governed by crystallographic slip is observed.

Figure 3b and d represent deformed ufg pillars with diameters of ~3.8 µm and ~0.4 µm. Corresponding stress-strain curves are also depicted in Figure 2b, where the dark blue curve corresponds to the 3.8 µm ufg pillar and the black curve to the 0.4 µm ufg pillar. In contrast to the sxx samples, the large ufg pillars indicate slight barrelling, which is also seen in macroscopic compression samples due to friction at the surface-tool interfaces. Grains near the free surface emerge and slip planes in the grain interior, corresponding to the planes of highest shear stresses, are visible (Figure 3d).

In-situ deformation and post-compression SEM images (Figure 3) reveal the deformation behaviour on the surface, but deformation processes in the pillar volume are not directly visible. Therefore, FIB cross sections of the deformed sxx and ufg pillars were made to perform EBSD scans of the deformed interior. In Figure 4a, the cross section of a FIB cut sxx pillar is shown with an overlay of the corresponding EBSD scan. The slip traces of the (110) planes are indicated by black lines. The different colours represent a slight rotation of ~2° of the deformed part of the pillar with respect to the base. Figure 4b and c shows EBSD scans from cross-sections of ufg pillars with diameters of ~4 µm and ~0.5 µm, respectively. Approximately 40000 grains are located in the volume of the large ufg pillar while the number of grains is reduced to ~80 in the pillar shown in Figure 4c.

A4 - Discussion

In general, strengthening occurs when dislocation motion is hindered by obstacles, whether they are precipitates, forest dislocations or grain boundaries [32]. Once the involved length scales are truncated, as in the case of small pillars, the truncation effect is then responsible for the size-dependent strengthening. Moreover, activation of different slip systems can also contribute to a different scaling behaviour [33-36].

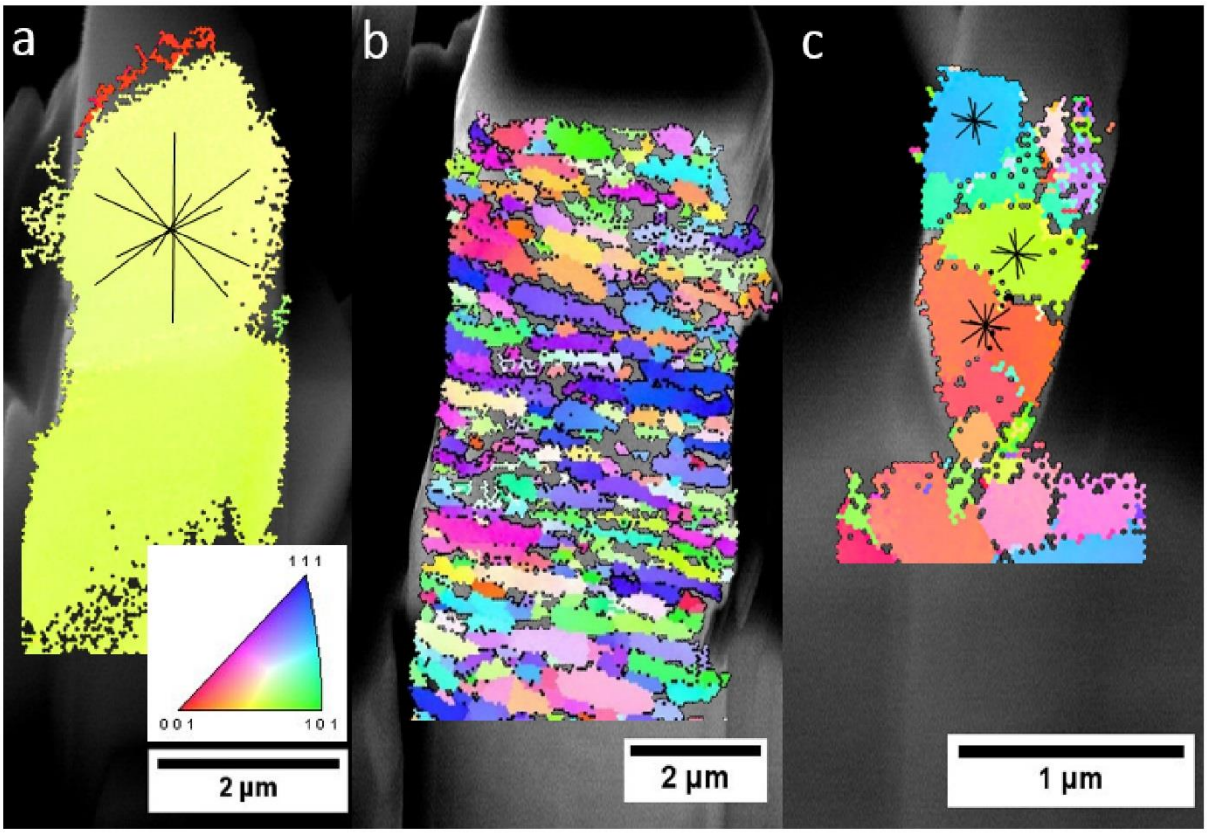

Figure 4: EBSD scans of cross-sections of different pillars and corresponding inverse pole figure. A) 2 µm sxx Cr pillar with (110) slip trace indicators showing ~2° misorientation between top and bottom part of the pillar, b) a 4 µm ufg pillar, and c) a 0.5 µm ufg pillar with (110) slip trace indicators for the larger grains.

To discuss the observed small scale deformation behaviour in detail, the schematic flow stress over pillar diameter diagram and the regarding sample microstructure (Figure 5a) are considered. As long as Frank-Read sources are controlling plastic deformation, a bulk strength is also expected in miniaturized compression tests, which is schematically represented by the red horizontal line for the sxx case. The obstacle spacing in terms of forest dislocations is smaller than the pillar diameter and a dislocation would bow out between obstacles (depicted as stars) on a preferred slip plane. If the pillar size decreases and the obstacle spacing approaches the pillar diameter, single armed sources [37] are responsible for plastic deformation. This yields to the sample size effect [1-4], evidenced by the increased slope of the red line for the sxx case. The blue lines including the top images in Figure 5a represent the deformation behaviour of ufg pillars. The top right pillar represents the case of a large sample, where the grain size is noticeably smaller than the pillar size. Dislocations bow out between obstacles or from boundaries in internal grains, and a

minority of single armed sources could act in surface grains. The stress-strain behaviour is similar to bulk samples due to a homogenous distribution of grains. The increased polycrystalline strength compared to sxx bulk strength is attributed to Hall-Petch strengthening [38,39]. In this case neither a size effect nor load drops are observable.

If the pillar diameter is decreased for a constant grain size, the number of grains inside the pillar decreases. As a direct consequence less obstacles and pinning points are present in the sample volume. The pillar in the middle of Figure 5a shows a small ufg specimen where the grain arrangement is not favourable for sxx deformation behaviour, indicated by the marked slip traces of the (110) slip planes that intersect a grain boundary before reaching the pillar surface.

In this simple case, no size effect would be expected, as dislocations are still blocked by grain boundaries, but individual slip events might be detectable in the stress-strain data, as evidenced by load drops in the stress-strain curves for small pillars (Figure 2). In load-controlled compression tests, strain bursts occur instead of load drops, but their origin is the same [30]. Ufg pillars show such features for pillar diameters smaller than 1 µm, where dislocation avalanches can easily exit at surface grains. Dislocations nucleated in grains being surrounded by other grains cannot exit on free surfaces. They rather pile-up at adjacent grain boundaries, which consequently yields to smaller load drops in the stress-strain curves of larger ufg samples. Such burst events are usually only detected for a limited number of grains. In large samples, they are typically averaged out.

If the grains are oriented in a more favourably way (top left pillar), slip traces reveal no intersections with boundaries and deformation as known for sxx pillars can occur, with the consequence that a size effect will be observed. In a more realistic scenario, surface grains will require higher external loads to cause yielding due to a reduced pile-up contribution for source activation, which will be more important for decreasing pillar diameters. Thus, the transition from ufg to sxx scaling behaviour might be gradual.

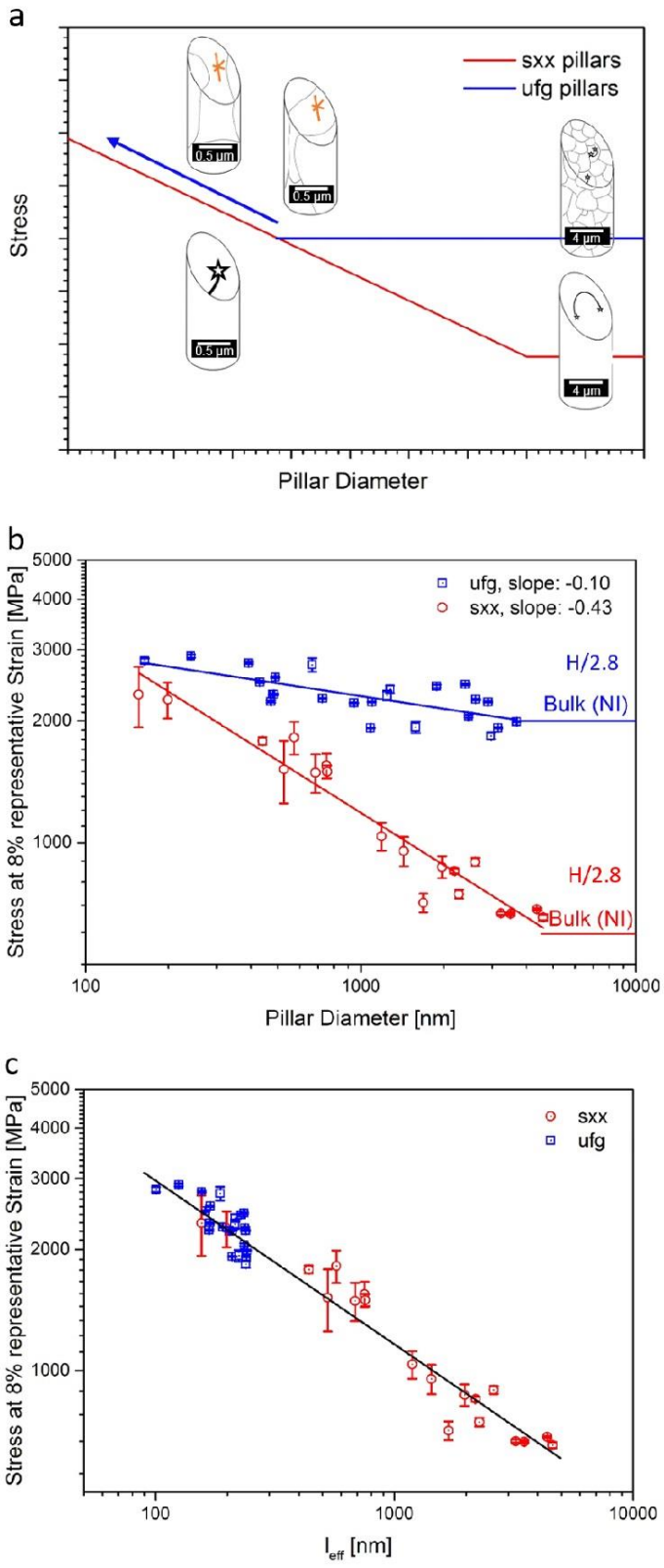

Figure 5: a) Schematic of the size effect in sxx and ufg pillars in a log-log stress-pillar diameter plot. The red and blue lines represent the behaviour of sxx samples and ufg pillars, respectively. b) Strengthening of sxx Cr and ufg Cr pillars evaluated at 8% flow stress and, c) strength data of both data sets collapses using a combined internal length scale leff. See text for more details.

Figure 5b depicts the representative flow stresses of the varying sized Cr pillars, evaluated at 8% plastic strain. This strain value was chosen to allow comparison with hardness tests performed with a Berkovich indenter (imposing 8% plastic strain [28]). Another reason for comparison of stresses at higher strain levels is to include the strain hardening behaviour within the first few percent of deformation to be comparable with previous bcc studies [4,15,33,34]. Red circles and blue squares indicate strength values of sxx and ufg pillars, respectively, with corresponding error bars resulting from uncertainties of determining the cross-sections and the noise of the indenter load without contact as a worst case limit.

Horizontal lines on the right represent bulk strengths and were taken for sxx samples from [27]. Bulk strengths of the ufg samples were calculated from hardness testing. They are in good agreement with the macroscopic compression test (Figure 2b) after removing the error in strain from misalignment.

The slope of the linear fit from the data points of the log-log plot in Figure 5b gives the power law scaling exponent n, which is 0.43 ± 0.03 for sxx pillars. While the scaling behaviour of bcc sxx pillars is well investigated, Cr has not been examined so far. Thus, it is interesting to note that this value fits well into the concept of Schneider *et al.* [4]. In fact, if the power law exponent is plotted against the homologous critical temperature (~0.68 for Cr), the model of Schneider would predict a power law scaling exponent of ~0.41, in close agreement with our results.

In the case of ufg pillars, the slope decreases due to the presence of grain boundaries and higher dislocation densities from HPT processing. The linear fit gives a scaling exponent of 0.10 ± 0.02, which reveals that a slight scaling behaviour is evident even in ufg pillars. The point of intersection of the two fit lines indicates the transition to sxx behaviour. It occurs at a pillar size of ~150 nm, which is in good agreement with the grain size of the material (Figure 1). In this situation, typically a single grain would span the pillar cross-section, leading to sxx deformation for both material conditions.

From the SEM images in Figure 3 it appears that the deformation behaviour is different between sxx and ufg pillars, which might have contributed to grain boundary mediated deformation, as reported in [40]. To investigate whether another length scale or deformation mechanism plays a dominant role, both data sets were analysed regarding to dislocation based plasticity. Taking into account sample size as well as

grain size in a weakest link concept, many approaches are found in literature. Keller *et al*. [41] and Chen *et al*. [42] investigated the influences of varying sample thickness and grain size on the mechanical properties in tensile tests, while Misra *et al.* [43], Zhang *et al*. [44], Guo *et al*. [45] and Knorr *et al*. [46] investigated the deformation behaviour in nano-scaled multilayers. Furthermore, Nicola *et al*. [47] applied such approaches on thin films. Bushby *et al*. [48] related an indentation contact size with the grain size. First weakest link concepts were suggested by Dunstan *et al*. [49]. They performed torsion tests on thin wires and related the responsible length scales, the grain size and a structure size (wire diameter) to an effective length scale l_{eff}. For our experiments, the extrinsic pillar diameter D and the intrinsic grain diameter d were related to l_{eff}. The two length scales interact with each other and result in a single scaling effect, for a situation where only dislocation slip is considered:

$$\frac{1}{l_{eff}} = \frac{1}{d} + \frac{1}{D}. \tag{1}$$

The length scale governing plastic deformation in equation (1) indicates that the grain size is the dominating part in ufg pillars, whereas for sxx pillars the pillar diameter is dominant (Figure 5c). For intermediate sizes, the coupling becomes more important. Note that a representative flow stress at 8% strain was again used to scale with the effective length scale of the pillars. It can be seen that sxx and ufg samples collapse on the same trend line (black), which implies that the scaling behaviour in both, ufg and sxx pillars, is controlled by the same deformation mechanism, namely dislocation motion.

The EBSD data, shown in Figure 4, support these assumptions. The ongoing dislocation motion in the sxx case (Figure 4a) leads to a slight rotation during compression, which is common behaviour due to lateral constraints [50-52]. Micron-sized ufg pillars (Figure 4b) deform similarly to bulk samples and show a comparable stress-strain behaviour. Grain size determinations also indicate comparable size distributions as for the initial HPT deformed material mentioned (Figure 1), and exclude distinct deformation induced grain growth [53,54]. Moreover, no indication of grain boundary sliding is observed in both micron- and sub-micron-sized pillars. In the case of a sub-micron sized pillar (Figure 4c), sxx deformation behaviour could be expected if one grain would span the whole pillar. For the given grain orientations, slip traces

indicate that the grain arrangement is unfavourable for sxx deformation. Therefore, the pillar deforms comparably to the larger ufg pillar with homogeneously distributed grains but at an increased flow stress level compared to bulk, as seen in Figure 2b.

In the case of polycrystalline pillars, only few and somewhat controversial results are reported in literature. Jang and Greer [55] investigated Ni-W pillars with a grain size of ~60 nm and found a size-induced weakening effect instead of a stress increase with decreasing pillar diameter below ~200 nm. In contrast, Rinaldi *et al.* [56] investigated comparable pure nanocrystalline Ni with a grain size of about 30 nm for samples in the size range from 160 nm to 272 nm and reported a size effect where smaller pillars are stronger. A scaling exponent of 0.38 to 0.66 [56] was observed depending on the strain level, where the defect density was always the same. Increasing the dislocation density by pre-straining of sxx Ni reduced the scaling behaviour from 0.66 to 0.16 [15,16].

Schreijäg *et al.* [57] investigated bcc metals (α-Fe and DC04, a low alloyed steel) with focus on the effect of sample size and microstructure on the strengthening behaviour tested by pillar compression. Their metal sheets were cold rolled and annealed, and the FIB fabricated pillars were in the size range between 500 nm and 22 µm for a grain size of about 50 µm, thus essentially single crystalline. Slip in their heat treated pillars did not necessarily end at grain boundaries and only small differences between sxx and heat treated polycrystalline pillars were found. In the case of the cold rolled material, grain boundaries acting as obstacles were reported not to play an effective role and dislocations did not pile up. Cold rolling resulted in a varying grain boundary character compared to HPT, caused by a much lower degree of deformation. Notably, the contained dislocation density in the rolled material should be comparable with the present ufg material processed via HPT of ~10^{14} to 10^{15} m^{-2} [58,59] containing mostly large angle grain boundaries. For Fe, which has a low thermal stress component at RT, the scaling exponent was reported as 0.81 by Schreijäg *et al.* [57] which is even higher than observed in fcc metals [1,2]. This strong scaling exponent has also been reported by Rogne and Thaulow for sxx Fe [36] and might be contributed to different crystal orientations. A scaling behaviour in strength of the cold rolled DC04 steel has not been observed by Schreijäg *et al.* [57], which is likely due to high dislocation density and large samples, comparable with results of pre-strained pillars [14-16].

Another approach to explain this strengthening is a statistical size effect as suggested by Henning and Vehoff [60]. By calculating Taylor factors and minimal grain areas over the specimen width, they could predict the initial point of yielding in their samples. This, however, requires simplifications such as a two-dimensional microstructure, which is not been guaranteed even in the smallest ufg pillars. Thus, we consider only flow stresses instead of critical resolved shear stresses, and do not attempt to address a statistical size effect.

Jang and Greer [55] and Rinaldi *et al.* [56] performed their experiments at low grain size to pillar size ratios of ~0.02 - 0.2 corresponding to a bulk situation, while the investigations from Schreijäg *et al.* [57] were conducted on high *d/D* ratios of ~2 – 100, thus essentially in the sxx regime. In the case of the present ufg pillars, a grain size to pillar size ratio of ~0.04 - 1 was investigated, thereby spanning the whole range of interest.

In this intermediate transition regime, the results presented show a non-negligible strength scaling behaviour in ufg pillars, emerging due to the comparable magnitude of the internal (microstructural) length scale and the pillar dimensions. Since the grain size *d* is ~160 nm (Figure 1), dislocation-mediated plasticity within the grains is most probably responsible for plastic deformation. As dislocations can exit to the surface, stronger near-surface grains gain importance with decreasing sample dimensions. This reduces dislocation pile-ups and local stresses and requires higher loads for plastic deformation. Thereby, near-surface grains contribute to the strength scaling exponent of 0.10 ± 0.02. Considering the situation from the sxx point of view, the reduced scaling exponent would also indicate a higher defect density compared to sxx samples [15]. The defect densities in the investigated samples were not determined explicitly. However, comparison with calculations from El-Awady [61] suggest that a dislocation density of ~10^{14} to 10^{15} m^{-2} [58,59] would yield to a scaling exponent of ~0.10, in good agreement with present results.

A5 - Conclusion

Size effect investigations on sxx Cr and ufg Cr were performed to study the interaction between internal microstructure and external sample dimensions. Sxx pillars reveal a scaling behaviour of ~0.43, in agreement with other bcc sxx pillars when normalized to the homologous critical temperature. Ufg pillars show a decreased scaling behaviour with a scaling exponent of ~0.10. This reduction is explained by the influence of free surfaces in small scale testing, as grains influenced by the pillar surface seem to be stronger than grains in the pillar volume. Dislocations can exit the near-surface grain, making them resistant to subsequent deformation. Current data analysis is based on dislocation plasticity at RT. Up to now, no differentiation between the effects of dislocation density and grain boundaries regarding the reduced scaling exponent are made. Possible influences of surface or boundary mediated processes, in particular at elevated temperature, will be investigated in the future.

A6 - Appendix: Supplementary Material

The supplementary videos of publication A are included digitally on the storage medium located at the end of the thesis.

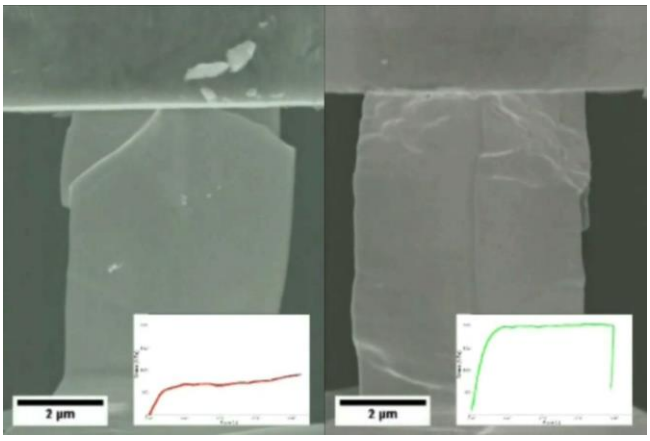

Video1: In-situ SEM compression test of two ~4 µm sized Cr pillars. The left sample is single crystalline while the right one contains an ufg microstructure. The insets show the corresponding stress-strain data.

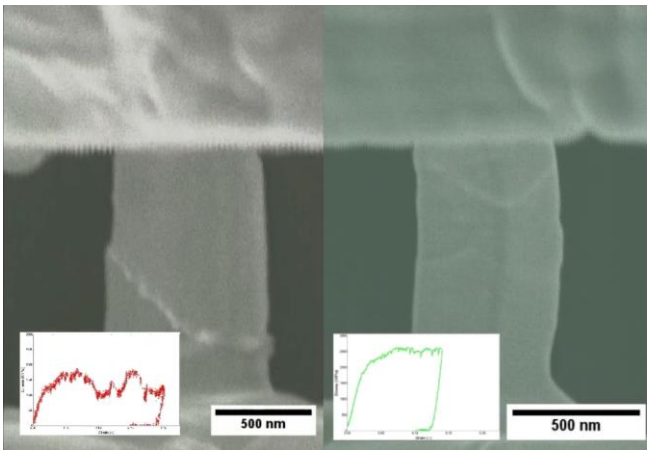

Video 2: In-situ SEM compression test of two ~0.6 µm sized Cr pillars with a single crystalline (left) and an ufg microstructure (right). The insets show the corresponding stress-strain data.

A - References

[1] M.D. Uchic, D.M. Dimiduk, J.N. Florando, W.D. Nix, Sample dimensions influence strength and crystal plasticity. Science 305 (2004) 986-989.

[2] M.D. Uchic, P.A. Shade, D.M. Dimiduk, Plasticity of micrometer-scale single crystals in compression. Annu. Rev. Mater. Res. 39 (2009) 8.1-8.26.

[3] J.R. Greer and J.T.M. De Hosson, Plasticity in small-sized metallic systems: Intrinsic vs. extrinsic size effect. Prog. Mater. Sci. 56 (2011) 654-724.

[4] A.S. Schneider, D. Kaufmann, B.G. Clark, C.P. Frick, P.A. Gruber, R. Mönig, O. Kraft, E. Arzt, Correlation between critical temperature and strength of small-scale bcc pillars. PRL 103 (2009) 105501.

[5] J.-Y. Kim, D. Jang, J.R. Greer, Tensile and compressive behaviour of tungsten, molybdenum, tantalum and niobium at the nanoscale. Acta Mater. 58 (2010) 2355-2363.

[6] J. Cui, G. Po, N. Ghoniem, Temperature insensitivity of the flow stress in body-centered cubic micropillar crystals. Acta Mater. 108 (2016) 128-137.

[7] B. Sestak, A. Seeger, Gleitung und Verfestigung in kubisch-raumzentrierten Metallen und Legierungen. Z. Met. 69 (1978) 195-202.

[8] A. Seeger, The temperature and strain-rate dependence of the flow stress of bcc metals: A theory based on kink-kink interactions. Z. Met. 72 (1981) 369-380.

[9] A.S. Schneider, C.P. Frick, E. Arzt, W.J. Clegg, S. Korte, Influence of test temperature on the size effect in molybdenum small-scale compression pillars. Phil. Mag. Let. 93 (2013) 331-338.

[10] J.R. Greer, C. Weinberger, W. Cai, Comparing the strength of f.c.c. and b.c.c. sub-micrometer pillars: Compression experiments and dislocation dynamics simulations. Mater. Sci. Eng. A 493 (2008) 21-25.

[11] V. Maier, C. Schunk, M. Göken, K. Durst, Microstructure-dependent deformation behaviour of bcc-metals - indentation size effect and strain rate sensitivity. Philos. Mag. 95 (2015) 1766-1779.

[12] O. Torrents Abad, J.M. Wheeler, J. Michler, A.S. Schneider, E. Arzt, Temperature-dependent size effects on the strength of Ta and W micropillars. Acta Mater. 103 (2016) 483-494.

[13] A. Rinaldi, P. Peralta, K. Sieradzki, E. Traversa, S. Licoccia, Role of dislocation density on the sample-size effect in nanoscale plastic yielding. J. Nanomech. Micromech. 2 (2012) 42-48.

[14] H. Bei, S. Shim, G.M. Pharr, E.P. George, Effects of pre-strain on the compressive stress-strain response of Mo-alloy single-crystal micropillars. Acta Mater. 56 (2008) 4762-4770.

[15] A.S. Schneider, D. Kiener, C.M. Yakacki, H.J. Maier, P.A. Gruber, N. Tamura, M. Kunz, A.M. Minor, C.P. Frick, Influence of bulk pre-straining on the size effect in nickel compression pillars. Mater. Sci. Eng. A 559 (2013) 147-158.

[16] J.A. El-Awady, M.D. Uchic, P.A. Shade, S.-L. Kim, S.I. Rao, D.M. Dimiduk, C. Woodward, Pre-straining effects on the power-law scaling of size-dependent strengthening in Ni single crystals. Scr. Mater. 68 (2013) 207-210.

[17] P.J.M. Janssen, J.P.M. Hoefnagels, T.H. de Keijser, M.G.D. Geers, Processing induced size effects in plastic yielding upon miniaturisation. J. Mech. Phys. Solids 56 (2008)2687-2706.

[18] D. Kiener, C. Motz, M. Rester, M. Jenko, G. Dehm, FIB damage of Cu and possible consequences for miniaturized mechanical tests. Mater. Sci. Eng. A 459 (2007) 262-272.

[19] A.T. Jennings, M.J. Burek, J.R. Greer, Microstructure versus size and mechanical properties of electroplated and single crystalline Cu nanopillars. PRL 104 (2010) 135503.

[20] R. Pippan, S. Scheriau, A. Taylor, M. Hafok, A. Hohenwarter, A. Bachmaier, Saturation of fragmentation during severe plastic deformation. Annu. Rev. Mater. Res. 40 (2010) 319-343.

[21] R.Z. Valiev, R.K. Islamgaliev, I.V. Alexandrov, Bulk nanostructured materials from severe and plastic deformation. Prog. Mater. Sci. 45 (2000) 103-189.

[22] S. Wurster, R. Treml, R. Fritz, M.W. Kapp, E.-M. Langs, M. Alfreider, C. Ruhs, P.J. Imrich, G. Felber, D. Kiener, Novel methods for the site specific preparation of micromechanical structures. Prakt. Met. Sonderband 46 (2014) 27-36.

[23] R. Wadsack, R. Pippan, B. Schedler, Structural refinement of chromium by severe plastic deformation. Fusion Engineering and Design 66-68 (2003) 265-269.

[24] D. Kiener, C. Motz, G. Dehm, R. Pippan, Overview on established and novel FIB based miniaturized mechanical testing using in-situ SEM. Int. J. Mat. Res. 100 (2009) 1074-1087.

[25] I.N. Sneddon, The relation between load and penetration in the axisymmetric Boussinesq Problem for a punch of arbitrary profile. Int. J. Engng. Sci. 3 (1965) 47-57.

[26] D. Kiener, W. Grosinger, G. Dehm, On the importance of sample compliance in uniaxial microtesting. Scr. Mater. 60 (2009)148-151.

[27] V. Maier, A. Hohenwarter, R. Pippan, D. Kiener, Thermally activated deformation processes in body-centered cubic Cr - How microstructure influences strain-rate sensitivity. Scr. Mater. 106 (2015) 42-45.

[28] A.G. Atkins, D. Tabor, Plastic Indentation in metals with cones. J. Mech. Phys. Solids 13 (1965) 149-164.

[29] A.V. Sameljuk, A.D. Vasilev, S.A. Firstov, Low temperature deformation and fracture behaviour of [100] and [110] chromium single crystals. Int. J. of Refractory Metals & Hard Materials 14 (1996) 249-255.

[30] O.L. Warren, S.A. Downs, T.J. Wyrobek, Challenges and interesting observations associated with feedback-controlled nanoindentation. Z. Met. 95 (2004) 287-296.

[31] D.I. Bolef, J. De Klerk, Anomalies in the Elastic Constants and Thermal Expansion of Chromium Single Crystals. Phys. Rev. 129 (1963) 1063-1067.

[32] E. Arzt, Size effects in materials due to microstructural and dimensional constraints: a comparative review. Acta. Mater. 46 (1998) 5611-5626.

[33] A.S. Schneider, B.G. Clark, C.P. Frick, P.A. Gruber, E. Arzt, Effect of orientation and loading rate on compression behaviour of small-scale Mo pillars. Mater. Sci. Eng. A 508 (2009) 241-246.

[34] A.S. Schneider, C.P. Frick, B.G. Clark, P.A. Gruber, E. Arzt, Influence of orientation on the size effect in bcc pillars with different critical temperatures. Mater. Sci. Eng. A 528 (2011) 1540-1547.

[35] S. Korte, W.J. Clegg, Discussion of the dependence of the effect of size on the yield stress in hard materials studied by microcompression of MgO. Philos. Mag. 91 (2011) 1150-1162.

[36] B.R.S. Rogne, C. Thaulow, Effect of crystal orientation on the strengthening of iron micro pillars. Mater. Sci. Eng. A 621 (2015) 133-142.

[37] T.A. Parthasarathy, S.I. Rao, D.M. Dimiduk, M.D. Uchic, D.R. Trinkle, Contribution to size effect of yield strength from the stochastics of dislocation source lengths in finite samples. Scr. Mater. 56 (2007) 313-316.

[38] E.O. Hall, The deformation and ageing of mild steel: III Discussion of results. Proc. Phys. Soc. Lond. B 64 (1951) 747-753.

[39] N.J. Petch, The cleavage strength of polycrystals. J. Iron Steel Inst. 174 (1953) 25-28.

[40] C. Wang, C. Wang, J. Xu, P. Zhang, D. Shan, B. Guo, Plastic deformation size effects in micro-compression of pure nickel with a few grains across diameter. Mater. Sci. Eng. A 636 (2015) 352-360.

[41] C. Keller, E. Hug, X. Feaugas, Microstructural size effects on mechanical properties of high purity nickel. International Journal of Plasticity 27 (2011) 635-654.

[42] X.X. Chen, A.H.W. Ngan, Specimen size and grain size effects on tensile strength of Ag microwires. Scripta Mater. 64 (2011) 717-720.

[43] A. Misra, J.P. Hirth, R.G. Hoagland, Length-scale-dependent deformation mechanisms in incoherent metallic multilayered composites. Acta Mater. 53 (2005) 4817-4824.

[44] J.Y. Zhang, G. Liu, J. Sun, Comparisons between homogeneous boundaries and heterophase interfaces in plastic deformation: Nanostructured Cu micropillars vs. nanolayered Cu-based micropillars. Acta Mater. 61 (2013) 6868-6881.

[45] W. Guo, E. Jägle, J. Yao, V. Maier, S. Korte-Kerzel, J.M. Schneider, D. Raabe, Intrinsic and extrinsic size effects in the deformation of amorphous CuZr/nanocrystalline Cu nanolaminates. Acta Mater. 80 (2014) 94-106.

[46] I. Knorr, N.M. Cordero, E.T. Lilleodden, C.A. Volkert, Mechanical behavior of nanoscale Cu/PdSi multilayers. Acta Mater. 61(2013) 4984-4995.

[47] L. Nicola, Y. Xiang, J.J. Vlassak, E. Van der Giessen, A. Needleman, Plastic deformation of freestanding thin films: Experiments and modelling. J. Mech. Phys. Solids 54 (2006) 2089-2110.

[48] A.J. Bushby, D.J. Dunstan, Size effects in yield and plasticity under uniaxial and non-uniform loading: experiment and theory. Philos. Mag. 91 (2011) 1037-1049.

[49] D. Dunstan, B. Ehrler, R. Bossis, S. Joly, K.M.Y. P'ng, A. Bushby, Elastic limit and strain hardening of thin wires in torsion. PRL 103 (2009) 155501.

[50] C. Kirchlechner, J. Keckes, C. Motz, W. Grosinger, M.W. Kapp, J.S. Micha, O. Ulrich, G. Dehm, Impact of instrumental constraints and imperfections on the dislocation structure in micron-sized Cu compression pillars. Acta Mat. 59 (2011) 5618-5626.

[51] C. Niederberger, W.M. Mook, X. Maeder, J. Michler, In situ electron backscatter diffraction (EBSD) during the compression of micropillars. Mater. Sci. Eng. A 527 (2010) 4306-4311.

[52] R. Maaß, S. Van Petegem, D. Grolimund, H. Van Swygenhoven, D. Kiener, G. Dehm, Crystal rotation in Cu single crystal micropillars: In situ Laue and electron backscatter diffraction. APL 92 (2008) 071905.

[53] F. Mompiou, M. Legros, Quantitative grain growth and rotation probed by in-situ TEM straining and orientation mapping in small grained Al thin films. Scr. Mater. 99 (2015) 5-8.

[54] D.S. Gianola, S. Van Petegem, M. Legros, S. Brandstetter, H. Van Swygenhoven, K.J. Hemker, Stress-assisted discontinuous grain growth and its effect on the deformation behaviour of nanocrystalline aluminum thin films. Acta Mater. 54 (2006) 2253-2263.

[55] D. Jang, J.R. Greer, Size-induced weakening and grain boundary-assisted deformation in 60nm grained Ni nanopillars. Scr. Mater. 64 (2011) 77-80.

[56] A. Rinaldi, P. Peralta, C. Friesen, K. Sieradzki, Sample-size effects in the yield behaviour of nanocrystalline nickel. Acta Mater. 56 (2008) 511-517.

[57] S. Schreijäg, D. Kaufmann, M. Wenk, O. Kraft, R. Mönig, Size and microstructural effects in the mechanical response of alpha-Fe and low alloyed steel. Acta Mater. 97 (2015) 94-104.

[58] B. Joni, E. Schafler, M. Zehetbauer, G. Tichy, T. Ungar, Correlation between the microstructure studied by X-ray line profile analysis and the strength of high-pressure-torsion processed Nb and Ta. Acta. Mater. 61 (2013) 632-642.

[59] Y. Miyajima, S. Okubo, H. Abe, H. Okumura, T. Fujii, S. Onaka, M. Kato, Dislocation density of pure copper processed by accumulative roll bonding and equal-channel angular pressing. Materials Characterization 104 (2015) 101-106.

[60] M. Henning, H. Vehoff, Statistical size effects based on grain size and texture in thin sheets. Mater. Sci. Eng. A 452 (2007) 453-602.

[61] J.A. El-Awady, Unravelling the physics of size-dependent dislocation-mediated plasticity. Nat. Comm. 6:5926 (2015) 1-9.

Publication B

Dominating Deformation Mechanisms in Ultrafine-grained Chromium across Length Scales and Temperatures

R. Fritz[1], D. Wimler[1], A. Leitner[1], V. Maier-Kiener[2], D. Kiener[1]

Acta Materialia 140 (2017) 176-187

[1] Department Materials Physics, Montanuniversität Leoben, Leoben, Austria

[2] Department Physical Metallurgy & Materials Testing, Montanuniversität Leoben, Leoben, Austria

B - Abstract

The microstructure influence on the thermally activated deformation behaviour of chromium is investigated for a more fundamental understanding on the deformation mechanisms contributing to plasticity in bcc metals. Therefore, scale-bridging experiments at variable temperatures and for varying strain-rates are performed, encompassing macroscopic compression tests in direct correlation to local in-situ SEM micro-compression experiments on taper-free pillars and advanced nanoindentation testing. For the first time, it is demonstrated that, independent of stress state, sample volume and surface fraction, a distinct temperature-dependent transition of the dominating deformation mechanism occurs. While at low temperatures the lattice resistance dominates, exceeding a critical temperature the dislocation interaction with grain boundaries becomes the rate limiting step. Finally, based on the vastly different fractions of grain boundaries in the tested sample volumes, a more comprehensive model on the deformation of bcc metals, in particular at small scales or for confined volumes is derived.

B1 - Introduction

Over the last decades, investigations on the elemental deformation mechanisms in different metals, in particular body-centred cubic (bcc) ones, were extended from originally coarse-grained (cg) states [1,2] to single-crystalline (sxx) [3,4], ultrafine-grained (ufg) [5-7] and even nano-crystalline (nc) [8,9] microstructures. Since macroscopic tests average deformation characteristics over several length scales, testing of limited sample volumes [10] offers the premise to assess specific intrinsic material behaviour. In these small dimensions, individual plasticity mechanisms, such as dislocation motion, dislocation interactions, dislocation pile-ups [9], or even diffusion-mediated processes such as grain boundary (GB) sliding [11,12] can potentially be isolated, thereby allowing identification and analysis of specific deformation modes.

A common approach to gain insight into the thermally activated deformation behaviour of bcc metals is to determine the strain-rate sensitivity (m) and the correspondent activation volume (ν) [13]. Therefore, constant strain-rate tests or/and strain-rate jump (SRJ) tests are conducted and the rate-dependent stress responses

are used to determine *m*. Since in this work the aim is to bridge from macroscopic experiments to small volumes, it is important to note that recent work on nc Ni, ufg Al and ufg Nb [14-16] revealed direct comparability of constant strain-rate tests and SRJ tests performed by nanoindentation, small-scale tension and compression experiments with macroscopic data.

Conventional cg or sxx face-centred cubic (fcc) metals exhibit *m*-values in the order of 10^{-3} [5,17-20]. If internal length scales for dislocation interaction become smaller, e.g. by decreasing the grain size, *m* increases by about one order of magnitude [9,17]. The corresponding ν (indicated in multiples of the cubed Burger's vector *b*) decreases from values well above 100 b^3 (cg microstructure) to a couple of 10 b^3 in ufg fcc metals [9,18]. This indicates a transition from forest dislocation interactions to dislocation-GB interactions. Further decreasing the grain size to the nc regime leads to low ν of ~1 b^3. These values are classically attributed to diffusion-driven processes [9].

To investigate the GB contribution in confined sample volumes, Zhang *et al.* [19,20] performed micro-compression tests on sxx and ufg Cu pillars and reported that *m* is strongly dependent on the sample diameter to grain diameter (*D/d*) ratio. While sxx and macroscopic polycrystalline Cu samples show low *m*-values of ~0.002, they reported ~0.10 - 0.15 for *D/d* ranging between 3 and 10. Thus, the high number of interfaces in the deformed volume strongly influences the deformation behaviour [5,9,21] as well as the yield stress [22-25] of pillars in the fcc case.

While the situation in fcc metals is quite well understood, the situation is less clear in bcc structures [26,27]. This prevails especially for cases where microstructure, microstructural constraints, loading conditions and variable sample sizes are taken into account. Moreover, the flow stress in bcc metals consists of two parts, namely the temperature independent athermal component (σ_a), which arises from long-range stresses caused by obstacles to dislocation motion, such as impurities or GBs, and the temperature and strain-rate dependent thermal component of the flow stress (σ_{th}), which stems from the resistance of the lattice itself, called the Peierls potential [1,28]. In the latter case, the movement of screw dislocations via the kink-pair mechanism becomes the dominating thermally activated contribution during low temperature deformation [29].

The temperature dependency varies with respect to a critical material specific temperature (T_c), upon which thermal activation eases the movement of screw dislocations with increasing temperature. Eventually, the lattice friction diminishes once T_c is reached at ~$0.2 \cdot T_m$ [29], with T_m being the melting temperature of the respective metal. Above this temperature (for Cr ~160°C [29]), the rate-dependent characteristics in bcc and fcc metals are comparable since the Peierls potential contribution vanishes. Therefore, screw dislocations exhibit a similar mobility as edge dislocations [28], which consequently leads to low m and corresponding high ν typical for fcc metals, as only long range stresses prevail.

In literature, investigations on bcc metals were conducted by Wei *et al.* [30-34] performing macroscopic compression tests and Zhou *et al.* [35] and Wu *et al.* [8] performing nanoindentation tests, addressing the rate-dependent deformation behaviour on V, W, Mo, Ta and Cr. Increasing m with increasing grain size was reported, opposite to reports on fcc metals [5,9,21].

More recently, Maier *et al.* [6,7] investigated the deformation mechanisms in sxx and ufg bcc metals by means of advanced nanoindentation techniques at room temperature (RT) for Cr and W [7], and at elevated temperatures for Cr [6]. For Cr, m at RT of ~0.07 in sxx samples was attributed to a strong contribution of the Peierls potential and a low mobility of screw dislocations [28] which govern the deformation process at low homologous temperatures underneath T_c via the kink pair mechanism [1,28,29]. Comparably lower m at RT of ~0.02 in ufg samples was referred to a prevailing contribution of the Peierls potential in combination with an increased athermal contribution due to GB strengthening. Overcoming T_c in the ufg state, a further increase of m was measured and related to a diminishing contribution of σ_{th} accompanied by an emerging dominant thermally activated dislocation-GB interaction. σ_a remains mostly constant with increasing temperature due to a thermally stable microstructure [6].

In this work, focus is placed towards a more comprehensive scale-bridging understanding of the deformation characteristics of bcc Cr by examining contributing factors such as microstructure, sample size, temperature and stress state. The corresponding effects on the deformation behaviour over four orders of magnitude concerning the sample size, taking into account rate effects at ambient as well as non-ambient conditions, are analysed in this study. Therefore, uniaxial macroscopic

compression tests, in-situ SEM micro-compression experiments, as well as multiaxial advanced nanoindentation experiments using different tip geometries were performed at variable strain-rates between RT and 400°C to determine *m*-values and activation volumes. The stress-strain response and occurring deformation mechanisms were compared with sxx Cr to assess the impact of GB contributions. Moreover, the rate-dependent properties and microstructural evolution will be related to the loaded material volume with respect to testing temperature (T_{test}) and fraction of GBs present within the specimen to assess size-dependent mechanism transitions.

B2 - Material Processing

The as-received polycrystalline ultra-high-purity Cr sheets (Cr-265, Plansee SE, Reutte, Austria) were cut by Electrical Discharge Machining (EDM, Brother HS-3100) to a cylinder with a diameter of ~30 mm and a height of ~7 mm. Subsequently, this cylinder was deformed via High Pressure Torsion (HPT) [36,37] using a rotational speed of 0.5 rpm and a pressure of 4.2 GPa at 200°C to an equivalent strain of ~360 (50 rotations) to reach an ufg microstructure. Subsequently, the Vickers hardness (Buehler MicroMet 5104, load of 500 gf) of ufg Cr was measured over the whole disk radius (*r*) and disk thickness on polished samples and is shown in Figure 1a on top of the half HPT disk.

Compression Testing

The EDM-cut macroscopic compression samples indicated in Figure 1a were subsequently ground and polished with SiC paper to achieve a smooth sample surface with final sample dimensions of $2 \cdot 2 \cdot 3$ mm³. They were machined in axial disc direction, where elongated grains from the HPT process are oriented perpendicular to the compression axis. The samples were held between two WC-Co plates and sample-plate interface friction during deformation was neglected. Testing was performed in air using a universal tensile testing unit (Zwick GmbH & Co KG, Ulm, Germany) modified with a load-reverse tool to a compression device. Loads were measured with a calibrated 10 kN load cell and strains were calculated from recorded time and the corresponding crosshead velocity.

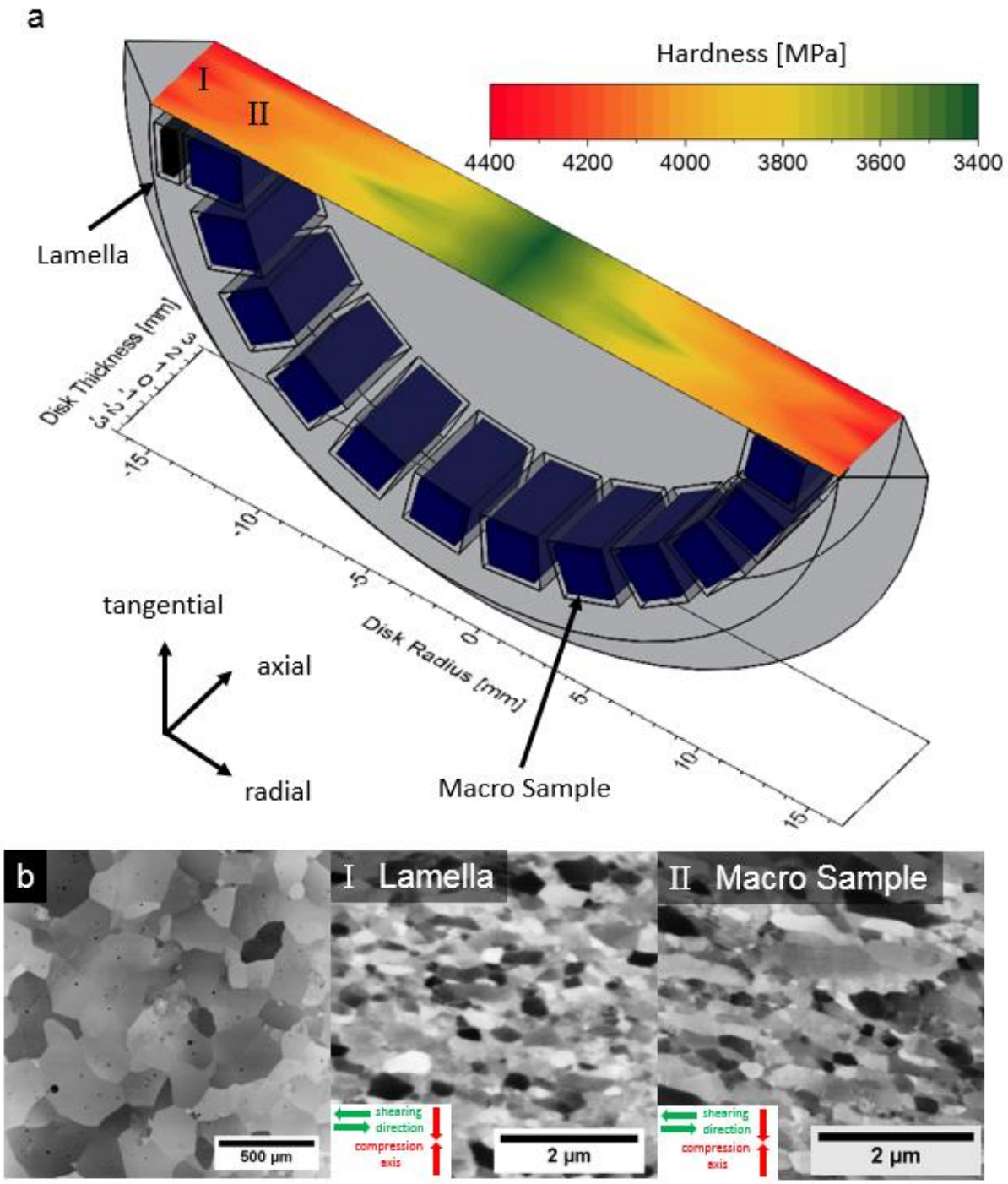

Figure 1: Half of a HPT-deformed Cr disk with corresponding hardness map and BSE images of the microstructure. a) EDM was used to cut a lamella (black – left side) from the HPT disk for FIB pillar preparation from a disk radius of 14 mm and several macroscopic compression samples from a radius range between 12 mm and 14 mm. The compression axis is the axial direction of the HPT sample. b) Microstructures before and after HPT deformation. The left image shows the as-received Cr (*d*~200 µm). I and II represent the microstructure after HPT deformation at a disk radius of 14 mm (lamella for pillar preparation, *d*~160 nm) and at a disk radius of ~12 mm (for macroscopic samples, *d*~300 nm), respectively.

High temperature pillar-compression

For micro-pillar compression tests at elevated temperature, a custom made, resistive heating device equipped with a ~12 µm sapphire flat punch (Synton-MDP AG, Nidau, Switzerland) was installed on the UNAT-SEM indenter. To achieve isothermal contact temperatures, the sample holder was also independently heated on the moveable stage of the SEM. Thermocouples were brazed nearby the indenter and the sample holders. Software control was implemented in LabView® (National Instruments Corp., Austin, Texas, USA) and temperature control was achieved with a PID feedback loop. With this setup, accurate measurements at temperatures up to 300°C are achievable without active cooling after a stabilisation time of ~30 min. For temperature calibration of the equipped indenter, a temperature matching procedure as suggested in [47] has been applied to tune the contact temperature between the indenter and the sample in order to minimize thermal drift. Further details about the setup are summarized in [48].

Nanoindentation

HPT-deformed macroscopic ufg samples as well as an sxx sample were mechanically and electrolytically polished to remove remaining deformation layers before nanoindentation testing. In order to measure thermally activated processes at various temperatures, nanoindentation strain-rate jump (SRJ) tests [14] were performed using a Nanoindenter G200 (Keysight Technologies, USA) equipped with a continuous stiffness measurement (CSM) unit to continuously record contact stiffness and to avoid local thermal drift [49]. Machine stiffness and tip shape calibrations were performed at RT according to the Oliver-Pharr method [50]. Strain-rate jumps for displacement segments of 500 nm each and strain-rate levels of $5 \cdot 10^{-2}$ s^{-1}, 10^{-2} s^{-1}, 10^{-3} s^{-1} and $5 \cdot 10^{-3}$ s^{-1} were performed. Furthermore, strain-rate controlled tests with a constant strain-rate of $5 \cdot 10^{-2}$ s^{-1} were conducted to compare to results from SRJ testing as well as uniaxial testing techniques. For all tests, the CSM frequency was set to 45 Hz and a harmonic displacement amplitude of 2 nm was superimposed.

For RT testing, a three-sided diamond Berkovich pyramid (imposing ~8% plastic strain, obtained from MicroStar Technologies, Huntsville, USA) as well as a diamond Cube Corner indenter (Synton-MDP AG, Nidau, Switzerland), which imposes ~20% plastic strain [51], were utilised. For high temperature measurements at 100°C, 150°C,

200°C, 250°C and 300°C a Berkovich pyramid tip made of sapphire (Synton-MDP AG, Nidau, Switzerland) was used. Independent heating of sample and indenter was achieved by a laser heating stage (SurfaceTec, Hückelhoven, Germany) and an active water-cooling system. Moreover, the maximum indentation depth for all indents was 2500 nm and tests under non-ambient conditions were performed in an inert gas environment (95% N_2 and 5% H_2) to exclude sampling issues and oxidation effects.

B3 - Results

Microstructure and hardness

The initial grain size of the as-received polycrystalline Cr was ~200 µm (Figure 1b, left). The mean grain size in the ufg lamella used for pillar preparation was ~160 ± 51 nm (Figure 1b, middle) and in the macroscopic compression samples, ranging from *r*~12 mm to *r*~14 mm ~300 ± 86 nm (Figure 1b, right). In both cases, grains are slightly elongated but no pronounced texture was observed. The average aspect ratio of elongated grains was 2.7/1 ± 0.09 in axial direction, and no pronounced substructure formation was observed.

Table 1: Purity and bulk hardness obtained by nanoindentation and Vickers micro-hardness measurements

Sample	Purity [%]	Method	Hardness [GPa]
sxx Cr	99.999	Nanoindentation	1.6 [6]
as-received polycrystalline Cr	99.9	Vickers	1.2 ± 0.04
ufg Cr, r ~14 mm	99.9	Vickers	4.4 ± 0.10
ufg Cr, r ~12 mm	99.9	Vickers	4.2 ± 0.10

Hardness values are presented in Table 1 and as colour code in Figure 1. Due to the radial strain gradient in the HPT device and in accordance with the microstructural variations, a slight hardness change was observed. Hardness values of 4.40 ± 0.10 GPa at *r* ~14 mm and 4.20 ± 0.10 GPa at *r*~12 mm were measured. A hardness deviation along the disk thickness (axial direction) of ± 0.10 GPa was observed at *r*~14 mm and ± 0.03 GPa at the centre of the disk. The change along the disk radius (radial direction) between the disk centre and ~14 mm is ± 1.00 GPa.

Stress-strain response

Exemplary engineering stress-strain curves of pillars and macroscopic compression samples are shown in Figure 2. The stress-strain responses with varying strain-rates for ~2 µm sxx and ufg pillars tested at RT are presented in Figure 2a. The flow stresses of sxx pillars are around 500 MPa, while for ufg samples an increase to ~2080 MPa at 8% plastic strain is evident. At the same time, the change in flow stress with varying strain-rate (high: ~$2 \cdot 10^{-2}$ s^{-1}, medium: ~$8 \cdot 10^{-3}$ s^{-1}, low: ~$3 \cdot 10^{-3}$ s^{-1}) is significantly less pronounced in the ufg states compared to sxx pillars. Related nanoindentation hardness data obtained with a Berkovich indenter are included as horizontal lines. Comparison of stress-strain data between RT and 230°C (Figure 2b) reveals decreased flow stresses for sxx and ufg pillars, and a diminishing work hardening for the pillars at elevated temperature. Figure 2c shows the stress-strain response of macroscopic ufg samples tested at a constant strain-rate of $3 \cdot 10^{-3}$ s^{-1} at different temperatures. The flow stress decreases with increasing temperature, and the strain hardening behaviour is less pronounced at elevated temperatures, in accordance with the micro-pillar data.

Figure 3a represents exemplary constant strain rate nanoindentation load-displacement curves compared to SRJ tests for sxx (red) and ufg Cr (blue), respectively, showing good match between the two techniques for the same strain rate. Figure 3b depicts nanoindentation hardness and Young's Modulus values plotted vs. indentation depth. The mean Young's Moduli extracted for sxx and ufg Cr (303 GPa) are close to the literature value of 294 GPa [52]. Finally, Figure 3c represents exemplary hardness divided by a constraint factor (C^*) of 2.8 vs. indentation depth plots for Cube Corner and Berkovich indentations in sxx and ufg Cr at RT, 200°C and 300°C. The strength in the ufg samples is generally higher due to grain refinement, and a decreased hardness is observed with increasing T_{test}. Differences between Cube Corner (20% representative strain) and Berkovich data (8% representative strain) at RT stem from the varying representative strain imposed to the material, which is conform to the uniaxial data. Moreover, the sxx indents exhibit a noticeable indentation size effect (ISE), which was accounted by analysing indentation data according to the model of Nix and Gao [53] to extract the bulk hardness H.

Post compression SEM images of macroscopic samples (Figure 4a) and micro-pillars (Figure 4b,c) reveal the appearance of the deformed samples corresponding to

the stress-strain curves in Figure 2. Figure 4a shows macroscopic samples deformed at RT and a strain-rate of $2 \cdot 10^{-2}$ s^{-1}, RT and $3 \cdot 10^{-3}$ s^{-1}, and 400°C at a strain-rate of $2 \cdot 10^{-3}$ s^{-1}, respectively. Figure 4b represents ~3 µm and ~4 µm ufg pillar deformed at low strain-rates at RT and 230°C, respectively. A bulk-like deformation behaviour is observed at all tested temperatures and strain-rates. Due to small sample dimensions and a comparatively large grain size, near-surface grains appear to be pushed out of the surface. This behaviour is observed for all different temperatures, strain-rates and pillar sizes, respectively. Figure 4c shows sxx pillars deformed at RT (left) and 230°C (middle). The former shows deformation by crystallographic slip on ill-defined slip planes as expected for the (100) orientation, whereby the latter exhibit a more localized slip behaviour with sharper slip bands. The insets in Figure 4b and c provide details of the sample surfaces.

Figure 5 depicts residual indents of Berkovich and Cube Corner imprints compared with images obtained from in-situ pillar-compression at comparable uniaxial strain. Figure 5a presents indents in ufg Cr at RT and 300°C, while Figure 5b gives a comparison of indents in sxx Cr at the corresponding temperatures. Figures 5c and d show in-situ SEM images of ufg Cr pillars during compression at ~8% plastic strain and post compression at ~20% plastic strain tested at RT and 230°C, respectively. Slight pile-up and emergence of grains from the surface is evident for the Cube Corner indents and coincides with the surface of the 20% deformed pillars.

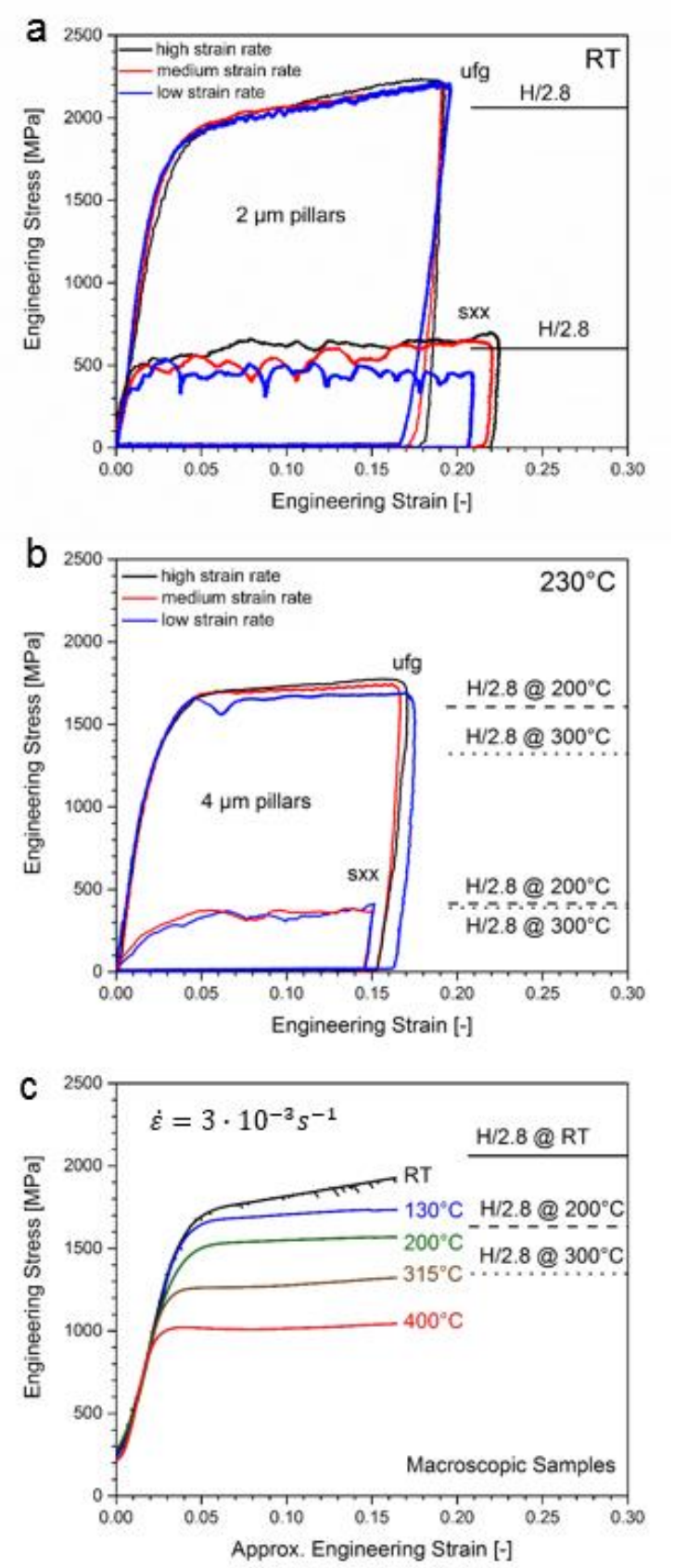

Figure 2: Comparison of stress-strain curves at different strain-rates and temperatures for sxx and ufg Cr samples. a) 2 µm Cr pillars tested at RT, b) 4 µm Cr pillars deformed at 230°C. c) Macroscopic ufg samples at varying temperatures for a strain-rate of $3 \cdot 10^{-3}$ s^{-1}.

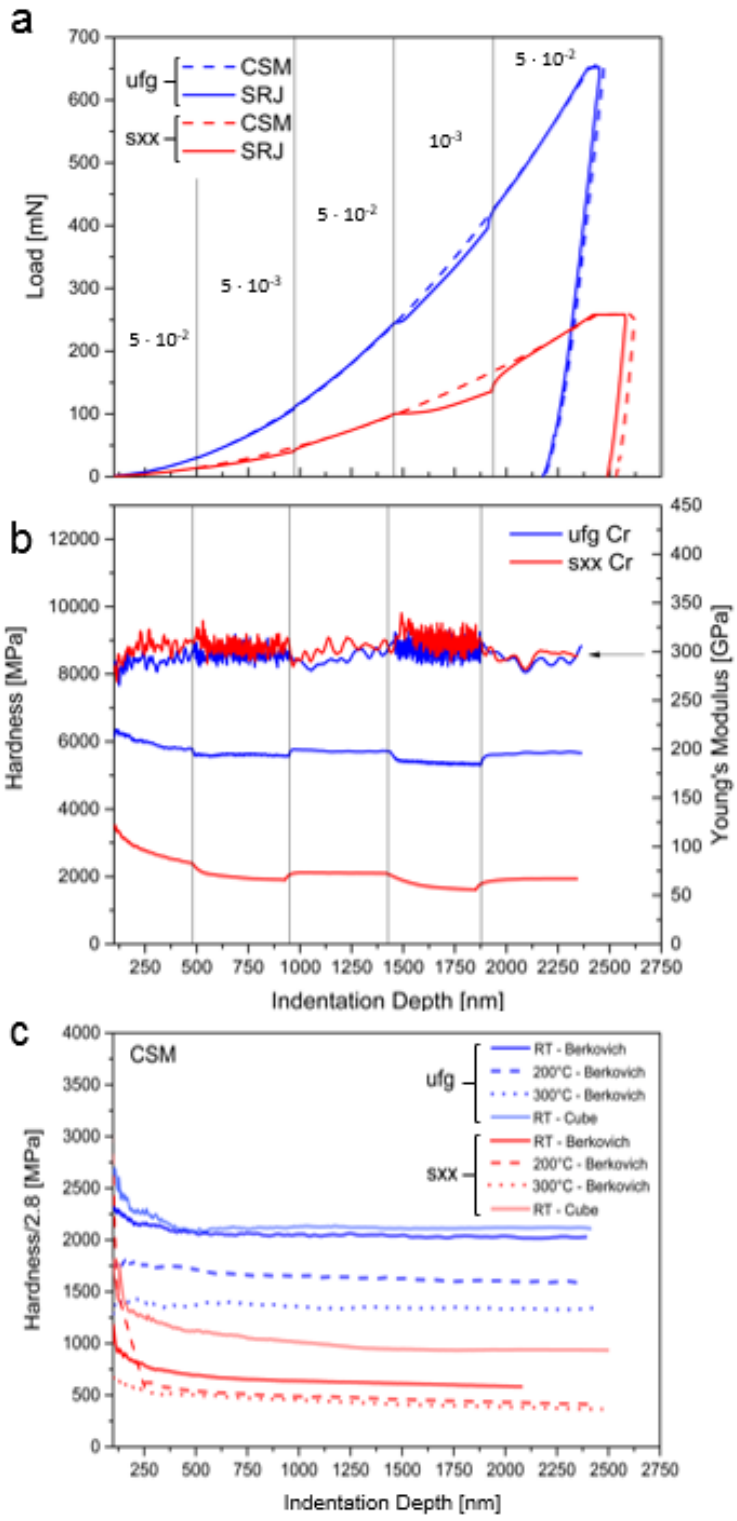

Figure 3: Nanoindentation data of sxx and ufg Cr at variable strain rates and temperatures. a) Comparison between constant strain rate (CSM) and strain rate jump (SRJ) experiments. b) Hardness and Young' Modulus vs. indentation depth. Validity of the measurement is indicated by the constant Young's Modulus of ~303 GPa over indentation depth. c) Hardness divided by a constraint factor of 2.8 vs. indentation depth for sxx and ufg samples tested with Berkovich and Cube Corner indenter tips at varying temperatures.

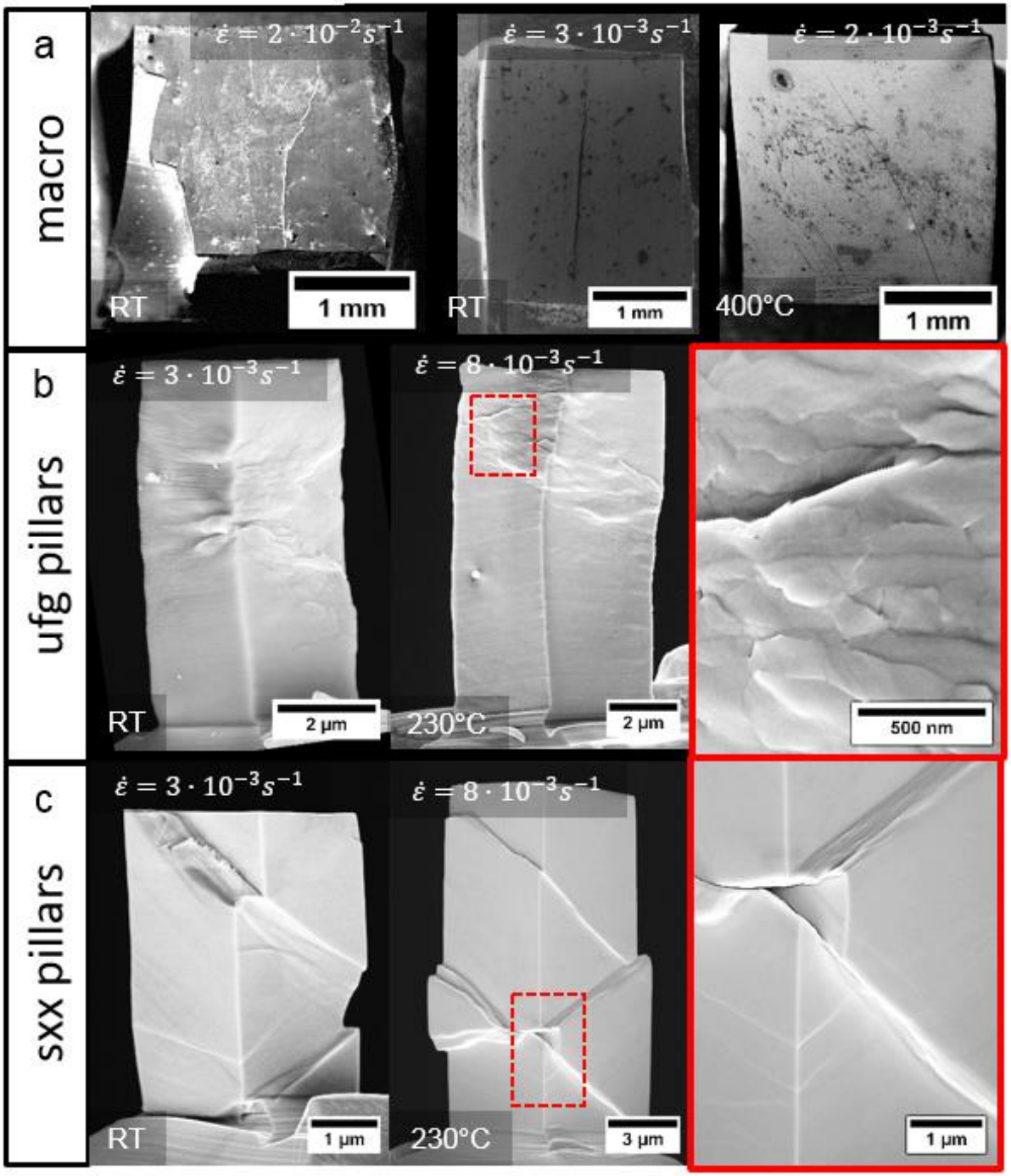

Figure 4: Post-deformation SEM images of macroscopic samples and micro-pillars. a) Macroscopic samples loaded at varying strain-rate and temperature. b) Ufg pillars with diameters of ~3 µm and ~4 µm tested at RT and 230°C, respectively. c) Deformed ~4 µm and ~6 µm sxx pillars at RT and 230°C. The insets indicate details of the deformed sample surfaces.

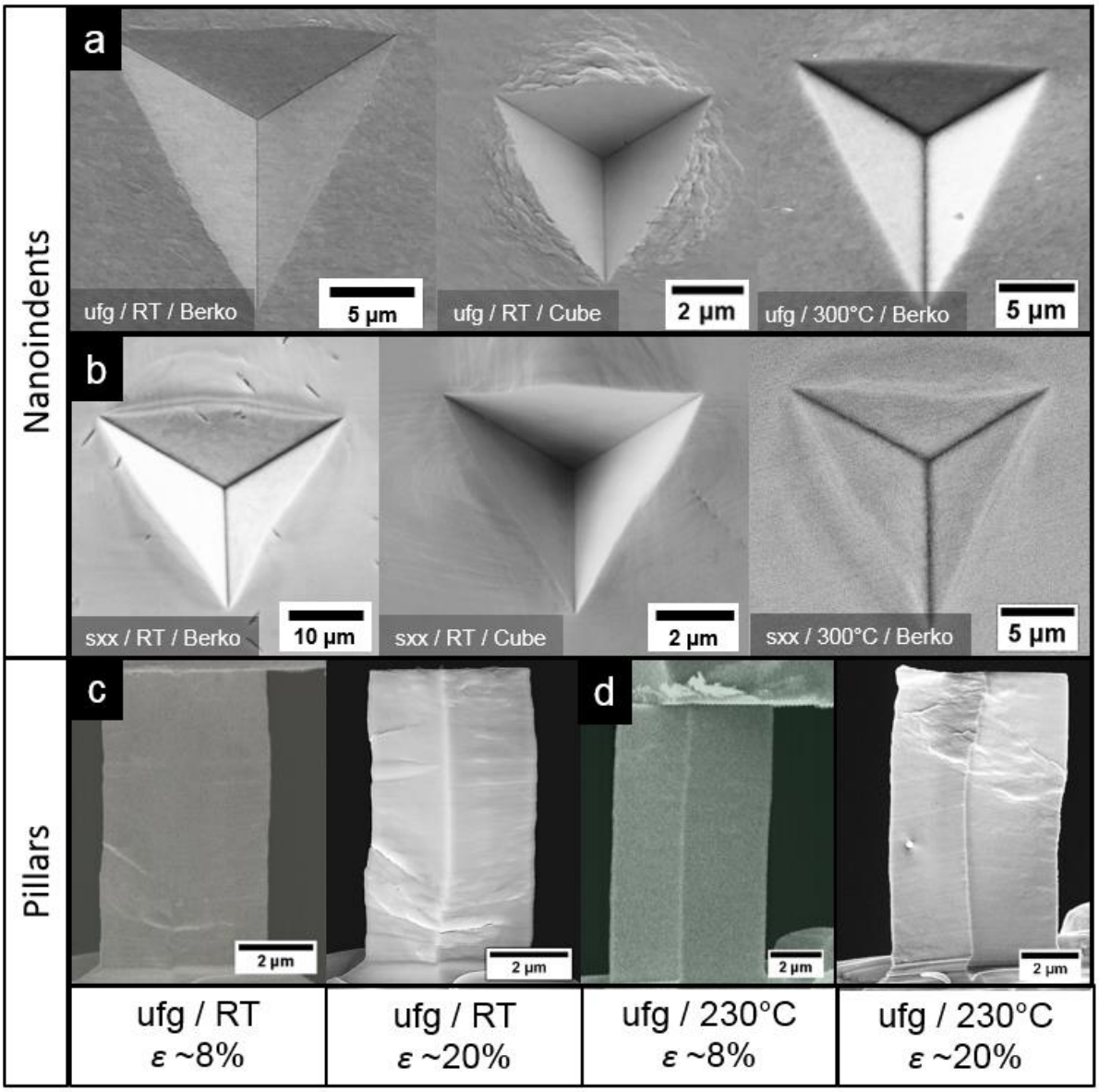

Figure 5: Residual impressions in a) ufg and b) sxx Cr performed with Berkovich or Cube Corner tips at varying temperature. For comparison, snapshots during in-situ SEM pillar-compression tests of ufg Cr at ~8% and ~20% plastic strain are shown in c) at RT and d) at 230°C. For details, see text.

B4 - Discussion

As long as sample size effects in micro-pillars [10,54,55] or an ISE during nanoindentation [53] are properly accounted for, a comparison of different testing techniques should generally lead to comparable results, as shown for different non-textured ufg fcc materials [14,15,51,56]. For the ufg micro-compression experiments, this is taken into account by the smaller internal grain size length-scale dominating over the sample size effect [10,54,55]. The dominant dislocation character in sxx and

ufg samples was considered to be of screw type, as suggested by Cheng *et al.* [57] for length scales larger ~300 nm. Regarding the nanoindentation data, this is considered by extrapolating to bulk hardness values from ISE affected nanoindentation data [53] as seen in Figure 3c. Moreover, pile-ups in the present case insignificantly influence hardness values, as indicated by the constant profiles of Young's Modulus as shown in Figure 3b. The choice of a reasonable constraint factor (C^*) is important to link nanoindentation hardness to a corresponding uniaxial stress. Several values for C^* are discussed in literature ranging from 2.5 to 3.0 for metals [14,51,58-64] to account for the multiaxial highly hydrostatic stress state during indentation. In the present work, 2.8 was chosen as proposed by Tabor [51].

Stress-strain characteristics

First, the stress-strain data (Figure 2 and 3) for different testing techniques will be discussed addressing RT behaviour (I), characteristics above T_c (II), followed by the temperature-dependent strain hardening behaviour (III), and the corresponding flow characteristics (IV).

(I) Stress values at 8% plastic strain in the ufg Cr pillars (~2080 MPa) and nanoindentation data (~2050 MPa) at RT are in good accordance, implying that global flow stresses are not affected by the used testing technique, the corresponding loading direction, or stress state. However, macroscopic samples (~1850 MPa) show slightly decreased stress values (Figure 2a and c). These differences can be explained by a slightly different grain size (Figure 1b) due to the imposed radius-dependent strain in the HPT device. The micron-sized pillars were FIB-milled at r ~14 mm, while macroscopic samples were machined from r ~12 mm to r ~14 mm. The larger grain size at the inner radius leads to an estimated flow stress decrease of ~250 MPa based on a simple Hall-Petch estimation [65,66], which is in accordance with the observed stress difference. Moreover, the elastic stiffness of the macroscopic compression tests is lower than in the pillar-compression tests since bottom and top faces of the samples deviate by <1° from perfect parallelism. The stress offset observable in Figure 2c is caused by slight pre-loading. However, due to the low to negligible work hardening, this is of minor concern for the data analysis at 8% flow stress.

(II) To check whether the flow stress decrease at elevated temperature results from an annealing effect during heating of the compression device or is induced by

plastic deformation, a thermal annealing approach was conducted where bulk samples were annealed for 30 minutes at various temperatures. Grain heights (black) as well as grain lengths (red) are shown in Figure 6a, indicating a slight increase of grain size and a decrease of grain aspect ratio (blue) upon annealing. The initial average grain size of ~160 nm at *r* ~14 mm increased to ~238 nm at 200°C, ~294 nm at 300°C and ~315 nm at 400°C. The corresponding decrease in flow stress was calculated based on a Hall-Petch estimation [65,66] and results in ~200 MPa, ~300 MPa and ~350 MPa, respectively. Due to the generally larger mean grain size in the macroscopic ufg samples, the flow stress at 8% plastic strain decreased by 300 MPa to 1550 MPa at 200°C (Figure 2c). Consequently, reduced flow stress values at elevated temperatures mainly result from grain growth effects during heating the material in the compression device.

(III) The different strain hardening behaviour of the uniaxially deformed samples tested at RT (Figure 2a) and elevated temperature (Figure 2b and c) could be explained by increased thermal activation at elevated temperature. In this case, screw dislocations cross-slip and therefore lead to a reduced pile-up of dislocations during deformation, thereby reducing work hardening at elevated temperature. At RT dislocations do pile-up and strain hardening takes place.

(IV) Stochastic events are observed for sxx pillars at every temperature tested. During compression, the number of load drops depends on both the machine dynamics (strain-rate) and whether displacement or load controlled mode is used [67] and is an indication of discrete dislocation activity. For large ufg pillars, no intermittent flow is observable regardless of the used strain-rate. Here, burst events in individual grains are averaged out due to the high number of grains in the deformed sample volume. Serrations in the stress-strain curve of the deformed macroscopic sample at RT (Figure 2c) indicate failure events, which are also evident on the surface of the deformed sample (Figure 4a). At elevated temperature, such cracking did not occur for any used strain-rate, which is attributed to the higher dislocation mobility that helps reducing dislocation pile-ups causing local stress concentrations. The fact that cracking is not observed in pillars is attributed to the significant smaller number of large defects in the miniaturized sample volume [68].

Overall, the SRJ tests as well as constant strain-rate deformation under uniaxial as well as multiaxial conditions revealed good comparability across all tested length-scales and temperatures.

Surface to volume considerations

Globally, the flow stress is strongly dependent on microstructure, temperature and strain-rate, as shown in Figures 2 and 3. On a local scale, surface contributions, enhanced at small scales by an increase in surface-to-volume fraction, might cause differences in deformation behaviour and should also depend on the ratio of sample dimension to grain size [22-25]. In Figure 4 and Figure 5, the local surface appearances are compared for different testing techniques. The detail in Figure 4b shows surface regions of ufg pillars at 230°C, where grains were pushed out of the sample surface due to high local deformation. Comparing the surface evolution with RT data, the temperature has no pronounced influence on the appearance of the surface. Considering the sxx case in Figure 4c, thermal activation causes a more localized deformation at elevated temperature [38], which is attributed to a more fcc-like slip behaviour.

Changing the applied stress state from uniaxial loading to multiaxial loading in nanoindentation, comparable observations were made on the residual impressions in ufg and sxx samples, as shown in Figure 5. In both cases of Cube Corner indentation, a pile-up formation with distinct differences in their appearance is observed. While slip lines are observed on the sxx sample surface in Figure 5b, grains partly emerge from the plastically deformed surface region in the ufg case. The residual surface topology increases with the amount of imposed strain (Berkovich 8%, Cube Corner 20%). No pronounced temperature effects were observed, as confirmed by an exemplary Berkovich impression performed at 300°C (Fig. 5a). Comparison with uniaxial in-situ pillar-compression experiments at RT and 230°C, at the same amount of plastic strain (Figure 5c and d), indicates almost no emergence of grains at ~8% global plastic strain. However, after ~20% strain (Figure 5c and d) several grains in the deforming areas were pushed out of the sample surface. This implies that the amount of applied strain is the dominant factor controlling surface topology evolution, while the stress state seems to be of minor influence. Investigations of the pillar volume, as shown in Figure 6b, reveal differences at individual temperatures. In Figure 6b, images I and II

show the microstructure at RT and after annealing at 230°C, respectively. Grain growth occurred during thermal setup and sample alignment before mechanical loading. The grain aspect ratio was reduced according to Figure 6a. After compression, FIB cross sections of deformed pillars (Figure 6b,III and IV) reveal the compression induced reduction of grain height in highly deformed zones, indicated by red arrows. In undeformed zones at the pillar base, the grain aspect ratio remained constant as shown for the undeformed state in Figure 6b,I and II. It is interesting to note that GB sliding [11,12] seems not to be dominant, as more sliding would be expected for higher deformation temperatures. This observation will be addressed in more detail in the next chapter.

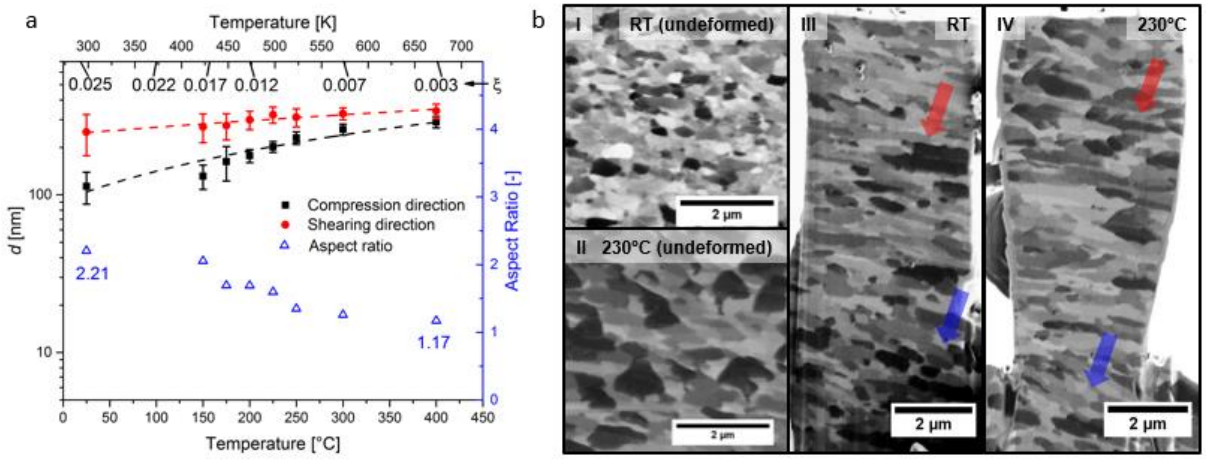

Figure 6: a) Results of annealing experiments of the as-deformed material, corresponding decrease of grain aspect ratio and selected grain shape coefficients ξ. b) The microstructure of ufg pillars in the undeformed state at RT and 230°C (I,II) and the resulting microstructures after pillar compression (III, IV).

Thermally activated deformation processes – from global to local flow behaviour

To examine the underlying deformation mechanisms in more detail, strain-rate sensitivities, *m*, were calculated [69] for all testing techniques using

$$m = \frac{\partial \ln \sigma}{\partial \ln \dot{\varepsilon}} \tag{1}$$

at a representative strain of 8%. Results are presented in Figure 7a, where *m* of sxx and ufg Cr are plotted against T_{test}. The obtained results are in good agreement with results on sxx [6] and cg Cr [1]. At RT, *m* for sxx (red) and ufg (blue) samples are

around 0.07 and 0.02, respectively. The reduced *m* for ufg samples compared to the sxx state is attributed to the higher athermal stress component, caused by dislocations interacting with GBs in the ufg states [6,7].

For sxx Cr, increasing T_{test} leads to a continuous decrease of *m* in Figure 7a. Above T_c (grey-shaded area), *m*-values in the order of 10^{-3} are determined, indicating strain-rate insensitive fcc-like plasticity, where deformation is not governed by thermal activation of screw dislocations anymore. This behaviour is in good accordance with other studies [28,38,44], showing that overcoming T_c the thermally activated component diminishes.

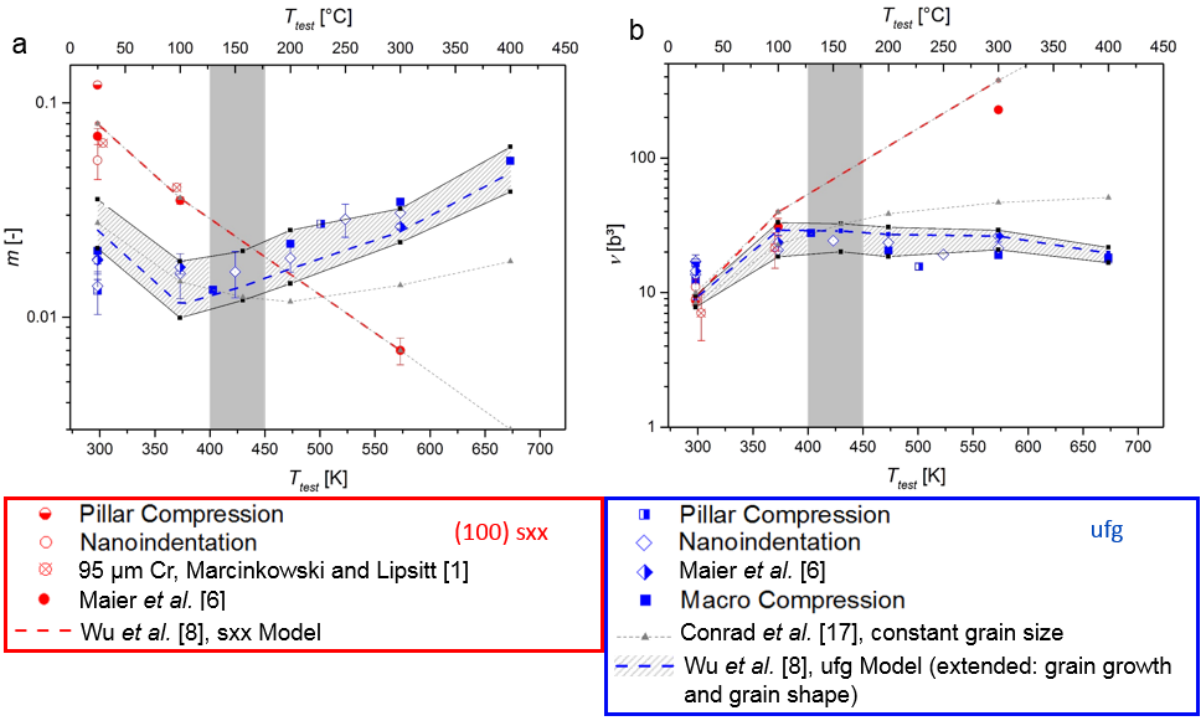

Figure 7: Evolution of the (a) strain-rate sensitivity *m* and (b) activation volume *v* of sxx (red) as well as ufg (blue) samples with temperature, supported by model predictions of Conrad [18] (constant v_{ath}) and a modified model of Wu *et al.* [8] ($v_{ath} = f(T)$, additionally accounting for variable grain shape coefficients). The grey-shaded area indicates the critical temperature T_c of Cr. Some data [6] are taken with permission of Elsevier.

In ufg samples, the general trend is significantly different from the sxx state. For temperatures below T_c, *m* slightly decreases due to increasing thermal activation, while interaction with GBs remains mostly unaffected. Overcoming T_c, *m* increases continuously with temperature. According to [6], this is mainly attributed to dislocation interactions with grain boundaries, as described also for ufg fcc metals [18,70]. An

additional contribution to the strain-rate sensitivity could stem from the reduction of the athermal stress contribution due to slight grain coarsening (see Figure 6). Thus, the overall *m* is a mixture of both, thermally activated dislocation-GB interactions and thermally activated grain coarsening. Notably, while the first contribution leads to an increasing *m*, the second one acts against it.

For further insights and to consider the influence of applied stress states especially in the sxx state, the corresponding activation volumes, ν [71], at T_{test} were calculated using

$$\nu = \frac{C \cdot k_B \cdot T_{test}}{m \cdot \sigma}, \quad (2)$$

where k_B is the Boltzmann constant, and *C* a factor dependent on the microstructure. For ufg Cr, *C* was set to $\sqrt{3}$, based on the van Mises relation linking shear stress to normal stress in polycrystalline aggregates. For sxx samples, the factor $\sqrt{3}$ is valid for nanoindentation, since a multiaxial stress state is present. For uniaxial compression testing on sxx pillars, *C* was set to the inverse Schmid factor (1/0.45), which corresponds to deformation on the expected {110} <111> slip systems [28,35]. To compare values of ν, normalisation with the cubed Burger's vector b ($2.5 \cdot 10^{-10}$ m for Cr [72]) is common practice. Results are presented in Figure 7b, where ν for sxx (red) and ufg samples (blue) are plotted against T_{test}, respectively. For sxx samples at RT, ν is ~9 b^3, and a slightly increased value of ~14 b^3 is observed for ufg samples. This is attributed to dislocation segments involved in formation of a double kink to overcome the next Peierls potential [8,43]. Comparable ν for uniaxial bulk data have been already reported by Glebovsky and Brunner [4], Wu et al. [8], Wei *et al*. [33], Kim *et al.* [41] and Schneider *et al.* [43] for sxx W, nc Cr, ufg Fe and sxx Mo, respectively. Increasing thermal activation at higher temperatures leads to an increase of ν to ~30 b^3 for both microstructures until T_c is reached. Overcoming T_c, ν still increases to values around 300 b^3 for sxx samples, indicative of a dislocation forest interaction process. In ufg samples, a rather constant ν of ~30 b^3 is observed for testing temperatures close to or exceeding T_c, independent of stress state and length scale. It is argued that dislocation-GB interactions dominate the deformation. The overall constant ν from 100°C to 400°C obtained by several testing techniques over various length scales further demonstrates that the deformation mechanism does not change, even though grain coarsening

occurred [73-75]. In other words, despite the vastly different surface-to-volume ratios probed by the different experiments, different length scales and stress states, the observed deformation mechanisms are governed mainly by dislocation-based plasticity. The rather constant values of *m* and ν with increasing strain, as shown in Figure 8a and b, further underline that the governing deformation mechanism does not change upon deformation, although with increasing amount of strain the dislocation density within the samples might vary, as evidenced from the differences in temperature dependent strain hardening behaviour as discussed in section 4.1. In literature, the initial dislocation densities of sxx and ufg bcc metals were reported to be ~10^{10} m^{-2} and ~10^{14} to ~10^{15} m^{-2} [76], respectively. Comparable values of $9.6 \cdot 10^{14}$ m^{-2} and $3.5 \cdot 10^{14}$ m^{-2} were reported for HPT deformed Nb and Ta, respectively [77]. Those differences might affect the flow stress values resulting in individual strength scaling behaviour in ufg compared to sxx samples, as reported in [78]. In the single crystal situation, the deformation behaviour is altered by substructure formation, as shown in pre-strained Ni samples [55] or during microstructural refinement by straining of copper crystals [79]. However, cell structures in the size range of 300 nm to 500 nm were reported. Indeed, in 160 nm sized grains, substructure formation is limited and GB's act as sinks and sources for dislocations [8]. Only few mobile dislocations are expected within the grain interior. Therefore, the accumulation of dislocations in the grain interior has only a minor influence on the governing deformation mechanisms, especially at higher strain values, as shown in Figure 8.

The standard deviations of *m* and ν are small for ufg samples but larger for sxx samples. As stochastic dislocation behaviour is more pronounced in the sxx case, load drops mainly contribute to this scatter. For the present as well as previous results at RT [78], no indication of diffusional deformation processes was found, since in that case one would expect *m*-values of 0.006 to 0.009 and ν-values of ~$1b^3$ as reported for 30 nm sized bcc Fe [80] and 50 nm sized bcc Ta [81], respectively.

Several attempts have been made to interpret the varying deformation mechanisms in fcc and bcc metals with respect to a varying grain size. The basic fcc model was established by Conrad [18] and considers a change in activation volume with grain size

$$\frac{1}{\nu} = \frac{1}{\nu^*} + \frac{M^2 \cdot G \cdot b}{\alpha \cdot 2 \cdot \pi \cdot K_{H-P} \cdot d^{1/2}} \cdot \frac{1}{\nu_{ath}}, \tag{3}$$

where M = 2.9 is the Taylor factor for Cr [8], G = 116 GPa is the shear modulus, α = 0.36, $K_{H\text{-}P}$ is the Hall-Petch coefficient of 1380 MPam$^{1/2}$ for Cr [82], ν^* is the activation volume related to thermal activation (see equation (2)) and ν_{ath} was set as a constant activation volume related to athermal dislocation emission at a GB at constant temperature. ν^* varies with temperature, as the lattice friction stress (~50 MPa for Cr at RT [82,83]) diminishes with increasing thermal activation. The Conrad model was extended by Wu *et al.* [8] to estimate apparent m- and ν-values for polycrystalline aggregates, using

$$\nu_{ath} = \xi \cdot d \cdot b^2, \tag{4}$$

where ξ is a grain shape coefficient which is constant for a certain temperature. Except equation (4), no further modifications of the fcc model were applied, as Conrad [18] already implemented a thermal stress component within the model to derive thermal activation volumes (ν^*). Results obtained by Wu *et al.* [8] show that *m*-values of Cr and Fe at RT can be correctly predicted over a wide range of varying grain sizes, as both, the friction stress (thermal) and dislocation interaction with GB's (athermal) contribute to the overall deformation. Moreover, the same requirements as mentioned for fcc metals hold true in bcc metals: the presence of intragranular dislocations restricted to their glide planes, dislocation pile-ups, and the absence of pronounced dislocation cells.

Values for ξ in dependence of the grain shape are included in Figure 6a. In the present case, ξ is temperature-dependent, as the aspect ratio of initially elongated grains decreased with increasing T_{test}, which was observed during the annealing approach (see section 4.1 and Figure 6a). Figure 7 presents Conrad's model [18] (grey dashed lines) for the sxx as well as the ufg case and the extended model of Wu *et al.* [8] (red dashed lines for sxx and blue dashed lines for the ufg case). Grey lines and the grey dashed area represent the minima and maxima of *m*- and ν-values due to varying grain shapes. While both models fit for the sxx case, Conrad's model neglects grain coarsening and the change of the grain aspect ratio during thermal setup. It therefore underestimates *m* at increasing temperatures for the ufg material. Modifying the model of Wu by taking into account not only the changing grain size, but also changing grain shape coefficients ranging from 0.025 (RT) to 0.003 (400°C) (see

Figure 6), the model fits the increasing *m*-values and low activation volumes at elevated temperatures well.

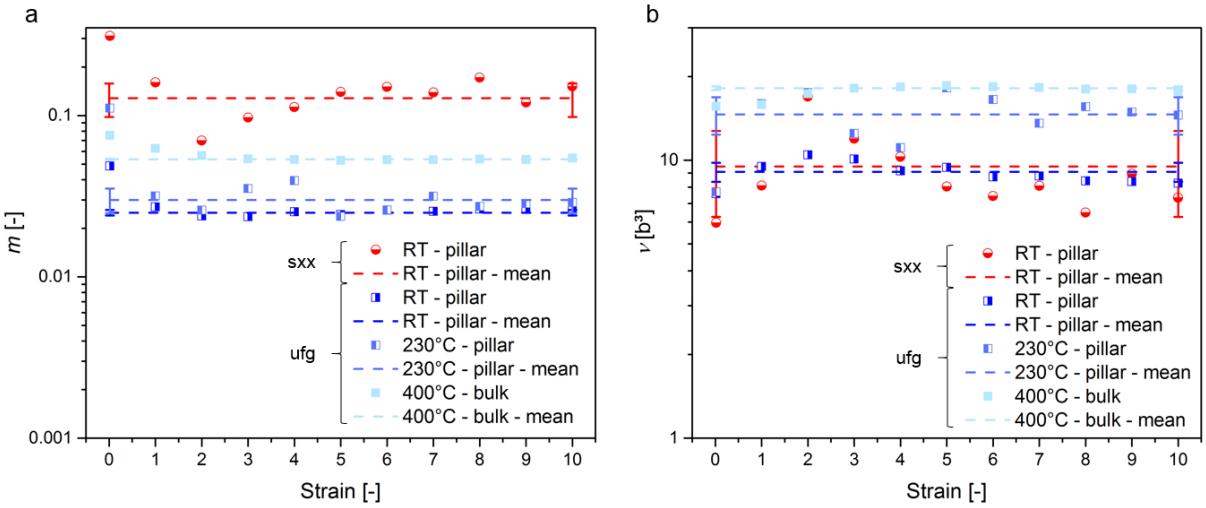

Figure 8: Invariance of (a) strain-rate sensitivity *m* and (b) activation volume ν with respect to strain for individual uniaxial tests at variable temperatures for sxx and ufg Cr. The larger scatter in sxx values originates from stochastic dislocation behaviour. For colour interpretation, the reader is referred to the online version.

Strain-rate sensitivity vs. interface fraction

In Figure 9, the impact of different surface-to-volume ratios and number of involved interfaces on the determined strain-rate sensitivity is shown. Here, the number of grains across the plastic volume (magenta dashed line) and the fraction of grains which are affected by the sample surface (green dashed line) were estimated for different sample geometries during uniaxial and multiaxial testing. Therefore, grains were estimated to be of cylindrical shape with an aspect ratio of 3:1, typical for HPT deformation [36,78]. For rectangular-shaped samples an equivalent cylindrical sample diameter *L* was calculated. The number of grains contained in the plastic volume were estimated by calculating the sample volume and division by the before mentioned cylindrical-shaped grain volume. The fraction of grains which are affected by the sample surface were estimated using the specimen's surface subtracted by the top and bottom faces which are in direct contact with the flat punch indenter and the bulk material. This lateral area was divided by the average cross-sectional area of a single grain. Considering the different indentations, a simplified hemispheric plastic zone [84]

after penetration to 2500 nm was taken into account for estimating the number of deformed grains per volume.

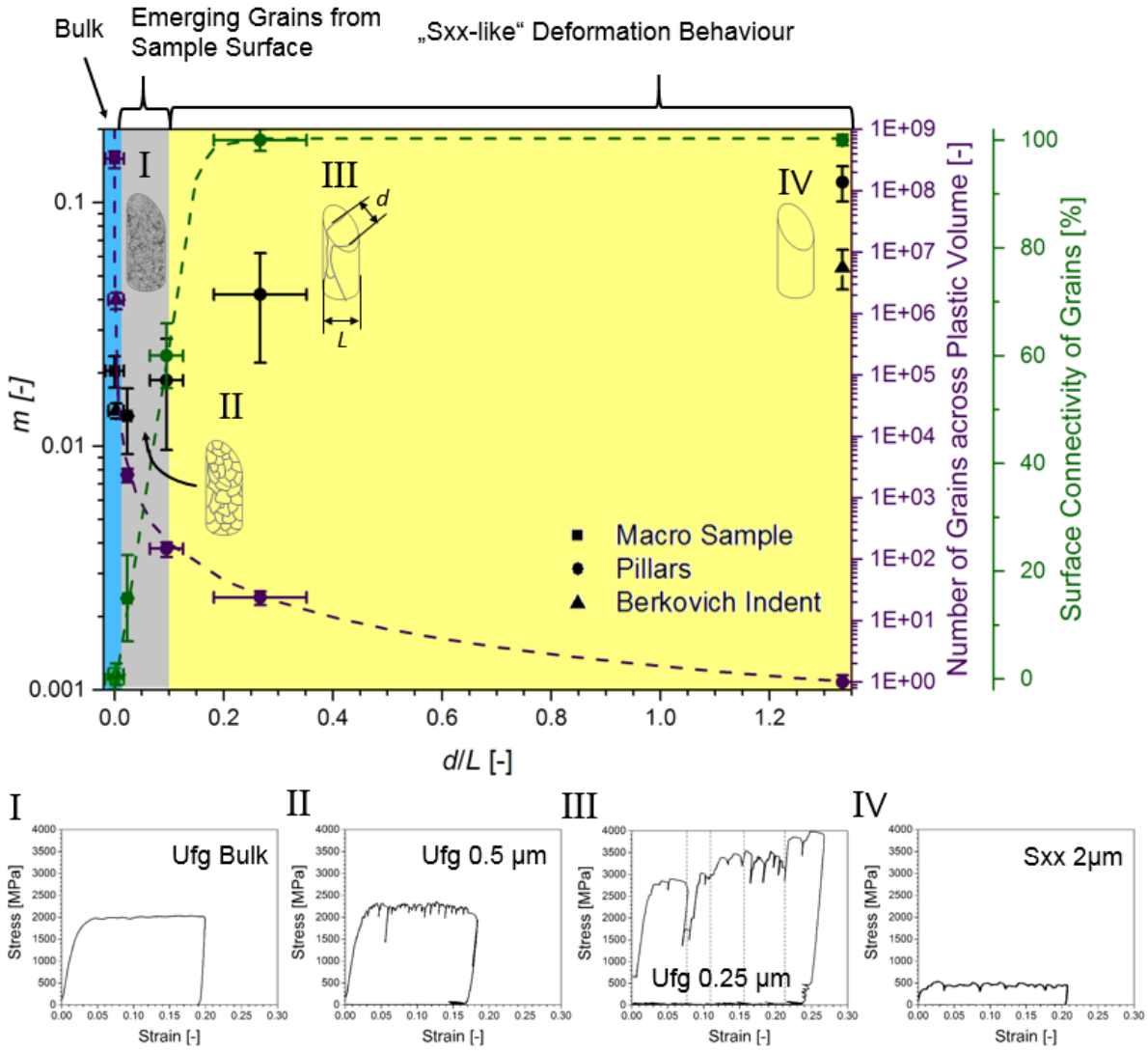

Figure 9: Strain-rate sensitivity (black), number of grains in the plastic volume (magenta) and corresponding connectivity of surface grains (green), dependent on sample size-normalized characteristic dimension *d*/*L*. The grey-shaded area shows a transition zone where grains tend to emerge from the sample surface. I) – IV) Corresponding stress-strain curves of pillars indicated. See text for more details. For colour interpretation, the reader is referred to the online version.

The volume of the residual imprint was therefore subtracted from the hemispheric plastic zone. The remaining volume was further divided by the volume of a single grain, as mentioned before. To consider the surface connectivity of grains, the base area of the hemispheric plastic zone was subtracted by the triangle-shaped surface area of the residual imprints and divided by the average cross-sectional area of a single grain.

Based on this, a comparison of *m*-values (black), number of interfaces across the plastic volume (magenta), and fraction of surface-connected grains (green) is presented in Figure 9 as a function of the ratio between grain size vs. sample size d/L. The error bars indicate the resultant error which was derived by taking the standard deviation upon grain size estimation into account (d = 160 ± 51 nm). Also shown are representative stress-strain curves of different micro-pillars.

The light blue area in Figure 9 indicates the macroscopic regime, where the sample size is much larger than the grain size. Only a diminishing fraction of grains is located directly at the sample surface, and no influence of near-surface grains is observed during deformation. Overcoming a *d/L* ratio of ~0.02, the amount of surface-affected grains increases drastically. In this regime, indicated by the grey shaded area, grains noticeably emerge from the sample surface and might affect the deformation behaviour. Overcoming *d/L* values of ~0.1, ~50% of the grains touch the surface, and the grain size approaches the size of the plastic zone. For these states an sxx-like deformation behaviour is expected (yellow area). Notably, due to pillar aspect ratios of 3:1 and the used representative grain diameter in this simplified model, a fully sxx sample volume is statistically reached for *d/L* ratios larger than 1.33. Below this, individual GBs might affect the plastic behaviour [85]. However, as long as crystallographic slip traces reveal no intersections with GBs or other internal obstacles [78], dislocations can glide through the crystal and exit on the pillar surface, corresponding to slip events in sxx pillars. Such characteristics are evident in representative stress-strain curves of small ufg pillars (Figure 9, II-IV), where serrations and load drops are commonly observed. For macroscopic experiments, a smooth flow behaviour (Figure 9, I) due to the large number of grains in the sample volume and *m*-values of ~0.02 are observed. Increasing the fraction of surface grains leads to a slight decrease of *m* to ~0.014 and serrated flow arises in the stress-strain curves (Figure 9, II and III). This is explained by slip events in individual grains. The scatter within evaluated *m*-values for such pillar sizes is quite large compared to bulk or sxx samples, because deformation is strongly affected by the local microstructure and crystal orientation. Figure 9, image III shows a 250 nm ufg pillar deformed in a uniaxial SRJ test [14,86]. Due to the stochastic deformation, the strain-rate jumps are hard to visualize and therefore marked with vertical dashed lines. Further increasing *d*/*L* ratios leads to a decreased scatter regarding *m*, as the probability for dislocations

interacting with individual GBs is decreased, until *m* of sxx bulk samples and corresponding stress-strain curves (Figure 9 IV) are obtained.

B5 - Summary & Conclusion

The effect of temperature, stress state and strain-rate on the mechanical behaviour of ultrafine-grained (ufg) Cr was examined, spanning from the sub-micron regime by uniaxial pillar-compression and multiaxial advanced nanoindentation testing to macroscopic uniaxial compression experiments. Results in terms of temperature-dependent flow behaviour, strain-rate sensitivity and corresponding activation volume agree well within the different experimental techniques, demonstrating that length scales and stress states have only minor influence on the overall deformation. The main conclusions can be summarized as followed:

(I) Flow characteristics for room temperature deformation of ufg Cr agree well within the different techniques. The decrease of the flow stress above T_c mainly results from temperature induced grain coarsening during heating of the compression device. The decrease of the thermal stress contribution is of minor importance.

(II) Deformation of single-crystalline samples is dominated by the Peierls potential up to the critical temperature T_c. Overcoming this temperature, the thermally activated component to the flow stress diminishes and a strain-rate insensitive behaviour with further increasing activation volumes is observed.

(III) Up to ~$0.87 \cdot T_c$, ufg samples deform by the thermally activated motion of screw dislocations, where the thermal stress contribution decreases with increasing temperature. This leads to a slight reduction of the strain-rate sensitivity.

(IV) Exceeding T_c, constant activation volumes and increasing *m*-values for ufg Cr are indicative for dislocation-grain boundary interactions as the dominant deformation mechanism. Grain coarsening due to annealing and a change in grain aspect ratio lead to a slight decrease of the activation volume, especially at elevated temperatures.

(V) The amount of implied strain during deformation shows significantly more influence on emerging surface grains than the stress state or the deformation temperature. The strain rate sensitivity and the activation volume remain constant with increasing strain indicating no changes in deformation mechanism. Grain boundary sliding has not been observed.

(VI) By extending existing models to incorporate the evolution of grain size and grain shape, the deformation mechanism characteristics m and ν in ufg Cr have been successfully modelled for varying temperatures.

(VII) A transition in m is observed from a polycrystalline behaviour to an sxx situation, which is controlled by the amount of interfaces in the tested volume. Free surfaces and stress states are of minor concern.

With these novel insights, we hope to contribute to a better understanding of the size-dependent interplay between grain boundaries and sample dimensions and their influence on the deformation of bcc metals over several length scales. For future investigations, it would be of interest to discriminate the individual contributions of dislocation- grain boundary interaction and grain growth to the total strain-rate sensitivity.

B - References

[1] M.J. Marcinkowski, H.A. Lipsitt, The plastic deformation of Chromium at low temperatures, Acta Metall. 10 (1962) 95–111.

[2] J. Weertman, Creep of polycrystalline Aluminium as determined from strain rate tests, J. Mech. Phys. Solids. 4 (1956) 230–234.

[3] A.S. Argon, S.R. Maloof, Plastic deformation of tungsten single crystals at low temperatures, Acta Metall. 14 (1966) 1449–1462.

[4] D. Brunner, V. Glebovsky, Analysis of flow-stress measurements of high purity tungsten single crystals, Mater. Lett. 44 (2000) 144–152.

[5] H.W. Höppel, J. May, P. Eisenlohr, M. Göken, Strain rate sensitivity of ultrafine-grained materials, Z. Met. 96 (2005) 566–571.

[6] V. Maier, A. Hohenwarter, R. Pippan, D. Kiener, Thermally activated deformation processes in body-centered cubic Cr - How microstructure influences strain-rate sensitivity, Scr. Mater. 106 (2015) 42–45.

[7] V. Maier, C. Schunk, M. Göken, K. Durst, Microstructure-dependent deformation behaviour of bcc-metals - indentation size effect and strain rate sensitivity, Philos. Mag. 95 (2015) 1766–1779.

[8] D. Wu, X.L. Wang, T.G. Nieh, Variation of strain rate sensitivity with grain size in Cr and other body-centred cubic metals, J. Phys. D. Appl. Phys. 47 (2014) 175303.

[9] M.A. Meyers, A. Mishra, D.J. Benson, Mechanical properties of nanocrystalline materials, Prog. Mater. Sci. 51 (2006) 427–556.

[10] M.D. Uchic, D.M. Dimiduk, J.N. Florando, W.D. Nix, Sample Dimensions Influence Strength and Crystal Plasticity, Science 305 (2004) 986–989.

[11] N.Q. Chinh, T. Csanadi, J. Gubicza, R.Z. Valiev, B.B. Straumal, T.G. Langdon, The effect of grain boundary sliding and strain rate sensitivity on the ductility of ultrafine-grained materials, MSF. 667–669 (2010) 677–682.

[12] T.G. Langdon, Grain boundary sliding revisited: Developments in sliding over four decades, J. Mater. Sci. 41 (2006) 597–609.

[13] M.F. Ashby, The deformation of plastically non-homogeneous materials, Philos. Mag. 21 (1970) 399–424.

[14] V. Maier, K. Durst, J. Mueller, B. Backes, H.W. Höppel, M. Göken, Nanoindentation strain-rate jump tests for determining the local strain-rate sensitivity in nanocrystalline Ni and ultrafine-grained Al, J. Mater. Res. 26 (2011) 1421–1430.

[15] J. Wehrs, G. Mohanty, G. Guillonneau, A. Taylor, X. Maeder, D. Frey, L. Philippe, S. Mischler, J.M. Wheeler, J. Michler, Comparison of In Situ Micromechanical Strain-Rate Sensitivity Measurement Techniques, JOM. 67 (2015) 1684–1693.

[16] J. Alkorta, J.M. Martínez-Esnaola, J.G. Sevillano, Critical examination of strain-rate sensitivity measurement by nanoindentation methods: Application to severely deformed niobium, Acta Mater. 56 (2008) 884–893.

[17] J. May, H.W. Höppel, M. Göken, Strain rate sensitivity of ultrafine-grained aluminium processed by severe plastic deformation, Scr. Mater. 53 (2005) 189–194.

[18] H. Conrad, Plastic deformation kinetics in nanocrystalline FCC metals based on the pile-up of dislocations, Nanotechnology. 18 (2007) 1–8.

[19] J.Y. Zhang, G. Liu, J. Sun, Strain rate effects on the mechanical response in multi- and single-crystalline Cu micropillars: Grain boundary effects, Int. J. Plast. 50 (2013) 1–17.

[20] J.Y. Zhang, X. Liang, P. Zhang, K. Wu, G. Liu, J. Sun, Emergence of external size effects in the bulk-scale polycrystal to small-scale single-crystal transition: A maximum in the strength and strain-rate sensitivity of multicrystalline Cu micropillars, Acta Mater. 66 (2014) 302–316.

[21] J. May, H.W. Höppel, M. Göken, Strain Rate Sensitivity of Ultrafine Grained FCC- and BCC-Type Metals, Mater. Sci. Forum. 503–504 (2006) 781–786.

[22] C. Keller, E. Hug, X. Feaugas, Microstructural size effects on mechanical properties of high purity nickel, Int. J. Plast. 27 (2011) 635–654.

[23] X.X. Chen, A.H.W. Ngan, Specimen size and grain size effects on tensile strength of Ag microwires, Scr. Mater. 64 (2011) 717–720.

[24] B. Yang, C. Motz, M. Rester, G. Dehm, Yield stress influenced by the ratio of wire diameter to grain size - a competition between the effects of specimen microstructure and dimension in micro-sized polycrystalline copper wires, Philos. Mag. 92 (2012) 3243–3256.

[25] P. Ghosh, A.H. Chokshi, Size Effects on Strength in the Transition from Single- to-Polycrystalline Behavior, Metall. Mater. Trans. A. 46 (2015) 5671–5684.

[26] Y. Cui, G. Po, N. Ghoniem, Temperature insensitivity of the flow stress in body-centered cubic micropillar crystals, Acta Mater. 108 (2016) 128–137.

[27] R. Huang, Q.-J. Li, Z.-J. Wang, L. Huang, J. Li, E. Ma, Z.-W. Shan, Flow stress in submicron bcc iron single crystals: Sample-size-dependent strain-rate sensitivity and rate-dependent size strengthening, Mater. Res. Lett. (2015) 1–7.

[28] B. Sestak, A. Seeger, Gleitung und Verfestigung in kubisch-raumzentrierten Metallen und Legierungen, Zeitschrift Für Met. 69 (1978) 195–202.

[29] A. Seeger, The temperature and strain-rate dependence of the flow stress of bcc metals: A theory based on kink-kink interactions, Z. Met. 72 (1981) 369–380.

[30] Q. Wei, T. Jiao, K.T. Ramesh, E. Ma, Nano-structured vanadium: processing and mechanical properties under quasi-static and dynamic compression, Scr. Mater. 50 (2004) 359–364.

[31] Q. Wei, T. Jiao, K.T. Ramesh, E. Ma, L.J. Kecskes, L. Magness, R. Dowding, V. Kazykhanov, R.Z. Valiev, Mechanical behavior and dynamic failure of high-strength ultrafine grained tungsten under uniaxial compression, Acta Mater. 54 (2005) 77–87.

[32] Q. Wei, Z.L. Pan, X.L. Wu, B.E. Schuster, L.J. Kecskes, R.Z. Valiev, Microstructure and mechanical properties at different length scales and strain rates of nanocrystalline tantalum produced by high-pressure torsion, Acta Mater. 59 (2011) 2423–2436.

[33] Q. Wei, S. Cheng, K.T. Ramesh, E. Ma, Effect of nanocrystalline and ultrafine grain sizes on the strain rate sensitivity and activation volume: fcc versus bcc metals, Mater. Sci. Eng. A. 381 (2004) 71–79.

[34] Q. Wei, Strain rate effects in the ultrafine grain and nanocrystalline regimes - influence on some constitutive responses, J Mater Sci. 42 (2007) 1709–1727.

[35] Q. Zhou, J. Zhao, J.Y. Xie, F. Wang, P. Huang, T.J. Lu, K.W. Xu, Grain size dependent strain rate sensitivity in nanocrystalline body-centered cubic metal thin films, Mater. Sci. Eng. A. 608 (2014) 184–189.

[36] R. Pippan, S. Scheriau, A. Taylor, M. Hafok, A. Hohenwarter, A. Bachmaier, Saturation of Fragmentation During Severe Plastic Deformation, Annu. Rev. Mater. Res. 40 (2010) 319–343.

[37] R.Z. Valiev, R.K. Islamgaliev, I. V Alexandrov, Bulk nanostructured materials from severe and plastic deformation, Prog. Mater. Sci. 45 (2000) 103–189.

[38] O. Torrents Abad, J.M. Wheeler, J. Michler, A.S. Schneider, E. Arzt, Temperature-dependent size effects on the strength of Ta and W micropillars, Acta Mater. 103 (2016) 483–494.

[39] A.S. Schneider, D. Kaufmann, B.G. Clark, C.P. Frick, P.A. Gruber, R. Mönig, O. Kraft, E. Arzt, Correlation between Critical Temperature and Strength of Small-Scale bcc Pillars, Phys. Rev. Lett. 103 (2009) 105501/1-4.

[40] M.D. Uchic, P.A. Shade, D.M. Dimiduk, Plasticity of Micrometer-Scale Single Crystals in Compression, Annu. Rev. Mater. Res. 39 (2009) 361–386.

[41] J.-Y. Kim, D. Jang, J.R. Greer, Tensile and compressive behavior of tungsten, molybdenum, tantalum and niobium at the nanoscale, Acta Mater. 58 (2010) 2355–2363.

[42] A.S. Schneider, C.P. Frick, B.G. Clark, P.A. Gruber, E. Arzt, Influence of orientation on the size effect in bcc pillars with different critical temperatures, Mater. Sci. Eng. A. 528 (2011) 1540–1547.

[43] A.S. Schneider, B.G. Clark, E. Arzt, C.P. Frick, P.A. Gruber, Effect of orientation and loading rate on compression behavior of small-scale Mo pillars, Mater. Sci. Eng. A. 508 (2009) 241–246.

[44] A.S. Schneider, C.P. Frick, E. Arzt, W.J. Clegg, S. Korte, Influence of test temperature on the size effect in molybdenum small-scale compression pillars, Philos. Mag. Lett. 93 (2013) 331–338.

[45] S. Wurster, R. Treml, R. Fritz, M.W. Kapp, E.-M. Langs, M. Alfreider, C. Ruhs, P.J. Imrich, G. Felber, D. Kiener, Novel methods for the site specific preparation of micromechanical structures, Prakt. Met. Sonderband. 46 (2014) 27–36.

[46] D. Kiener, C. Motz, G. Dehm, Micro-compression testing: A critical discussion of experimental constraints, Mater. Sci. Eng. A. 505 (2009) 79–87.

[47] J.M. Wheeler, J. Michler, Elevated temperature, nano-mechanical testing in situ in the scanning electron microscope, Rev. Sci. Instrum. 84 (2013) 45103.

[48] R. Fritz, D. Kiener, Development and Application of a Heated In-situ SEM Micro-Testing Device, Measurement. 110 (2017) 356–366.

[49] V. Maier, A. Leitner, R. Pippan, D. Kiener, Thermally Activated Deformation Behavior of ufg-Au: Environmental Issues During Long-Term and High-Temperature Nanoindentation Testing, JOM. 67 (2015) 2934–2944.

[50] W.C. Oliver, G.M. Pharr, An improved technique for determining hardness and elastic modulus using load and displacement sensing indentation experiments, J. Mater. Res. 7 (1992) 1564–1583.

[51] D. Tabor, The Hardness of Metals, OUP Oxford, Oxford UK, 1951.

[52] D.I. Bolef, J. De Klerk, Anomalies in the Elastic Constants and Thermal Expansion of Chromium Single Crystals, Phys. Rev. 129 (1963) 1063–1067.

[53] W.D. Nix, H. Gao, Indentation size effects in crystalline materials: a law for strain gradient plasticity, J. Mech. Phys. Solids. 46 (1998) 411–425.

[54] E. Arzt, Size effects in materials due to microstructural and dimensional constraints: a comparative review, Acta Mater. 46 (1998) 5611–5626.

[55] A.S. Schneider, D. Kiener, C.M. Yakacki, H.J. Maier, P.A. Gruber, N. Tamura, M. Kunz, A.M. Minor, C.P. Frick, Influence of bulk pre-straining on the size effect in nickel compression pillars, Mater. Sci. Eng. A. 559 (2013) 147–158.

[56] A. Leitner, V. Maier-Kiener, D. Kiener, Extraction of Flow Behavior and Hall-Petch Parameters Using a Nanoindentation Multiple Sharp Tip Approach, Adv. Eng. Mater. (2016) 1–9.

[57] G.M. Cheng, W.W. Jian, W.Z. Xu, H. Yuan, P.C. Millett, Y.T. Zhu, Grain Size Effect on Deformation Mechanisms of Nanocrystalline bcc Metals, Mater. Res. Lett. 1 (2013) 26–31.

[58] L. Prandtl, Über die Härte plastischer Körper, Nachrichten von Der Gesellschaft Der Wissenschaften Zu Göttingen, Math. Klasse. 1920 (1920) 74–85.

[59] A.G. Atkins, D. Tabor, Plastic Indentation in metals with cones, J. Mech. Phys. Solids. 13 (1965) 149–164.

[60] K.L. Johnson, The correlation of indentation experiments, J. Mech. Phys. Solids. 18 (1970) 115–126.

[61] A. Bolshakov, G.M. Pharr, Influences of pileup on the measurement of mechanical properties by load and depth sensing indentation techniques, J. Mater. Res. 13 (1998) 1049–1058.

[62] J.L. Hay, W.C. Oliver, A. Bolshakov, G.M. Pharr, Using the ratio of loading slope and elastic stiffness to predict pile-up and constraint factor during indentation, in: MRS Proc., 1998: p. 101.

[63] S.-D. Mesarovic, N.A. Fleck, Spherical indentation of elastic-plastic solids, Proc. R. Soc. London A Math. Phys. Eng. Sci. 455 (1999) 2707–2728.

[64] S. Shim, J. Jang, G.M. Pharr, Extraction of flow properties of single-crystal silicon carbide by nanoindentation and finite-element simulation, Acta Mater. 56 (2008) 3824–3832.

[65] E.O. Hall, The Deformation and Ageing of Mild and Steel: III and Discussion of Results, Proc. Phys. Soc. B. 64 (1951) 747–753.

[66] N.J. Petch, The cleavage strength of polycrystals, J. Iron Steel Inst. 174 (1953) 25–28.

[67] O.L. Warren, S.A. Downs, J. Wyrobek, Challenges and interesting observations associated with feedback-controlled nanoindentation, Z. Met. 95 (2004) 287–296.

[68] T. Klünsner, S. Wurster, P. Supancic, R. Ebner, M. Jenko, J. Glätzle, A. Püschel, R. Pippan, Effect of specimen size on the tensile strength of WC-Co hard metal, Acta Mater. 59 (2011) 4244–4252.

[69] E.W. Hart, Theory of the tensile test, Acta Metall. 15 (1967) 351–355.

[70] H. Conrad, Grain-size dependence of the flow stress of Cu from millimeters to nanometers, Metall. Mater. Trans. A. 35 (2004) 2681–2695.

[71] G.B. Gibbs, The Thermodynamics of thermally-activated dislocation glide, Phys. Stat. Sol. 10 (1960) 507–512.

[72] C.P. Brittain, R.W. Armstrong, G.C. Smith, Hall-Petch Dependence for ultrafine grain size electrodeposited Chromium, Scr. Metall. 19 (1985) 89–91.

[73] D.S. Gianola, S. Van Petegem, M. Legros, S. Brandstetter, H. Van Swygenhoven, K.J. Hemker, Stress-assisted discontinuous grain growth and its effect on the

deformation behavior of nanocrystalline aluminum thin films, Acta Mater. 54 (2006) 2253–2263.

[74] F. Mompiou, M. Legros, Quantitative grain growth and rotation probed by in-situ TEM straining and orientation mapping in small grained Al thin films, Scr. Mater. 99 (2015) 5–8.

[75] H.W. Höppel, Mechanical properties of ultrafine grained metals under cyclic and monotonic loads: An Overview, Mater. Sci. Forum. 503–504 (2006) 259–266.

[76] D. Wu, T.G. Nieh, Incipient plasticity and dislocation nucleation in body-centered cubic chromium, Mater. Sci. Eng. A. 609 (2014) 110–115.

[77] B. Joni, E. Schafler, M. Zehetbauer, G. Tichy, T. Ungar, Correlation between the microstructure studied by X-ray line profile analysis and the strength of high-pressure-torsion processed Nb and Ta, Acta Mater. 61 (2013) 632–642.

[78] R. Fritz, D. Lutz, V. Maier-Kiener, D. Kiener, Interplay between Sample Size and Grain Size: Single Crystalline vs. Ultrafine-grained Chromium Micropillars, Mater. Sci. Eng. A. 674 (2016) 626–633.

[79] K. Wang, N.R. Tao, G. Liu, J. Lu, K. Lu, Plastic strain-induced grain refinement in the nanometer scale in a Mg alloy, Acta Mater. 54 (2006) 5281–5291.

[80] T.R. Malow, C.C. Koch, P.Q. Miraglia, K.L. Murty, Compressive mechanical behavior of nanocrystalline Fe investigated with an automated ball indentation technique, Mater. Sci. Eng. A. 252 (1998) 36–43.

[81] J.P. Ligda, B.E. Schuster, Q. Wei, Transition in the deformation mode of nanocrystalline tantalum processed by high-pressure torsion, Scr. Mater. 67 (2012) 253–256.

[82] D. Wu, J. Zhang, J.C. Huang, H. Bei, T.G. Nieh, Grain-boundary strengthening in nanocrystalline chromium and the Hall-Petch coefficient of body-centered cubic metals, Scr. Mater. 68 (2013) 118–121.

[83] H. Conrad, W. Hayes, Correlation of the Thermal Component of the Yield Stress of Body Centered Cubic Metals, Aerosp. Corp. 4 (1963) 33.

[84] M. Mata, O. Casals, J. Alcala, The plastic zone size in indentation experiments: The analogy with the expansion of a spherical cavity, Int. J. Solids Struct. 43 (2006) 5994–6013.

[85] P.J. Imrich, C. Kirchlechner, D. Kiener, G. Dehm, In Situ TEM Microcompression of Single and Bicrystalline Samples: Insights and Limitations, Jom. 67 (2015) 1704–1712.

[86] J.M. Wheeler, C. Niederberger, C. Tessarek, S. Christiansen, J. Michler, Extraction of plasticity parameters of {GaN} with high temperature, in situ micro-compression, Int. J. Plast. 40 (2013) 140–151.

Publication C

Development and Application of a Heated In-situ SEM Micro-Testing Device

R. Fritz[1], D. Kiener[1]

Measurement 110 (2017) 356-366

[1] Department Materials Physics, Montanuniversität Leoben, Leoben, Austria

C - Abstract

Understanding temperature-dependent deformation behaviour of small material volumes is a key issue in material science, especially the deformation behaviour of bcc metals at elevated temperatures is of particular interest for small-scale structural applications. Therefore, a custom-built heating device consisting of independently resistive-heated sample and indenter, and adaptable to existing micro-indenters, is presented. Key parameters of material selection, design of components and temperature control are outlined. Testing temperatures ranging from room temperature up to ~300°C are reached with low drift and without active cooling. To demonstrate the functionality, a variety of in-situ SEM micromechanical experiments were conducted at room temperature and 230°C, respectively. Examples of micro-pillar compression on single crystalline and ultrafine-grained Chromium, as well as notched cantilever fracture experiments on ultrafine-grained Chromium show assets of this powerful tool, allowing more detailed insights into temperature-dependent deformation and fracture behaviour.

C1 - Introduction

Measurement techniques to determine small-scale deformation behaviour at elevated temperature are increasing in popularity since several years. Initially, ex-situ nanoindentation techniques at elevated temperature [1-3] were used to determine mechanical properties such as Hardness or Young's Modulus of a large variety of materials [4-7], and further enhanced to investigate incipient plasticity [8-10]. By increasing test temperatures, the complexity of instrumental setups increased ensuing the purpose of minimizing thermal drift and oxidation problems [1,5,11]. To reduce such inaccuracies, several attempts are reported in literature. Exemplary, testing equipment is purged with inert gases [12-15] or relocated into a vacuum chamber [16-20] to minimize remaining impurities in the atmosphere or to reduce thermal drift and noise.

Parallel to the ongoing development of ex-situ nanoindentation experiments at elevated temperature, in-situ testing techniques inside a scanning electron microscope (SEM) performed at room temperature (RT) became popular [21-22]. By combining instrumented small-scale indentation techniques with the advantages of an SEM, such as high vacuum, vibration damping and direct observation of dynamic processes, a

powerful tool to investigate material behaviour in-situ at non-ambient conditions became available [17-19]. Wheeler *et al.* [23] were the first to report about an advanced in-situ SEM measurement approach up to 200°C. Initially, the system was used to perform in-situ nanoindentation experiments on bulk metallic glasses utilizing a cube corner indenter to correlate measured load-displacement curves with surface shear offset displacements as a function of temperature. However, independent heating and temperature monitoring of sample and indenter was shown to be mandatory [11,24], as temperature gradients are responsible for drift issues. Heating of sample and indenter might be achieved by resistive [11,16,24] or laser heating equipment [25,26]. To reach temperatures above 300°C, a cooling system to minimize thermal drift would be necessary [11,24].

Once the device operates stable at elevated temperature, attention has to be paid to temperature calibration and balancing issues. To calibrate contact temperatures, Wheeler *et al.* [27] discussed several potential ways to assess unavoidable thermal gradients within the limited hot zone. One approach is to indent the respective thermocouples used for temperature monitoring and to measure thermal drift by the use of a pre-set dwell time. Besides that, Raman spectroscopy was suggested as a non-contact technique and an accuracy of ±10°C was reported [27]. Additionally, a temperature matching procedure [24] placing sample and indenter into contact was developed to balance isothermal contact temperatures, instead of measuring displacement drift as conducted in earlier approaches [11].

Nowadays, in-situ platforms with temperature ranges spanning from -140°C [28-31] up to 800°C [26] are available. Constraints such as condensation of moisture for low temperature testing and oxidation issues at elevated temperature have to be taken into account. With that in mind, ex-situ or in-situ investigation of temperature-dependent material behaviour became widely accessible. Due to the limited availability of heatable in-situ SEM testing devices, most of the literature up to now deals with ex-situ nanoindentation [32,33] and pillar compression inside a vacuum chamber [34]. Only a few reports about in-situ investigations to study temperature dependent material behaviour were conducted on bcc [34], fcc [35] or hcp metals [36].

To further explore thermally activated deformation processes in bcc metals and to correlate instrumented testing data with occurring deformation mechanisms on small-scaled samples, this work describes the development, and first experiments on

a custom-built in-situ heating device which can be re-fitted to an existing micro-indenter in an SEM. Special focus is put to material selection, efficient design of components and temperature control. Moreover, finite element simulations were conducted to get knowledge about unavoidable temperature gradients. The capabilities of the described system are exemplarily shown by performing in-situ micro compression tests on taper-free, single crystalline (sxx) and ultrafine-grained (ufg) Cr pillars, as well as notched cantilever fracture experiments on ufg Cr to evaluate fracture toughness values between RT and 300°C. Moreover, obtained flow stress data were compared with results obtained from macroscopic tests and served to validate experiments.

C2 - Materials and methods

SEM and attached micro-indenter

The utilized indenter positioning system is attached to the chamber of an SEM (Zeiss LEO 982, Oberkochen, Germany, Figure 1a) to save operational space. Several flanges for signal feedthroughs (indenter control, power supply, thermocouples) are provided on the wall of the vacuum chamber door. An Everhart Thornley Detector (SE-detector) as well as an In-Lens detector are installed for imaging purposes and an attached plasma cleaner (XEI Scientific Inc., Redwood City, USA) is available to remove organic residues. The sample is mounted on a separately controlled stage (Figure 1b) and the UNAT-SEM micro-indenter (Zwick GmbH & Co. KG, Ulm, Germany) used for testing is shown in detail in Figure 1c, already modified by the heating device. Initially, this micro-indenter was first described in [17]. In the present setup of the SEM, four axes (x_1, y_1, z_1, r_1) allow to position the sample to coincide with the electron beam (Figure 1b). In-plane alignment is achieved by x_1 and y_1, z_1 is used to adapt the working distance and r_1 allows to rotate the sample to align it with the indenter loading axis. Four axes on the indenter side (x_2, y_2, z_2, r_2) allow to position the indenter into the electron beam (Figure 1c). x_2 and y_2 are necessary for in-plane positioning, z_2 and r_2 for adapting the desired working distance and inclination angle. The ranges of indenter and sample movement are summarized in Table 1.

Material selection

To develop an in-situ heating device, material selection for all components is of major importance. As the heating device operates in vacuum atmosphere, materials with considerably high vapour pressure and a sufficient service temperature are crucial. Service temperature in this context describes the maximum temperature where a material can be used for an extended time period without significant deformation, oxidation, chemical reactions, loss of strength or creep, or other primary properties for which the material is normally used [37].

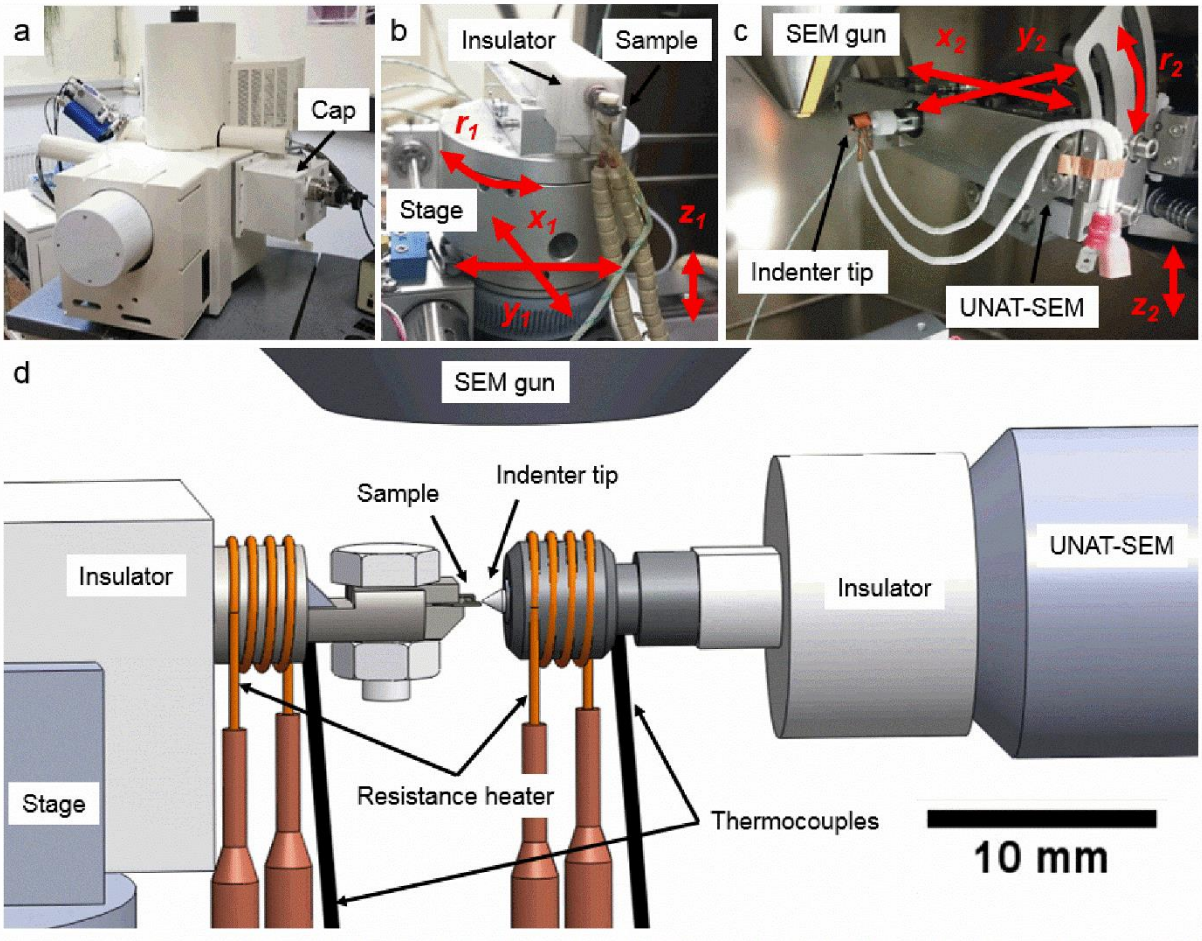

Figure 1: Schematic of the present high temperature in-situ SEM testing setup. (a) Adapted SEM with cap (right) containing the micro-indenter and positioning stage. SEM stage (b) and micro-indenter (c), adapted with custom-built heating devices. Red arrows indicate available positioning axes. (d) Detail of heated parts inside the SEM chamber.

Only non-magnetic materials are advised inside an SEM, and diffusional processes and chemical reactions must be taken into account when sample and indenter get in contact at elevated temperature [3]. Moreover, the coefficient of thermal

expansion (*CTE*) should be in the same range for materials which are in direct contact. There is high demand for minimized material volumes to enable localized heating to permit fast heating rates, as well as requirements regarding operational space inside the SEM (working distance ~5 mm). Figure 1d shows a detail of heated parts within the SEM chamber. The material selection process of each component is described below and material properties are listed in Table 2.

Table 1: Motion ranges of the sample stage and indenter, as well as the specifications of the SEM and micro-indenter in the present setup

SEM		Micro-Indenter	
x_1	±75 mm	x_2	~50 mm
y_1	±75 mm	y_2	~50 mm
z_1	±25 mm	z_2	25 mm
r_1	360°	r_2	0 – 25°
Filament type	Field emission gun	Max. displacement	±50 µm
Acceleration voltage	1 – 30 kV	Noise level of displacement measurement	<1 nm
Typical system vacuum	$6 \cdot 10^{-5}$ mbar	Max. force	±500 mN
Typical column vacuum	$1 \cdot 10^{-9}$ mbar	Noise level of force measurement	<10 µN
		Travel range of the piezo actuator	>100 µm
		Maximum voltage of the piezo actuator	-20 V to +120 V

Wheeler *et al.* [3] summarized several benefits and disadvantages of indenter materials. To choose an appropriate one, reference [3] was used as a guideline for the selection process. Parameters such as oxidation resistance, high melting point as well as high Young's Modulus and hardness are obligatory. High specific heat capacity (c_p), electrical resistivity (R) as well as machinability are necessary, and therefore only a small number of eligible materials such as diamond, some carbides (B_4C, SiC, WC), nitrides (cBN), oxides (Al_2O_3) and metal composites such as WC-Co remain suitable. Moreover, the increased diffusivity of dopants at elevated temperature has to be taken into account. A classic example regarding diffusional problems is the indentation of low carbon steel with metastable diamond [3] or indentation of pure tungsten with a WC indenter tip. As soon as indenter and sample are in contact, in both cases carbon might diffuse at elevated temperature from the carbon rich indenter side to the indented metal

as long as concentration gradients remain present. In the present case, Sapphire (Al_2O_3) was utilized as material for the flat punch indenter tip, shown in Figure 2a. Initially, a conductive Sapphire Berkovich indenter tip was obtained from Synton MDP AG (Nidau, Switzerland) to perform nanoindentation experiments. At a later time, the tip of the indenter was prepared to a flat punch by FIB milling (Zeiss LEO 1540 XP, Oberkochen, Germany) to its final dimensions of ~10 · 6 µm², as shown in Figure 2a.

Table 2: Selected materials and decisive properties for the material selection process [37]

Material	Usage	c_p $[J/kg \cdot K]$	λ $[W/m \cdot K]$	R $[\Omega \cdot cm \cdot 10^{-6}]$	CTE $[10^{-6}/K]$	$T_{service}$ [°C]
Mo	Tip holder	255-275	129-147	5.2-6	4.8-5.5	1310
V	Sample holder	480-505	28-32	19-30	8-8.6	530
Cu	Power supply lines, clamps	383-387	390-398	1.91-1.95	16.8-16.9	360
Constantan©	Resistive wire	410	23	0.49	13.5	600
Macor©	Screw joints, insulation	774-805	1.4-1.56	10^{22}-10^{24}	12.7-13.2	730
Ceramabond© 569	Adhesive	-	20.5	-	7.6	1377
Al_2O_3	Flat punch	790-800	20-25.6	10^{19}-10^{21}	8.8-9.2	1230
WC	Wedge	184-190	28-88	63.1-100	4.5-7.1	727

To conduct micro cantilever fracture experiments, a WC wedge was mechanically ground and subsequently FIB-milled to its final shape. WC was chosen as one of the most stable indenter materials, although it can be vulnerable in combination with tungsten or iron at elevated temperature [3]. As shown in Figure 2b and c, the tip radius is ~500 nm and the length of the wedge is ~120 µm.

To conduct micro cantilever fracture experiments, a WC wedge was mechanically ground and subsequently FIB-milled to its final shape. WC was chosen as one of the most stable indenter materials, although it can be vulnerable in combination with tungsten or iron at elevated temperature [3]. As shown in Figure 2b and c, the tip radius is ~500 nm and the length of the wedge is ~120 µm.

The *CTE* of Sapphire and WC restrict the material selection of the indenter tip holder (Figure 1d), as they should equally expand during heating to minimize thermally induced stresses. Moreover, c_p as well as thermal conductivity (λ) were maximized to bring and store thermal energy into the material. Only a few machinable metals such

as Ta, Mo, Nb, Zr, Cr and V remain suitable within these restrictions. Mo and V were chosen to be the material of choice for the indenter tip holder and the sample holder, respectively (see Table 2 and Figure 1d). As brazing and clamping of the miniaturized indenter tips is not straight forward to achieve, tips were instead glued to their holders using a high temperature adhesive (Ceramabond 569©), which is a two component ceramic bond providing a service temperature of 1650°C. By increasing the amount of thinner, the viscosity of the glue was easily adjusted. A low viscosity in the present case was important, as the glue was sucked by capillary forces into the fitting of the indenter tip and the tip holder. Subsequently, the glue was cured in a convection oven for two hours at 94°C.

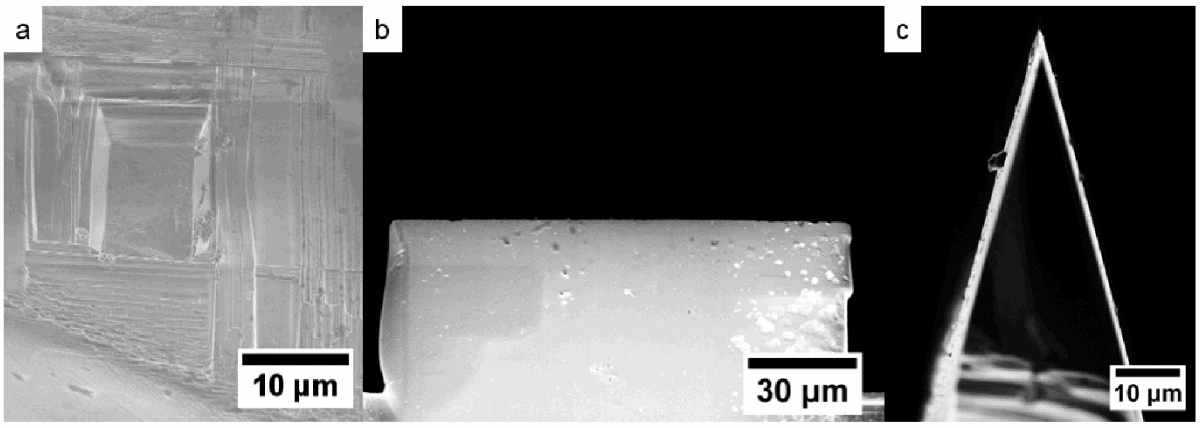

Figure 2: Indenter tips suited for the heating device. (a) A 10 · 6 µm² sapphire flat punch and (b and c) a WC wedge having a length of ~120 µm, a tip radius of ~500 nm and an opening angle of ~30°.

To mount the lamella-shaped, macroscopic samples [38,39] on the heatable sample holder (Figure 1d), they are fixed on the V holder by a screw made out of Macor© ceramic. This ceramic is machinable, resists high temperatures and provides a low λ and high R. Common screws in the size of a few millimetres are usually made from brass or low alloyed, magnetic steels and are therefore not well suited.

For exact temperature measurements, Type K (Chromel / Alumel) thermocouples with a temperature range of -200°C up to 1200°C were utilized and brazed close to sample and indenter tip (Figure 1d). An eutectoid 72Ag28Cu braze (Brazetec 7200, Ögussa GmbH, Vienna, Austria) providing a service temperature of 1300 K was used to fix the thermocouple at the indenter tip holder made out of Mo. Due to poor adhesion between the V sample holder and the eutectoid braze, an interlayer braze (Cu7Mn3Co,

Brazetec 21-68, Ögussa GmbH, Vienna, Austria) was first brazed on the surface of the sample holder. The thermocouple was subsequently fixed using the eutectoid braze to the sample holder. More importantly, the thermocouples were attached to the holders before the indenter was glued into its shaft, as the braze melts at about 1000°C. Zinc-based brazes as well as brass holders were neglected in the material selection process, as zinc might evaporate at a relatively low vapour pressure and alter the heating device as well as the SEM interior.

To reach a considerable high testing temperature, the resistive-heated filaments of choice must produce thermal energy efficiently. In the present case, filament wires had to be very flexible, as they need to be looped around the holders and stay in contact with them (Figure 1d). In fact, filaments were formed to coils to ease their placement over the holders. They are made out of Konstantan©, a frequently used heating wire material having a wire diameter of 0.4 mm. It consists of 55% Cu, 44% Ni and 1% Mn. The Konstantan© coils are connected by Cu clamps to thicker Cu wires that directly lead to the chamber feedthroughs. The Cu wires are insulated with ceramic beads (Tectra GmbH, Frankfurt, Germany). To further thermally insulate the tip shaft of the micro indenter from heat, a ceramic spacer made out of Macor© is placed between the heated indenter tip and the indenter mechanics (Figure 1c and d). Further, the heated sample holder is mounted on a Macor© spacer, which is fixed to the SEM stage to prevent heating, as shown in Figure 1b and d.

Power- and temperature control

To resistively heat sample and indenter separately inside the SEM, a TOE 8952-20 dual-output DC power supply (Toellner Electronic Instruments GmbH, Herdecke, Germany) providing a voltage range of 0-20 V and a current range of 0-20 A was used. To properly measure the desired temperatures, thermocouples were connected to an USB TC-08 data logger (Pico Technology, St. Neots, UK) providing an accessible temperature range of -270°C to 1280°C. By converting voltage into temperature, sampling rates of up to 10 measurements per second are achieved. An automatic cold junction compensation is used to record corresponding temperatures at eight individual positions within the whole setup. Software control and temperature monitoring was implemented in LabView® (National Instruments Corp., Austin, Texas, USA), and temperature control was achieved using a PID feedback loop. An exemplary heating

procedure up to ~230°C, with sample and indenter being out of contact, is shown in Figure 3a.

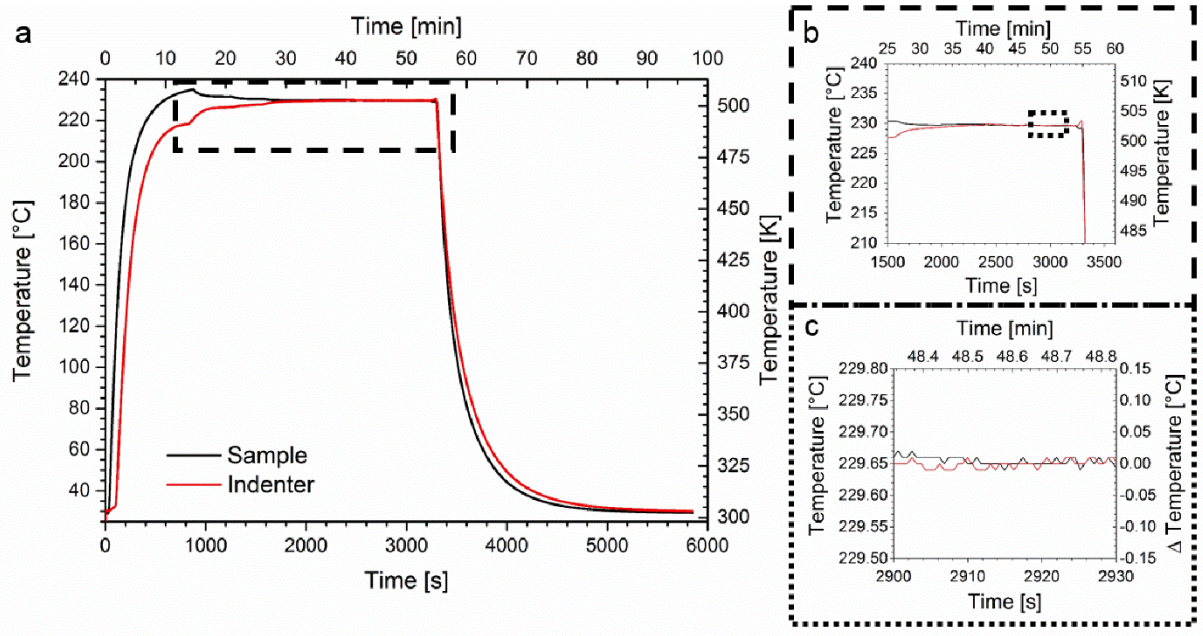

Figure 3: Representative heating procedure of sample and indenter. a) Stable heating to the desired temperature and subsequent cooling to RT is possible within 90 min. b) After ~30 min, a constant temperature is achieved. c) Temperatures can be adjusted with an accuracy of ~0.1°C.

Within 30 minutes, a constant and stable temperature at both thermocouples is achieved, while the accuracy of the controlled temperatures is ±0.1°C, as shown in Figure 3b and c. The situation of heated sample and indenter in contact requires temperature calibration and matching for various reasons [27]. Unfortunately, it is not possible to directly braze thermocouples on the micron-sized samples or the indenter. Holders, samples and indenters are made out of different materials, and therefore exact temperature measurements are not possible. Wheeler *et al.* [3,24,27] suggested individual temperature calibration techniques as well as a temperature matching procedure, which is recommended before testing at elevated temperature. For further, more detailed information about temperature calibration, different to previous assessments we also utilized simulation approaches, as described in section 2.4.

Temperature calibration by numerical simulation

The full experimental setup was recreated true to original data in 3D using a CAD program. The geometry was loaded into the finite element program Abaqus (Dassault Systems, Providence, RI, USA) to conduct heat flow calculations. A biased mesh size was used with a coarser mesh for larger, less significant parts, while for micron-sized parts a very fine mesh has been utilized. Material properties used in the calculations are shown in Table 2. Moreover, convection within the vacuum chamber was neglected and characteristic radiation properties of each material as suggested in [37] were chosen. Sample and indenter were first placed out of contact and separately heated, as shown in Figure 4. A constant, direct current and independent powers (*P*) at the sample and indenter side were used to reach constant temperatures (268°C) at the marked positions of the thermocouples after a heating time of 3600 s. Positions of thermocouples at the sample and the indenter holder are indicated in Figure 4 as T_1^S and T_1^I, respectively. Resulting temperature gradients are presented as colour code in Figure 4, indicating different absolute temperatures at the sample and the indenter tip. Those differences are of major importance and should be minimized when bringing sample and indenter in contact to perform elevated temperature experiments at minimum drift.

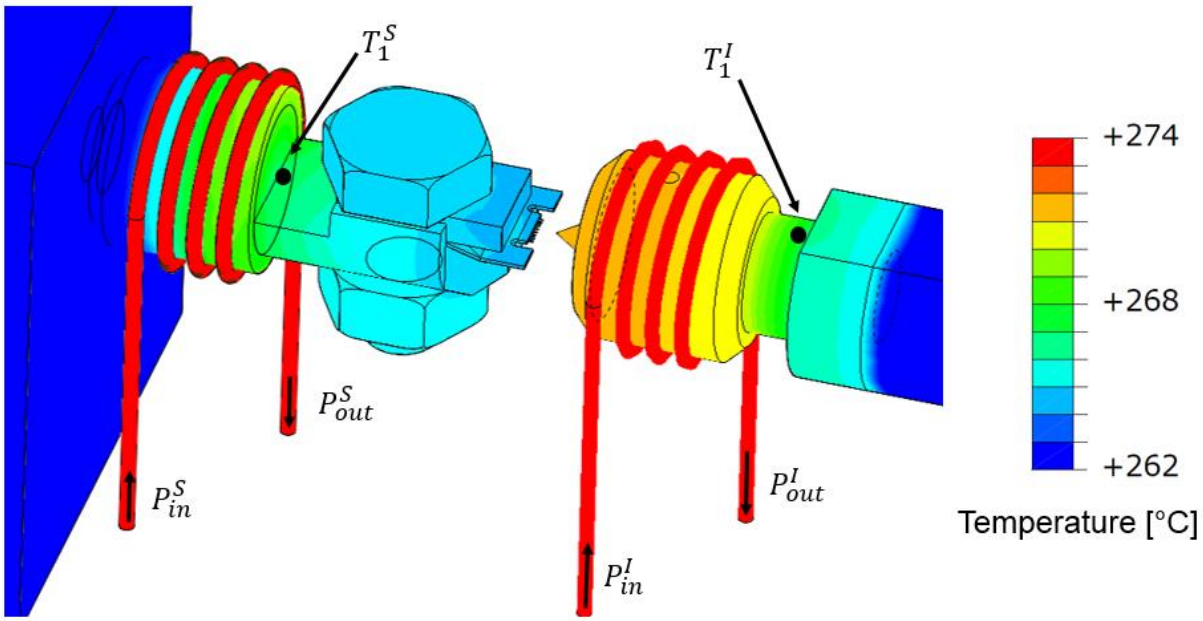

Figure 4: Temperature distribution in heated parts inside the SEM. Temperature at individual thermocouples at sample (T_1^S) and indenter (T_1^I) is constant, but large temperature gradients and differences in absolute temperature at the sample and the indenter tip are observed.

This situation is shown in Figure 5a, where a flat punch indenter is in contact with a 1 µm sized pillar. The details of the contact situation are shown in Figure 5b. A large temperature gradient occurs although temperatures of thermocouples T_1^S and T_1^I are equilibrated. This results in thermal as well as displacement drift. To get rid of such inaccuracies, a detailed knowledge of remaining temperature gradients and the absolute temperature at the sample and the indenter are necessary.

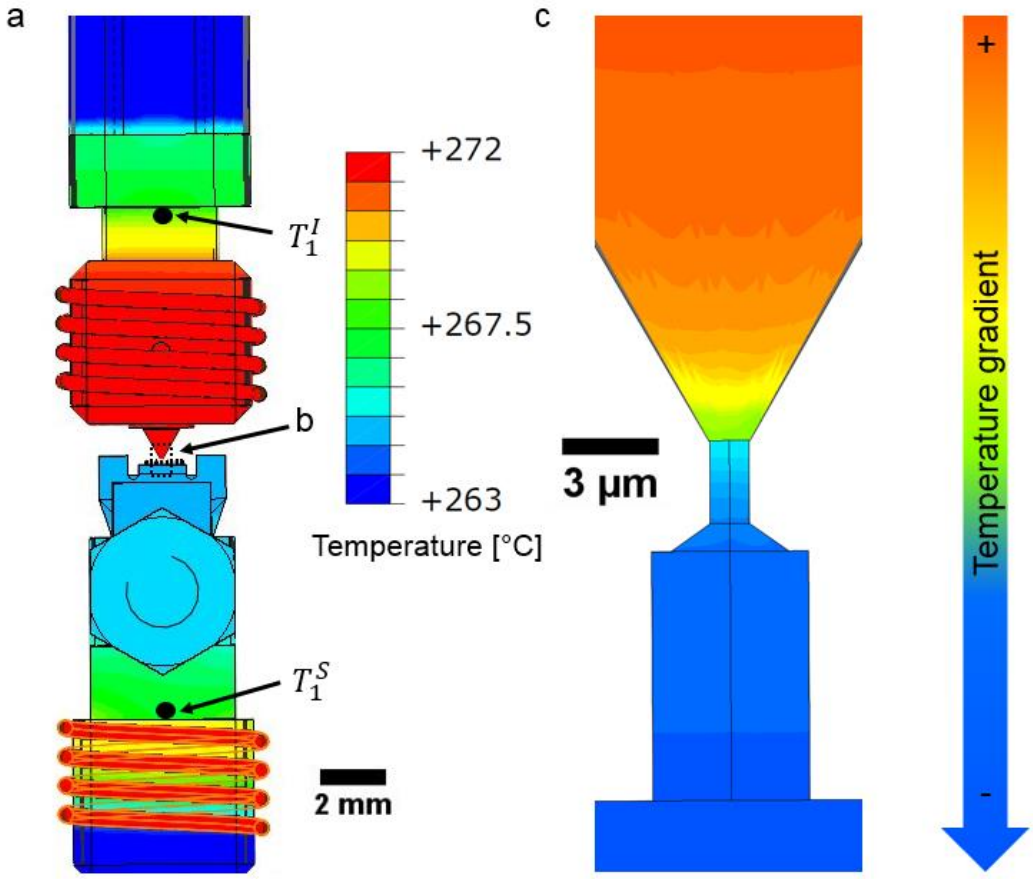

Figure 5: Although the thermocouples T_1^S and T_1^I are at the same temperature (a), a large temperature gradient resulting in thermal drift occurs when bringing sample and indenter in contact (b). (c) Detail of the contact situation with a large temperature gradient.

To underline the importance of temperature calibration, the material of the tested lamella-shaped specimens was varied and temperature gradients were analysed, as shown in Figure 6. T_2^S and T_3^S in Figure 6a and b indicate individual positions of temperature measurement on the specimen fixation and directly at the pillar. Design limitations such as the distances between heated parts, thermocouples and the sample, as well as sample geometry are of major influence of temperature gradients,

as shown in Figure 6b. By heating different specimens with varying λ such as Cu, W or Si, it becomes evident that samples with high thermal conductivity such as Cu allow lower temperature gradients compared to W or Si samples (Figure 6c). Nonetheless, within the present setup gradients up to 7°C and more are possible between thermocouple and specimen, as thermal properties strongly influence the temperature distribution. Thus, to ensure equilibrium temperatures, a procedure to match sample and indenter tip temperature is inevitable before each experiment.

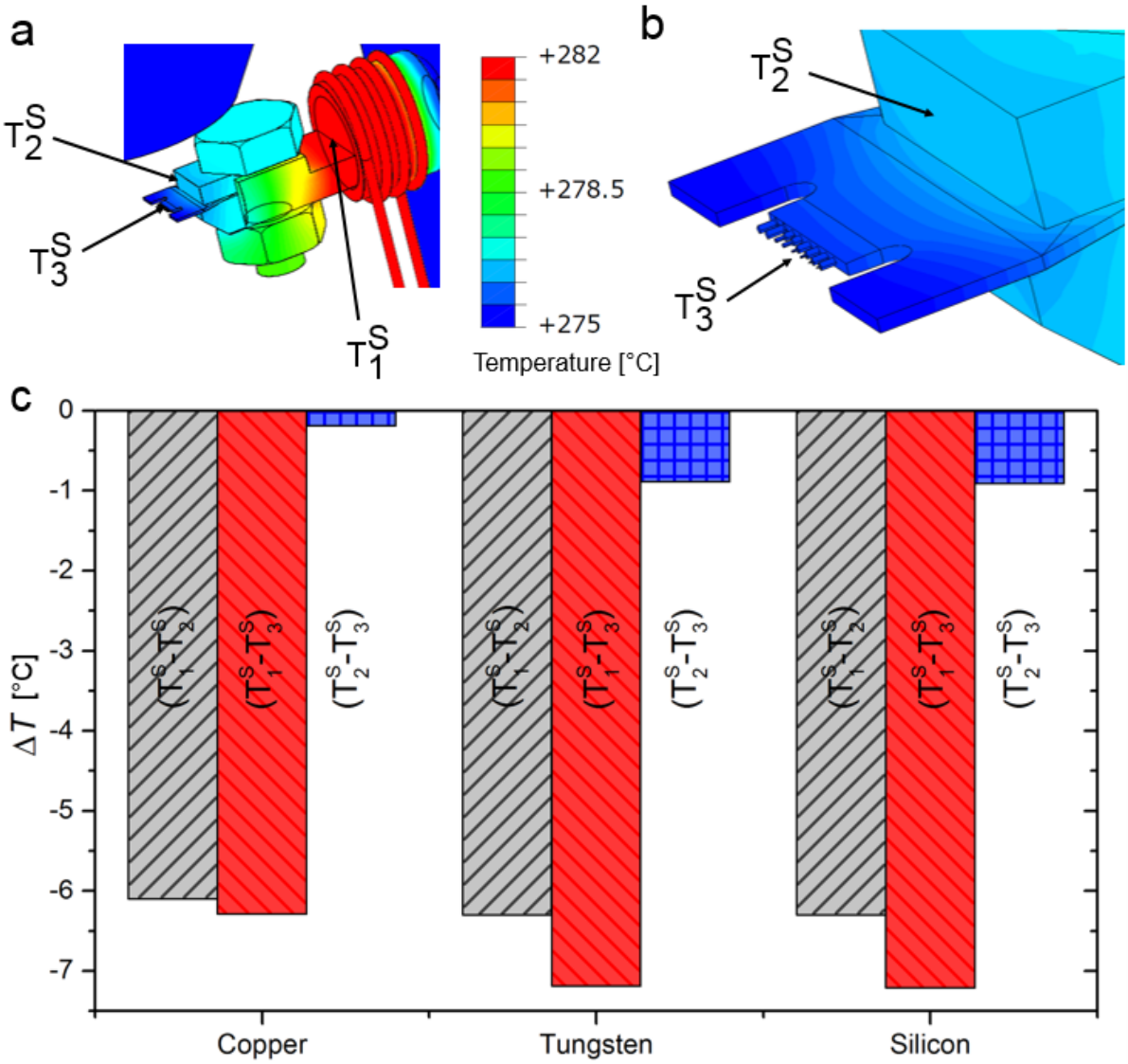

Figure 6: Influence of varying specimen material on temperature gradients. (a) and (b) indicate local temperature distribution and positions of temperature measurement, the gradient of which are reported in (c).

Temperature matching

Figure 7a presents a temperature matching procedure as suggested in [24] conducted with the present setup. Thereby, sample and indenter are brought into contact several times and temperature shifts are analysed in a hold period at pre-defined, constant low load to minimize creep influences. In the first contact situation, as shown in Figure 7a, the cold tip and the hot sample, for example, are not in equilibrium causing a temperature drop on a thermocouple as well as displacement drift. Contact situation two shows the same non-equilibrium condition for the opposite temperature misadjustment, exemplary shown for a cold sample and a hot indenter situation. To balance the contact temperature, this procedure has to be repeated until temperature change is minimized during contact, indicating zero temperature shift (Contact 3), where no detectable temperature difference between tip and sample is observed. This process can be linearly extrapolated to zero shift and is shown in Figure 7b. Subsequently, the setup is ready to perform experiments at the adjusted elevated temperature.

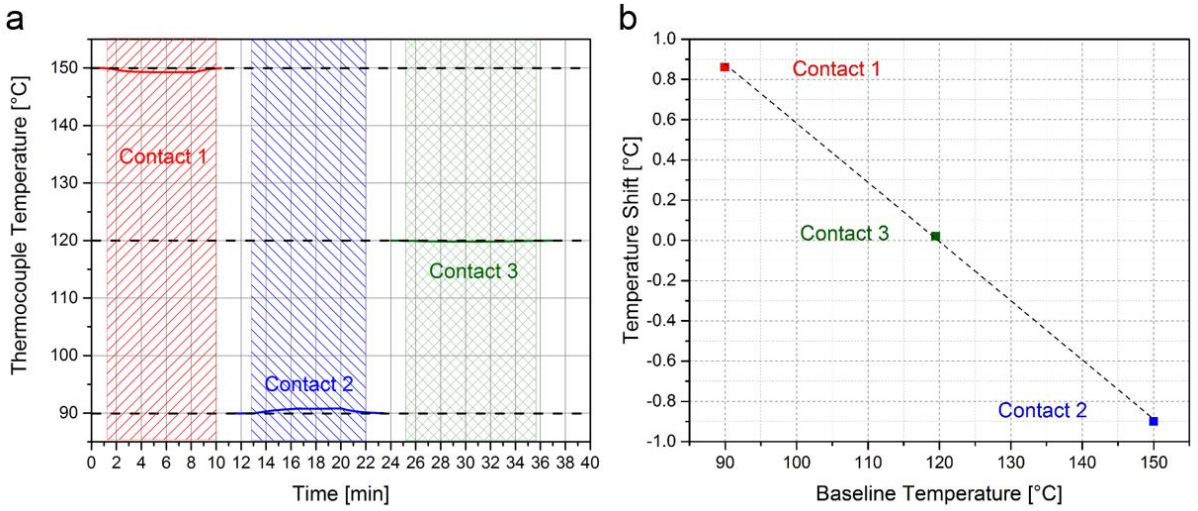

Figure 7: (a) Exemplary temperature matching procedure to infer the isothermal contact temperature and (b) determining the zero-shift working temperature by linear extrapolation. The procedure was taken from [24].

Material preparation

An sxx Cr rod oriented in (100) was obtained from Mateck GmbH (Jülich, Germany) and the polycrystalline Cr was provided as sheet by Plansee SE (Reutte, Austria). The polycrystalline Cr was deformed via HPT [40,41] to reach an ufg microstructure. A pressure of 4.2 GPa at 200°C and a rotational speed of 0.5 rpm for 50 rotations resulted in an equivalent strain of ~360 and a grain size of ~160 nm [42]. No pronounced texture, but slightly elongated grains with an aspect ratio of ~3:1 were observed in the as-deformed microstructure in axial direction. Wire cutting, sample polishing and ion milling [38,39] as well as FIB preparation of the non-tapered pillars using milling currents of 1 nA and 100 pA for rough cutting and final polishing, respectively, were used. Pillar fabrication with a size range of ~0.2 µm to 6 µm and an aspect ratio of 3:1 was initially described in [39] and [42]. Moreover, $9 \cdot 9 \cdot 45$ µm³ sized cantilevers were milled from an ufg Cr lamella. Due to larger sample sizes, milling currents of 5 nA for rough cutting and 500 pA for final polishing were used. To initiate a pre-crack in the cantilevers, FIB notches were fabricated using the line-milling mode. A FIB current of 500 pA and a milling time per length of milling of 6.5 s/µm resulted in a notch depth of ~1.5 µm. Both sample geometries were fabricated in axial direction with respect to the HPT orientation and load was applied perpendicular to elongated grains. A similar preparation process was initially shown and further detailed in [43]. Tests were carried out utilizing the above described SEM with the attached micro-indenter as described in section 2.1. To analyse crack growth of the pre-notched cantilevers and the dynamics of the compressive deformation, images during in-situ testing were captured with 1 frame per second. High resolution SEM images (Zeiss LEO 1525, Oberkochen, Germany) were recorded after deformation to analyse the resultant surface evolution. Finally, cross sections were milled into the highly deformed zones of the cantilevers to investigate the microstructure as well as crack propagation during elevated temperature testing.

Data analysis

All tests were conducted in displacement-controlled mode. For compression tests, a constant nominal strain rate of $3 \cdot 10^{-3}$ s^{-1} was applied and pillars were deformed to ~20% strain. Recorded force-displacement data was corrected to take into account the stiffness of the lamella [44], and sample sink-in [45] was considered.

Additional weight acting on the force transducer (~10 g) of the indenter tip shaft, including the thermocouple and the resistive wire, affect the force measurement by a lateral load. Therefore, the transducers were calibrated before conducting the experiments by performing air indentations over the whole displacement range of the transducer. The resultant positive slope of the force-displacement signal was then used to correct the signals to zero-load.

Engineering stress was calculated by taking the top pillar area into account and engineering strain was calculated using the height of the non-tapered pillars.
Cantilevers were bent utilizing a displacement rate of 1 µm/min, as suggested in [43] and deformed to a maximum load line displacement of 8 µm, which corresponds to a bending angle of ~15°. To investigate fracture morphologies and to open the crack tip, cantilevers were further bent downwards. Width (*W*), height (*B*), bending length (*L*) and crack length (a_0) of the specimens are shown in Table 3. They were used to calculate fracture toughness values according to [46]

$$K_Q = \frac{F_Q \cdot L}{B \cdot W^{3/2}} \cdot f\left(\frac{a}{W}\right). \quad (1)$$

The force F_Q was determined according to ASTM E-399 [46], and the geometry factor *f(a/W),* which describes the influence of the pre-crack, was taken from [47]. As requirements for plane strain fracture toughness are not fulfilled, results are presented as conditional fracture toughness values and indicated with the subscript "*Q*". K_Q determined this way gives a lower limit for fracture toughness [43]. As linear elastic fracture mechanics (LEFM) is only applicable for hard and brittle materials, the *J*-integral approach is commonly used for large-scale yielding of small samples. According to ASTM E 813-89 [48], *J* is given as the sum of elastic and plastic components

$$J = \frac{K_Q^2 \cdot (1-\upsilon^2)}{E} + \frac{\eta \cdot A_{pl}}{B \cdot (W-a_0)}, \quad (2)$$

where υ=0.21 is the Poisson ratio, *E*=294 GPa is the Young's Modulus of Cr [49], η=2 is a constant and A_{pl} represents the plastic work of the experiment (area beneath the load-displacement curve). *J*-Δa curves were calculated and fitted according to [43]

using crack extension values obtained from the in-situ experiment at each step of unloading. To compare fracture toughness values from elastic plastic fracture mechanics (EPFM, *J*-integral) with LEFM (K_Q), *J* is converted to

$$K_{Q,J} = \sqrt{\frac{J \cdot E}{1-\upsilon^2}}, \tag{3}$$

which gives an upper bound for fracture toughness values [43].

Table 3: Cantilever dimensions and conditional fracture toughness values at RT and 230°C for ufg Cr in axial direction.

Temperature	*W* [µm]	*B* [µm]	*L* [µm]	a_0 [µm]	K_Q [MPam$^{1/2}$]	$K_{Q,J}$ [MPam$^{1/2}$]
RT	8.834	8.989	37.3	1.589	2.43	16.98
230°C	7.995	9.340	32.5	1.805	1.43	16.81

C3 - Results

Figure 8a shows representative engineering stress-strain curves of pillar compression experiments at RT (black) and 230°C (red) on ufg Cr (solid line) and sxx Cr (dashed line). Yield stress values at RT of ~400 MPa and ~100 MPa at 230°C were measured for sxx Cr. Refining the microstructure into the ufg regime leads to an increase of yield strength to ~1100 MPa and 950 MPa at RT and 230°C, respectively, according to Hall and Petch [50,51]. Figure 8b and d show deformed ufg pillars, and Figure 8c and e present deformed sxx samples, at RT and 230°C, respectively. To further provide detailed knowledge of ongoing deformation mechanisms in ufg Cr, cantilever fracture experiments were designed using the obtained uniaxial test data.
Results of cantilever fracture experiments in terms of bending stress-displacement plots and post-deformation SEM images of ufg fracture samples, deformed at RT (black) and 230°C (red) are shown in Figure 9. To compare yield stress values with results obtained by uniaxial testing (Figure 8), stresses were calculated using the remaining ligament size W-a_0. Figure 9a depicts typical linear elastic loading of the cantilevers followed by a transition into the plastic regime. Strain hardening up to a displacement of ~4 µm is observed by a subsequent softening until the maximum displacement of 8 µm was reached.

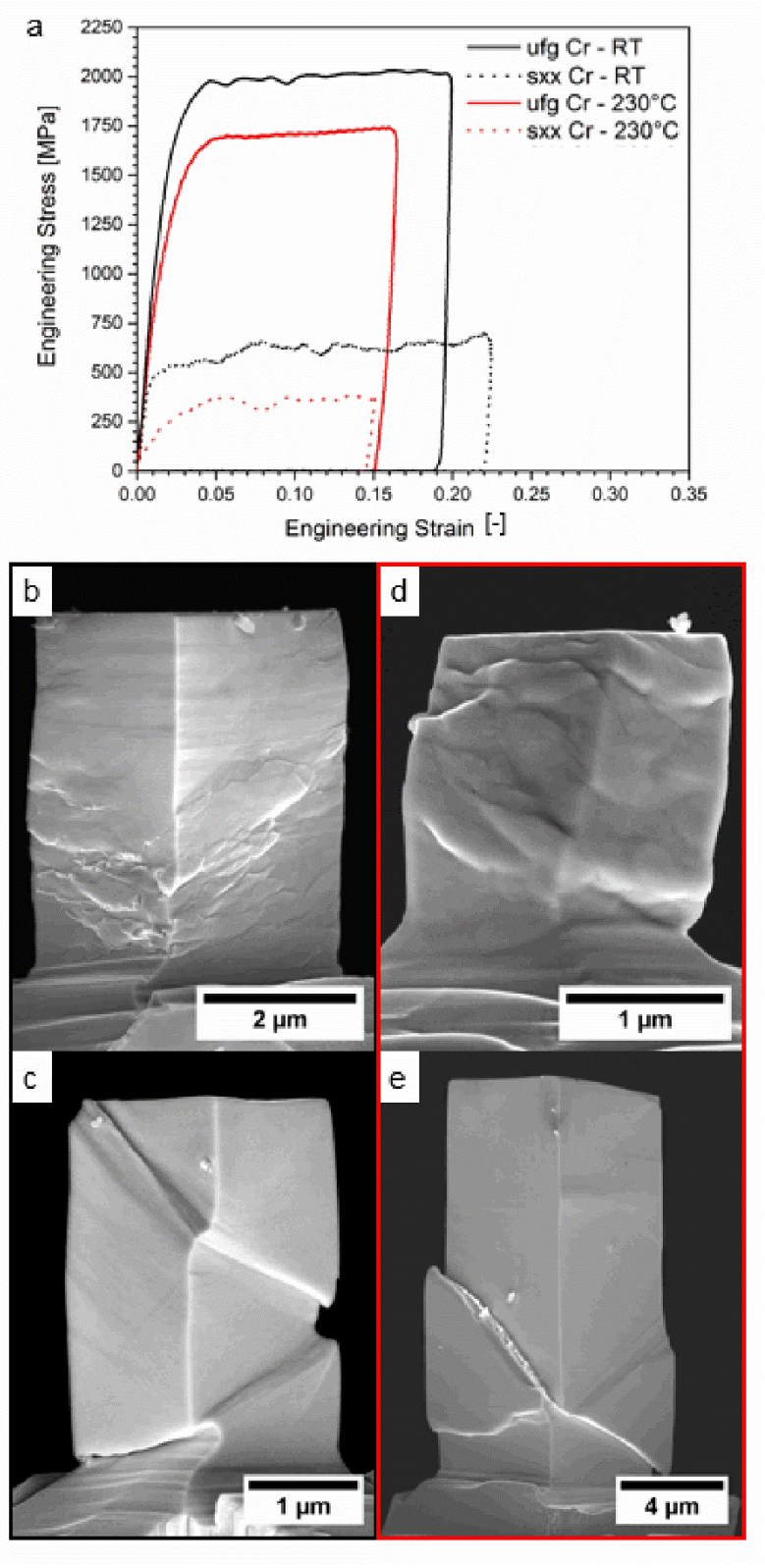

Figure 8: (a) Engineering stress-strain curves showing the deformation behaviour of ufg (solid lines) and sxx (dashed lines) Cr pillars at RT (black) and 230°C (red). (b-e) Post compression SEM images of deformed pillars. (b) and (c) show deformed ufg and sxx pillars at RT, (d) and (e) present an ufg and an sxx pillar, respectively, deformed at 230°C.

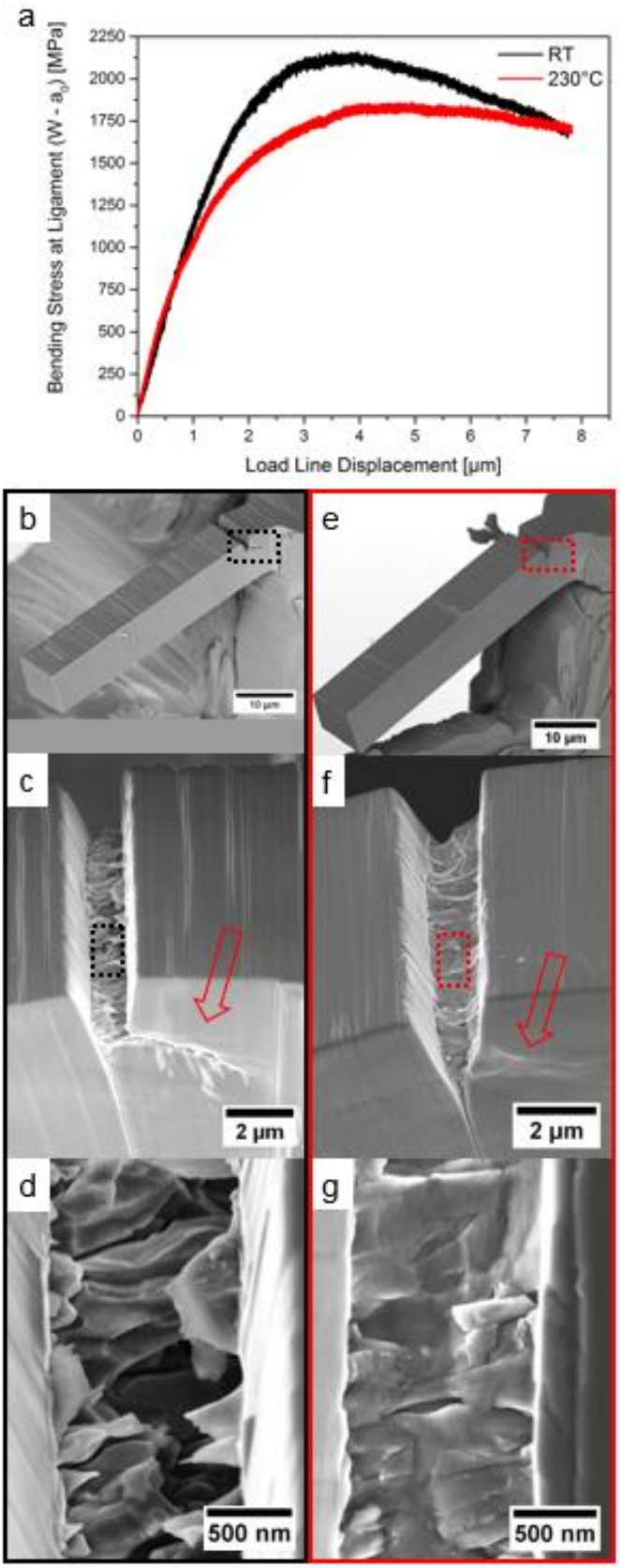

Figure 9: (a) Bending stress-displacement curves of notched ufg cantilevers deformed at RT (black) and 230°C (red). (b-g) depict details of the fracture morphologies at corresponding temperatures.

Figure 9b-d and e-g show deformed cantilevers and corresponding fracture morphologies at the respective temperatures. The crack propagation is clearly affected by the testing temperature (Figure 9c and f), indicated by red arrows. At RT, the extending crack deflects and propagates perpendicular to the loading direction, while at 230°C blunting without crack extension nor crack deflection is observed. This behaviour is also reflected by the varying fracture morphology presented in Figure 9d and g, where an inclined view into the opened cracks is shown.

C4 - Discussion

Numerical simulation

The conducted numerical simulation indicates material- as well as sample geometry-dependent temperature gradients if temperatures at the indicated thermocouples are equilibrated. The knowledge of such gradients is of major importance regarding measurements at non-ambient conditions and helps minimizing thermal drift. Moreover, numerical simulations are inevitable if a temperature matching procedure is not feasible due to limitations of the sample geometry eg. by testing samples on needle-shaped specimens at elevated temperatures [44,52].

Pillar compression

Literature values of macroscopic yield stresses for sxx Cr at RT [53] are found to be ~300 MPa in (100) orientation for tensile experiments, and failure occurred by void nucleation and coalescence. In the present case, a sample size effect leading to yield stresses of ~400 MPa is expected within the size regime of a few microns, as shown by Uchic *et al.* [54]. Size effects in sxx Cr are separately discussed in [42].

The flow stress decrease in ufg Cr at 230°C (Figure 8a) partly results from a grain size increase, as well as a vanishing contribution of the thermal stress component, as commonly observed in bcc metals at elevated temperature [33]. Figure 10a and b present the undeformed microstructures in the ufg Cr lamella at RT and 230°C. The mean grain size increased from ~160 nm to ~350 nm and a reduction of grain aspect ratio was observed. An estimation of the flow stress decrease by simple Hall-Petch relation [50,51] results in a flow stress reduction of 200 MPa. The Hall-Petch coefficient of Cr ($k_{H\text{-}P}$=1380 MPaμm$^{1/2}$) was taken from [55]. Moreover, flow stress values of sxx

(530 MPa) as well as ufg Cr (2050 MPa) obtained by nanoindentation [33] and macroscopic tests [42] at RT and elevated temperature are well within the range of flow stress values obtained with the present heating setup.

Post compression SEM images of ufg pillars as shown in Figure 8b and d show no distinct differences. SEM images of sxx pillars (Figure 8c and e) indicate differences in deformation behaviour. The propagation of screw dislocations via cross-slip is the rate-limiting mechanism at low temperatures in bcc metals [56]. Considering the sample surface in figure 8c, slip steps are not well-defined, which gives evidence of cross-slip processes. At elevated temperature the surface morphology in Figure 8e reveals sharp slip steps, indicating reduced cross-slip of screw dislocations due to thermal activation [34]. Moreover, the decrease in flow stress from ~400 MPa at RT to ~100 MPa at 230°C in sxx samples indicates a decrease of the thermal stress component of ~300 MPa.

Fracture processes

Fracture toughness of semi-brittle materials such as bcc metals is mostly investigated on sxx samples [43,57-62]. For polycrystalline samples with defined pre-notches, only few ex-situ [63-68] and in-situ studies [69] are found in literature. Fracture toughness and deformation behaviour of bcc metals are strongly dependent on strain rate, grain size and temperature [33,70]. Thermal activation reduces the high Peierls stress and therefore eases the movement of screw dislocations. This results in a semi-brittle deformation behaviour for a specific microstructure and loading condition, indicated by a specific ductile-to-brittle transition temperature (DBTT) [71].

Bohnert *et al.* [61] showed that fracture toughness values of sxx W are strongly dependent on notch geometry, which was also supported by finite element simulations. In contrast to that, fracture toughness values are not significantly influenced by the miniaturized specimen geometry, as long as assumptions for large-scale yielding are made. The effect of notch type on fracture toughness was investigated by Wurster *et al.* [43], where fracture toughness values of natural notched sxx W cantilevers were compared to FIB-notched cantilevers. No influence of notch type as well as specimen size were reported in the micron regime. Fracture toughness of polycrystalline, macroscopic samples was summarized in [64], indicating that fracture mechanisms for ufg metals differ from large-grained samples. Cantilevers in the present case are well

below sample dimensions investigated in [64]. Approx. 2500 grains are located within the cantilever cross section. The lower limit of fracture toughness's (K_Q) as well as upper limits ($K_{Q,J}$ from *J*-Integral) are summarized in Table 3. Figure 10c and d show details of the pre-notched samples. No distinct differences are observed before testing, which might be reflected by comparable fracture toughness values at RT and 230°C. All values are expected to lie below the characteristic DBTT of Cr, which is between 320°C and 390°C in the undeformed condition [72]. Moreover, yield stresses of uniaxial deformed samples (1100 MPa at RT and 950 MPa at 230°C) and cantilever fracture experiments (1130 MPa at RT and 910 MPa at 230°C) indicate comparably plastic limits for the different testing techniques. However, post deformation SEM images (Figure 9) do reveal differences related to crack initiation and propagation. At RT, the cantilever fails at the pre-notch and the crack immediately deflects and extends perpendicular to the loading direction (Figure 9 b and c). Moreover, grains were pulled out of the fracture surface (Figure 9d). Blunting instead of crack extension and crack deflection was observed in SEM images of the cantilever deformed at 230°C (Figure 9e, f and g). Grains tended to show a more ductile behaviour compared to RT. Figure 10e and f show FIB cross sections of the highly deformed zone of the cantilevers at RT and 230°C, respectively, and confirm different deformation behaviour. At RT, the crack propagated on an intercrystalline crack path in the direction of the elongated grain structure. Such phenomena was already shown in [63] and [64]. No transgranular fracture was expected, as the grain size was too small for sufficient pile-up within the grains [64]. Decohesion processes at the grain boundaries were observed on triple junctions. At 230°C, blunting instead of crack extension was observed (Figure 10 f). However, both experiments show that grain boundaries act as an effective barrier against crack growth [69]. While the crack extension in ufg Cr along grain boundaries is indicative for the RT experiment, blunting around the pre-crack was observed at elevated temperature.

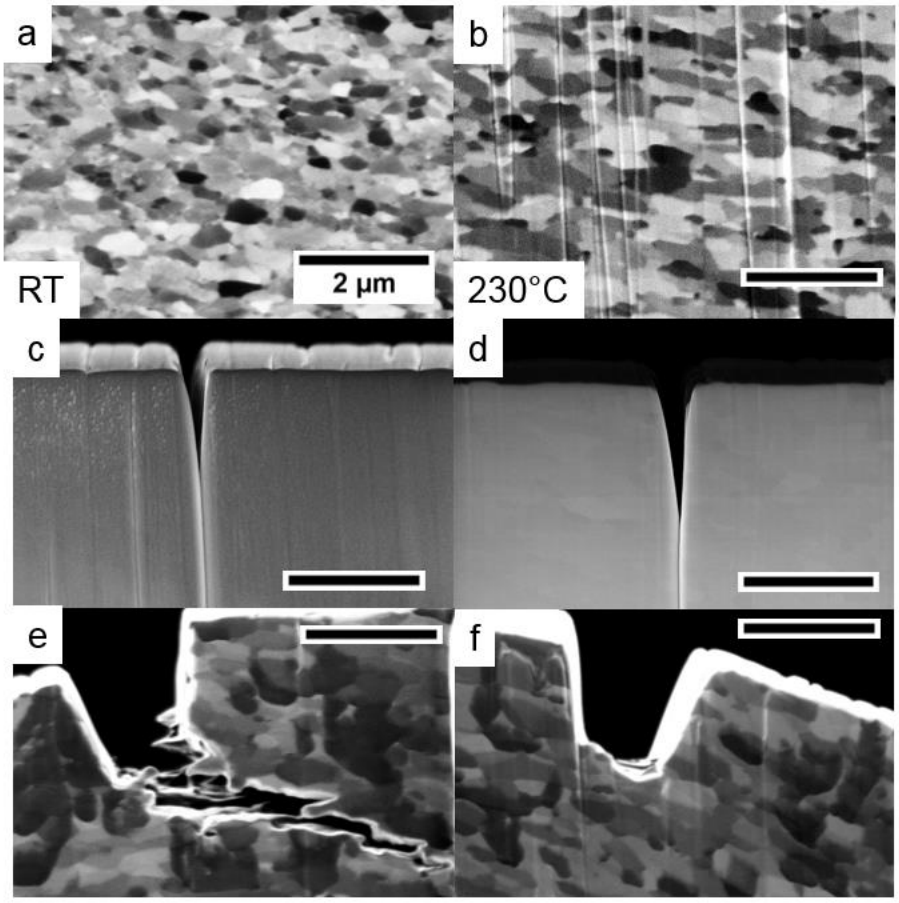

Figure 10: Comparison of microstructure as well as cross sections of the deformed cantilevers. Undeformed ufg Cr microstructure at RT (a) and 230°C (b). The mean grain size increased from ~160 nm to ~350 nm. (c) and (d) show details of the pre-notches. (e) Crack deflection along the orientation of elongated grains at RT. (f) At 230°C plastic deformation and crack tip blunting without crack growth is observed.

C5 - Conclusion

The development and characterization as well as first experiments on a custom-built in-situ heating device were presented. A maximum temperature of 300°C was shown to be achievable by separately resistive-heated indenter and sample. Finite element simulation results underline the importance of appropriate temperature calibration procedures followed by exact temperature matching. Quantitative in-situ experiments such as pillar compression and cantilever fracture testing at elevated temperatures were shown to be possible with high resolution inside the SEM. Pillar compression experiments on single crystalline as well as ultrafine-grained Chromium samples reveal an expected flow stress decrease due to a reduced thermal stress component, which goes along with a temperature-induced change of the

microstructure in ultrafine-grained Chromium. Cantilever-based fracture experiments on ultrafine-grained Chromium show almost constant fracture toughness values at RT and 230°C, although crack propagation and crack deflection mechanisms already changed with increasing temperature towards more ductile deformation.

C - References

[1] C.A. Schuh, C.E. Packard, A.C. Lund, Nanoindentation and contact-mode imaging at high temperatures, J. Mater. Res. 21 (2006) 725–736.

[2] Z.C. Duan, A.M. Hodge, High-temperature nanoindentation- New developments and ongoing challenges, JOM. 61 (2009) 32–36.

[3] J.M. Wheeler, J. Michler, Invited Article: Indenter materials for high temperature nanoindentation, Rev. Sci. Instrum. 84 (2013) 101301.

[4] B.N. Lucas, W.C. Oliver, Time Dependent Indentation Testing at Non-Ambient Temperatures Utilizing the High Temperature Mechanical Properties Microprobe, MRS Proc. 356 (1995) 645–650. doi:10.1557/PROC-356-645.

[5] J.F. Smith, S. Zheng, High temperature nanoscale mechanical property measurements, Surf. Eng. 16 (2000) 143–146.

[6] B.D. Beake, J.F. Smith, High-temperature nanoindentation testing of fused silica and other materials, Philos. Mag. A. 82 (2002) 2179–2186.

[7] J. Xia, C.X. Li, H. Dong, Hot-stage nano-characterisations of an iron aluminide, Mater. Sci. Eng. A. 354 (2003) 112–120.

[8] D.E. Kramer, K.B. Yoder, W.W. Gerberich, Surface constrained plasticity: oxide rupture and the yield point process, Philos. Mag. A. 81 (2001) 2033–2058.

[9] C.A. Schuh, J.K. Mason, A.C. Lund, Quantitative insight into dislocation nucleation from high-temperature nanoindentation experiments., Nat. Mater. 4 (2005) 617–621.

[10] M. Rebelo De Figueiredo, M.D. Abad, A.J. Harris, C. Czettl, C. Mitterer, P. Hosemann, Nanoindentation of chemical-vapor deposited Al2O3 hard coatings at elevated temperatures, Thin Solid Films. 578 (2015) 20–24.

[11] N.M. Everitt, M.I. Davies, J.F. Smith, High temperature nanoindentation - the importance of isothermal contact, Philos. Mag. 91 (2011) 1221–1244.

[12] A. Sawant, S. Tin, High temperature nanoindentation of a Re-bearing single crystal Ni-base superalloy, Scr. Mater. 58 (2008) 275–278.

[13] J.C. Trenkle, Packard C E, C.A. Schuh, Hot Nanoindentation in inert Environments, Rev. Sci. Instrum. 81 (2010) 73901.

[14] S. Korte, W.J. Clegg, Micropillar compression of ceramics at elevated temperatures, Scr. Mater. 60 (2009) 807–810.

[15] S. Korte, J.S. Barnard, R.J. Stearn, W.J. Clegg, Deformation of silicon - Insights from microcompression testing at 25-500°C, Int. J. Plast. 27 (2011) 1853–1866.

[16] S. Korte, R.J. Stearn, J.M. Wheeler, W.J. Clegg, High temperature microcompression and nanoindentation in vacuum, J. Mater. Res. 27 (2012) 167–176.

[17] D. Kiener, C. Motz, G. Dehm, R. Pippan, Overview on established and novel FIB based miniaturized mechanical testing using in-situ SEM, Int. J. Mat. Res. 100 (2009) 1074–1087.

[18] M. Legros, D.S. Gianola, C. Motz, Quantitative In Situ Mechanical Testing in Electron Microscopes, MRS Bull. 35 (2010) 354–360.

[19] D.S. Gianola, C. Eberl, Micro- and nanoscale tensile testing of materials, Jom. 61 (2009) 24–35.

[20] A.J. Harris, B.D. Beake, D.E.J. Armstrong, M.I. Davies, Development of High Temperature Nanoindentation Methodology and its Application in the Nanoindentation of Polycrystalline Tungsten in Vacuum to 950 °C, Exp. Mech. (2016) 1–12.

[21] B. Moser, J. Kuebler, H. Meinhard, W. Muster, J. Michler, Observation of instabilities during plastic deformation by in-situ SEM indentation experiments, Adv. Eng. Mater. 7 (2005) 388–392.

[22] B. Moser, K. Wasmer, L. Barbieri, J. Michler, Strength and fracture of Si micropillars: A new scanning electron microscopy-based micro-compression test, J. Mater. Res. 22 (2007) 1004–1011.

[23] J.M. Wheeler, R. Raghavan, J. Michler, In situ SEM indentation of a Zr-based bulk metallic glass at elevated temperatures, Mater. Sci. Eng. A. 528 (2011) 8750–8756.

[24] J.M. Wheeler, J. Michler, Elevated temperature, nano-mechanical testing in situ in the scanning electron microscope, Rev. Sci. Instrum. 84 (2013) 45103.

[25] V. Maier, A. Leitner, R. Pippan, D. Kiener, Thermally Activated Deformation Behavior of ufg-Au: Environmental Issues During Long-Term and High-Temperature Nanoindentation Testing, JOM. 67 (2015) 2934–2944.

[26] J.M. Wheeler, D.E.J. Armstrong, W. Heinz, R. Schwaiger, High temperature nanoindentation: The state of the art and future challenges, Curr. Opin. Solid State Mater. Sci. 19 (2015) 354–366.

[27] J.M. Wheeler, P. Brodard, J. Michler, Elevated temperature, in situ indentation with calibrated contact temperatures, Philos. Mag. 92 (2012) 3128–3141.

[28] S.-W. Lee, Y. Cheng, I. Ryu, J.R. Greer, Cold-temperature deformation of nano-sized tungsten and niobium as revealed by in-situ nano-mechanical experiments, Sci. China Technol. Sci. 57 (2014) 652–662.

[29] A.B. Hagen, C. Thaulow, Low temperature in-situ micro-compression testing of iron pillars, Mater. Sci. Eng. A. 678 (2016) 355–364.

[30] A.B. Hagen, B.D. Snartland, C. Thaulow, Temperature and orientation effects on the deformation mechanisms of α-Fe micropillars, Acta Mater. 129 (2017) 398–407.

[31] A. Lupinacci, J. Kacher, A. Eilenberg, A.A. Shapiro, P. Hosemann, A.M. Minor, Cryogenic in situ microcompression testing of Sn, Acta Mater. 78 (2014) 56–64.

[32] K. V. Rajulapati, M.M. Biener, J. Biener, A.M. Hodge, Temperature dependence of the plastic flow behavior of tantalum, Philos. Mag. Lett. 90 (2010) 35–42.

[33] V. Maier, A. Hohenwarter, R. Pippan, D. Kiener, Thermally activated deformation processes in body-centered cubic Cr - How microstructure influences strain-rate sensitivity, Scr. Mater. 106 (2015) 42–45.

[34] O. Torrents Abad, J.M. Wheeler, J. Michler, A.S. Schneider, E. Arzt, Temperature-dependent size effects on the strength of Ta and W micropillars, Acta Mater. 103 (2016) 483–494.

[35] J.M. Wheeler, C. Kirchlechner, J.S. Micha, J. Michler, D. Kiener, The effect of size on the strength of FCC metals at elevated temperatures: annealed copper, Philos. Mag. (2016) 1–17.

[36] J.M. Wheeler, C. Niederberger, C. Tessarek, S. Christiansen, J. Michler, Extraction of plasticity parameters of {GaN} with high temperature, in situ micro-compression, Int. J. Plast. 40 (2013) 140–151.

[37] Granta Design Limited, CES Edupack, (2016).

[38] S. Wurster, C. Motz, M. Jenko, R. Pippan, Micrometer-Sized Specimen Preparation Based on Ion Slicing Technique, Adv. Eng. Mater. 12 (2010) 61–64.

[39] S. Wurster, R. Treml, R. Fritz, M.W. Kapp, E.-M. Langs, M. Alfreider, C. Ruhs, P.J. Imrich, G. Felber, D. Kiener, Novel methods for the site specific preparation of micromechanical structures, Prakt. Met. Sonderband. 46 (2014) 27–36.

[40] R. Pippan, S. Scheriau, A. Taylor, M. Hafok, A. Hohenwarter, A. Bachmaier, Saturation of Fragmentation During Severe Plastic Deformation, Annu. Rev. Mater. Res. 40 (2010) 319–343.

[41] R.Z. Valiev, R.K. Islamgaliev, I. V Alexandrov, Bulk nanostructured materials from severe and plastic deformation, Prog. Mater. Sci. 45 (2000) 103–189.

[42] R. Fritz, D. Lutz, V. Maier-Kiener, D. Kiener, Interplay between Sample Size and Grain Size: Single Crystalline vs. Ultrafine-grained Chromium Micropillars, Mater. Sci. Eng. A. 674 (2016) 626–633.

[43] S. Wurster, C. Motz, R. Pippan, Characterization of the fracture toughness of micro-sized tungsten single crystal notched specimens, Philos. Mag. 92 (2012) 1803–1825.

[44] D. Kiener, W. Grosinger, G. Dehm, On the importance of sample compliance in uniaxial microtesting, Scripta. 60 (2009) 148–151.

[45] I. Sneddon, The relation between load and penetration in the axisymmetric Boussinesq Problem for a punch of arbitrary profile, Int. J. Engng Sci. 3 (1965) 47–57.

[46] ASTM International, ASTM Standard E399-09, West Conshokocken, PA, 2003.

[47] S. Wurster, C. Motz, R. Pippan, Notched-cantilever and –tensile testing on the micrometer scale – Effects of constraints on plasticity and fracture behaviour, in: Proc. 18th Eur. Conf. Fract., Dresden, 2010.

[48] ASTM International, ASTM Standard E813-89, West Conshokocken, PA, 2003.

[49] D.I. Bolef, J. De Klerk, Anomalies in the Elastic Constants and Thermal Expansion of Chromium Single Crystals, Phys. Rev. 129 (1963) 1063–1067.

[50] E.O. Hall, The Deformation and Ageing of Mild and Steel: III and Discussion of Results, Proc. Phys. Soc. B. 64 (1951) 747–753.

[51] N.J. Petch, The cleavage strength of polycrystals, J. Iron Steel Inst. 174 (1953) 25–28.

[52] C. Howard, R. Fritz, M. Alfreider, D. Kiener, P. Hosemann, The influence of microstructure on the cyclic deformation and damage of copper and an oxide dispersion strengthened steel studied via in-situ micro-beam bending, Mater. Sci. Eng. A. 687 (2017) 313–322.

[53] A. V Sameljuk, A.D. Vasilev, S.A. Firstov, Low temperature deformation and fracture behaviour of [100] and [110] chromium single crystals, Int. J. Refract. Met. Hard Mater. 14 (1996) 249–255.

[54] M.D. Uchic, D.M. Dimiduk, J.N. Florando, W.D. Nix, Sample Dimensions Influence Strength and Crystal Plasticity, Science (80-.). 305 (2004) 986–989.

[55] D. Wu, J. Zhang, J.C. Huang, H. Bei, T.G. Nieh, Grain-boundary strengthening in nanocrystalline chromium and the Hall-Petch coefficient of body-centered cubic metals, Scr. Mater. 68 (2013) 118–121.

[56] B. Sestak, A. Seeger, Gleitung und Verfestigung in kubisch-raumzentrierten Metallen und Legierungen, Zeitschrift Für Met. 69 (1978) 195–202.

[57] P. Gumbsch, Brittle fracture and the brittle-to-ductile transition of tungsten, J. Nucl. Mater. 323 (2003) 304–312.

[58] B. Gludovatz, S. Wurster, A. Hoffmann, R. Pippan, A study into the crack propagation resistance of pure tungsten, Eng. Fract. Mech. 100 (2013) 76–85.

[59] J. Riedle, P. Gumbsch, H.F. Fischmeister, V.G. Glebovsky, V.N. Semenov, Fracture studies of tungsten single crystals, Mater. Lett. 20 (1994) 311–317.

[60] C. Bohnert, S.M. Weygand, N.J. Schmitt, R. Schwaiger, O. Kraft, Orientation Dependence of the Fracture Behavior of Single-crystal Tungsten, Procedia Mater. Sci. 3 (2014) 479–484.

[61] C. Bohnert, N.J. Schmitt, S.M. Weygand, O. Kraft, R. Schwaiger, Fracture toughness characterization of single-crystalline tungsten using notched micro-cantilever specimens, Int. J. Plast. 81 (2016) 1–17.

[62] J. Skogsrud, C. Thaulow, Effect of crystallographic orientation on nanomechanical modelling of an iron single crystal cracked cantilever beam, Mater. Sci. Eng. A. 685 (2017) 274–283.

[63] A. Hohenwarter, S. Wurster, Deformation and fracture characteristics of ultrafine-grained vanadium, Mater. Sci. Eng. A. 650 (2016) 492–496.

[64] R. Pippan, A. Hohenwarter, The importance of fracture toughness in ultrafine and nanocrystalline bulk materials, Mater. Res. Lett. 4 (2016) 127–136.

[65] M. Faleschini, H. Kreuzer, D. Kiener, R. Pippan, Fracture toughness investigations of tungsten alloys and SPD tungsten alloys, J. Nucl. Mater. 367–370 (2007) 800–805.

[66] R. Wadsack, R. Pippan, B. Schedler, Chromium- a material for fusion technology, Fusion Eng. Des. 58--59 (2001) 743–748.

[67] R.W. Margevicius, J. Riedle, P. Gumbsch, Fracture toughness of polycrystalline tungsten under mode I and mixed mode I/II loading, Mater. Sci. Eng. A. 270 (1999) 197–209.

[68] D. Rupp, R. Mönig, P.A. Gruber, S.M. Weygand, Fracture toughness and microstructural characterization of polycrystalline rolled tungsten, Int. J. Refract. Met. Hard Mater. 28 (2010) 669–673.

[69] S. Kobayashi, S.M. Ohr, In situ fracture experiments in b.c.c. metals, Philos. Mag. A. 42 (1980) 763–772.

[70] V. Maier, C. Schunk, M. Göken, K. Durst, Microstructure-dependent deformation behaviour of bcc-metals - indentation size effect and strain rate sensitivity, Philos. Mag. 95 (2015) 1766–1779.

[71] Y. Harada, M. Ohmori, Ductile-brittle transition behavior of rolled chromium, J. Mater. Process. Technol. 153–154 (2004) 93–99.

[72] R. Wadsack, R. Pippan, B. Schedler, Structural refinement of chromium by severe plastic deformation, Fusion Eng. Des. 66–68 (2003) 265–269.

Publication D

Interface-dominated Strength Scaling Behaviour in Ultrafine-grained Tungsten Samples

R. Fritz[1], A. Leitner[1], V. Maier-Kiener[2], R. Pippan[3], D. Kiener[1]

Submitted to a SCI Journal

[1] Department Materials Physics, Montanuniversität Leoben, Leoben, Austria
[2] Department Physical Metallurgy & Materials Testing, Montanuniversität Leoben, Leoben, Austria
[3] Erich Schmid Institute of Materials Science, Austrian Academy of Science, Leoben, Austria

D - Abstract

The influence of microstructure on the strength scaling behaviour of ultrafine-grained W is investigated by scale-bridging experiments over four length scales. By performing macroscopic compression, nanoindentation and in-situ scanning electron microscope micro-compression tests, the plastically deformed volume was thoroughly reduced until a transition from bulk-like to single crystalline deformation behaviour was observed. Occurrent events in stress-strain curves and post-compression images were related to apparent deformation mechanisms commonly observed for polycrystalline bcc metals. Further, the small-scale deformation behaviour and the influence of interfaces and free surfaces are discussed and related to the single crystal situation. Additionally, thermally activated deformation mechanisms in W are identified and discussed based on rate- and temperature-dependent properties, such as strain-rate sensitivity and activation volume. The results demonstrate that the free surface in small volumes explicitly alters the strength scaling behaviour in ultrafine-grained W and that the formation of cracks and decohesion processes are only of minor importance. Indeed, dislocation mediated crystal plasticity remains dominant spanning all length-scales investigated.

D1 - Introduction

Small-scale testing techniques such as pillar compression experiments reveal novel insights into the strength scaling behaviour of confined volumes. Since Uchic *et al.* [1] reported a size effect [2] in focused ion beam (FIB) machined single crystalline (sxx) compression samples, ex-situ as well as in-situ pillar compression experiments inside scanning electron microscopes (SEM) increased in popularity [3-6]. In the last years, the strength scaling behaviour of sxx, face-centred cubic (fcc) [7-11] and body-centred cubic (bcc) [12-19] metals was extensively studied. Nowadays, it is established that the strength σ in such confined volumes scales with a power-law with the sample diameter as the base and n the strength scaling exponent ($\sim d^{-n}$). Typical n-values for fcc metals are ~0.6. The mechanisms responsible for such a scaling behaviour are interpreted based on a single-armed source model by Parthasarathy *et al.*, see [20]. More detailed mechanisms are discussed in [21]. Notably, the crystal orientation, or more precisely the number of active slip systems [22-24], as well as dislocation density

[25-27] additionally affect *n*. While fcc metals can be regarded as athermal [11], in bcc structures the strength scaling exponent is furthermore dependent on a thermal stress component, which limits the movement of screw dislocations via the kink-pair mechanism [28-30]. Metals such as W exhibit a high thermal stress component at room temperature (RT), evidenced by *n*-values of ~0.2 - 0.4 [8,12,15,19,23,30]. Contrarily, bcc metals with rather low melting points (T_m) such as Nb or Fe show reduced thermal stress components resulting in strength scaling exponents of 0.48 [30] and 0.59 [17], respectively. If thermal activation reaches ~$0.2 \cdot T_m$ [29], screw dislocations are not hindered by the Peierls potential anymore and propagate with the same velocity as edge dislocations. At this critical temperature (T_c), the strength scaling behaviour in bcc metals approaches towards the fcc value.

A variation of *n* is not only the result of intrinsic effects [7]. Beside varying thermal stress contributions, extrinsic effects [31], a preparation induced effect or FIB damage [32-34], or processing induced modifications [35] may alter the strength scaling behaviour and must be taken into account.

To comprehensively study the effects of individual interfaces, experiments spanning from the macroscopic to the microscopic regime are necessary. Testing macroscopic samples results in obtaining bulk properties. In fact, several tensile, compression and also simulation studies were conducted on sxx [36-41] as well as polycrystalline samples [42-46] where the interplay of intrinsic length-scales contributes to strengthening mechanisms in macroscopic volumes.

On the other hand, miniaturized testing techniques are necessary to investigate characteristic mechanisms, for example, interaction of dislocations with twin boundaries [47] or grain boundaries [45,48-50]. Dislocations can be trapped [51,52] within the small sample volume and pile-up on internal interfaces. However, it is still under debate how grain boundaries or general interfaces affect the strength scaling characteristics.

To contribute to this topic, in this work the influence of interfaces on the deformation and the strength scaling behaviour of ultrafine-grained (ufg) W is investigated by providing a constant grain size. The interplay of grain boundaries with confined volumes is investigated by thoroughly reducing the deformed volumes until an sxx state is achieved. Therefore, macroscopic compression, nanoindentation and in-situ pillar compression tests are performed at various temperatures and strain-rates.

By doing so, the influence of grain boundaries on the strength scaling exponent and the contribution of the thermal stress component are examined. Finally, acting deformation mechanisms are analysed in terms of strain-rate sensitivity (m) and activation volume (ν).

D2 - Materials and Methods

The sxx W was grown by electron beam zone melting [53] and examined previously micro- and macroscopically by Wurster *et al.* [54]. The crystal was aligned in either (100) or (110) orientation to test multiple slip orientations [36]. A lamella with ~1 mm thickness was cut using a diamond wire saw and subsequently ground and polished to remove plastically deformed surface layers.

A forged sheet of ultra-high purity W with an initial grain size of ~5 µm was provided by Plansee SE (Reutte, Austria). The as-received sample was cut by electron discharge machining (EDM, Brother HS-3100) to cylinders of 30 mm in diameter and 7 mm in height and subsequently deformed via high pressure torsion (HPT [55-59]) to achieve an ufg microstructure having mostly large angle grain boundaries. After 10 rotations at 600°C using a rotational speed of 0.2 rpm and a pressure of 4 GPa, an equivalent strain of ~7500% at a radius of 14 mm was imposed. A lamella as described in [60] and several rectangular-shaped macroscopic samples having final dimensions of $2 \cdot 2 \cdot 3$ mm³ were machined by EDM from a disk radius of ~14 mm in axial direction of the HPT disk to avoid strain gradients and hence varying grain sizes within the specimens. Prior to microstructural investigations, nanoindentation tests and macroscopic compression tests, the macroscopic samples were mechanically and electrolytically polished.

The grain size was determined using back-scattered electron (BSE) images and electron backscattered diffraction (EBSD) grain orientation maps using a high resolution SEM (Zeiss LEO 1525, Oberkochen, Germany).

Non-tapered rectangular pillars in the size range between 150 nm and 5 µm and with an aspect ratio (pillar height to diameter) of 3:1 were milled out of the fabricated lamella using a dual-beam SEM-FIB workstation (Zeiss LEO 1540 XP, Oberkochen, Germany) [60]. Pillar compression tests on samples larger than 1 µm were performed in-situ in an SEM (Zeiss LEO 982, Oberkochen, Germany) equipped with an UNAT-SEM indenter (Zwick GmbH & Co. KG, Ulm, Germany) [61,62]. Samples having

dimensions below 1 µm were tested in the SEM-FIB utilizing a Hysitron PI-85 Picoindenter (Bruker Nano Surfaces, Minneapolis, MN, USA). The indenters were equipped with conductive diamond flat punches obtained from Synton-MDP AG (Nidau, Switzerland) with diameters of ~8 µm and ~6 µm, respectively. All tests were performed at RT in displacement-controlled mode at constant displacement rates that were adapted to the individual pillar geometry to achieve a constant nominal strain-rate of $3 \cdot 10^{-3}$ s^{-1} in order to exclude strain-rate effects. Further corrections for sample sink-in [63] and machine stiffness [64] were taken into account.

Macroscopic compression tests were performed in air using a universal tensile testing unit (Zwick GmbH & Co. KG, Ulm, Germany) modified with a load reverse tool to a compression device. In order to measure thermally activated processes, tests were conducted at constant strain-rates between 10^{-2} and 10^{-4} s^{-1} for temperatures ranging between RT and 610°C. Loads were measured utilizing a 10 kN load cell and strains were calculated from recorded time and corresponding crosshead velocity. All compression samples were strained to ~20% engineering strain and engineering stresses were calculated using the top area of pillars and macroscopic samples before deformation.

Nanoindentation tests were performed using a Nanoindenter G200 (Keysight Technologies, USA) equipped with a continuous stiffness measurement (CSM) unit. The CSM frequency was set to 45 Hz and a harmonic displacement amplitude of 2 nm was superimposed for all tests. CSM was used to continuously record contact stiffness to check the Young's Modulus / displacement profile which is horizontal for mechanically isotropic materials. For RT testing, a three-sided diamond Berkovich pyramid, imposing ~8% plastic strain (MicroStar Technologies, Huntsville, USA), as well as a diamond Cube Corner indenter, imposing ~20% plastic strain (Synton-MDP AG, Nidau, Switzerland) [65,66] were utilised. Strain-rate controlled tests with a constant strain-rate of $5 \cdot 10^{-2}$ s^{-1} were conducted to compare to flow stress values obtained from uniaxial testing techniques. High temperature measurements were realized using a surface laser heating system with independent heating capacity of indenter tip and sample. Experiments were conducted at 100°C, 150°C, 200°C, 250°C and 300°C using a Berkovich pyramid tip made of sapphire (Synton-MDP AG, Nidau, Switzerland). Strain-rate jump tests [67] for displacement segments of 500 nm each and strain-rate levels of $5 \cdot 10^{-2}$ s^{-1}, 10^{-2} s^{-1}, $5 \cdot 10^{-3}$ s^{-1} (high temperature) and $5 \cdot 10^{-}$

^{2} s^{-1}, 5 · 10^{-3} s^{-1} and 10^{-3} s^{-1} (RT), respectively, were performed to investigate thermally activated processes. The maximum indentation depth for all indents was set to ~2500 nm. Machine stiffness and tip-shape calibrations were performed at RT according to the Oliver-Pharr method [68]. Further details about the heating setup are described in [69].

D3 - Results

The grain size of the HPT deformed W sample was determined using area equivalent circle diameters. The analysis resulted in average grain sizes of 530 ± 170 nm and 480 ± 230 nm for Figure 1a and b, respectively. In the BSE image, substructures and low angle grain boundaries were not accounted as boundaries thus resulting in a larger average grain size. Slightly elongated grains in shearing direction were observed, but no pronounced texture was evidenced. Moreover, grain boundaries with mostly large angle character (87.2%) were detected, as shown in Figure 1c. Here, neighbouring grains showing 15° misorientation or more are accounted as large angle GBs.

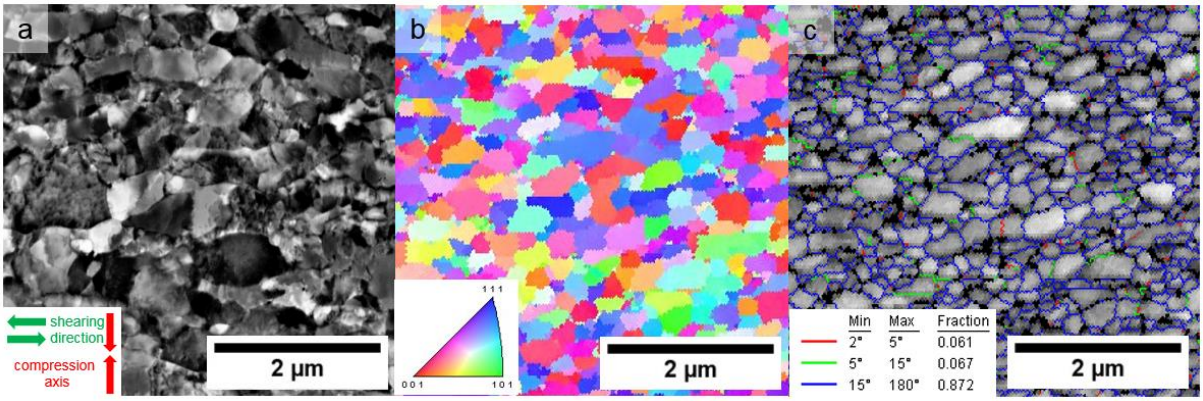

Figure 1: Microstructure of ufg W at a disc radius of 14 mm in axial direction. (a) BSE image, red arrows indicate the compression direction and green arrows the shearing direction during severe plastic deformation. (b) EBSD image of the respective microstructure and the corresponding inverse pole figure. (c) The majority of grain boundaries (87.2%) show large angle character.

The bulk hardness (*H*) of (110) oriented sxx and ufg W at RT was determined by nanoindentation using a Berkovich and a Cube Corner indenter. Corresponding load-displacement curves are shown in Figure 2a. The corresponding indentation sizes are 116.2 µm³ (Berkovich) and 13.3 µm³ (Cube Corner) for sxx W and 39.7 µm³

(Berkovich) and 14.6 µm³ (Cube Corner) for ufg W. Hardness values were converted to flow stresses using $H = \sigma \cdot C^*$ with the constraint factor $C^* = 2.8$ [66,70]. Bulk values of H were obtained by extrapolating the hardness profile to large displacements according to the Nix and Gao model [71], as shown in Figure 2b. Although the moduli of sxx W (393 GPa) and ufg W (402 GPa) show slight variations, they are well in the range of literature values of 380 - 420 GPa [72].

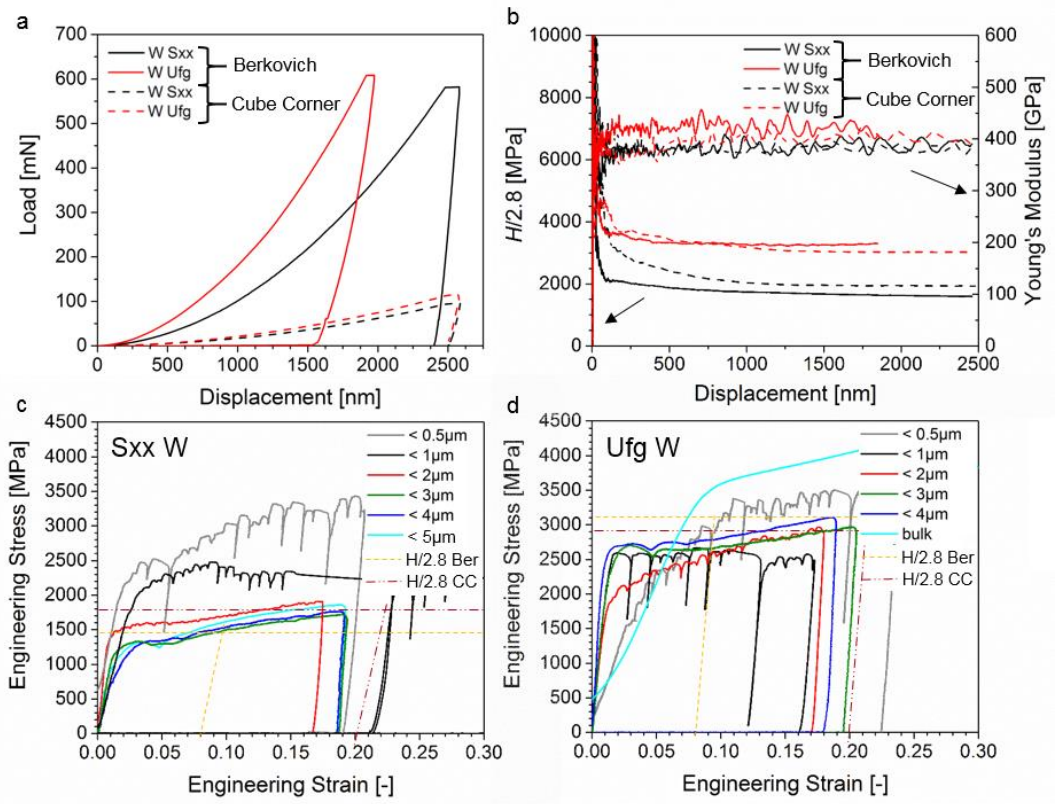

Figure 2: Multi- and uniaxial test data of sxx and ufg W determined using nanoindentation and compression tests. (a) Load-displacement curves obtained with Berkovich and Cube Corner indenters. (b) H/2.8 and Young's moduli vs. indentation depth to obtain bulk properties. (c, d) Exemplary engineering stress-strain curves of the respective sxx and ufg W with a large variety of sample sizes. See text for details.

Furthermore, flow stress values for sxx W resulted in 1470 MPa (Berkovich) and 1790 MPa (Cube Corner), while for ufg values of 3110 MPa (Berkovich) and 2930 MPa (Cube Corner) were obtained, which are in accordance with literature data [66].

Figure 2c and d present engineering stress-strain curves of (100) oriented sxx and ufg W. In both cases large samples show continuous flow curves. As the sample size decreases (below 3 µm), stress values in sxx W samples (Figure 2c) increase and

stochastic events such as load drops are observed more frequently. A contrary behaviour is observed for ufg W samples (Figure 2d), where flow stresses decrease with decreasing sample sizes. At sample diameters of ~3 µm, first serrations in the stress-strain curves are observed. Further decreasing the sample size leads to an apparent increase of flow stress values and pronounced load drops are detected, comparable to small sxx W samples.

Post compression SEM images of various ufg W samples are shown in Figure 3. In total 36 bulk samples each having a size of 2 · 2 · 3 mm³, as shown in Figure 3a, were tested from RT up to 610°C. At low temperatures and at every strain-rate tested, cracks developed during compression. Above 450°C, plastic deformation without crack initiation and propagation was observed. This behaviour is indicative for a rate- and grain size dependent brittle-to-ductile transition temperature (BDTT) [73,74]. Figure 3b and c show a residual Berkovich and a residual Cube Corner impression at RT, respectively. Figure 3d-i depict deformed ufg W pillars of various sizes. Larger pillars in Figure 3d and e show intercrystalline failure at grain boundaries, which is common for ufg W [75,76]. A side view and magnified details of Figure 3d are displayed in Figure 3h and i, respectively, indicated by the red coloured arrow and the rectangle. The white arrows indicate decohesion and failure at grain boundary triple points, which were also observed in residual imprints (Figure 3b and c). Figure 3f represents an ufg pillar where the sample size is approximately the grain size and in Figure 3g, the sample size was further reduced and sxx deformation behaviour was observed.

The plastic deformation behaviour of sxx and ufg W is also provided in the supplementary videos, where Video 1 represents the deformation behaviour of ~5 µm and ~0.3 µm sized sxx W pillars. Video 2 indicates the deformation behaviour of a ~3 µm, ~1.3 µm and a ~0.3 µm sized ufg W samples. In larger ufg pillars, the observation of cracks developing at grain boundary junctions should be noticed.

Figure 4 presents SEM images of etched (a) and FIB-prepared cross sections of deformed compression samples. Figure 4a shows a crack tip observed in macroscopic samples. The varying pattern (points and triangles) on individual grains indicate etch pits resulting from HPT deformation and refer to dislocations which align perpendicular to the etched surface (estimated dislocation density ~$1.65 \cdot 10^{14}$ m^{-2}). The major crack propagated on an intercrystalline path and additional small cracks are observable at grain boundary triple junctions, indicated by white arrows. The cross-sections of

Figure 4b-e indicate pillars exhibiting comparable deformation mechanisms as observed in bulk samples, even though the number of grains in the deformed volume is drastically reduced. Once the sample size is reduced to the average grain size (Figure 4f) or below (Figure 4g) the probability for crack nucleation at grain boundary junctions decreases. Pronounced plasticity is observed for the smallest pillar (300 nm, Figure 4g), sxx-like slip steps indicated by the green arrow are visible.

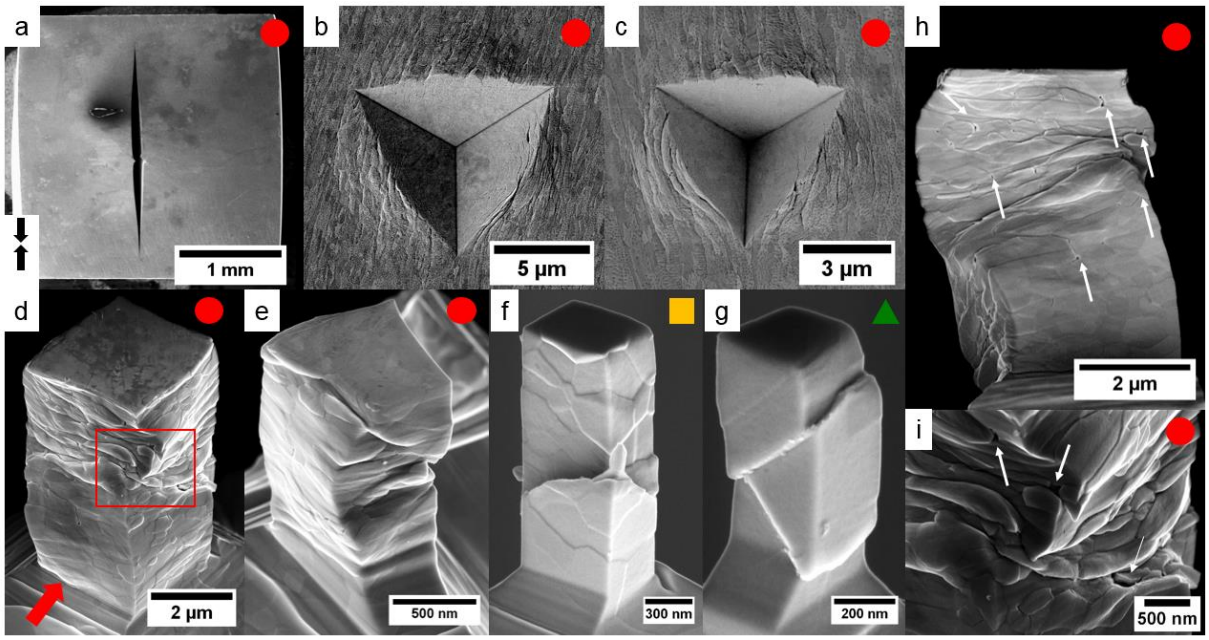

Figure 3: Post-compression SEM images of various ufg W samples. The sample size decreases accordingly to the presented alphabetic order. (a) Deformed bulk sample (strain-rate of $2 \cdot 10^{-3}$ s^{-1}) showing a large crack in compression direction (black arrows). (b) and (c) represent a Berkovich and a Cube Corner indent, respectively. Images (d) to (i) show deformed pillars. (h) and (i) show details, which were marked in (d) and white arrows indicate decohesion at grain boundary triple junctions. Coloured symbols refer to different deformation regimes.

D4 - Discussion

Before comparing multi- and uniaxial stress data, some considerations should be made. Nanoindentation with self-similar pyramidal tips results in multiaxial stress-states underneath the indent, accompanied by multiple slip events. To facilitate comparison with uniaxial test data, the (100) orientation was chosen as a multiple slip orientation for uniaxial compression tests. Secondly, the choice of an appropriate value for C^* to convert hardness into flow stresses influences validation of the uniaxial test data. However, if C^* is considered to be in the range of 2.5 - 3, rather than 2.8 used in

Figure 2, the change of stress values of ~10% would only insignificantly affect present results. Thirdly, the Young's modulus to hardness (*E*/*H*) ratio [77] and the rate-dependence of the tested material [78] might affect the load response of the indenter, resulting in conceivable errors. The *E*/*H* ratio for the investigated ufg W is ~130, therefore a possible phase shift of the indenter signal should be only of minor influence. To eliminate influences from the rate-dependence of the material, the experiments were conducted at the same constant strain-rates.

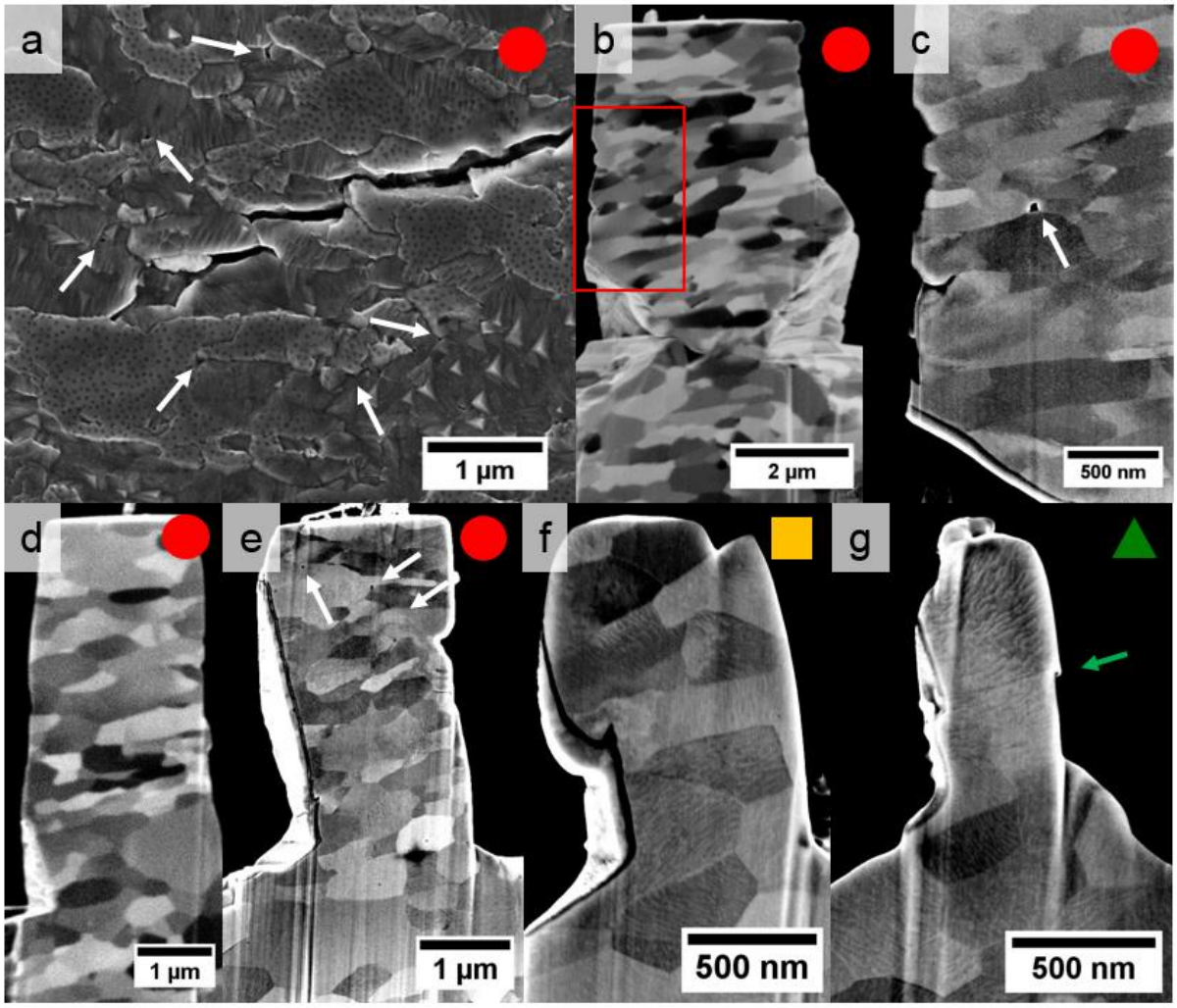

Figure 4: Cross sections of uniaxial deformed compression samples. (a) Crack tip observed in a macroscopic sample, indicating intercrystalline fracture. Pillar cross sections of 3 µm (b), 2 µm (d), 1.3 µm (e), 0.7 µm (f) and 0.3 µm (g) demonstrate the decreasing number of grains within individual samples. (c) presents a magnified inset of (b) indicated by the red rectangle. White arrows indicate cracks and decohesions at triple points of grain boundaries, while the green arrow marks a slip step. Coloured symbols refer to different deformation regimes. Please note that the cross sectional FIB cuts are slightly inclined compared to the pillar compression direction.

Furthermore, the plastically deformed volumes vary with the indenter geometry and mechanical properties [79,80], which is apparent in the load-displacement data in Figure 2a. The load limit of the nanoindentation device was reached for the Berkovich indent in ufg W (Figure 2a, solid red line) and therefore the maximum indentation depth is lower. In Figure 2b, a cross-over of the hardness signals of the Berkovich and the Cube Corner indent for ufg W is observed. This behaviour is related to the comparatively high strain during indentation with a Cube Corner indenter. Here, more surface grains are affected during Cube Corner indentation, which might contribute to an apparent strength decrease. Relatively seen, the formation of cracks and decohesion at grain boundaries additionally alter hardness values, displaying lower stress values for the Cube Corner indent. Lastly, it should be noted that in terms of nanoindentation the induced representative strain will depend on the apex angle of the used tip and varying capabilities of strain hardening are examined, which affects the stress level [66]. However, as long as the contact stiffness is properly accounted for (indicated by horizontal hardness and Young's modulus values in Figure 2b) the test can be considered valid.

The gap in flow stress values between sxx and ufg W results from microstructural refinement according to Hall and Petch [81,82]. Estimation of a yield stress value using a friction stress of $\tau^* = 345$ MPa [8], a mean grain size of 480 ± 230 nm and a Hall-Petch coefficient of 1.86 $MPam^{-1/2}$ [66] results in ~3000 ± 700 MPa, in agreement with ufg W bulk data obtained from macroscopic compression tests and nanoindentation data (Figure 2d). However, the elastic loading stiffness of the bulk sample is reduced in Figure 2d and not comparable with pillar compression experiments. Alignment of bulk samples was hindered due to lower stiffness of the compression equipment, resulting in a sample misalignment of ~1°. The displacement of the bulk sample was measured at the machine crosshead, and only approximated strains are given for the bulk sample.

To discuss the observed deformation behaviour over several length scales, the flow stress is plotted against the plastically deformed volume of individual experiments in Figure 5. For uniaxial compression tests, the plastically deformed volume is defined by the sample base area and height. Considering the different indentations, a simplified hemispheric plastic zone after penetration to maximum displacement was taken into account. Stresses at 8% plastic strain were chosen to allow comparison with Berkovich

nanoindentation data and to include occurrent strain hardening. Pillar compression and nanoindentation data of sxx W is indicated by black dots and a black triangles, respectively. The black guideline through sxx W data demonstrates its strength scaling behaviour, which is ~0.21 ± 0.02 for the (100) orientation. The ufg W data in Figure 5 is separated into three different regimes. Red, orange and green symbols (also used in Figures 2 and 3) indicate bulk behaviour, a transition regime where the sample size is in the order of the grain size, and ufg W pillars that deform alike sxx W pillars, respectively. Error bars in Figure 5 result from the out-of-contact noise of the indenter load signal and uncertainties in determining pillar cross sections to compute stress values. As previously shown in Figure 2d, ufg bulk W samples reveal the highest flow stress levels. By decreasing the plastically deformed volume, flow stress values begin to decrease until the transition regime in Figure 5 is reached. Here, pillars deform without crack initiation, and upon further reducing the sample dimension sxx deformation behaviour is evidenced. Decreasing flow stress values, however, are explained by an increasing importance of free surfaces in decreasing sample volumes.

In ~500 nm sized grains, dislocation debris developed from the initial HPT deformation process remains in the grain interior as evident from the contrast variation within grains in the BSE micrograph shown in Figure 1a. During plastic deformation, dislocation sources in the grains will operate and emitted dislocations that pile-up at grain boundaries within the sample volume [76,83]. In grains located at free surfaces, dislocation debris and generated dislocations exit the pillar surface which lead to a decreased strength. With decreasing sample size the relative fraction of surface grains notably rises [84,85], hence the stress values decrease until the sample size approaches the grain size and source-controlled strengthening [20] dominates the deformation. Notably, the point of intersection of the drawn guidelines of sxx and ufg W in Figure 5 correlates well with the grain size of the present sample.

Comparable experiments were conducted on ufg Cr containing mostly large angle GBs, and results were reported in [45]. There, a continuous increase of flow stress was observed by decreasing the sample size. However, the grain size reported for ufg Cr was ~160 nm. Within such small structures, GBs act as sinks and sources for dislocations [86] and the grain interior contains only a very limited number of dislocations [87]. In such a situation, grains located at the free surface remain stronger and lead to a scaling behaviour where smaller is stronger. In both cases near-surface

grains are smaller in size compared to internal grains due to FIB machining, which seems to be of minor influence for the observed behaviour.

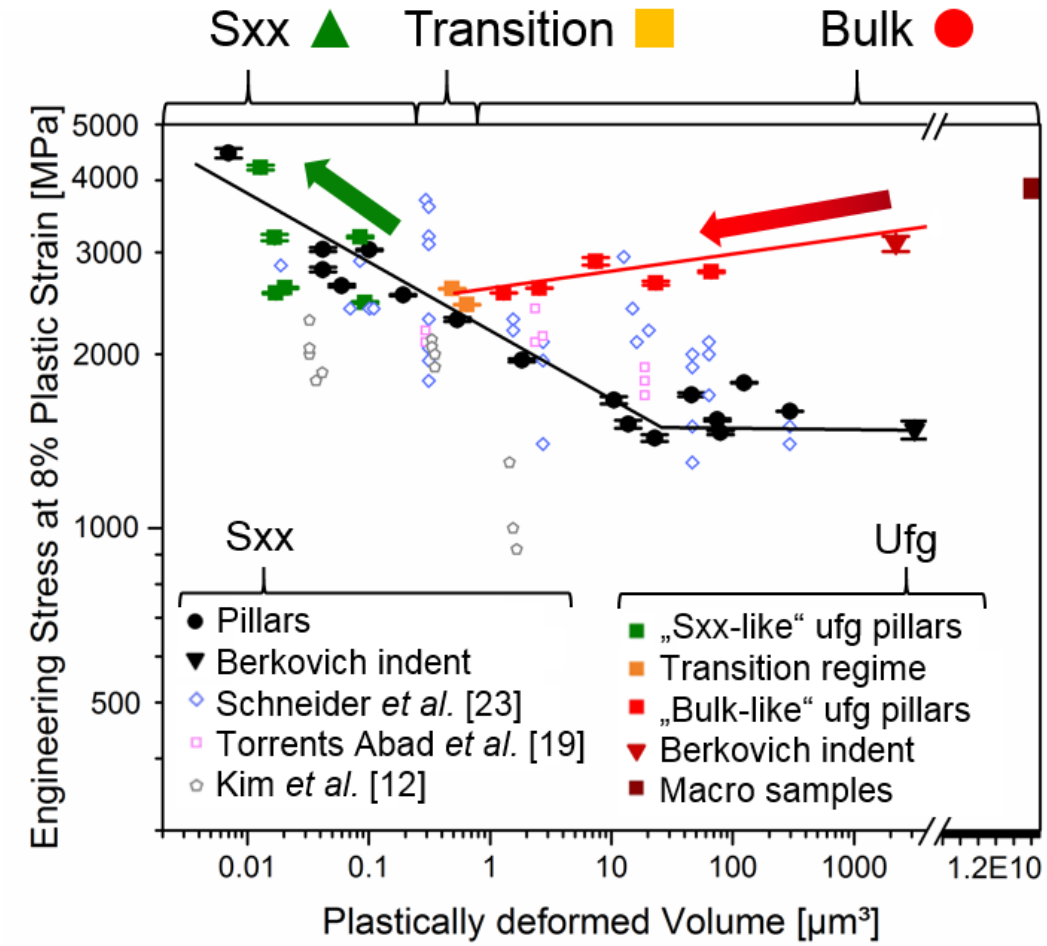

Figure 5: Engineering stress at 8% plastic strain vs. plastically deformed volume of tested sxx and ufg W. Filled symbols indicate data from this work, while open symbols are literature data, respectively. See text for more details.

Open symbols in Figure 5 indicate literature data of (100) oriented sxx W. Only small variations in scaling behaviour are found and summarized in Figure 6a by comparing *n*-values from close to the yield point up to 10% plastic strain. Our data is indicative for a constant strength scaling behaviour with strain, implying that the present deformation mechanism does not change during deformation. Small variations are attributed to alignment uncertainties at low strains and serrated flow at increased strain levels. Indeed, *n*-values ranging between 0.2 - 0.4 were reported in literature [8,12,15,19,23,28]. Our data is in close agreement to Schneider *et al.* [23,28], while the differences to other works could be explained by dissimilar strain-rates, a varying

impurity content or different initial dislocation densities within the samples used in those studies [21].

Dislocations in ufg W form substructures and pile-up at grain boundaries in the sample interior and therefore might change the deformation behaviour [88]. Indeed, a comparison of strain hardening rates (Θ) of differently sized ufg and sxx samples, shown in Figure 6b, demonstrates individual pile-up situations. Here, strain hardening rates were calculated from engineering stress-strain curves using a tangent approach. Bulk-like ufg pillars show comparable Θ as observed for macroscopic samples. However, once the sample size is reduced to the order of the grain size, reduced strain hardening behaviour indicates sxx-like deformation behaviour, dislocations can easily exit on the pillar surface.

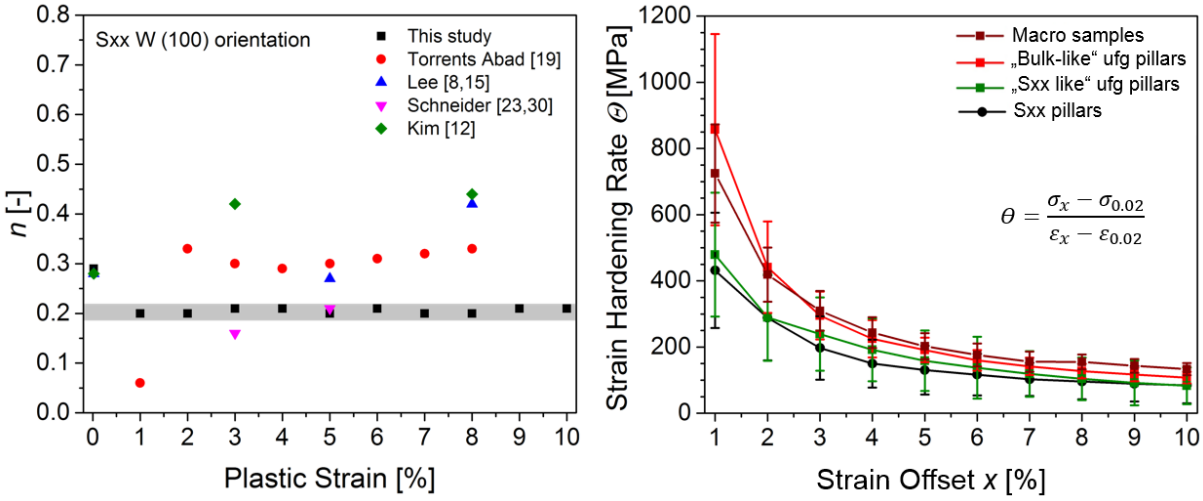

Figure 6: (a) Strength scaling exponent *n* plotted against plastic strain and comparison with literature data. (b) Strain hardening rates Θ obtained from sxx and ufg W using a tangent approach (inset). Clear differences in Θ between bulk-like configurations and single crystalline situations are evidenced.

To relate the observed behaviour to occurring deformation mechanisms and to estimate a possible contribution of decohesion, failure, or grain boundary sliding [89,90], plastic deformation can be related to intrinsic mechanisms in terms of strain-rate sensitivity (m) and activation volume (ν) [28,91]. For sxx and polycrystalline fcc metals such as Ni, Al or Cu, strain-rate effects were investigated, for example, in [92-94]. Prevailing deformation mechanisms in bcc metals such as V, W, Mo, Ta and Cr, were reported by Wei *et al.* [95,96], Zhou *et al.* [97], Wu *et al.* [86], Maier *et al.* [98,99] and Fritz *et al.* [100].

Fritz *et al.* [100] recently obtained thermally activated deformation behaviour over a wide range of temperatures using several testing techniques on sxx Cr and ufg Cr. Comparable tests on the same length-scales were conducted within this work on W, and the resultant *m*- and ν-values as a function of a relative testing temperature (T_{test}/T_c) are plotted in Figure 7a and b, respectively, to compare variable bcc metals with different thermal stress components at RT. The critical temperatures (T_c) for W and Cr used in Figure 7 are 800K [39] and 430K [29], respectively. Low temperature data on Cr from RT down to liquid nitrogen was additionally added from [101]. The W data of [39] was not added, as stress relaxation tests were utilized to obtain *m*-values. However, a comparable trend was observed for sxx W.

The coloured arrows in Figure 7a and b represent the trend of the rate-dependent properties in bcc metals. They reveal that comparable mechanisms dominate in sxx and ufg W and Cr, respectively. Importantly, in the Cr study [100] no cracking was present. This allows us to exclude fracture and thus embrittlement of GBs via segregation of interstitial atoms [102] as a dominant influencing mechanism. Moreover, the Cr data enlarges the discussed range of relative temperatures. At low relative temperatures *m*-values for sxx Cr and W are ~0.02. First, an increase of *m* is displayed until peak *m*-values of ~0.07 are reached at T_{test}/T_c = 0.65. A comparable trend for low temperature deformation of sxx W, Nb, V, and Ta was found by Brunner and Glebovsky [39] and Christian and Masters [103] and is explained by the thermally activated interaction of kink pairs with interstitial atoms. Approaching and overcoming T_c, thermal activation eases the movement of kink pairs until *m*-values in the order of 10^{-3} are reached, as common for low Peierls potential materials such as fcc metals. Contrarily to that, *m*-values for ufg counterparts slightly decrease from low temperatures until T_c, followed by a continuous increase up to a relative temperature of 1.6.

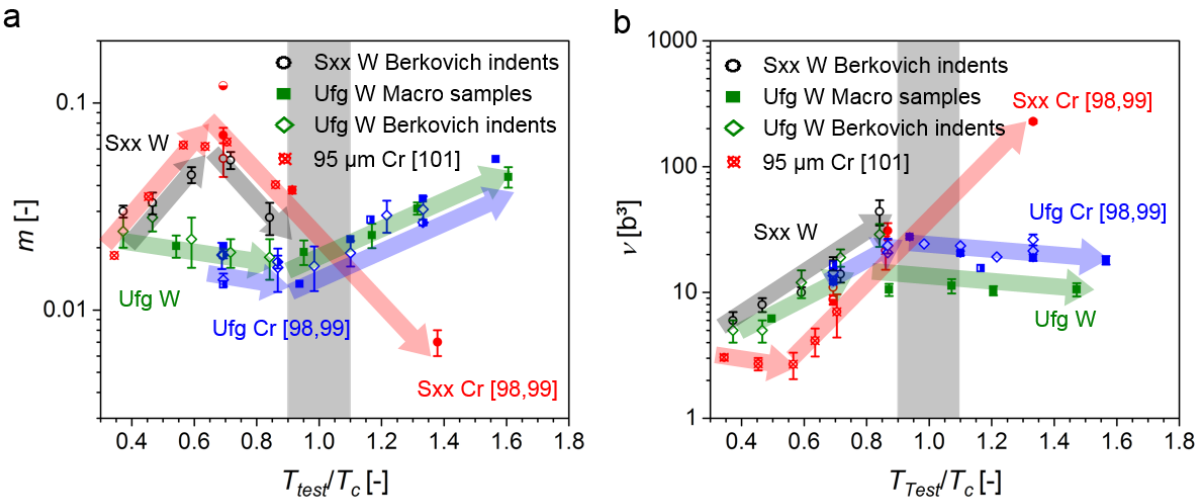

Figure 7: Evolution of strain-rate sensitivity m (a) and activation volume ν (b) with relative temperature for W and Cr. Cr data was taken with permission from [99] and [101]. Coloured arrows are trend lines. See text for details.

The deformation mechanisms based on the varying microstructure for the different bcc metals are indicated in Figure 7b, where the corresponding ν-values are plotted vs. T_{test}/T_c. To compare activation volumes, they are normalized by the Burgers vector of the respective metal (b = 2.741 · 10^{-10} m for W) and expressed in multiples of b^3. At low temperatures, ν-values of 4 - 7 b^3 were calculated for sxx W and Cr using the common equations described in [95]. Those quantities are attributed to the kink pair mechanism, which is active in bcc metals at low temperatures [29]. However, ν seems to remain constant in sxx Cr until T_{test} = 0.55 · T_c. Here, thermal activation of kinks might be hindered by interstitial atoms. This idea is verified by a pronounced yield strength observed in tensile stress-strain data [101], which was the base for the calculated activation volumes. As stated before, the same trends were found for sxx W, Nb, V and Ta in [39,103] and related to interaction of kinks with impurities. Additionally, m- and ν-values from [101] were calculated at the lower yield point, while nanoindentation data and test data from compression experiments were evaluated at ~8% plastic strain. By further increasing the temperature, the impurities are no effective obstacle anymore and movement of kink pairs is eased due to thermal activation, indicated by an increase of the activation volume. Overcoming T_c for the sxx case gives ν-values of ~200 b^3, indicative for dislocation-dislocation interaction, a common mechanism observed in fcc metals.

In ufg W and ufg Cr the activation volume increases at relative low temperatures comparably to the sxx states, indicating again a rate-limiting step based on the propagation of kink-pairs. However, upon passing T_c, ν-values remain rather constant at ~20 b^3. This behaviour is indicative for dislocation-grain boundary interactions, as previously reported for ufg Cr. Thus, the comparison to Cr in Figure 7 demonstrates dislocation mediated plasticity as the dominant deformation mechanism in sxx and ufg W, while crack formation in ufg W seems to be of minor influence on the underlying plasticity mechanisms.

D5 - Conclusion

Interface-dominated strength scaling behaviour in ultrafine-grained W was studied to investigate the interaction of grain boundaries with dislocations in bcc crystals. As a result of increasing importance of free surfaces, dislocations in near-surface grains exit the pillar surface without substructure formation and therefore the grains show decreased strength, while dislocations pile-up in inner grains. By reducing the plastically deformed volumes, the increasing number of near-surface grains leads to a gradual reduction of flow stress values until the sample size reaches the order of the grain size. There, after passing a transition regime, single crystalline slip in individual grains was activated even in ufg pillars. Moreover, the influence of decohesion at grain boundary triple points on thermally activated processes was examined and compared to ultrafine-grained Cr where no cracking occured. In both materials interfaces contribute to the deformation behaviour in terms of dislocation-grain boundary interactions and no noticeable influence can be attributed to crack nucleation and decohesion processes. This deformation results in constant activation volumes at elevated temperature, while at low temperatures the propagation of double-kinks remains the rate-limiting deformation mechanism.

D6 - Appendix: Supplementary Material

The supplementary videos of publication D are included digitally on the storage medium located at the end of the thesis.

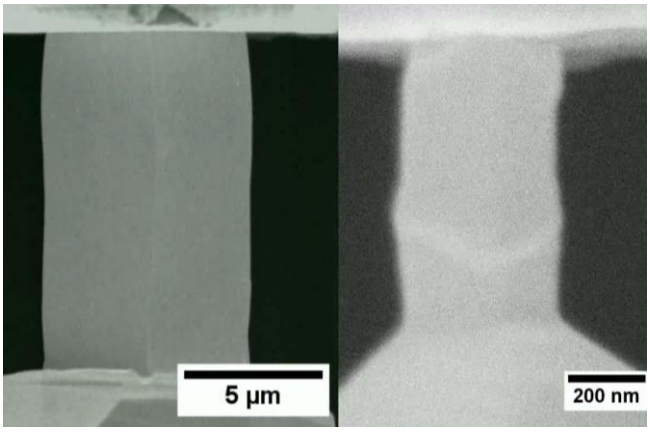

Video1: In-situ SEM compression test of two sxx W pillars. The sample diameters are ~5 µm (left) and 0.3 µm (right).

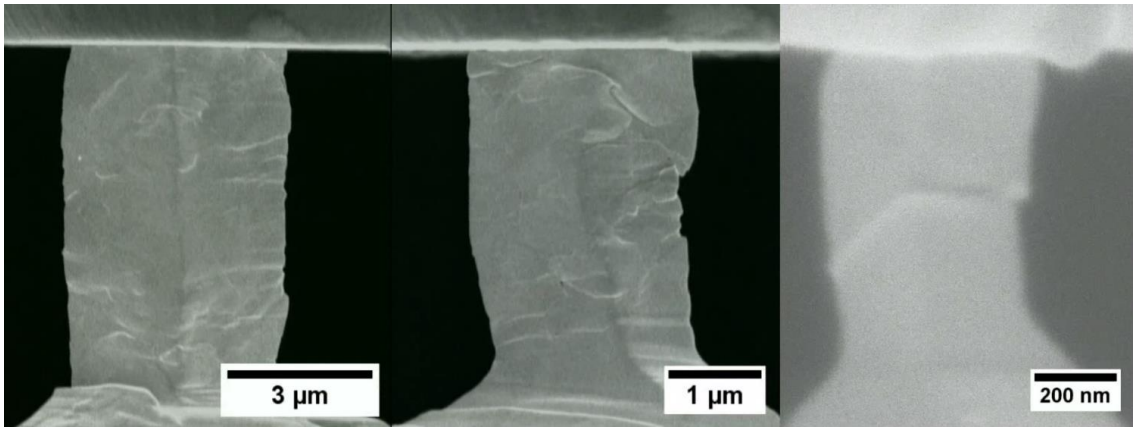

Video2: In-situ SEM compression test of three ufg W pillars. The sample diameters are ~3 µm, ~1.3 µm and a ~0.3 µm (from left to right). A transition in deformation behaviour from bulk to single-crystalline-like is illustrated.

D - References

[1] M.D. Uchic, D.M. Dimiduk, J.N. Florando, W.D. Nix, Sample Dimensions Influence Strength and Crystal Plasticity, Science 305 (2004) 986–989.

[2] O. Kraft, P.A. Gruber, R. Mönig, D. Weygand, Plasticity in Confined Dimensions, Annu. Rev. Mater. Res. 40 (2010) 293–317.

[3] D. Kiener, C. Motz, T. Schöberl, M. Jenko, G. Dehm, Determination of Mechanical Properties of Copper at the Micron Scale, Adv. Eng. Mater. 8 (2006) 1119–1125.

[4] D. Kiener, C. Motz, G. Dehm, Micro-compression testing: A critical discussion of experimental constraints, Mater. Sci. Eng. A. 505 (2009) 79–87.

[5] M. Legros, D.S. Gianola, C. Motz, Quantitative In Situ Mechanical Testing in Electron Microscopes, MRS Bull. 35 (2010) 354–360.

[6] D.S. Gianola, C. Eberl, Micro- and nanoscale tensile testing of materials, Jom. 61 (2009) 24–35.

[7] J.R. Greer, J.T.M. De Hosson, Plasticity in small-sized metallic systems: Intrinsic versus extrinsic size effect, Prog. Mater. Sci. 56 (2011) 654–724.

[8] S.-W. Lee, W.D. Nix, Size dependence of the yield strength of fcc and bcc metallic micropillars with diameters of a few micrometers, Philos. Mag. 92 (2012) 1238–1260.

[9] Z.-W. Shan, R.K. Mishra, S.A. Syed Asif, O.L. Warren, A.M. Minor, Mechanical annealing and source-limited deformation in submicrometre-diameter Ni crystals, Nat. Mater. 7 (2007) 115–119.

[10] C. Zhou, I.J. Beyerlein, R. LeSar, Plastic deformation mechanisms of fcc single crystals at small scales, Acta Mater. 59 (2011) 7673–7682.

[11] J.M. Wheeler, C. Kirchlechner, J.S. Micha, J. Michler, D. Kiener, The effect of size on the strength of FCC metals at elevated temperatures: annealed copper, Philos. Mag. (2016) 1–17.

[12] J.-Y. Kim, D. Jang, J.R. Greer, Tensile and compressive behavior of tungsten, molybdenum, tantalum and niobium at the nanoscale, Acta Mater. 58 (2010) 2355–2363.

[13] D. Kaufmann, R. Mönig, C.A. Volkert, O. Kraft, Size dependent mechanical behaviour of tantalum, Int. J. Plast. 27 (2011) 470–478.

[14] A.S. Schneider, C.P. Frick, E. Arzt, W.J. Clegg, S. Korte, Influence of test temperature on the size effect in molybdenum small-scale compression pillars,

Philos. Mag. Lett. 93 (2013) 331–338.

[15] S.-W. Lee, Y. Cheng, I. Ryu, J.R. Greer, Cold-temperature deformation of nano-sized tungsten and niobium as revealed by in-situ nano-mechanical experiments, Sci. China Technol. Sci. 57 (2014) 652–662.

[16] A.B. Hagen, C. Thaulow, Low temperature in-situ micro-compression testing of iron pillars, Mater. Sci. Eng. A. 678 (2016) 355–364.

[17] B.R.S. Rogne, C. Thaulow, Strengthening mechanisms of iron micropillars, Philos. Mag. (2014) 1–15.

[18] S.M. Han, T. Bozorg-Grayeli, J.R. Groves, W.D. Nix, Size effects on strength and plasticity of vanadium nanopillars, Scr. Mater. 63 (2010) 1153–1156.

[19] O. Torrents Abad, J.M. Wheeler, J. Michler, A.S. Schneider, E. Arzt, Temperature-dependent size effects on the strength of Ta and W micropillars, Acta Mater. 103 (2016) 483–494.

[20] T.A. Parthasarathy, S.I. Rao, D.M. Dimiduk, M.D. Uchic, D.R. Trinkle, Contribution to size effect of yield strength from the stochastics of dislocation source lengths in finite samples, Scr. Mater. 56 (2007) 313–316.

[21] J.A. El-Awady, Unravelling the physics of size-dependent dislocation-mediated plasticity, Nat Comms. 6 (2015) 5926.

[22] A.S. Schneider, B.G. Clark, E. Arzt, C.P. Frick, P.A. Gruber, Effect of orientation and loading rate on compression behavior of small-scale Mo pillars, Mater. Sci. Eng. A. 508 (2009) 241–246.

[23] A.S. Schneider, C.P. Frick, B.G. Clark, P.A. Gruber, E. Arzt, Influence of orientation on the size effect in bcc pillars with different critical temperatures, Mater. Sci. Eng. A. 528 (2011) 1540–1547.

[24] B.R.S. Rogne, C. Thaulow, Effect of crystal orientation on the strengthening of iron micro pillars, Mater. Sci. Eng. A. 621 (2015) 133–142.

[25] H. Bei, S. Shim, G.M. Pharr, E.P. George, Effects of pre-strain on the compressive stress-strain response of Mo-alloy single-crystal micropillars, Acta Mater. 56 (2008) 4762–4770.

[26] A.S. Schneider, D. Kiener, C.M. Yakacki, H.J. Maier, P.A. Gruber, N. Tamura, M. Kunz, A.M. Minor, C.P. Frick, Influence of bulk pre-straining on the size effect in nickel compression pillars, Mater. Sci. Eng. A. 559 (2013) 147–158.

[27] J.A. El-Awady, M.D. Uchic, P.A. Shade, S.-L. Kim, S.I. Rao, D.M. Dimiduk, C.

Woodward, Pre-straining effects on the power-law scaling of size-dependent strengthening in Ni single crystals, Scr. Mater. 68 (2013) 207–210.

[28] H. Conrad, Thermally activated deformation of metals, J. Met. (1964) 582–588.

[29] B. Sestak, A. Seeger, Gleitung und Verfestigung in kubisch-raumzentrierten Metallen und Legierungen, Zeitschrift Für Met. 69 (1978) 195–202.

[30] A.S. Schneider, D. Kaufmann, B.G. Clark, C.P. Frick, P.A. Gruber, R. Mönig, O. Kraft, E. Arzt, Correlation between Critical Temperature and Strength of Small-Scale bcc Pillars, Phys. Rev. Lett. 103 (2009) 105501/1-4.

[31] J.Y. Zhang, X. Liang, P. Zhang, K. Wu, G. Liu, J. Sun, Emergence of external size effects in the bulk-scale polycrystal to small-scale single-crystal transition: A maximum in the strength and strain-rate sensitivity of multicrystalline Cu micropillars, Acta Mater. 66 (2014) 302–316.

[32] Y. Xiao, J. Wehrs, H. Ma, T. Al-Samman, S. Korte-Kerzel, M. Göken, J. Michler, R. Spolenak, J.M. Wheeler, Investigation of the deformation behavior of aluminum micropillars produced by focused ion beam machining using Ga and Xe ions, Scr. Mater. 127 (2017).

[33] A.T. Jennings, M.J. Burek, J.R. Greer, Microstructure versus Size and Mechanical Properties of Electroplated and Single Crystalline Cu Nanopillars, PRL. 104 (2010) 135503.

[34] D. Kiener, C. Motz, M. Rester, M. Jenko, G. Dehm, FIB damage of Cu and possible consequences for miniaturized mechanical tests, Mater. Sci. Eng. A. 459 (2007) 262–272.

[35] P.J.M. Janssen, J.P.M. Hoefnagels, T.H. de Keijser, M.G.D. Geers, Processing induced size effects in plastic yielding upon miniaturisation, J. Mech. Phys. Solids. 56 (2008) 2687–2706.

[36] A.S. Argon, S.R. Maloof, Plastic deformation of tungsten single crystals at low temperatures, Acta Metall. 14 (1966) 1449–1462.

[37] D. Brunner, V. Glebovsky, The plastic properties of high-purity W single crystals, Mater. Lett. 42 (2000) 290–296.

[38] D. Brunner, Comparison of Flow Stress Measurements on high purity tungsten single crystals with the kink pair theory, JIM, Mater. Trans. 41 (2000) 152–160.

[39] D. Brunner, V. Glebovsky, Analysis of flow-stress measurements of high purity tungsten single crystals, Mater. Lett. 44 (2000) 144–152.

[40] D. Brunner, Temperature dependence of the plastic flow of high-purity tungsten single crystals, Int. J. Mater. Res. 101 (2010) 1003–1013.

[41] D. Cereceda, M. Diehl, F. Roters, D. Raabe, J.M. Perlado, J. Marian, Unraveling the temperature dependence of the yield strength in single-crystal tungsten using atomistically-informed crystal plasticity calculations, Int. J. Plast. 78 (2016) 242–265.

[42] Q. Wei, T. Jiao, K.T. Ramesh, E. Ma, L.J. Kecskes, L. Magness, R. Dowding, V. Kazykhanov, R.Z. Valiev, Mechanical behavior and dynamic failure of high-strength ultrafine grained tungsten under uniaxial compression, Acta Mater. 54 (2005) 77–87.

[43] Z. Li, C. Hou, M. Huang, C. Ouyang, Strengthening mechanism in micro-polycrystals with penetrable grain boundaries by discrete dislocation dynamics simulation and Hall-Petch effect, Comput. Mater. Sci. 46 (2009) 1124–1134.

[44] S. Saha, M.A. Motalab, M. Mahboob, Investigation on mechanical properties of polycrystalline W nanowire, Comput. Mater. Sci. 136 (2017) 52–59.

[45] R. Fritz, D. Lutz, V. Maier-Kiener, D. Kiener, Interplay between Sample Size and Grain Size: Single Crystalline vs. Ultrafine-grained Chromium Micropillars, Mater. Sci. Eng. A. 674 (2016) 626–633.

[46] S. Schreijäg, D. Kaufmann, M. Wenk, O. Kraft, R. Mönig, Size and microstructural effects in the mechanical response of alpha-Fe and low alloyed steel, Acta Mater. 97 (2015) 94–104.

[47] P.J. Imrich, C. Kirchlechner, D. Kiener, G. Dehm, In Situ TEM Microcompression of Single and Bicrystalline Samples: Insights and Limitations, Jom. 67 (2015) 1704–1712.

[48] N. Kheradmand, H. Vehoff, A. Barnoush, An insight into the role of the grain boundary in plastic deformation by means of a bicrystalline pillar compression test and atomistic simulation, Acta Mater. 61 (2013) 7454–7465.

[49] N. V Malyar, G. Dehm, C. Kirchlechner, Strain rate dependence of the slip transfer through a penetrable high angle grain boundary in copper, Scr. Mater. 138 (2017) 88–91.

[50] N. V Malyar, J.S. Micha, G. Dehm, C. Kirchlechner, Size effect in bi-crystalline micropillars with a penetrable high angle grain boundary, Acta Mater. 129 (2017) 312–320.

[51] J.A. El-Awady, S.I. Rao, C. Woodward, D.M. Dimiduk, M.D. Uchic, Trapping and escape of dislocations in micro-crystals with external and internal barriers, Int. J. Plast. 27 (2011) 372–387.

[52] K.S. Ng, A.H.W. Ngan, Effects of trapping dislocations within small crystals on their deformation behavior, Acta Mater. 57 (2009) 4902–4910.

[53] V.G. Glebovsky, V.N. Semenov, V. V Lomeyko, Influence of the crystallization conditions on the structural perfection of Mo and W single crystals, J. Cryst. Growth. 87 (1988) 142–150.

[54] S. Wurster, C. Motz, R. Pippan, Characterization of the fracture toughness of micro-sized tungsten single crystal notched specimens, Philos. Mag. 92 (2012) 1803–1825.

[55] R. Pippan, S. Scheriau, A. Taylor, M. Hafok, A. Hohenwarter, A. Bachmaier, Saturation of Fragmentation During Severe Plastic Deformation, Annu. Rev. Mater. Res. 40 (2010) 319–343.

[56] R.Z. Valiev, R.K. Islamgaliev, I. V Alexandrov, Bulk nanostructured materials from severe and plastic deformation, Prog. Mater. Sci. 45 (2000) 103–189.

[57] A. V Ganeev, R.K. Islamgaliev, R.Z. Valiev, Refinement of tungsten microstructure upon severe plastic deformation, Phys. Met. Metallogr. 115 (2014) 139–145.

[58] L.J. Kecskes, K.C. Cho, R.J. Dowding, B.E. Schuster, R.Z. Valiev, Q. Wei, Grain size engineering of bcc refractory metals: Top-down and bottom-up-Application to tungsten, Mater. Sci. Eng. A. 467 (2007) 33–43.

[59] Q. Wei, H. Zhang, B.E. Schuster, K.T. Ramesh, R.Z. Valiev, L.J. Kecskes, R. Dowding, L. Magness, K. Cho, Microstructure and mechanical properties of super-strong nanocrystalline tungsten processed by high-pressure torsion, Acta Mater. 54 (2006) 4079–4089.

[60] S. Wurster, R. Treml, R. Fritz, M.W. Kapp, E.-M. Langs, M. Alfreider, C. Ruhs, P.J. Imrich, G. Felber, D. Kiener, Novel methods for the site specific preparation of micromechanical structures, Prakt. Met. Sonderband. 46 (2014) 27–36.

[61] D. Kiener, C. Motz, G. Dehm, R. Pippan, Overview on established and novel FIB based miniaturized mechanical testing using in-situ SEM, Int. J. Mat. Res. 100 (2009) 1074–1087.

[62] R. Fritz, D. Kiener, Development and Application of a Heated In-situ SEM Micro-

Testing Device, Measurement. 110 (2017) 356–366.

[63] I. Sneddon, The relation between load and penetration in the axisymmetric Boussinesq Problem for a punch of arbitrary profile, Int. J. Engng Sci. 3 (1965) 47–57.

[64] D. Kiener, W. Grosinger, G. Dehm, On the importance of sample compliance in uniaxial microtesting, Scripta. 60 (2009) 148–151.

[65] D. Tabor, The Hardness of Metals, OUP Oxford, Oxford UK, 1951.

[66] A. Leitner, V. Maier-Kiener, D. Kiener, Extraction of Flow Behavior and Hall-Petch Parameters Using a Nanoindentation Multiple Sharp Tip Approach, Adv. Eng. Mater. (2016) 1–9.

[67] V. Maier, K. Durst, J. Mueller, B. Backes, H.W. Höppel, M. Göken, Nanoindentation strain-rate jump tests for determining the local strain-rate sensitivity in nanocrystalline Ni and ultrafine-grained Al, J. Mater. Res. 26 (2011) 1421–1430.

[68] W.C. Oliver, G.M. Pharr, An improved technique for determining hardness and elastic modulus using load and displacement sensing indentation experiments, J. Mater. Res. 7 (1992) 1564–1583.

[69] V. Maier, A. Leitner, R. Pippan, D. Kiener, Thermally Activated Deformation Behavior of ufg-Au: Environmental Issues During Long-Term and High-Temperature Nanoindentation Testing, JOM. 67 (2015) 2934–2944.

[70] A.G. Atkins, D. Tabor, Plastic Indentation in metals with cones, J. Mech. Phys. Solids. 13 (1965) 149–164.

[71] W.D. Nix, H. Gao, Indentation size effects in crystalline materials: a law for strain gradient plasticity, J. Mech. Phys. Solids. 46 (1998) 411–425.

[72] E. Grünwald, R. Nuster, R. Treml, D. Kiener, G. Paltauf, R. Brunner, Young ' s Modulus and Poisson ' s Ratio Characterization of Tungsten Thin Films via Laser Ultrasound, Mater. Today Proc. 2 (2015) 4289–4294.

[73] P. Gumbsch, J. Riedle, A. Hartmaier, H.F. Fischmeister, Controlling factors for the Brittle-to-Ductile transition temperature in Tungsten Single Crystals, Science 282 (1998) 1293–1295.

[74] P. Gumbsch, Brittle fracture and the brittle-to-ductile transition of tungsten, J. Nucl. Mater. 323 (2003) 304–312.

[75] M. Faleschini, H. Kreuzer, D. Kiener, R. Pippan, Fracture toughness

investigations of tungsten alloys and SPD tungsten alloys, J. Nucl. Mater. 367–370 (2007) 800–805.

[76] J. Reiser, J. Hoffmann, U. Jäntsch, M. Klimenkov, S. Bonk, C. Bonnekoh, M. Rieth, A. Hoffmann, T. Mrotzek, Ductilisation of tungsten (W): On the shift of the brittle-to-ductile transition (BDT) to lower temperatures through cold rolling, Int. J. Refract. Met. Hard Mater. 54 (2016) 351–369.

[77] B. Merle, V. Maier-Kiener, G.M. Pharr, Influence of modulus-to-hardness ratio and harmonic parameters on continuous stiffness measurement during nanoindentation, Acta Mater. 134C (2017) 167–176.

[78] A. Leitner, V. Maier-Kiener, D. Kiener, Dynamic nanoindentation testing: Is there an influence on a material's hardness?, Mater. Res. Lett. (2017).

[79] K.L. Johnson, The correlation of indentation experiments, J. Mech. Phys. Solids. 18 (1970) 115–126.

[80] M. Mata, O. Casals, J. Alcala, The plastic zone size in indentation experiments: The analogy with the expansion of a spherical cavity, Int. J. Solids Struct. 43 (2006) 5994–6013.

[81] E.O. Hall, The Deformation and Ageing of Mild and Steel: III and Discussion of Results, Proc. Phys. Soc. B. 64 (1951) 747–753.

[82] N.J. Petch, The cleavage strength of polycrystals, J. Iron Steel Inst. 174 (1953) 25–28.

[83] A.A.N. Nemeth, J. Reiser, D.E.J. Armstrong, M. Rieth, The nature of the brittle-to-ductile transition of ultra fine grained tungsten (W) foil, Int. J. Refract. Met. Hard Mater. 50 (2015) 9–15.

[84] B. Yang, C. Motz, W. Grosinger, G. Dehm, Cyclic loading behavior of micro-sized polycrystalline copper wires, Procedia Eng. 2 (2010) 925–930.

[85] B. Yang, C. Motz, M. Rester, G. Dehm, Yield stress influenced by the ratio of wire diameter to grain size - a competition between the effects of specimen microstructure and dimension in micro-sized polycrystalline copper wires, Philos. Mag. 92 (2012) 3243–3256.

[86] D. Wu, X.L. Wang, T.G. Nieh, Variation of strain rate sensitivity with grain size in Cr and other body-centred cubic metals, J. Phys. D. Appl. Phys. 47 (2014) 175303.

[87] F. Mompiou, M. Legros, A. Boé, M. Coulombier, J.P. Raskin, T. Pardoen, Inter-

and intragranular plasticity mechanisms in ultrafine-grained Al thin films: An in situ TEM study, Acta Mater. 61 (2013) 205–216.

[88] M.W. Kapp, C. Kirchlechner, R. Pippan, G. Dehm, Importance of dislocation pile-ups on the mechanical properties and the Bauschinger effect in microcantilevers, J. Mater. Res. 30 (2015) 791–797.

[89] N.Q. Chinh, T. Csanadi, J. Gubicza, R.Z. Valiev, B.B. Straumal, T.G. Langdon, The Effect of Grain Boundary Sliding and Strain Rate Sensitivity on the Ductility of Ultrafine-Grained Materials, MSF. 667–669 (2010) 677–682.

[90] T.G. Langdon, Grain boundary sliding revisited: Developments in sliding over four decades, J. Mater. Sci. 41 (2006) 597–609.

[91] A. Seeger, The temperature and strain-rate dependence of the flow stress of bcc metals: A theory based on kink-kink interactions, Z. Met. 72 (1981) 369–380.

[92] J. Wehrs, G. Mohanty, G. Guillonneau, A. Taylor, X. Maeder, D. Frey, L. Philippe, S. Mischler, J.M. Wheeler, J. Michler, Comparison of In Situ Micromechanical Strain-Rate Sensitivity Measurement Techniques, JOM. 67 (2015) 1684–1693.

[93] J. May, H.W. Höppel, M. Göken, Strain rate sensitivity of ultrafine-grained aluminium processed by severe plastic deformation, Scr. Mater. 53 (2005) 189–194.

[94] J.Y. Zhang, G. Liu, J. Sun, Strain rate effects on the mechanical response in multi- and single-crystalline Cu micropillars: Grain boundary effects, Int. J. Plast. 50 (2013) 1–17.

[95] Q. Wei, S. Cheng, K.T. Ramesh, E. Ma, Effect of nanocrystalline and ultrafine grain sizes on the strain rate sensitivity and activation volume: fcc versus bcc metals, Mater. Sci. Eng. A. 381 (2004) 71–79.

[96] Q. Wei, Strain rate effects in the ultrafine grain and nanocrystalline regimes - influence on some constitutive responses, J Mater Sci. 42 (2007) 1709–1727.

[97] Q. Zhou, J. Zhao, J.Y. Xie, F. Wang, P. Huang, T.J. Lu, K.W. Xu, Grain size dependent strain rate sensitivity in nanocrystalline body-centered cubic metal thin films, Mater. Sci. Eng. A. 608 (2014) 184–189.

[98] V. Maier, C. Schunk, M. Göken, K. Durst, Microstructure-dependent deformation behaviour of bcc-metals - indentation size effect and strain rate sensitivity, Philos. Mag. 95 (2015) 1766–1779.

[99] V. Maier, A. Hohenwarter, R. Pippan, D. Kiener, Thermally activated deformation

processes in body-centered cubic Cr - How microstructure influences strain-rate sensitivity, Scr. Mater. 106 (2015) 42–45.

[100] R. Fritz, D. Wimler, A. Leitner, V. Maier-Kiener, D. Kiener, Dominating Deformation Mechanisms in Ultrafine-grained Chromium across Length Scales and Temperatures, Acta Mater. submitted (2017).

[101] M.J. Marcinkowski, H.A. Lipsitt, The plastic deformation of Chromium at low temperatures, Acta Metall. 10 (1962) 95–111.

[102] K. Leitner, P.J. Felfer, D. Holec, J. Cairney, W. Knabl, A. Lorich, H. Clemens, S. Primig, Towards grain boundary segregation engineering of molybdenum materials, Mater. Des. submitted (2017).

[103] J.W. Christian, B.C. Masters, Low-temperature deformation of body-centred cubic metals. I. yield and flow stress measurements, Proc. R. Soc. London. Ser. A. 281 (1964) 223–239.

Appendix

In the Appendix, Publication E, Publication F, screenshots of the graphical user interface of the in-situ heating control coded in LabVIEW, and the block diagram of the code are attached. The LabVIEW program for temperature control is included digitally on the storage medium located at the end of the thesis.

S. Wurster, R. Treml, R. Fritz, M. W. Kapp, E. Langs, M. Alfreider, C. Ruhs, P.J. Imrich, G. Felber, D. Kiener

Novel Methods for the Site Specific Preparation of Micromechanical Structures

Neuartige Verfahren zur ortspezifischen Präparation mikromechanischer Strukturen

Presented at the Metallography Conference 2014 in Leoben, Austria

Vorgetragen auf der Metallographietagung 2014 in Leoben, Österreich
Übersetzung: E. Engert

Abstract

The ongoing trend towards miniaturization in various fields of material science requires the capability to investigate the local mechanical properties of the concerned structures by miniaturized mechanical experiments. Besides nanoindentation, miniaturized experiments such as micro-compression, micro-tension, micro-bending, or micro-fracture tests were employed frequently in recent times. A major challenge for these experiments is the fabrication of specimens. Therefore, we present different approaches to prepare miniaturized testing objects in a site specific way, using strategies that employ chemical etching, broad beam ion milling, and focussed ion beam milling. Depending on the required sample size and precision, the typical strategies for sample fabrication will be outlined, and the benefits and drawbacks of the techniques

Kurzfassung

Der anhaltende Trend hin zur Miniaturisierung in verschiedenen Bereichen der Materialforschung erfordert die Möglichkeit der Untersuchung lokaler mechanischer Eigenschaften betreffender Strukturen mittels miniaturisierter mechanischer Versuche. Neben der Nanoindentation werden in jüngster Zeit häufig miniaturisierte Experimente wie beispielsweise Mikrodruck-, Mikrozug-, Mikrobiege- oder Mikrobruchversuche durchgeführt. Die Herstellung der Proben stellt hier eine große Herausforderung dar. Wir stellen daher verschiedene Ansätze zur ortsspezifischen Präparation miniaturisierter Prüfobjekte vor, bei denen Strategien wie chemisches Ätzen, Ionenpolieren mit breitem Strahlenbündel (Broad Beam Ion Milling) und Ionenätzen mit fokussierten Ionenstrahlen (Focused Ion Beam Milling) zum Einsatz kommen. Entsprechend der erforderlichen Probengröße und Präzision werden die typischen Strategien

Authors:

Stefan Wurster, Reinhard Fritz, Eva Langs, Markus Alfreider, Gabriele Felber, Daniel Kiener Department Materials Physics, Montanuniversität Leoben, Leoben, Austria
Ruth Treml, Christian Ruhs Materials Center Leoben, Leoben, Austria
Marlene Kapp, Peter Julian Imrich, Erich Schmid Institute, Austrian Academy of Sciences, Leoben, Austria

are discussed. Finally, applications of specimens produced by the different procedures are presented.

zur Probenherstellung erläutert und die Vor- und Nachteile dieser Techniken behandelt. Im letzten Teil werden Anwendungsbereiche für die mit den verschiedenen Verfahren hergestellten Proben vorgestellt.

1. Introduction

It is well known that the strength of a material depends on two crucial factors, the controlling internal material length scale, for example the grain size, dislocation or precipitate spacing [1–4], and/or the sample dimension itself [5–8]. In the first case, the microstructural features hinder the motion of dislocations, while in the latter case the free surface of the sample: (i) limits the size of the dislocation sources that fit into the specimen, or (ii) permits dislocations to leave the specimen through the free surface. Furthermore, (iii) if the specimen is very small and the dislocation density is low, the sample will statistically not contain a significant number of dislocations. For these scenarios either the applied stress that is needed to operate a dislocation source, essentially based on the Orowan stress required to bow a dislocation [9], or the lack of dislocation sources to be activated, lead to higher stress for plastic deformation of objects with reduced dimensions.

The miniaturization of components and devices concerns several fields of application, for example microelectronics, medical applications, telecommunication, and mobility. For the sake of simplicity, we will limit the general considerations to microelectronics. Due to the ongoing miniaturization, typical conducting lines in microelectronics applications are nowadays in the micrometer and sub-micrometer regime, with a continuing trend to further reduction. This increases the demand of thermal, mechanical and electronic load bearing capability of the used materials

1. Einleitung

Es ist allgemein bekannt, dass die Festigkeit eines Werkstoffes von zwei entscheidenden Faktoren abhängt: der maßgebenden inneren Längenskala des Materials, beispielsweise Korngröße, Versetzungsabstand oder Abstand der Ausscheidungen [1–4] bzw. den Probenabmessungen selbst [5–8]. Im ersten Fall behindern die mikrostrukturellen Merkmale die Versetzungsbewegung. Im zweiten Fall beeinflusst die freie Oberfläche der Probe: (i) die Größe der Versetzungsquellen, die in der Probe Platz finden, oder (ii) ermöglicht es Versetzungen, über diese aus der Probe auszutreten. (iii) Ferner wird die Probe keine statistisch signifikante Menge an Versetzungen aufweisen, wenn sie sehr klein und die Versetzungsdichte gering ist. Für diese Szenarien führt entweder die für die Aktivierung einer Versetzungsquelle erforderliche einwirkende Spannung, im Wesentlichen basierend auf der Orowan-Spannung, die erforderlich ist, um eine Versetzung zu auszubauchen [9], oder der Mangel an zu aktivierenden Versetzungsquellen selbst zu höherer Spannung für die plastische Verformung von Objekten mit geringen Abmessungen.

Miniaturisiert werden Komponenten und Geräte in verschiedenen Anwendungsbereichen wie beispielsweise der Mikroelektronik, bei medizinischen Anwendungen, in der Telekommunikation und im Bereich Mobilität. Der Einfachheit halber werden wir die allgemeinen Betrachtungen auf den Bereich der Mikroelektronik beschränken. In Mikroelektronik-Anwendungen sind heute entsprechend einer anhaltenden Miniaturisierung typische Leiterbahnen im Mikrometer- bzw. Submikrometergrößenbereich zu finden, wobei der Trend hin zu weiterer Größenreduzierung geht. Dies führt zu einer steigenden Nachfrage nach Werkstof-

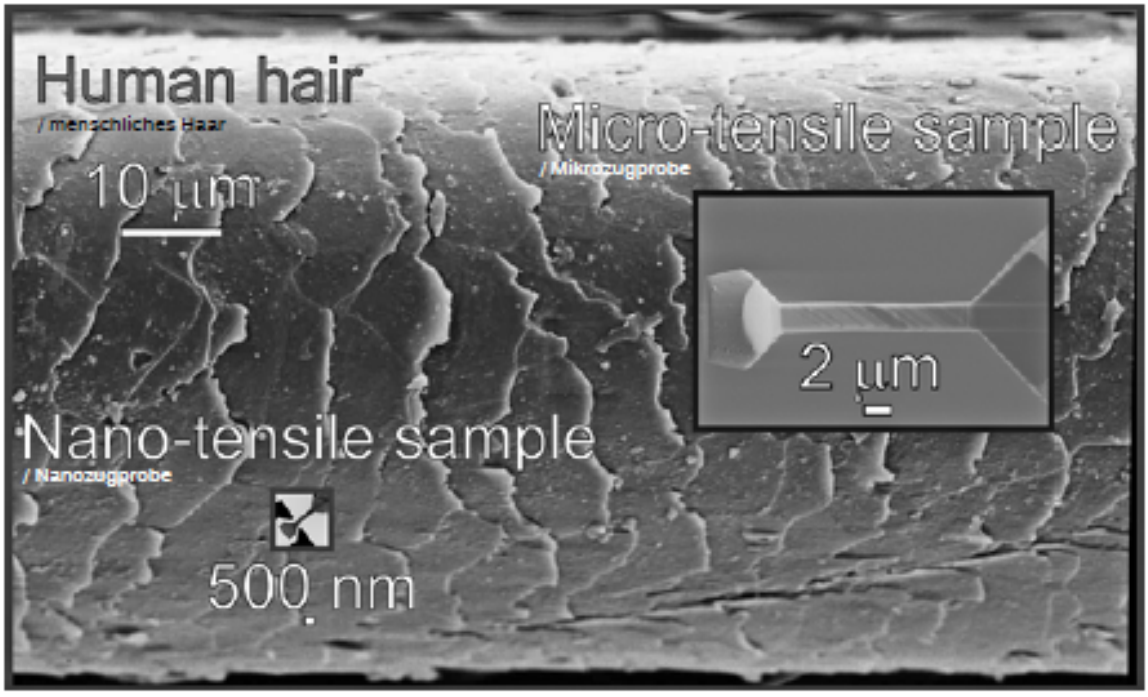

Fig. 1 Comparison between a human hair, a 2 µm Cu micro-tensile sample, and a 300 nm nano-tensile specimen.

***Bild 1:** Vergleich eines Menschenhaars mit einer Cu-Mikrozugprobe (2 µm) und einer Nanozugprobe (300 nm).*

and requires the development of new material systems with superior performance under these loading conditions. In this size regime, significant size effects on material properties are observed [5–8]. Thus, in order to enable a reliable design of novel products, it is indispensable to experimentally measure the stresses sustained by such small scale structures at their native length scale. To get an idea of the approximate dimensions, Fig. 1 presents the comparison of a human hair with a typical 3 µm micro-tensile sample and a 300 nm nano-tensile sample.

It is obvious that such structures cannot be produced by a classical top-down approach. There are some special bottom-up processes that can grow such small structures, such as whisker growth [10, 11],

fen mit thermischer, mechanischer und elektronische Belastbarkeit, was wiederum die Entwicklung neuer Werkstoffsysteme mit besserer Leistungsfähigkeit unter solchen Belastungszuständen bedingt. In dieser Größenordnung werden erhebliche Auswirkungen der Größe auf die Werkstoffeigenschaften beobachtet [5–8]. Für die zuverlässige Ausgestaltung neuer Produkte ist es somit unabdingbar, die in solchen kleinen Strukturen auftretenden Spannungen experimentell auf der tatsächlich auftretenden Längenskala zu messen. Zur Veranschaulichung der ungefähren Größenordnung zeigt Bild 1 den Vergleich eines menschlichen Haares mit einer typischen Mikrozugprobe (3 µm) und einer Nanozugprobe (300 nm).

Es liegt auf der Hand, dass solche Strukturen unter Anwendung klassischer Top-down-Verfahren nicht hergestellt werden können. Es gibt einige spezielle Bottom-up-Verfahren, anhand derer solche kleinen Strukturen gezüchtet wer-

electrodeposition [12, 13], or lithographic processes [14]. While these processes are capable of delivering a large number of samples, they are typically silicon-based techniques that require dedicated fabrication facilities and suffer flexibility with respect to the materials systems that can be processed straight forward. Therefore, we will place our focus on alternative approaches that can be realized with common metallographic preparation techniques such as electrochemical etching, broad beam ion milling/polishing, and focussed ion beam (FIB) milling.

2. Miniaturized Sample Preparation

The major strength of the FIB is the ability to machine almost any vacuum compatible material to various geometries with the precision of a few nanometers [15, 16]. However, the amount of removable material with a 30 keV Ga^+ ion beam is in the order of 1 $\mu m^3 nA^{-1} s^{-1}$ [15, 17, 18], depending significantly on the sputtered material and sputtering angle, as well as the required production precision which dictates the final milling current. To the authors' experience, the production steps within the FIB are the bottleneck of sample production. Therefore, it is of general interest to minimize the amount of material to be removed by FIB milling. To avoid unwanted material modifications during material thinning, as it would occur, for example, during grinding and polishing, the use of contact-pressure free techniques such as electrochemical etching or broad beam ion milling are preferable.

2.1 Electrochemical Etching

Using electrochemical etching, comparably large amounts of material can be removed with respect to the actual sample size, which is on the order of tens of nanometers to tens of micrometers. This technique is by itself not position selective and precise enough to

den können, z. B. Whiskerbildung [10, 11], Elektrodeposition [12, 13] oder lithographische Verfahren [14]. Durch solche Prozesse kann eine große Anzahl an Proben hergestellt werden. Sie sind allerdings typischerweise siliziumbasiert, was hierfür vorgesehene Herstellungsanlagen voraussetzt. Ferner fehlt es hier an der Flexibilität bezüglich weiterer verarbeitbarer Materialsysteme. Wir konzentrieren uns daher auf alternative Konzepte, die mit gängiger metallographischer Präparationstechnik umgesetzt werden können, beispielsweise elektrochemisches Ätzen, Breitstrahlionenpolieren und Ionenätzen mit fokussierten Ionenstrahlen (FIB).

2. Miniaturisierte Probenpräparation

Der wesentliche Vorteil des FIB liegt in der Möglichkeit, fast jeden vakuumtauglichen Werkstoff mit einer Genauigkeit im Nanometerbereich zu bearbeiten [15, 16]. Die mit einem 30 keV Ga^+ Ionenstrahl abtragbare Materialmenge liegt allerdings in einer Größenordnung von 1 $\mu m^3 nA^{-1} s^{-1}$ [15, 17, 18]. Sie hängt erheblich vom gesputterten Werkstoff, dem Sputterwinkel und der erforderlichen Präzision bei der Herstellung ab, die die letztendliche Stromstärke beim Ionenätzen vorgibt. Gemäß den Erfahrungen der Autoren stellen die FIB-Herstellungsschritte den Engpass bei der Probenanfertigung dar. Daher ist es von allgemeinem Interesse, die Menge an durch FIB-Ätzen abzutragenden Materials zu reduzieren. Um während der Ausdünnung des Materials unerwünschte Werkstoffveränderungen zu vermeiden, wie sie beispielsweise während dem Schleifen und Polieren auftreten, sind anpressdruckfreie Techniken wie z. B. das elektrochemische Ätzen oder das Breitstrahlionenpolieren vorzuziehen.

2.1 Elektrochemisches Ätzen

Bei elektrochemischem Ätzen können hinsichtlich der tatsächlichen Probengröße (im zweistelligen Nanometer- bis Mikrometerbereich) vergleichsweise große Materialmengen abgetragen werden. Diese Technik arbeitet nicht ortsselektiv und präzise genug, um endkon-

fabricate near net shape mechanical testing samples. However, etching of the material of interest allows to remove unwanted material modifications originating, for example, from a cutting or grinding process. Rods and wires can be shaped to the form of long needles [19], or thin lamellas can be prepared in a selective way to prepare single grain boundaries [17, 20]. Subsequent use of the FIB enables to place single or multiple samples onto the thin freestanding structure. This approach significantly reduces the amount of material to be removed by FIB milling and limits the possibility of unwanted material re-deposition. Moreover, these approaches prevent any unintended contact between the testing tip and any material surrounding the specimen. They provide a free sight onto the sample during *in situ* micromechanical testing, e. g. in the scanning electron microscope [21, 22]. The required preparation steps to FIB machined miniaturized samples starting from electrochemically etched needles or wedges will be described below.

2.2 Broad Beam Ion Milling

A limitation of electrochemical processes is their selectivity. Thus, once multiple materials or phases are of interest, a homogenous material removal can become very challenging or even impossible. In such situations, broad beam ion milling techniques can be beneficially applied. We use a Hitachi E-3500 ion milling system that operates with an Ar^+ beam and an acceleration voltage up to 6 kV and beam currents of ~100 µA. The diameter of the beam is in the range of several hundreds of micrometers, following a Gaussian profile. The sputter yield is lower compared to the FIB, which is counterbalanced by an increased ion current (4–7 orders of magnitude) and an increased beam diameter (~5 orders of magnitude). This allows

turnahe Proben (Near-Net-Shape-Fertigung) für mechanische Prüfungen herzustellen. Allerdings ermöglicht das Ätzen des entsprechenden Werkstoffes das Abtragen unerwünschter, vom Zuschneiden oder Schleifen etc. stammender Werkstoffmodifikationen. Stäbe und Drähte können zu langen Nadeln geformt werden [19] oder dünne Lamellen können gezielt präpariert werden, um einzelne Korngrenzen aufzubereiten [17, 20]. Die anschließende Anwendung des FIB ermöglicht ein Aufsetzen einzelner oder mehrerer Proben auf die dünne, freistehende Struktur. Dieses Vorgehen reduziert erheblich die durch FIB abzutragende Materialmenge und schränkt eine mögliche unerwünschte Werkstoffablagerung ein. Darüber hinaus wird durch solches Vorgehen jeglicher unbeabsichtigte Kontakt zwischen der Prüfspitze und einem die Probe umgebenden Material vermieden. Es gewährleistet weiters während der mikromechanischen In-situ-Prüfung, z. B. im Rasterelektronenmikroskop, eine freie Sicht auf die Probe [21, 22]. Im Folgenden werden die erforderlichen Präparationsschritte für mittels FIB bearbeitete miniaturisierte Proben ausgehend von elektrochemisch geätzten Nadeln oder Klingen beschrieben.

2.2 Breitstrahlionenpolieren

Elektrochemische Vorgänge werden unter anderem durch ihre Selektivität beschränkt. Liegen mehrere zu untersuchende Werkstoffe oder Phasen vor, erweist sich ein homogener Materialabtrag möglicherweise als schwierig oder gar unmöglich. In solchen Fällen kann der Einsatz der Ionenpolierverfahren mit breitem Strahlenbündel von Vorteil sein. Wir verwenden einen Hitachi E-3500 Ionenpolierer, der mit einem Ar^+-Strahl arbeitet. Das Gerät verfügt über eine Beschleunigungsspannung von bis zu 6 kV und eine Strahlstromstärke von ~100 µA. Der Strahldurchmesser liegt im dreistelligen Mikrometerbereich und folgt einem Gaußschen Profil. Die Sputterausbeute ist im Vergleich zum FIB niedriger, was durch einen erhöhten Ionenstrom (4–7 Größenordnungen) und einen größeren Strahldurchmesser (~5 Größenordnungen)

to remove hundred thousands of µm³ of material in reasonable time. The sputtered areas have a width and depth of several hundreds of micrometers [23]. The material of interest, which shall not be affected by the milling process, is protected by a mask that is placed on top of the region of interest using an optical microscope. The mask shadows the ion beam and fully prevents material removal. The accuracy of positioning the mask is not better than a few micrometers. As such, the lateral selectivity of this technique is limited to this accuracy. Nonetheless, it allows to prepare cross-sections over large areas, the production of free-standing lamellas with a thickness of a few micrometers, or even readymade micro-samples when adding structured masks to the process. Thus, broad beam ion milling serves as a universal tool to pre-shape material systems not accessible by electrochemical etching or too large for FIB milling, and in some cases it allows even to fabricate net shape micro-samples. This is particularly useful for materials that cannot be processed with the Ga^+ beam in the FIB (e.g. aluminium, polymers, etc.), as these materials would be altered and even damaged. In the following, we will describe the above mentioned applications in more detail.

2.2.1 *Cross-Sections*

The simplest (and original) application is the perpendicular preparation of a material cross-section at an edge. This would be challenging by electrochemical etching, since corners would always be rounded off by preferential attack. With the FIB, such cross-sections could be prepared, but within reasonable time using broad beam ion milling, large dimensions of more than 10,000 µm² can be polished perpendicular to the material surface at a chosen position within few hours. To this purpose, shown in

ausgeglichen wird. So wird das Abtragen von hunderttausenden µm³ an Material in einem angemessenen Zeitraum möglich. Die gesputterten Bereiche weisen eine Breite und Tiefe von mehreren hundert Mikrometern auf [23]. Das zu untersuchende Material, welches durch den Polierprozess nicht beeinträchtigt werden darf, wird durch einer Maske geschützt, die mittels lichtoptischen Mikroskops vorab auf den entsprechenden Bereich gelegt wird. Die Maske verhindert das Auftreffen des Ionenstrahls und unterbindet den Werkstoffabtrag vollständig. Sie wird mit einer Genauigkeit von nicht mehr als einigen Mikrometern positioniert, wodurch die laterale Selektivität dieser Technik auf diese Genauigkeit begrenzt wird. Dennoch ermöglicht sie die Präparation von Querschnitten über ausgedehnte Bereiche hinweg, die Fertigung von freistehenden Lamellen mit einer Dicke von einigen wenigen Mikrometern oder, bei zusätzlichem Einsatz strukturierter Masken, sogar von gebrauchsfertigen Mikroproben. So dient das Breitstrahlpolieren als universal einsetzbare Technik zur Präparation von Materialsystemen, die für elektrochemisches Ätzen nicht zugänglich oder für das FIB-Ätzen zu groß wären. In einigen Fällen ermöglicht es sogar die Herstellung von Mikroproben mit Endkontur, was besonders nützlich ist für Materialien, die mittels Ga^+-Strahl im FIB nicht bearbeitet werden können (z.B. Aluminium, Polymere, etc.), da sie verändert und sogar beschädigt würden. Im Folgenden beschreiben wir zuvor erwähnte Anwendungen im Detail.

2.2.1 *Querschnitte*

Die einfachste (und ursprüngliche) Anwendung ist die senkrechte Präparation eines Materialquerschnittes an einer Kante. Beim elektrochemischen Ätzen wäre dies schwierig, da die Ecken durch einen bevorzugten Angriff immer abgerundet würden. Solche Querschnitte könnten mittels FIB angefertigt werden. Durch Breitstrahlionenpolieren kann jedoch großdimensioniert (Größenordnung > 10,000 µm²) in wenigen Stunden an einer ausgewählten Stelle senkrecht zur Werkstoffoberfläche poliert werden. Hierfür wird die Probe, wie in Bild 2

Figs. 2a to c: *Broad ion beam cross-section preparation of a thin film on substrate.*

Bilder 2a bis c: *Querschnittspräparation einer Dünnschicht auf Substrat mit breitem Ionenstrahlbündel.*

Fig. 2, the sample is partially covered by a thick mask (a), then the Ar^+ beam is used to sputter a cross-section into the material surface (b), thereby exposing the film microstructure and film/substrate interface (c) for in depth analysis.

2.2.2 *Free-Standing Films or Lamellas*

The inspection of a buried microstructure is one application for ion milling. However, when aiming towards micro-mechanical testing it is more important to prepare free standing lamellas out of bulk samples or thin films on substrates. For films on substrates this can in some cases be achieved by electrochemical removal of the substrate [24]. However, the broad beam ion milling approach shown in Fig. 3 works for any kind of film/substrate as well as for bulk materials. By covering the film (or any other area of interest) with the protecting mask, only the substrate is removed (b), creating a large free-standing lamella that can be used, for example, for subsequent FIB sample structuring (c, d). For very thin films also part of the substrate has to be covered to prevent damage of the film.

Another possibility not shown here is to prepare a thin lamella across the film on substrate by repeating the process shown in Fig. 2 from the other side as well, as demonstrated recently elsewhere [25]. Such lamellas, where the film of interest is on top of the prepared lamella, can serve as pre-form for shaping bending beams in the FIB to meas-

gezeigt, teilweise von einer dicken Maske bedeckt (a). Hiernach wird mittels Ar^+-Strahl ein Querprofil in die Materialoberfläche gesputtert (b). So wird das Gefüge der Schicht und die Grenzfläche Schicht/Substrat für eine eingehende Analyse freigelegt (c).

2.2.2 *Freistehende Schichten oder Lamellen*

Das Ionenpolieren wird beispielsweise zur Untersuchung einer verdeckten Mikrostruktur angewendet. Soll allerdings mikromechanisch geprüft werden, ist es wichtiger, freistehende Lamellen aus Bulkproben oder Dünnschichten auf Substraten anzufertigen. Dies gelingt in einigen Fällen für Schichten auf Substraten durch elektrochemisches Abtragen des Substrats [24]. Das in Bild 3 gezeigte Breitstrahlionenpolierverfahren eignet sich allerdings sowohl für jegliche Art von Schicht/Substrat als auch für Massivmaterial. Durch ein Abdecken der Schicht (oder eines anderen zu untersuchenden Bereichs) mit der Schutzmaske wird lediglich das Substrat abgetragen (b), wodurch eine große freistehende Lamelle entsteht, die beispielsweise bei der nachfolgenden FIB-Probenstrukturierung verwendet werden kann (c, d). Für sehr dünne Schichten muss zusätzlich ein Teil des Substrats abgedeckt werden, um Schäden an der Schicht zu vermeiden.

Eine weitere, hier nicht vorgestellte, Möglichkeit, ist die Präparation einer dünnen Lamelle durch Schicht und Substrat durch die Wiederholung des in Bild 2 gezeigten Vorgangs von der anderen Seite, wie es kürzlich an anderer Stelle dargelegt wurde [25]. Solche Lamellen, bei denen sich die entsprechende Schicht an der Oberseite der präparierten Lamelle befin-

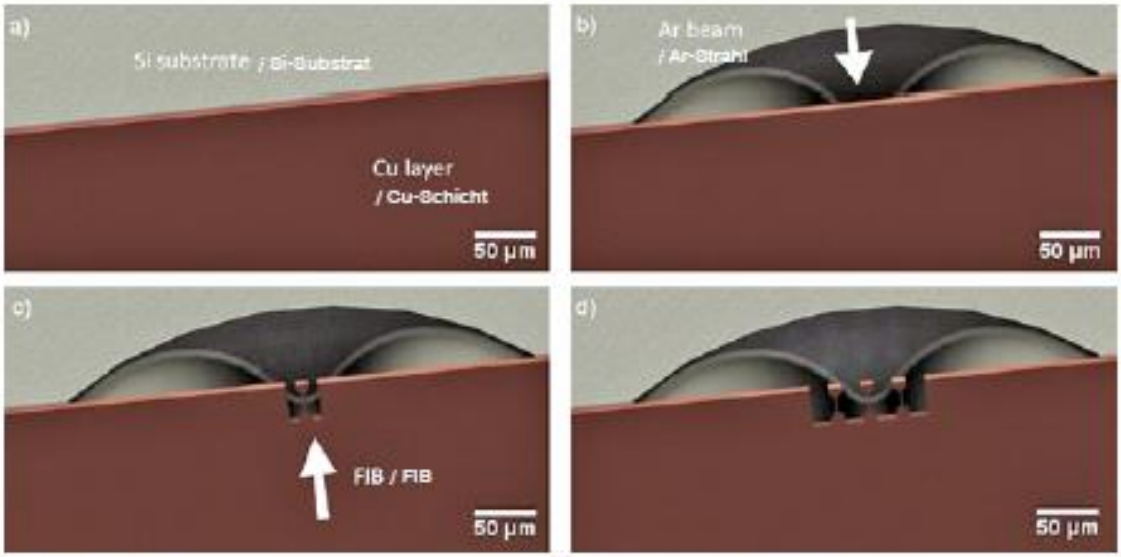

Figs. 3a to d: *Preparation of a free-standing thin film or lamella (a, b), that can subsequently be FIB structured.*

Bilder 3a bis d: *Präparation einer freistehenden Dünnschicht oder Lamelle (a, b), die hiernach FIB-strukturiert werden kann.*

ure stresses in the thin films, an example of which is shown below.

2.2.3 *Mask-Structured Microsamples*

Finally, once a free-standing lamella was created by either electrochemical etching or broad beam ion slicing (Fig. 4a), in the next step the sample can be rotated by 90° and a protecting stencil mask put in place on top (b), after which another ion milling process is performed (c), similar to what was suggested in [26]. This then allows the FIB-less creation of micro-samples (Fig. 4d).

Notably, this approach is limited to somewhat larger samples sizes in the upper micrometer regime. Nonetheless, this is a very exciting range that is typically only accessible by lithographic techniques, as it is too small for conventional machining, and too large or very ineffective for FIB machining. Given the limited flexibility of lithographic

det, können als Ausgangsform zur Produktion von Biegebalken im FIB dienen, um dann Spannungen in den Dünnschichten zu messen. Ein Beispiel hierfür wird nachfolgend beschrieben.

2.2.3 *Anhand von Masken strukturierte Mikroproben*

Nach der Fertigung einer freistehenden Lamelle durch elektrochemisches Ätzen oder auch durch Breitstrahlionenpolieren (Bild 4a) kann die Probe schließlich um 90° gedreht und eine schützende Schablone (bzw. Masken) aufgebracht werden (4b). Hiernach wird erneut, ähnlich den Ausführungen in [26], ionenpoliert (c). Auf diese Weise können anschließend Mikroproben ohne FIB angefertigt werden (Bild 4d).

Zu beachten ist, dass sich die Anwendung dieses Verfahrens auf etwas größere Proben im oberen Mikrometerbereich beschränkt. Dennoch handelt es sich hier um einen sehr interessanten Bereich, der typischerweise lediglich über lithographische Verfahren zugänglich ist, da er für konventionelle maschinelle Bearbeitung zu klein und für die FIB-

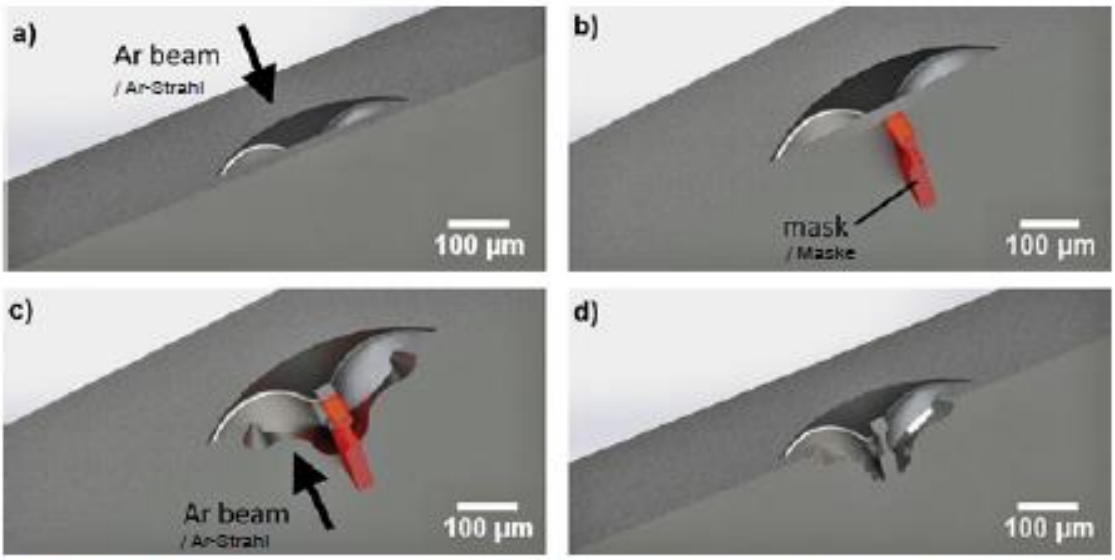

Figs. 4a to d: Preparation of micro-tensile samples using stencil masks during broad ion beam sputtering of a previously thinned lamella.

***Bilder 4a bis d:** Präparation von Mikrozugproben unter Verwendung von Schablonen beim Ionenstrahlsputtern einer zuvor gedünnten Lamelle.*

processes with respect to the used materials, we think that this mask supported broad beam ion milling approach, which can be applied to literally any kind of material that tolerates vacuum and low energy Ar^+ ion impact, is definitely a very valuable sample fabrication strategy.

2.3 Focussed Ion Beam Milling

In the following paragraphs, we will detail the steps to prepare miniaturized samples with well defined geometries [19, 27–30], and in particular without the taper, which is typical for many of these micro-samples [31]. Needles or lamellas, fabricated in the previous steps, will serve as pre-forms.

2.3.1 Samples on a Needle

Cutting of a specimen on top of a needle [19] is performed essentially in four steps

Bearbeitung entweder generell zu groß oder sehr ineffektiv wäre. Angesichts der eingeschränkten Flexibilität der Lithographie-Verfahren bezüglich der verwendeten Werkstoffe denken wir, dass diese unter Verwendung von Schablonen durchgeführte Technik des Breitstrahlionenpolierens, die bei nahezu allen Werkstoffarten, die vakuumtauglich sind und die Wechselwirkung mit niederenergetischen Ar^+-Ionen zulassen, eine durchaus sehr nützliche Strategie der Probenherstellung darstellt.

2.3 Ionenätzen mit fokussierten Ionenstrahlen

In den nachfolgenden Abschnitten werden wir die Schritte zur Präparation miniaturisierter Proben mit eindeutig definierten Geometrien im Detail vorstellen [19, 27–30], im Besonderen ohne die Dickenzunahme, wie sie für viele dieser Mikroproben typisch ist [31]. In vorangegangenen Schritten hergestellte Nadeln oder Lamellen dienen als Ausgangspunkt.

2.3.1 Proben auf einer Nadel

Das Fertigen einer Probe aus einer Nadelspitze [19] erfolgt im Wesentlichen in vier

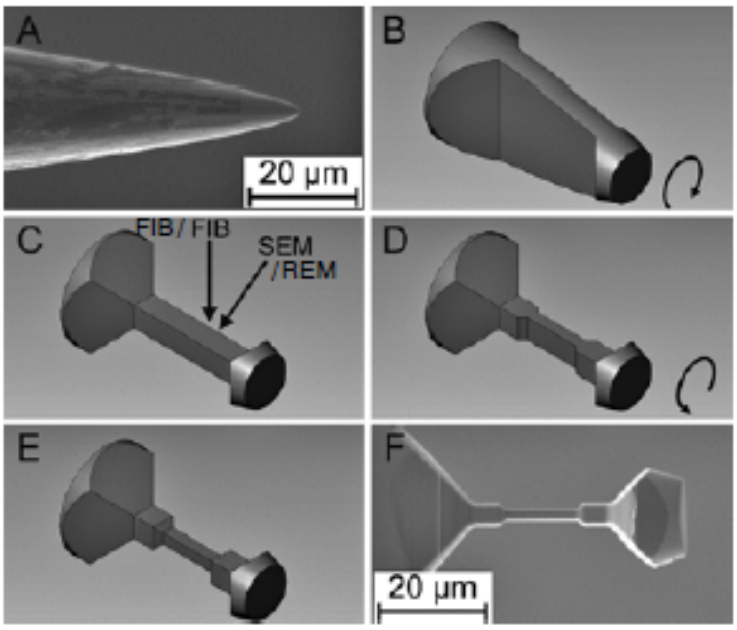

Figs. 5a to f: Stepwise FIB fabrication of a miniaturized tensile sample from an electrochemically etched tip (after [19]).

***Bilder 5a bis f:** Schrittweise FIB-Fertigung einer miniaturisierten Zugprobe aus einer elektrochemisch geätzten Spitze (entsprechend [19]).*

(see Fig. 5). First, the apex of the needle is removed and two parallel sides are rough cut into the tip using ion currents in the order of 1 nA (b). Next, the sample is rotated by 90° along the wire axis and the perpendicular sides are coarse cut (c). In the subsequent step, the milling current is reduced to about 100 pA, giving less-damaged, smoother polished surfaces, and the final sample geometry is milled on the latter two sides (d). Finally, the sample is rotated back by 90° and the first two sides are finished according to the desired geometry (e).

To avoid angular errors during the 90° rotation procedures, it is suggested that the needle is fixed into a block with perpendicular side planes that eases the repeated rotation operation. A drawback of this needle approach is that only a single specimen is fabricated at a time. On the other hand, this single specimen is easily accessible from all directions for testing and analysis, shadowing during, for example, electron back scatter diffraction analysis [32] is easily avoided. Moreover, due to the needle approach, such

Schritten (siehe Bild 5). Zunächst wird die äußerste Nadelspitze entfernt. Mittels Ionenströmen (1 nA) werden dann zwei parallele Flanken grob in den Stumpf geschnitten (b). Die Probe wird 90° die Drahtachse gedreht und die senkrechten Flanken werden grob zugeschnitten (c). Im folgenden Schritt wird der Ionenstrom auf etwa 100 pA reduziert, was zu weniger Beschädigungen und glatteren, polierten Oberflächen führt. Die exakte Probengeometrie wird dann in beide Flanken geschnitten (d). Schließlich wird die Probe um 90° zurückgedreht und die ersten beiden Flanken werden je nach gewünschter Geometrie endbearbeitet (e).

Um während der 90°-Drehungen Winkelfehler zu vermeiden, wird empfohlen, die Nadel in einem Block mit rechtwinkeligen Seitenflächen zu befestigen, was die wiederholte Drehung vereinfacht. Ein Nachteil dieser Nadeltechnik ist die Tatsache, dass nur jeweils eine Probe hergestellt werden kann. Andererseits ist diese Einzelprobe für Prüfungen und Analysen leicht von allen Seiten zugänglich. Ein Abschatten, wie es beispielsweise bei der Analyse mittels Rückstreuelektronenbeugung eintreten kann [32], ist einfach zu vermeiden. Wird das Nadel-

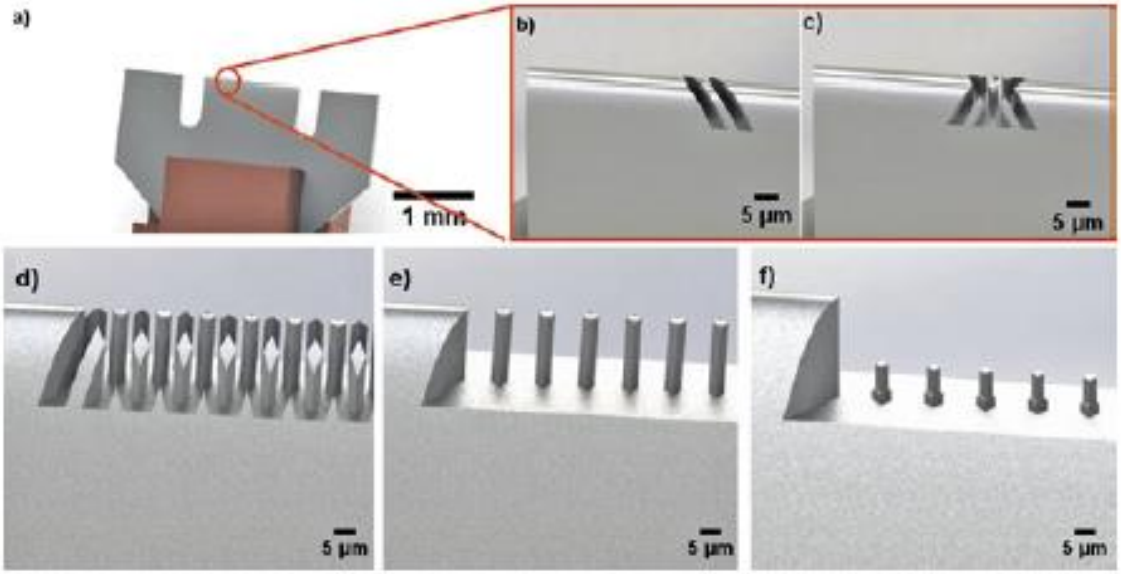

Figs. 6a to f: *Sequential steps to prepare a series of compression samples by FIB along an electrochemically prepared lamella.*

Bilder 6a bis f: *Schrittfolge zur Präparation einer Reihe von Druckproben mittels FIB entlang einer elektrochemisch präparierten Lamelle.*

samples can readily be used for atom probe tomography after deformation [33].

2.3.2 Samples on a Wedge

In order to place several samples along a lamella but still enabling a well controlled geometry and being free of taper over the sample height, it is recommended to place the samples at a rotation of 45° with respect to the parallel lamella side [17]. This would be very difficult for un-rotated samples, as they block the view of sight from one to another along the direction parallel to the lamella. The FIB based fabrication steps are as follows (Fig. 6): The lamella is mounted under an axial inclination of 45° with respect to the non-tilted sample stage in a holder that again allows for repeatable 90° sample rotation around the length axis (a). In a first step, coarse slots are cut into the 45° inclined lamella (b). Next the sample is re-mounted after 90° axial rotation and the perpendicular slots are cut (c). The remnant

verfahren angewendet, können solche Proben ferner nach der Verformung ohne Weiteres mittels Atomsondentomographie untersucht werden [33].

2.3.2 Proben auf einer Klinge

Um mehrere Proben entlang einer Lamelle zu platzieren und trotzdem eine genau kontrollierte Geometrie ohne Dickenzunahme über der Probenhöhe zu gewährleisten, wird empfohlen, sie in Bezug auf die parallele Lamellenseite mit einer Drehung um 45° zu positionieren [17]. Für nicht gedrehte Proben wäre dies sehr kompliziert, da sie einander die Sicht entlang der zur Lamelle parallelen Richtung versperren. Im Folgenden werden die FIB-basierten Herstellungsschritte beschrieben (Bild 6): Die Lamelle wird in einem Halter mit einer Achsrotation von 45° bezüglich des nicht geneigten Probentisches fixiert, der wiederum eine reproduzierbare Probendrehung von 90° um die Längsachse ermöglicht (a). In einem ersten Schritt werden in die um 45° geneigte Lamelle grobe Schlitze geschnitten (b). Dann wird die Probe nach einer axialen Drehbewe-

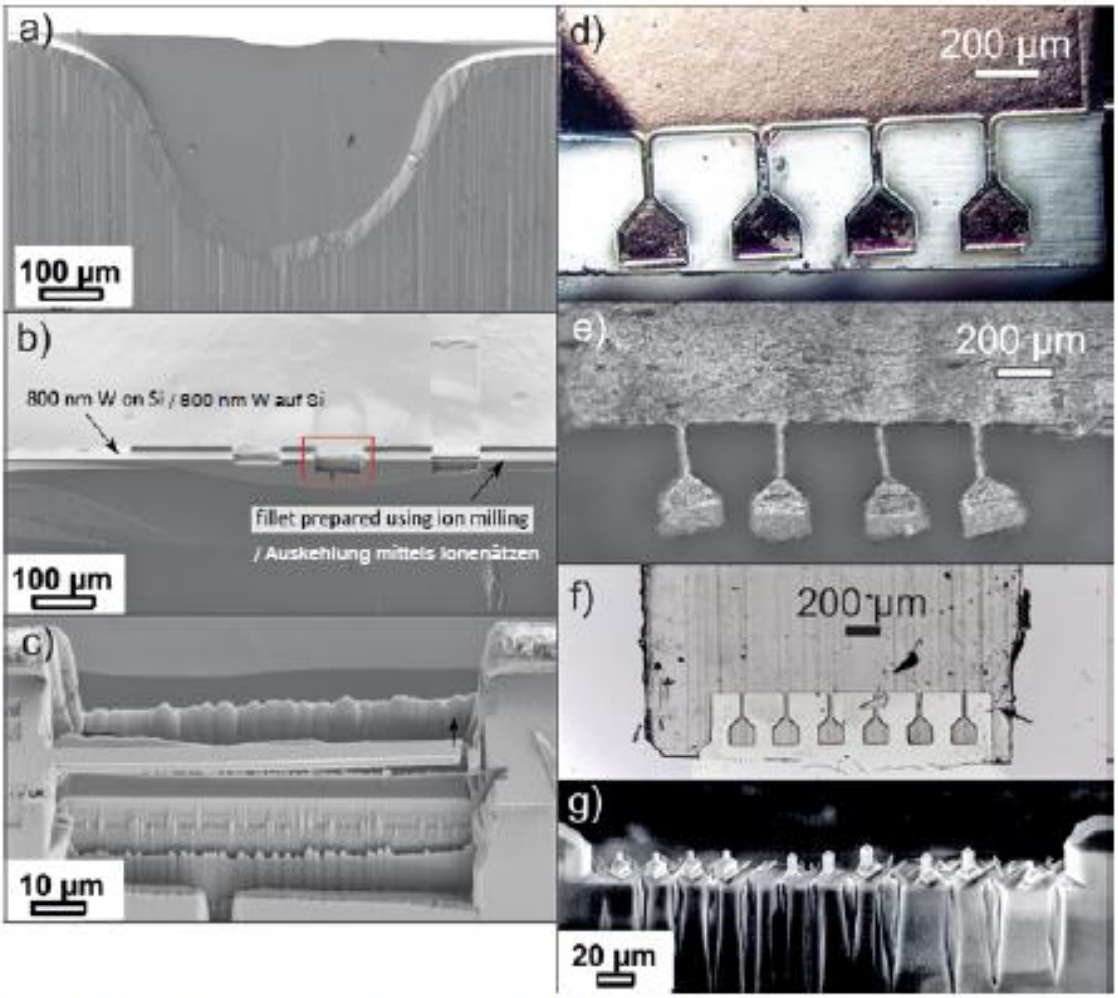

Figs. 7a to g: Selected examples of miniaturized structures prepared by the aforementioned techniques. Please refer to text for further details.

Bilder 7a bis g: *Ausgewählte Beispiele von durch vorgenannte Techniken angefertigten miniaturisierten Strukturen. Weitere Einzelheiten hierzu finden Sie im Text.*

tips of the initial lamella that were hidden by the coarse structured compression specimens are subsequently removed in a top down milling step (d). To this purpose, the sample is mounted with the specimens' compression direction parallel to the ion beam. After this, the sample is put back in the previous position and the two perpendicular sample sides are subsequently finished by fine polishing as outlined before (e, f).

gung um 90° wieder aufgesetzt und Schlitze senkrecht zu den ersten geschnitten (c). Die verbleibenden Spitzen der ursprünglichen Lamelle, die von den grob strukturierten Druckproben verdeckt wurden, werden hiernach in einem Top-down-Ätzschritt abgetragen (d). Dafür wird der Prüfkörper mit der Druckrichtung parallel zum Ionenstrahl montiert. Danach wird die Probe in die vorherige Position zurückgebracht. Die beiden senkrechten Probenseiten werden dann mittels Feinpolieren wie zuvor beschrieben endbearbeitet (e, f).

Notably, the fact that three corners of a square cross-section specimen are visible during *in situ* deformation rather than only two for the case of un-rotated pillars increases the information that can be gained during such experiments.

3. Applications

Lastly, we would like to show some applications of the introduced techniques in order to give an idea of what is possible within few hours and using rather simple techniques. Fig. 7a shows a broad ion beam thinned piece of single crystal W [23], where the extended dimensions of the thinned area are clearly visible. The preparation of a free-standing lamella with a thin film on top of a Si substrate [25] is shown in Fig. 7b. Within this thin lamella, a bending beam (Fig. 7c) is FIB fabricated to measure the stresses in the thin film from the resulting beam curvature [25, 34]. Fig. 7d shows a series of lithographically prepared Cu stencil masks [14] placed on top of an Al lamella, while Fig. 7e and f present samples fabricated by this mask aided ion milling approach from rolled 16 µm thick Cu foil and a 20 µm thick PET film, respectively. These samples can subsequently be tested under the optical microscope or *in situ* in the scanning electron microscope without requirement for further FIB machining or polishing. At last, Fig. 7g presents a series of compression samples with sizes between 1 µm and 4 µm fabricated by FIB on top of an electrochemically prepared single crystal Mg[11–20] wedge.

4. Summary

With the increasing trend in miniaturization, experimental determination of mechanical properties of miniaturized samples is getting increasingly important. Here we outline

Insbesondere die Tatsache, dass drei Ecken einer Probe quadratischen Querschnitts während der In-situ-Verformung sichtbar sind und nicht nur zwei, wie im Falle von nicht gedrehten Proben, sorgt dafür, dass während eines solchen Experiments mehr Informationen gewonnen werden können.

3. Anwendungen

Schließlich möchten wir einige Anwendungen der eingeführten Techniken vorstellen, um eine Vorstellung zu vermitteln, was in einigen wenigen Stunden und unter dem Einsatz eher einfacher Techniken möglich ist. Bild 7a zeigt ein mittels Breitionenstrahl gedünntes Stück eines W-Einkristalls [23]. Der ausgedehnte, gedünnte Bereich ist hier deutlich erkennbar. Bild 7b zeigt die Präparation einer freistehenden Lamelle mit einer Dünnschicht auf einem Si-Substrat [25]. Innerhalb dieser dünnen Lamelle wird ein Biegebalken (Bild 7c) mittels FIB angefertigt, der dazu dient, die Spannungen in der Dünnschicht, die in eine Balkendurchbiegung resultieren, zu messen [25, 34]. Bild 7d zeigt eine Reihe von mittels Lithographie präparierten Cu-Schablonen [14], die auf einer Al-Lamelle platziert wurden. Die Bilder 7e und f zeigen Proben, welche unter Anwendung dieses Ionenätzverfahrens mit Masken jeweils aus gewalzter 16 µm dicker Cu-Folie bzw. einer 20 µm dicken PET-Folie gefertigt wurden. Diese Proben können dann mittels Lichtmikroskop oder *in situ* im Rasterelektronenmikroskop untersucht werden. Eine weitere FIB-Bearbeitung oder Polieren ist nicht erforderlich. Schlussendlich zeigt Bild 7g eine Reihe von mittels FIB hergestellten Druckproben mit einer Größe zwischen 1 und 4 µm auf der Spitze einer elektrochemisch gedünnten einkristallinen Mg-[11–20]-Klinge.

4. Zusammenfassung

Im Zuge des stärker werdenden Trends hin zur Miniaturisierung gewinnt die experimentelle Bestimmung mechanischer Eigenschaften mikromechanischer Proben immer mehr an

different approaches that can be applied for pre-shaping or final shaping of miniaturized mechanical test specimens based on electrochemical etching, broad beam ion milling, and FIB machining. Moreover, some selected applications are presented to show the possibilities of the different methods.

5. Acknolwedgement

The authors thank the organizers for the opportunity to present their work at the 14. Metallographic Conference 2014 in Leoben, Austria. Financial support by the Austrian Science Fond FWF (project numbers I 1020-N20 and P 25325-N20) is gratefully acknowledged. Further financial support by the Austrian Federal Government (837900) (in particular from the Bundesministerium für Verkehr, Innovation und Technologie and the Bundesministerium für Wirtschaft, Familie und Jugend) represented by Österreichische Forschungsförderungsgesellschaft mbH and the Styrian and the Tyrolean Provincial Government, represented by Steirische Wirtschaftsförderungsgesellschaft mbH and Standortagentur Tirol, within the framework of the COMET Funding Programme is appreciated.

Bedeutung. Wir geben hier einen Überblick über verschiedene Verfahren, die angewendet werden können, um miniaturisierte Proben für mechanischer Tests auf Grundlage von elektrochemischem Ätzen, Breitstrahlionenpolieren und FIB-Bearbeitung vor- oder endzuformen. Zusätzlich werden ausgewählte Beispiele vorgestellt, welche die möglichen Anwendungsgebiete der verschiedenen Verfahren zeigen.

5. Danksagung

Die Autoren bedanken sich bei den Organisatoren dafür, dass sie ihre Arbeit bei der 14. Internationalen Metallographie-Tagung 2014 in Leoben, Österreich, vorstellen konnten. Wir bedanken uns für die finanzielle Unterstützung seitens des Österreichischen Fonds zur Förderung der wissenschaftlichen Forschung, FWF, (Projektnummern I 1020-N20 und P 25325-N20). Wir bedanken uns zudem für die finanzielle Unterstützung durch die österreichische Bundesregierung (837900) (insbesondere durch das Bundesministerium für Verkehr, Innovation und Technologie und das Bundesministerium für Wirtschaft, Familie und Jugend), repräsentiert von der Österreichischen Forschungsförderungsgesellschaft mbH, und durch die Steiermärkische und Tiroler Landesregierung, repräsentiert von der Steirischen Wirtschaftsförderungsgesellschaft mbH und der Standortagentur Tirol im Rahmen des Förderprogramms COMET.

References / Literatur

[1] Petch, N. J.: The Cleavage Strength of Polycrystals. J. Iron Steel, 174, 1953, p. 25.

[2] Hall, E. O.: The Deformation and Ageing of Mild Steel. Proc. Phys. Soc. Lond. B, 64, 1951, p. 747.
DOI: 10.1088/0370-1301/64/9/303

[3] Arzt, E.: Size effects in materials due to microstructural and dimensional constraints: a comparative review. Acta Mater., 46, 1998, p. 5611.
DOI: 10.1016/S1359-6454(98)00231-6

[4] Kiener, D.; Rester, M.; Scheriau, S.; Yang, B.; Pippan, R.; Dehm, G.: Influence of External and Internal Length Scale of the Flow Stress of Copper. Int. J. Mat. Res., 98, 2007, p. 1047.
DOI: 10.3139/146.101578

[5] Uchic, M. D.; Shade, P. A.; Dimiduk, D.: Plasticity of Micrometer-Scale Single Crystals in Compression. Ann. Rev. Mater. Res., 39, 2009, p. 361.
DOI: 10.1146/annurev-matsci-082908-145422

[6] Uchic, M. D.; Dimiduk, D. M.; Florando, J. N.; Nix, W. D.: Sample Dimensions Influence

Strength and Crystal Plasticity. Science, 305, 2004, p. 986.
DOI: 10.1126/science.1098993

[7] Dehm, G.: Miniaturized single-crystalline fcc metals deformed in tension: New insights in size-dependent plasticity. Prog. Mater. Sci., 54, 2009, p. 664.
DOI: 10.1016/j.pmatsci.2009.03.005

[8] Kraft, O.; Gruber, P. A.; Mönig, R.; Weygand, D.: Plasticity in Confined Dimensions. Ann. Rev. Mater. Res., 40, 2010, p. 293.
DOI: 10.1146/annurev-matsci-082908-145409

[9] Orowan, E. Discussion on Internal Stresses. Symposium on Internal Stresses in Metals and Alloys. London: The Institute of Metals, 1948. p.451.

[10] Brenner, S. S.: Growth and Properties of Whiskers. Science, 128, 1958, p. 569.
DOI: 10.1126/science.128.3324.569

[11] Richter, G.; Hillerich, K.; Gianola, D. S.; Mönig, R.; Kraft, O.; Volkert, C. A.: Ultrahigh Strength Single Crystalline Nanowhiskers Grown by Physical Vapor Deposition. Nano Lett., 9, 2009, p. 3048.
DOI: 10.1021/nl9015107

[12] Dou, R.; Derby, B.: The strength of gold nanowire forests. Scripta Mater., 59, 2008, p. 151.
DOI: 10.1016/j.scriptamat.2008.02.046

[13] Burek, M. J.; Greer, J. R.: Fabrication and Microstructure Control of Nanoscale Mechanical Testing Specimens via Electron Beam Lithography and Electroplating. Nano Lett., 10, 2010, p. 69.
DOI: 10.1021/nl902872w

[14] Smolka, M.; Motz, C.; Detzel, T.; Robl, W.; Griesser, T.; Wimmer, A.; Dehm, G.: Novel temperature dependent tensile test of freestanding copper thin film structures. Rev. Sci. Instrum., 83, 2012, p. 064702.
DOI: 10.1063/1.4725529

[15] Volkert, C. A.; Minor, A. M.: Focused ion beam microscopy and micromachining. MRS Bull., 32, 2007, p. 389.
DOI: 10.1557/mrs2007.62

[16] Giannuzzi, L. A.; Stevie, F. A.: A review of focused ion beam milling techniques for TEM specimen preparation. Micron, 30, 1999, p. 197.
DOI: 10.1016/S0968-4328(99)00005-0

[17] Moser, G.; Felber, H.; Rashkova, B.; Imrich, P. J.; Kirchlechner, C.; Grosinger, W.; Motz, C.; Dehm, G.; Kiener, D.: Sample Preparation by Metallography and Focused Ion Beam for Nanomechanical Testing. Pract. Metallogr., 49, 2012, p. 343.
DOI: 10.3139/147.110171

[18] Ziegler, J. F.; Biersack, J. P.; Littmark, U. The Stopping Range of Ions in Matter. New York: Pergamon Press, 1985.

[19] Kiener, D.; Grosinger, W.; Dehm, G.; Pippan, R.: A further step towards an understanding of size-dependent crystal plasticity: In-situ tension experiments of miniaturized single crystal copper samples. Acta Mater., 56, 2008, p. 580.
DOI: 10.1016/j.actamat.2007.10.015

[20] Imrich, P. J.; Kirchlechner, C.; Motz, C.; Dehm, G.: Differences in deformation behavior of bicrystalline Cu micropillars containing a twin boundary or a large-angle grain boundary. Acta Mater., 73, 2014, p. 240.
DOI: 10.1016/j.actamat.2014.04.022

[21] Kiener, D.; Motz, C.; Dehm, G.; Pippan, R.: Overview on established and novel FIB based miniaturized mechanical testing using in-situ SEM. Int. J. Mat. Res., 100, 2009, p. 1074.
DOI: 10.3139/146.110149

[22] Gianola, D. S.; Sedlmayr, A.; Monig, R.; Volkert, C. A.; Major, R. C.; Cyrankowski, E.; Asif, S. A. S.; Warren, O. L.; Kraft, O.: In situ nanomechanical testing in focused ion beam and scanning electron microscopes. Rev. Sci. Instrum., 82, 2011, p. 063901.
DOI: 10.1063/1.3595423

[23] Wurster, S.; Motz, C.; Jenko, M.; Pippan, R.: Micrometer-Sized Specimen Preparation Based on Ion Slicing Technique. Adv. Eng. Mater., 12, 2010, p. 61.
DOI: 10.1002/adem.200900263

[24] Matoy, K.; Schönherr, H.; Detzel, T.; Schöberl, T.; Pippan, R.; Motz, C.; Dehm, G.: A comparative micro-cantilever study of the mechanical behavior of silicon based passivation films. Thin Solid Films, 518, 2009, p. 247.
DOI: 10.1016/j.tsf.2009.07.143

[25] Schöngrundner, R.; Treml, R.; Antretter, T.; Kozic, D.; Ecker, W.; Kiener, D.; Brunner, R.: Critical assessment of the determination of residual

stress profiles in thin films by means of the ion beam layer removal method. Thin Solid Films, 564, 2014, p. 321.
DOI: 10.1016/j.tsf.2014.06.003

[26] Shade, P. A.; Kim, S.-L.; Wheeler, R.; Uchic, M. D.: Stencil mask methodology for the parallelized production of microscale mechanical test samples. Rev. Sci. Instrum., 83, 2012, p. 053903.
DOI: 10.1063/1.4720944

[27] Kiener, D.; Motz, C.; Schöberl, T.; Jenko, M.; Dehm, G.: Determination of Mechanical Properties of Copper at the Micron Scale. Adv. Eng. Mater., 8, 2006, p. 1119.
DOI: 10.1002/adem.200600129

[28] Kiener, D.; Motz, C.; Dehm, G.: Micro-compression testing: A critical discussion of experimental constraints. Mater. Sci. Eng. A, 505, 2009, p. 79.
DOI: 10.1016/j.msea.2009.01.005

[29] Kiener, D.; Motz, C.; Grosinger, W.; Weygand, D.; Pippan, R.: Cyclic response of copper single crystal micro-beams. Scripta Mater., 63, 2010, p. 500.
DOI: 10.1016/j.scriptamat.2010.05.014

[30] Kiener, D.; Minor, A. M.: Source Truncation and Exhaustion: Insights from Quantitative in situ TEM Tensile Testing. Nano Lett., 11, 2011, p. 3816.
DOI: 10.1021/nl201890s

[31] Greer, J. R.; De Hosson, J. T. M.: Plasticity in small-sized metallic systems: Intrinsic versus extrinsic size effect. Prog. Mater. Sci., 56, 2011, p. 654.
DOI: 10.1016/j.pmatsci.2011.01.005

[32] Niederberger, C.; Mook, W. M.; Maeder, X.; Michler, J.: In situ electron backscatter diffraction (EBSD) during the compression of micropillars. Mater. Sci. Eng. A, 527, 2010, p. 4306.
DOI: 10.1016/j.msea.2010.03.055

[33] Xie, K. Y.; Shrestha, S.; Cao, Y.; Felfer, P. J.; Wang, Y.; Liao, X.; Cairney, J. M.; Ringer, S. P.: The effect of pre-existing defects on the strength and deformation behavior of α-Fe nanopillars. Acta Mater., 61, 2013, p. 439.
DOI: 10.1016/j.actamat.2012.09.022

[34] Massl, S.; Keckes, J.; Pippan, R.: A direct method of determining complex depth profiles of residual stresses in thin films on a nanoscale. Acta Mater., 55, 2007, p. 4835.
DOI: 10.1016/j.actamat.2007.05.002

Bibliography

DOI 10.3139/147.110331
Pract. Metallogr. 52 (2015) 3; page 131 – 146

ISSN 0032–678X

Materials Science & Engineering A 687 (2017) 313–322

Contents lists available at ScienceDirect

Materials Science & Engineering A

journal homepage: www.elsevier.com/locate/msea

The influence of microstructure on the cyclic deformation and damage of copper and an oxide dispersion strengthened steel studied via in-situ micro-beam bending

C. Howard[a,*], R. Fritz[b], M. Alfreider[b], D. Kiener[b], P. Hosemann[a]

[a] University of California, 2111A Etcheverry Hall, Berkeley, CA 94720-1730, USA
[b] Department of Materials Physics, Montanuniversität Leoben, A-8700, Leoben, Austria

ARTICLE INFO

Keywords:
Low cycle fatigue (LCF)
Micro-bending
Cyclic damage
Micromechanics

ABSTRACT

Service materials are often designed for strength, ductility, or toughness, but neglect the effects of cyclic time-variable loads ultimately leading to macroscopic mechanical failure. Fatigue originates as local plasticity that can first only be observed on the micro scale at defects serving as stress concentrators such as inclusions or grain boundaries. Thus, a recently developed technique to perform in-situ observation of micro scale bending fatigue experiments was applied. Micro-beams fabricated from copper, single grained and ultrafine grained (ufg), and an oxide dispersion strengthened (ODS) steel were subject to cyclic deformation and subsequent damage. The elastic stiffness, yield strength, dissipated energy, and maximum stress were measured as a function of cycle number and plastic strain amplitude. From these properties, cyclic stress–strain curves were developed. Initial pronounced monotonic hardening and an increasing Bauschinger effect were observed in all samples with increasing strain amplitude. Cyclic stability was maintained until plastic strain amplitudes reached a critical value. At this point, dramatic cyclic softening and microcracking occurred. The critical strain amplitude was found to be approximately 5.4×10^{-3} for the copper with a refined grain structure and 1.2×10^{-2} for the steel specimen. Grain rotation and noticeable changes in sub-grain structure were evident in the ufg copper after a critical strain amplitude of $\varepsilon_a=8.3\times10^{-3}$. In-situ micro fatigue bending couples the cyclic evolution of bulk mechanical properties measurements with real-time electron microscopy analysis techniques of damage and failure mechanisms, which renders it a powerful method for developing novel fatigue resistant materials.

1. Introduction

The mechanical properties of materials can strongly depend on the size of the specimen tested, especially for components with smallest dimensions below 10 μm. Size effects have been extensively studied for various stress states during monotonic loading via indentation [1–4], compression [5–9], tension [10,11], and bending [12–15]. However, size effects during cyclic loading have only been investigated for limited stress states such as pure tension or torsion in thin wires [16–21]. Size effect investigations employing full load reversals have been explored using thin films that are only small in one dimension [22], on single crystal copper [23], and on rather large polycrystalline copper samples (20 μm × 20 μm) [19]. The full load reversal cyclic response of micro specimens of dimensions less than 10 μm with complex microstructures in multiple dimensions has now been investigated with an emphasis on grain boundary misorientation evolution of an ufg copper specimen processed via high pressure torsion (HPT) [24].

The aim of this work is to study the low cycle fatigue (LCF) behavior of micron-sized engineering alloys with complex microstructures to develop a method for fatigue testing suited for irradiated micro specimens. Micron sized samples are a useful approach when total sample volume is limited, specific regions within a material need to be sampled, or in the case of hazardous materials where large material quantities are to be avoided. For example, the amount of nuclear reactor components available to be analyzed is often limited due to space limitations inside the core as well as the high activity of retrieved samples. This minimizes the total amount of materials handled. Also, many ion irradiated materials have a limited sample volume available due to the limited penetration depth of ions in materials [25]. Therefore small-scale mechanical testing methods allow for the evaluation of mechanical properties [26–32]. The approach of small-scale samples to evaluate property changes due to irradiation has been widely utilized in the past, and the present work serves to extend these techniques to perform cyclic bending tests on micro-samples.

* Corresponding author.
E-mail address: cam7745@berkeley.edu (C. Howard).

http://dx.doi.org/10.1016/j.msea.2017.01.073
Received 8 September 2016; Received in revised form 20 January 2017; Accepted 21 January 2017
Available online 22 January 2017

Therefore, a recently developed simple in-situ technique to perform cyclic bending tests on micro-samples is applied [23]. As test materials, copper and an oxide dispersion strengthened (ODS) steel were examined, both as single grained micro-beams and the copper as a micro-beam with a refined microstructure smaller than the sample size due to severe plastic deformation processing. Copper is an especially interesting material to evaluate this new technique due to the fact that data from many uniaxial small scale mechanical testing techniques is available for copper, and it serves as a good benchmarking material [10,33–47]. Moreover, the macroscopic fatigue properties of single crystals and ufg material are well documented in several publications [48–61]. Modifying the microstructure of the copper via Equal Channel Angular Pressing (ECAP) [52–54] allows one to study the effect of refined grain structure on the cyclic behavior. In addition, oxygen free, electronic high conductivity ECAP copper remains a promising candidate for accelerator structures due to its ultrahigh electrical conductivity [55]. ODS steels, such as the material PM 2000, introduce oxide nanoclusters as dislocation motion barriers which leads to enhanced strength and creep resistance. In addition, ultrafine grained (ufg) material and material with large amounts of inert precipitates provide an abundance of defect sinks, which are believed to enhance radiation tolerance compared to their simpler structured counterparts [56]. Of course PM 2000 is an older ODS alloy with limited oxide particle density compared to newer generation ODS alloys, but it is one of the few alloys that has been previously commercially produced and is more widely available [57,58].

While materials with complex pre-existing microstructures such as ECAP copper and ODS PM 2000 steel have superior macroscopic monotonic strength and radiation tolerance compared to their coarse grained and single crystal counterparts, their macroscopic fatigue properties are not always beneficial to the overall structure. Pertaining to fatigue life, ufg materials exhibit improved properties in the high cycle regime [48], whereas they are inferior to conventional materials in the low cycle regime [50]. Advanced prediction methodologies require knowledge of cyclic stress-strain behavior and damage evolution with regards to cyclic softening/hardening. For polycrystalline materials, damage is directly related to microstructural instabilities that may eventually lead to microstructural changes such as grain coarsening, as previously evidenced during macroscopic low cycle strain controlled fatigue tests on ECAP copper [51]. Micro fatigue testing is deployed here in order to evaluate the small sample sizes resulting from ECAP and ODS processes, but even more so in preparation of deploying similar tests on ion beam or reactor irradiated materials, where small sample sizes are the only way to obtain mechanical property values. This present study focuses on the mechanical fatigue properties of micro specimens for ECAP copper and ODS PM 2000 steel by using single grained copper and ODS PM 2000 micro-beams as comparisons.

2. Material and experimental procedures

Rods with dimensions of 0.5 mm×0.5 mm×20 mm were cut from generic course grain copper stock, a cross-sectional 25 mm diameter disc slice from an ufg copper rod (ECAP deformed, 8 deformation passes via route Bc prepared by Valiev et al. [52–54]), and a PLANSEE (Plansee SE, Reutte, Austria) PM 2000 ODS steel alloy. A bright field transmission electron microscope (BF-TEM) image collected in a 300 kV JEOL 3010 transmission electron microscope (TEM) chamber under high vacuum for the ECAP copper sample can be seen in Fig. 1, showing the resulting microstructure. All rods were mounted in holders depicted in Fig. 2a for further sample preparation alignment, and positioning during in-situ Scanning Electron Microscopy (SEM) testing and post analysis. Subsequent electrochemical etching using Struers Electrolyte A2 for the PM 2000 and Struers Electrolyte D2 for the copper resulted in sharper tips with a radius of approximately 30 μm, as shown in Fig. 2b, to reduce the use of a Focused Ion Beam (FIB) for fabricating the bend beam geometries. Furthermore, this etching also ensures removal of a possible deformation layer from the diamond wire cutting process used for making the rods [39].

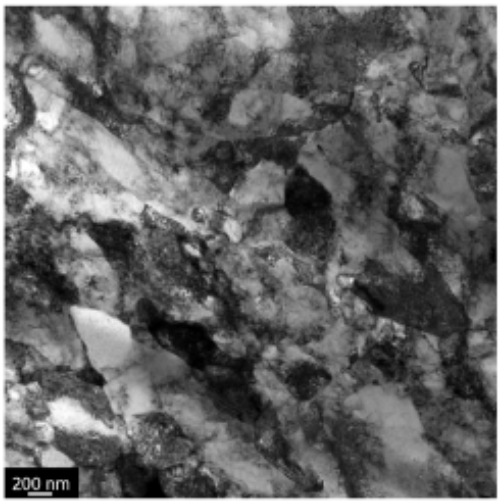

Fig. 1. Non-fatigued microstructure of the ufg ECAP copper sample via Bright Field Transmission Electron Microscope (BF-TEM) imaging.

A Zeiss Leo 1540 XB (Oberkochen, Germany) dual beam SEM/FIB workstation was used to cut four bending beams with the following final dimensions, height by width by length (h×w×l): 3.6 μm×3.1 μm×31.2 μm for the single grained copper, 4.6 μm×4.5 μm×29.7 μm for the ECAP copper, and 4.7 μm×2.1 μm×23.9 μm for the single grained PM 2000. A Ga^+ ion current of 10 nA was applied for rough milling steps, and 100 pA was used for final shaping to reduce the ion damage.

Sample loading was performed in-situ using an UNAT-SEM indenter (Zwick GmbH & Co KG, Ulm, Germany) [59] mounted inside a Zeiss Leo 982 SEM (Oberkochen, Germany). For sample bending, a tungsten needle was modified to a gripping shape by FIB to have a 7.7 μm wide opening, shown in Fig. 3c. First rough cuts using 10 nA and final polishing cuts at 100 pA were used to ensure a flat smooth bending contact surface. This gripper was then attached to the microindenter and aligned with respect to the incoming electron beam. The in-situ setup shown in Fig. 3b is required for alignment between the specimen and gripper without unwanted contact prior to loading, and also allows to adjust the bending length, l_b, along the beam length, L. Displacement controlled sample loading is performed with a displacement ratio of $R = u_{min}/u_{max} = -1$, where u_{min} is the minimum displacement below the neutral axis rest position and u_{max} is the maximum displacement above the neutral axis rest position. The sinusoidal displacement is applied at a frequency of 0.033 s^{-1}, and an example of a single ±2.3 μm loading cycle is displayed in Fig. 3d. The measured load-displacement data for this cycle is shown in Fig. 3a.

SEM images were taken during the first and last individual loading cycles at the displacement positions indicated by the insets shown in Fig. 3a for subsequent compliance correction and to get a visual impression of the evolving surface damage. Examination of the in-situ SEM images pointed out a compliance of the entire copper mini rod, indicated by the low unloading slope in Fig. 3a. This was accounted for using the base displacement measured from the in-situ SEM images [39,59]. After this simple correction, Young's moduli of 115 ± 11 GPa for the single-grained copper bar and 142 ± 14 GPa for the ECAP copper bar were evaluated for the elastic loading cycles, compared to a bulk modulus of 130 GPa for copper [60]. A Young's modulus of 280 ± 14 GPa for the single-grained PM 2000 was evaluated for the elastic cycles, compared to a bulk modulus of 215 GPa for PM 2000 [61]. After each in-situ fatigue testing sequence, the specimens were examined using high resolution SEM imaging.

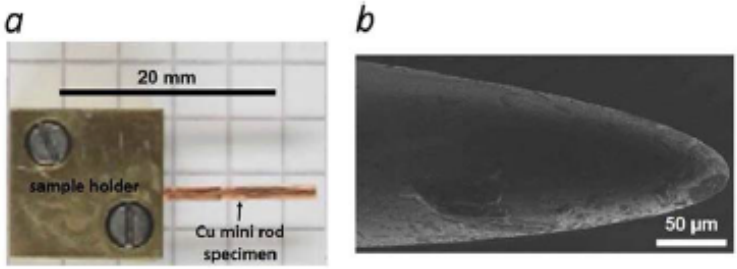

Fig. 2. (a) Sample holder machined for holding mini rod specimens to be electropolished (b) Electro-chemically sharpened needle tip.

While the first cycles were always in the elastic regime to perform the required stiffness correction, subsequent cycles were performed to larger displacements to include plastic deformation. These occurred in approximate 100 cycle increments on each of the four specimens. The first strain amplitude at which 100 cycles took place was such that enough plastic deformation occurred to produce a clear yield point (deviation from linear elastic loading) that could be observed in real time during inspection of the load versus displacement curves while the testing was being performed. Subsequent testing in 100 cycle increments with strain amplitudes beyond these values for each sample caused more plastic deformation and damage. This step by step testing method was employed in order to obtain the elastic loading, yield points, and subsequent behavior past yielding for each material in order to develop a cyclic stress-strain curve. The approximate strain rates for all tests were calculated as the minimum and maximum calculated strains for all micro-beams divided by the time it took for the apparatus to reach maximum displacement from zero displacement, one quarter cycle ($t_{1/4}$=7.5 s). This range is between $2.13\times10^{-4}\ s^{-1}$ and $2.00\times10^{-3}\ s^{-1}$. Corrections for the points when the gripper and sample were not in contact, the 1.7 µm gap seen in Fig. 3a, were performed every half cycle in order to obtain cyclic loading curves that mirror those of macroscopic fatigue tests. This zero force gap segment occurs due to the limitations associated with the precision of FIB fabrication, leaving the final dimensions of the micro bending beams a bit smaller than the width of the gripper, whereas during macroscopic fatigue testing, the loading apparatus and specimen are always in contact.

The elastic modulus, yield strength and maximum stress were evaluated for every half cycle, and the energy dissipated was calculated for each cycle. The elastic modulus was measured by fitting the linear elastic portions of each half cycle. The yield strength was then taken as the first recorded point which deviated from linear elastic loading behavior. The energy dissipated for a cycle was calculated using a numerical point by point trapezoidal integration of the area within the hysteresis loop. In addition to the assessment of the cyclic stability of these mechanical properties and evolution of these mechanical properties as a function of plastic strain amplitude, cyclic stress-strain curves were constructed from the points of maximum strain in the stable hysteresis loops at each plastic strain amplitude.

All stress and strain values are taken to be those at the root of the beams and at the surface fiber of the beams denoted as point P in Fig. 3b, the point on the bending beam which encounters the highest stress and strain conditions. From linear elastic beam theory and simple geometric relationships, they can be given as

$$\varepsilon = \frac{uh}{2L_b^2}, \tag{1}$$

where u is the displacement recorded, h is the thickness of the bar, L is the length of the bar, and l_b is the bending length of the bar. Moreover,

$$\sigma = \frac{6Fl_b}{bh^2}, \tag{2}$$

where b is the width of the bar, F is the recorded load, and all other

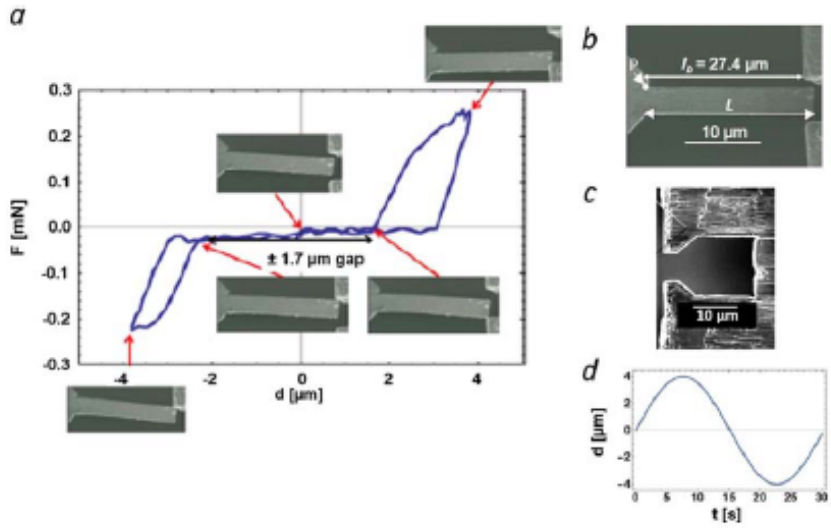

Fig. 3. (a) Measured load (F) versus displacement (d) data. The insets show SEM images recorded in-situ during the loading cycle to depict the contact between sample and gripper and correct the sample compliance. (b) Aligned bending sample and gripper before loading. (c) Tungsten wire with a FIB fabricated 7.7 µm wide opening for sample gripping. (d) Prescribed displacement versus time graph for a single bending cycle.

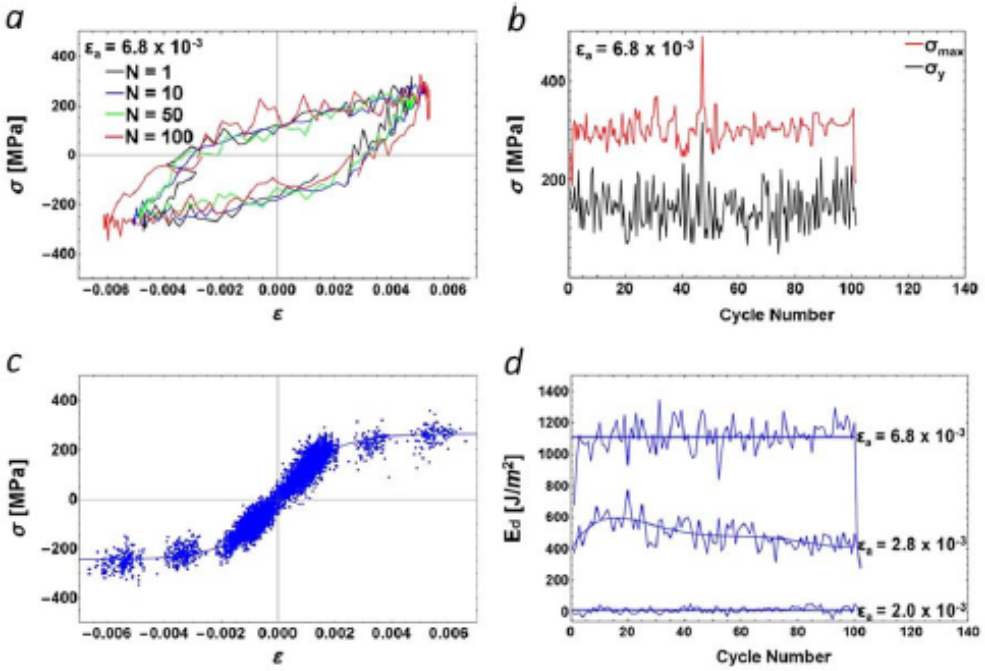

Fig. 4. The cyclic mechanical properties of the single-grained copper micro-beam. (a) Selected stress versus strain curves at cycles N=1, N=10, N=50, and N=100 for a plastic strain amplitude of 6.8×10^{-3}. (b) Yield strength and maximum stress as a function of cycle number for plastic strain amplitude of 6.8×10^{-3}. (c) Cyclic stress versus strain curve. (d) Energy dissipated per cycle as a function of cycle number at three selected plastic strain amplitudes.

parameters have been previously defined above.

3. Results

3.1. Copper

Fig. 4 depicts the results of the low cycle fatigue testing on the single grained copper micro-beam. The single grained copper micro-beam is found to experience yielding at plastic strain amplitudes $\geq1.6\times10^{-3}$. Cyclic stability with respect to the yield strength occurred over the course of 100 cycles at plastic strain amplitudes of 2.8×10^{-3}, $\sigma_y=148\pm35$ MPa, and 6.8×10^{-3}, $\sigma_y=142\pm43$ MPa, as seen in Fig. 4a and b. Cyclic stability with respect to maximum stress values indicating stable hysteresis loops was also evidenced for these plastic strain amplitudes. This is evidenced by the average maximum stress values over 100 cycles. For $\varepsilon_a=2.8\times10^{-3}$, $\sigma_{max}=270\pm35$ MPa, and for $\varepsilon_a=6.8\times10^{-3}$, $\sigma_{max}=301\pm29$ MPa. This is referenced in the supporting data, Fig. 4s parts e and f. For all plastic strain amplitudes investigated, cyclic stability with respect to elastic modulus was evidenced as values ranged from 105 GPa to 126 GPa on average. The cyclic stress-strain curve shown in Fig. 4c exhibits an initial regime of stress increase with increase in ε_a up to approximately 2.0×10^{-3}, followed by a stable plateau regime for $2.0\times10^{-3}<\varepsilon_a<7.0\times10^{-3}$ where the stress remains constant at ~250 MPa. The initial yield point of the single grained copper micro-beam occurs at 200 MPa, but over the course of fatiguing this yield point has dropped to approximately 140 MPa, as referenced in supporting document Fig. 4s part g. Practically all of this 60 MPa softening occurred when increasing the plastic strain amplitude from 2.3×10^{-3} to 2.8×10^{-3}. However, the maximum stress values have become saturated, even at $\varepsilon_a=1.6\times10^{-3}$. Over the course of increasing ε_a by 5.2×10^{-3}, maximum stress values only increase by 50 MPa. Fig. 4d depicts the energy dissipated per cycle for selected plastic strain amplitudes. In the elastic regime at $\varepsilon_a=1.6\times10^{-3}$, very little energy is dissipated, $E_{el}=13\pm18$ J/m^2, meaning that for plastic strain amplitudes less than or equal to this value, the cyclic deformation is elastic within the resolution of our experimental setup. However, as ε_a increases to values greater than 2.0×10^{-3}, noticeable amounts of energy are dissipated each cycle, indicative of plastic deformation. For $\varepsilon_a=2.8\times10^{-3}$, the steady state energy dissipated per cycle during stable hysteresis loops is $E_{el}=496\pm87$ J/m^2. There appears to be an initial period of increasing energy dissipated per cycle up to 600 J/m^2 within the first 20 cycles, after which a gradual decay back to the stable quantity occurs over the following 80 cycles. For $\varepsilon_a=6.8\times10^{-3}$, instant stability is reached and maintained for the entire 100 cycle interval at $E_{el}=1111\pm112$ J/m^2. The most rapid increase in energy dissipated per cycle occurs for $2.3\times10^{-3}<\varepsilon_a<2.8\times10^{-3}$. A graph of the energy dissipated per cycle as a function of plastic strain amplitude can be seen in the supporting document Fig. 4s part h.

Fig. 5 depicts the results of the low cycle fatigue testing on the ECAP copper micro-beam. Contrary to the results for the single grained copper beam, it can be seen that the polycrystalline material undergoes cyclic work hardening followed by softening as plastic strain amplitudes are increased. No stable plateau stress region exists for the ECAP copper micro-beam. Instead, a period of cyclic work hardening after the yield point occurs between $2\times10^{-3}<\varepsilon_a<4\times10^{-3}$, followed by a period of cyclic softening for $\varepsilon_a>4\times10^{-3}$ as evidenced in Fig. 5c. Representative stress-strain hysteresis loops and analysis of cyclic stability of yield stress and maximum stress over the first 100 cycles for these plastic strain amplitudes can be found in the supporting data Fig. 5s parts e through l. When looking more closely at the cyclic stability of the first 100 cycles at selected plastic strain amplitudes, it can be seen that yield strength and maximum stress values are quite stable. There does exist an exception over the range of plastic strain amplitudes $5.4\times10^{-3}<\varepsilon_a<8.3\times10^{-3}$ shown in Fig. 5b, where σ_{max} values decrease from 453 ± 39 MPa to 341 ± 28 MPa and σ_y values decrease from 304 ± 34 MPa to 165 ± 35 MPa. An analysis of the yield

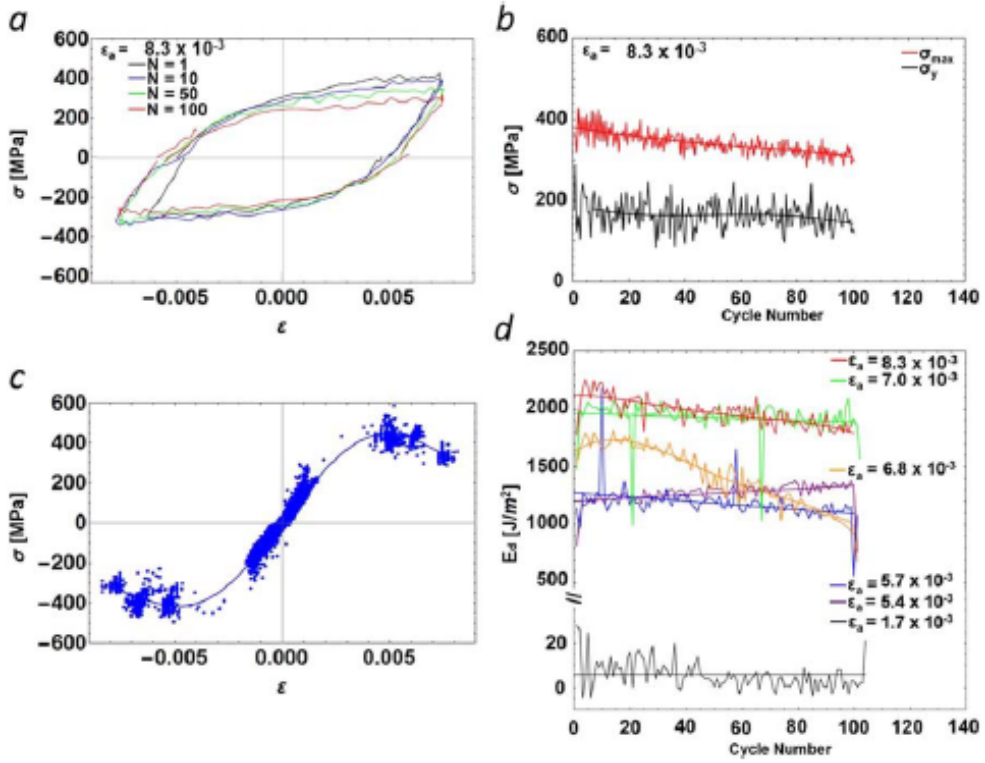

Fig. 5. The cyclic mechanical properties of the ECAP copper micro-beam. (a) Selected stress versus strain curves at cycles N=1, N=10, N=50, and N=100 for plastic strain amplitudes of 8.26×10^{-3} (b) Yield strength and maximum stress as a function of cycle number for a plastic strain amplitude of 8.26×10^{-3}. (c) Cyclic stress versus strain curve. (d) Energy dissipated per cycle as a function of cycle number at six selected plastic strain amplitudes.

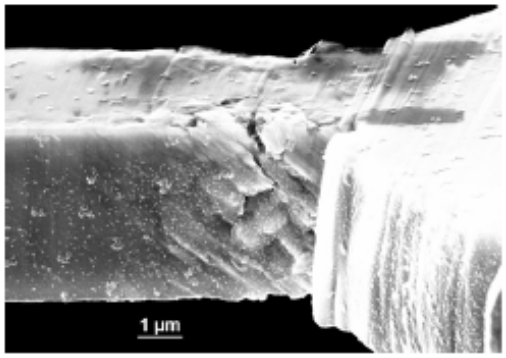

Fig. 6. Microcrack and associated damage found in the ECAP Cu micro-beam after cycling at $\varepsilon_a=6.81\times10^{-3}$ was completed.

and maximum stress as a function of plastic strain amplitudes can be found in the supporting data Fig. 5s part m. It is noteworthy that the ECAP copper micro-beam yield points and maximum stress points remain higher than those of the single-grained micro-beam over the entire range of plastic strain amplitudes in this study. The energy dissipated per cycle seen in Fig. 5d is also stable for most plastic strain amplitudes. At $\varepsilon_a=1.7\times10^{-3}$, $E_{cf}=6\pm6$ J/m^2, indicative that this is a purely elastic deformation regime, and it steadily increases as more plastic deformation occurs up to $\varepsilon_a=5.4\times10^{-3}$, where $E_{cf}=1272\pm89$ J/m^2. As plastic deformation becomes more severe at higher plastic strain amplitudes, there is a point at $\varepsilon_a=6.8\times10^{-3}$ where the energy dissipated per cycle rapidly decreases from 1700 J/m^2 to 1000 J/m^2 from cycle number 20 to cycle number 100. When observing high resolution SEM micrographs of the first and last cycle at this plastic strain amplitude, a micro crack appears to have formed on the bottom of the bar at its root. In addition, more surface deformation on the top surface near the root is noticeable, as seen in Fig. 6. At higher strains, $7.0\times10^{-3}<\varepsilon_a<8.3\times10^{-3}$, the energy dissipated per cycle appears to reach a plateau at 1950 J/m^2. An analysis of the energy dissipated per cycle as a function of plastic strain amplitude can be found in the supporting data Fig. 5s part n.

An attempt was made to monitor the evolution of the microstructure of the ECAP copper micro-beam by performing EBSD scans before testing to capture the initial grain structure and after 100 cycles of bending at selected plastic strain amplitudes beginning with $\varepsilon_a=5.4\times10^{-3}$. The EBSD scans of the deformed root portions of the beam after incremental stages of cyclic loading can be seen in Fig. 7c. Average kernel grain misorientation within one selected grain in the root region of the beam can be found in Fig. 7d. The average global misorientation distribution angle for all grains deemed to be in the root region of the beam (≤2 μm from the base) as a function of plastic strain amplitude, and the average grain size as a function of plastic strain amplitude were measured after selected test segments and can be found in Fig. 7 parts a and b. The grains that underwent the most deformation after bending (≤2 μm from the root) appear to have undergone noticeable coarsening from initial average sizes ~300 nm to sizes ~575 nm over the range of plastic strain amplitudes evaluated.

3.2. PM 2000

Fig. 8 depicts the results of the low cycle fatigue testing on the single grained PM 2000 micro-beam. EBSD prior to testing confirmed

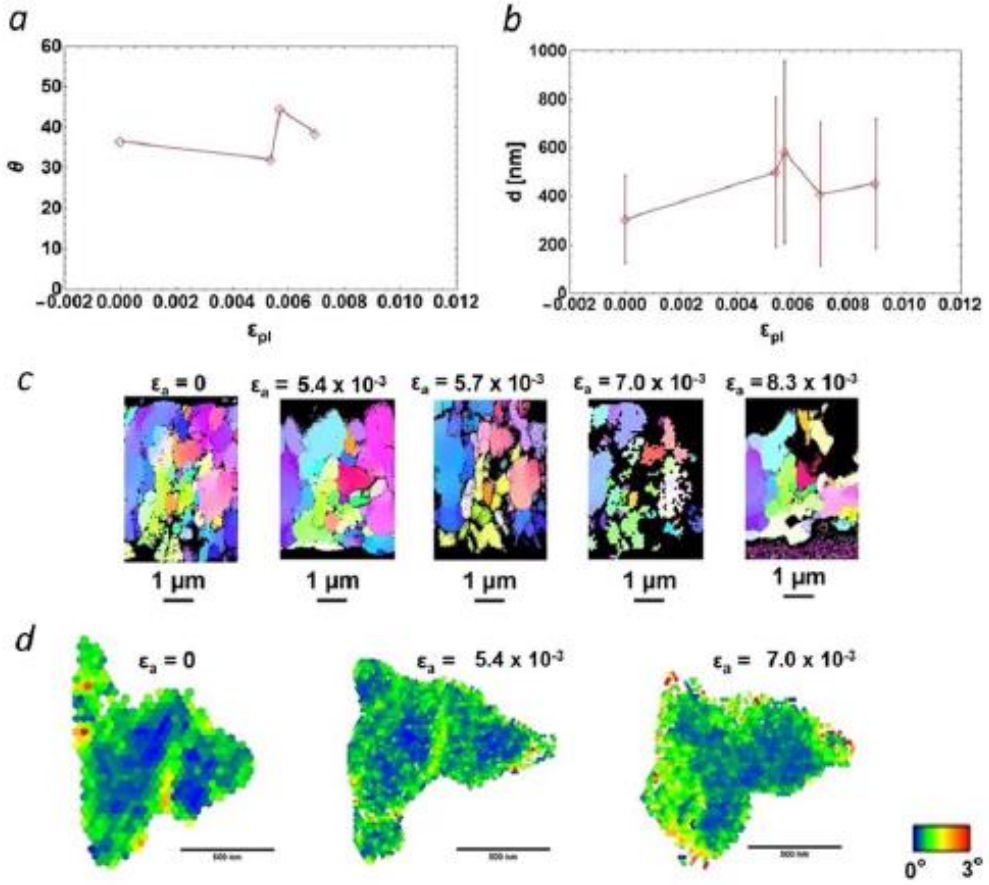

Fig. 7. Microstructural evolution of the ECAP Cu micro-beam after various stages (denoted by their plastic strain amplitudes) of cyclic loading for 100 cycles. (a) global average misorientation distribution as a function of plastic strain amplitude for grains ≤2 μm from the root of the micro-beam, and (b) average grain size as a function of plastic strain amplitude for grains ≤2 μm from the root of the micro-beam (c) EBSD Inverse Pole Figure maps of the deformed root of the ECAP Cu fatigue bar (d) Kernel average misorientation angle of a selected grain in the root region of the micro-beam.

the presence of only one grain in the entire micro-beam. Similar to the behavior of the single grained copper micro-beam, an initial strain amplitude region of elastically increasing stress for $\varepsilon_a < 3\times10^{-3}$ is seen. At $\varepsilon_a=3\times10^{-3}$, the cyclic stress-strain yield point occurs, after which there is a stable stress plateau region, 900–950 MPa, for $3\times10^{-3} < \varepsilon_a < 1\times10^{-2}$. For $\varepsilon_a > 1\times10^{-2}$, it appears as if stress again increases with increasing plastic strain amplitudes. The yield strength and maximum stress values also show three distinct regions, a decrease in σ_y for $\varepsilon_a < 4.3\times10^{-3}$, stability in σ_y for $4.3\times10^{-3} < \varepsilon_a < 1.1\times10^{-2}$, and a second decrease in σ_y for $\varepsilon_a > 1.1\times10^{-2}$. Cyclic stability for the first 100 cycles with respect to yield strength and maximum stress values at ε_a values of 6.0×10^{-3}, 8.5×10^{-3}, and 1.1×10^{-2} is evident as seen in Fig. 8s parts e through j in the supporting data. In addition, these yield strengths and maximum stresses remain constant with respect to one another. From lowest to highest ε_a, the σ_y values are 421 ± 84 MPa, 447 ± 68 MPa, and 494 ± 94 MPa and the σ_{max} values are 841 ± 40 MPa, 933 ± 46 MPa, and 906 ± 54 MPa as seen in Fig. 8s part k in the supporting data. However, for $\varepsilon_a=1.19\times10^{-2}$, rapid cyclic softening from 1000 MPa down to 400 MPa in σ_{max} and 450–150 MPa in σ_y occurs almost immediately, after cycle number 10, over the course of the first 100 cycles as seen in Fig. 8a and b. The energy dissipated per cycle follows a steady linear increase from $3.1\times10^{-3} < \varepsilon_a < 1.1\times10^{-2}$ as seen in Fig. 8s part l. It is evident that the deformation is completely elastic for $\varepsilon_a < 3.1\times10^{-3}$, $E_{cl}=19\pm19$ J/m^2. The energy dissipated per cycle is cyclically stable over the first 100 cycles for ε_a values of 6.0×10^{-3}, 8.5×10^{-3}, and 1.1×10^{-2} and increases from 1685 ± 76 J/m^2 to 4975 ± 189 J/m^2. At $\varepsilon_a=1.2\times10^{-2}$, the energy dissipated per cycle immediately rapidly decreases similar to the trend in decrease of σ_y from 6000 J/m^2 to 1900 J/m^2.

4. Discussion

4.1. Copper

At first single grained micro-beam fatigue properties are discussed in order to define a reference point to which the ufg specimens will be compared against. On the macroscopic scale, it is understood that although ufg materials are strengthened, this does not translate into superior fatigue properties across the entire fatigue life spectrum. This phenomenon is especially true in low cycle fatigue as performed in this previous study [55]. In our study, we evaluate if this phenomenon translates to micro scale mechanical testing.

In order to remain consistent in verifying the grain structure of all samples investigated, EBSD scans before and after testing were performed on the single grained specimen as well. It was found that the single grained micro-beam had its $(0\bar{1}2)$ plane parallel to the

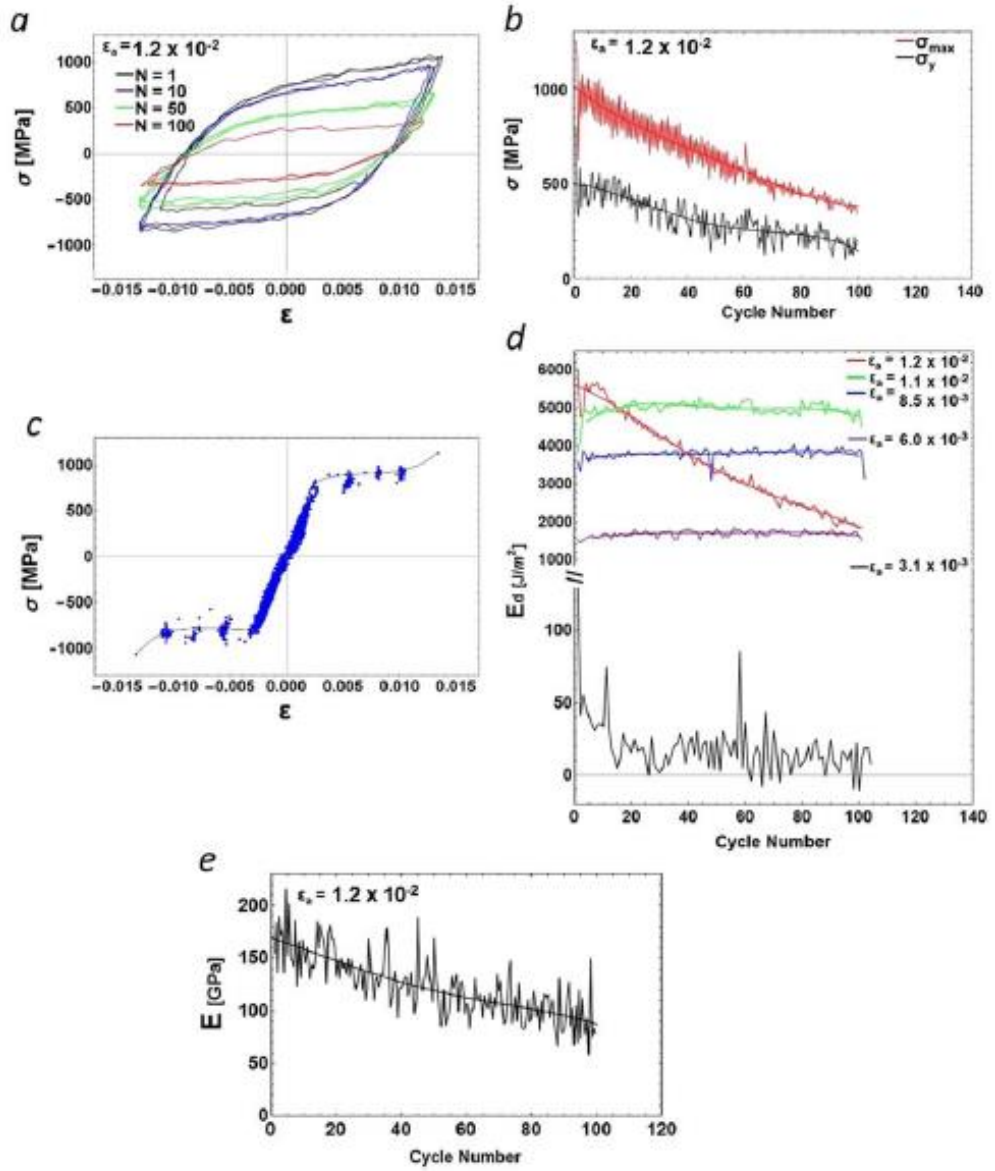

Fig. 8. The cyclic mechanical properties of the single-grained PM 2000 micro-beam. (a) Selected stress versus strain curves at cycles N=1, N=10, N=50, and N=100 for a plastic strain amplitude of 1.19×10^{-2}, (b) Yield strength and maximum stress as a function of cycle number for a plastic strain amplitude of 1.19×10^{-2}. (c) Cyclic stress versus strain curve. (d) Energy dissipated per cycle as a function of cycle number at five selected plastic strain amplitudes. (e) Elastic modulus as a function of cycle number for a plastic strain amplitude of 1.19×10^{-2}.

loading direction. Considering that the deformation occurs via slip plane activation, the most likely slip system, $(1\bar{1}1)$ $[10\bar{1}]$, has the highest Schmid factor equal to 0.49. A cyclic shear stress-shear strain curve was generated and compared to macroscopic data in Fig. 9a which was oriented with its highest Schmid factor equal to 0.5. It is found that the shear strain is significantly higher in the micro-beam bending test compared to the macroscopic compression-tension fatigue test.

It is well documented by Mughrabi [49] that the low cycle fatigue behavior of single crystal copper can be divided into three regimes: an initial regime of increasing stress with increasing cyclic strain, a steady-state plateau regime of constant stress with increasing strain, and a second region of increasing stress with increasing cyclic strain amplitude. Mughrabi defines the plastic resolved shear strain amplitude, γ_{pl}, as the hysteresis loop half width at zero stress. The three regimes occur as follows: the first at $\gamma_{pl} < 6\times10^{-5}$, the second at $6\times10^{-5} < \gamma_{pl} < 7.5\times10^{-5}$, and the third at $\gamma_{pl} > 7.5\times10^{-5}$. In this study γ_{pl} is similarly defined as the average of the maximum and minimum strain of the hysteresis loop. The first region of stress increase with strain increase can be defined as $\gamma_{pl} < 2\times10^{-5}$. The steady state stress plateau region occurs for $2\times10^{-5} < \gamma_{pl} < 7\times10^{-5}$. Unfortunately, the maximum γ_{pl} in this study was 7×10^{-5} so the transition to the third regime was not captured, but the entire steady-state stress plateau of the single-grained micro-beam falls within the larger bounds Mughrabi defines for his steady state stress plateau in [49]. It can be noted that the strain regimes are comparable even though this study operates at stress values significantly higher than in [49] due to dimensional reductions

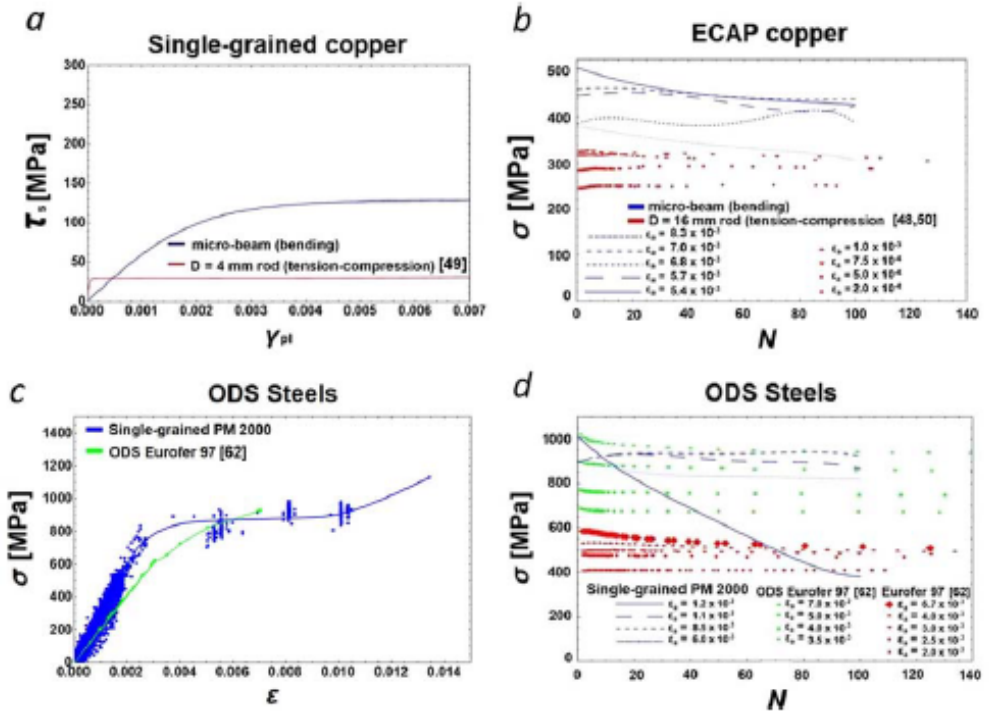

Fig. 9. A comparison of cyclic stress–strain curves generated from micro-beams tested in this study with those generated from previous macroscopic fatigue studies for (a) single-grained copper and (c) ODS steels. A comparison of maximum stress values measured as a function of cycle number, N, for micro-beams tested in this study with those generated from previous macroscopic fatigue studies for (b) ECAP copper and (d) ODS steels.

from 4 mm diameter to ~4 μm in cross section. In Fig. 9a, it can be further seen that the plateau shear stress for the micro-beam is 130 MPa, whereas the plateau shear stress for the macroscopic test is 30 MPa. Due to the higher yield strengths for smaller structures, an increased lower bound of the stable plateau for micro-specimens is not unexpected.

Shifting from the single crystal materials to their ufg companions, Hoeppel et al. extensively studied grain coarsening and cyclic softening during the fatigue of ECAP copper in [51]. For strain controlled fatigue testing of ECAP copper, both phenomena occur for plastic strain amplitudes in the range of $2\times10^{-4} < \varepsilon_{pl} < 1\times10^{-3}$, and are intensified as plastic strain amplitudes approach the lower bound. However, cyclic softening in terms of maximum stress values did not occur until well over 100 cycles were performed, which is consistent with our study. The most significant cyclic softening in terms of reduction in stress occurred between cycle number 1000 and 100,000 for these plastic strain amplitudes. Our cyclic studies monitoring the stress evolution over 100 cycle intervals involved higher plastic strain amplitudes in the range $5.4\times10^{-3} < \varepsilon_{pl} < 8.3\times10^{-3}$. Thus, unfortunately, this range is not in the optimal regime to observe grain coarsening, and even if it were, cycling would need to be carried out beyond 1000 cycles, possibly out to as high as 100,000 cycles in order to see fatigue effects on stresses and microstructure. Due to current experimental design limitations, this large number of cycles is not feasible to conduct. However, the present work indicates grain rotation and the disappearance of orientation gradients across subgrain structures with increasing plastic strain amplitude in the deformed root region of the beam, as seen in Fig. 7. The hysteresis loops for the cyclic deformation created from $\varepsilon_{pl}=5.4\times10^{-3}$ and $\varepsilon_{pl}=7.0\times10^{-3}$ (found in the supporting data, Fig. 5s parts e and i) are indicative of this behavior in that as the number of cycles, N, increases, the loops become flatter, meaning they are less able to undergo strain hardening. In addition, a smaller circular grain in the center of the root of the beam appears to have practically disappeared after 100 cycles at $\varepsilon_a=8.3\times10^{-3}$. Steady state stress values recorded in [51] for $\varepsilon_{pl}=1\times10^{-3}$ are approximately 320 MPa, whereas our steady state stress values for $5\times10^{-3} < \varepsilon_{pl} < 8\times10^{-3}$ are 400–500 MPa. This can be seen in Fig. 9b. Cyclic softening within the first 100 cycles is negligible, at most 10 MPa in the range of ε_{pl} for Hoeppel, but for our studies cyclic softening up to 60 MPa occurs in the ECAP copper micro-beam for $\varepsilon_{pl}=5.4\times10^{-3}$ and 8.3×10^{-3}. It is hypothesized that the high amount of free surfaces in the micro samples may account for some portion of the eventual softening as fatiguing to larger plastic strain amplitudes was performed.

4.2. PM 2000

Although PM 2000 is a ferritic iron–chromium body centered cubic steel containing nano oxide precipitates, meaning that the dominance of the *[111]* primary slip plane for face centered cubic materials such as single crystal copper does not exist, there still appears to be three similar distinct regimes of its cyclic stress-strain curve. The initial regime of increasing stress with increasing strain can be defined as $\varepsilon_{pl} < 2\times10^{-3}$. The steady state stress plateau region occurs for $2\times10^{-3} < \varepsilon_{pl} < 1\times10^{-2}$. A transition to the third region of increasing stress with further increasing strain appears to occur for $\varepsilon_{pl} > 1\times10^{-2}$. In addition, we can note the agreement between cyclic stress–strain curves of our single grained PM 2000 to that of a bulk F/M Eurofer 97 fatigue sample found in literature as shown in Fig. 9c. Cyclic strengths at four selected plastic strain amplitudes can be found in Table 1. This may provide evidence for the nano oxide precipitates in these materials serving as cyclic strength determining features because there is little indication of a size effect.

Similar fatigue studies on a ferritic–martensitic ODS Eurofer 97 steel were performed in [62], showing gradual cyclic softening within

Table 1
Cyclic strengths of ODS alloys at selected strain amplitudes.

ε_a	Eurofer 97 ODS [62] (MPa)	Single-Grained PM 2000 ODS (MPa)
3.5×10^{-3}	690	950
4×10^{-3}	760	950
5×10^{-3}	875	900
7×10^{-3}	1025	900

the first 100 cycles, beginning at plastic strain amplitudes of 5×10^{-3}. However, for the single-grained PM 2000 micro-beam, dramatic cyclic softening did not occur until a plastic strain amplitude of 1.2×10^{-2} as seen in Fig. 8a, b, and d. A decrease of ~570 MPa occurs at this plastic strain amplitude for the micro-beam over the first 100 cycles, but a decrease of only 75 MPa occurs over the first 100 cycles for the macroscopic fatigue testing in [62] at a plastic strain amplitude of 7×10^{-3}. The dramatic softening in the micro-beam is due to damage formation in the beam, i.e. microcrack formation and growth that can be detected by a reduction in elastic stiffness over cycle number. Over the course of 100 cycles, the elastic modulus decreased from 170 GPa down to 80 GPa as seen in Fig. 8e. This is also measured by a dramatic 4 kJ/m^2 drop in energy dissipated per cycle. However it is not believed that this dramatic cyclic softening is a size effect when shifting from micro-beams to large scale fatiguing because at a plastic strain amplitude of 5×10^{-3}, the stress recorded from Eurofer ODS steel in [62] decreases from 875 MPa to 850 MPa and the stress of the single-grained PM 2000 micro-beam follows a similar trend, decreasing from 900 MPa to 825 MPa. Their cyclic stress-strain curves show no indication of size effects as seen in Fig. 9c. It is hypothesized that the density and size of nano-oxide dispersoids make them sufficient to be the strength determining features during fatigue.

Fatigue studies on martensitic and ferritic steels and their ODS companions have shown that the ODS variants exhibit increased cyclic strength. The ODS variants are 100–350 MPa stronger than their non-ODS counterparts at 923 K [63]. However, studies have not been performed comparing the cyclic strengths of an ODS steel and that same ODS steel after being cold worked using a severe plastic deformation technique. Fig. 9c shows the cyclic stress strain curves of the PM 2000 ODS steel compared to an ODS Eurofer 97 steel, and Table 1 shows four selected strain amplitudes from fatigue testing at room temperature from our studies and the study in [62] on Eurofer ODS.

5. Conclusion

The preceding studies have shown that using micro-beams to perform low cycle fatigue experiments is an effective way of measuring the mechanical properties elastic modulus, yield strength, and maximum stress as well as producing cyclic stress-strain curves and measuring the energy dissipated per cycle for both single crystal and polycrystalline materials, which turns out to be well suited as a damage indicator, as confirmed by the in-situ observations. In addition, by measuring the energy dissipation of the micro-beams, the onset of damage formation can be identified. For all specimens except the single grained copper, micro-beam bending fatigue is an acceptable way to measure bulk mechanical properties because many strength determining features are sampled whether they are grain boundaries, dislocations, or nano oxide particles. Dislocation pileup within these micro-beams occurs exactly as it would in a macroscopic fatigue specimen.

This method can be extended to fatigue testing of materials that have dimensional constraints such as nuclear materials where size is limited due to material availability and safe handling. More fatigue testing on the micro scale should be extended to cover a wider range of plastic strain amplitudes, crystal structures, and microstructures in order to more completely compare the results of micro scale fatigue experiments to macro scale fatigue experiments.

Acknowledgement

The Austrian Marshall Plan Foundation is acknowledged for providing the infrastructure for collaborative research between scholars at UC Berkeley and Montanuniversität Leoben. In addition, the Austrian Science Fund (FWF) is credited for financial support (Project no. P 25325-N20). The National Center for Electron Microscopy at Lawrence Berkeley National Laboratory is recognized for use of the 300 kV JEOL 3010 TEM for bright-field TEM investigations. Work at the Molecular Foundry was supported by the Office of Science, Office of Basic Energy Sciences, of the U.S. Department of Energy under Contract No. DE-AC02-05CH11231.

Appendix A. Supplementary material

Supplementary data associated with this article can be found in the online version at http://dx.doi.org/10.1016/j.msea.2017.01.073.

References

[1] W.D. Nix, H. Gao, Indentation size effects in crystalline materials: a law for strain gradient plasticity, J. Mech. Phys. Solids 46 (3) (1998) 411–425.
[2] J.G. Swadener, E.P. George, G.M. Pharr, The correlation of the indentation size effect measured with indenters of various shapes, J. Mech. Phys. Solids 50 (4) (2002) 681–694.
[3] A.A. Elmustafa, D.S. Stone, Indentation size effect in polycrystalline FCC metals, Acta Mater. 50 (14) (2002) 3641–3650.
[4] G.M. Pharr, G.E. Herbert, Y. Gao, The indentation size effect: a critical examination of experimental observations and mechanistic interpretations, Annu. Rev. Mater. Res. 40 (2010) 271–292.
[5] M.D. Uchic, et al., Sample dimensions influence strength and crystal plasticity, Science 305 (5686) (2004) 986–989.
[6] D.M. Dimiduk, M.D. Uchic, T.A. Parthasarathy, Size-affected single-slip behavior of pure nickel microcrystals, Acta Mater. 53 (15) (2005) 4065–4077.
[7] M.D. Uchic, D.M. Dimiduk, A methodology to investigate size scale effects in crystalline plasticity using uniaxial compression testing, Mater. Sci. Eng.: A 400 (2005) 268–278.
[8] J.R. Greer, J. Th.M. De Hosson, Plasticity in small-sized metallic systems: intrinsic versus extrinsic size effect, Prog. Mater. Sci. 56 (6) (2011) 654–724.
[9] D. Kiener, C. Motz, G. Dehm, Micro-compression testing: a critical discussion of experimental constraints, Mater. Sci. Eng.: A 505 (1) (2009) 79–87.
[10] D. Kiener, et al., A further step towards an understanding of size-dependent crystal plasticity: in situ tension experiments of miniaturized single-crystal copper samples, Acta Mater. 56 (3) (2008) 580–592.
[11] D.S. Gianola, C. Eberl, Micro-and nanoscale tensile testing of materials, JOM 61 (3) (2009) 24–35.
[12] C. Motz, T. Schöberl, R. Pippan, Mechanical properties of micro-sized copper bending beams machined by the focused ion beam technique, Acta Mater. 53 (15) (2005) 4269–4279.
[13] C. Motz, et al., Micro-bending tests: a comparison between three-dimensional discrete dislocation dynamics simulations and experiments, Acta Mater. 56 (9) (2008) 1942–1955.
[14] E. Demir, D. Raabe, F. Roters, The mechanical size effect as a mean-field breakdown phenomenon: example of microscale single crystal beam bending, Acta Mater. 58 (5) (2010) 1876–1886.
[15] J. Geng, J.W. Angus, A microcantilever investigation of size effect, solid-solution strengthening and second-phase strengthening for <a> prism slip in alpha-Ti, Acta Mater. 59 (15) (2011) 5970–5981.
[16] B. Yang, et al., Stress-controlled fatigue behaviour of micro-sized polycrystalline copper wires, Mater. Sci. Eng.: A 515 (1) (2009) 71–78.
[17] D. Liu, et al., Anomalous plasticity in the cyclic torsion of micron scale metallic wires, Phys. Rev. Lett. 110 (24) (2013) 244301.
[18] A. Wimmer, et al., Damage evolution during cyclic tension–tension loading of micron-sized Cu lines, Acta Mater. 67 (2014) 297–307.
[19] A. Wimmer, et al., Cyclic bending experiments on free-standing Cu micron lines observed by electron backscatter diffraction, Acta Mater. 83 (2015) 460–469.
[20] D.J. Dunstan, et al., Elastic limit and strain hardening of thin wires in torsion, Phys. Rev. Lett. 103 (15) (2009) 155501.
[21] D.J. Dunstan, et al., Yield and plastic flow of soft metals in small volumes loaded in tension and flexure (92)Philos. Mag. 25–27 (2012) 3199–3215.
[22] K. Takashima, et al., Fatigue crack growth behavior of micro-sized specimens prepared from an electroless plated Ni-P amorphous alloy thin film, Mater. Trans. 42 (1) (2001) 68–73.
[23] D. Kiener, et al., Cyclic response of copper single crystal micro-beams, Scr. Mater. 63 (5) (2010) 500–503.
[24] M.W. Kapp, et al., Structural instabilities during cyclic loading of ultrafine-grained

copper studied with micro bending experiments, Acta Mater. 125 (2017) 351–358.
[25] P. Hosemann, C. Shin, D. Kiener, Small scale mechanical testing of irradiated materials, J. Mater. Res. 30 (09) (2015) 1231–1245.
[26] N. Igata, et al., Proton irradiation creep of thin foil specimens of type 304 austenitic stainless steel and the thickness effects on their mechanical properties, J. Nucl. Mater. 122 (1) (1984) 354–358.
[27] K. Miyahara, et al., The effects of grain and specimen sizes on mechanical properties of type 316 austenitic stainless steel, J. Nucl. Mater. 133 (1985) 506–510.
[28] A. Kohyama, et al., Specimen size effects on mechanical properties of 14 MeV neutron irradiated metals, J. Nucl. Mater. 155 (1988) 1354–1358.
[29] A. Kohyama, K. Hamada, H. Matsui, Specimen size effects on tensile properties of neutron-irradiated steels, J. Nucl. Mater. 179 (1991) 417–420.
[30] Y. Kohno, et al., Specimen size effects on the tensile properties of JPCA and JFMS, J. Nucl. Mater. 283 (2000) 1014–1017.
[31] C. Shin, et al., Evaluation of irradiation effects on fracture strength of silicon carbide using micropillar compression tests, Exp. Mech. 53 (4) (2013) 687–697.
[32] C. Shin, et al., Development and testing of microcompression for post irradiation characterization of ODS steels, J. Nucl. Mater. 444 (1) (2014) 43–48.
[33] D. Kiener, et al., Determination of mechanical properties of copper at the micron scale, Adv. Eng. Mater. 8 (11) (2006) 1119–1125.
[34] D. Kiener, A.M. Minor, Source truncation and exhaustion: insights from quantitative in situ TEM tensile testing, Nano Lett. 11 (9) (2011) 3816–3820.
[35] D. Kiener, C. Motz, G. Dehm, Dislocation-induced crystal rotations in micro-compressed single crystal copper columns, J. Mater. Sci. 43 (7) (2008) 2503–2506.
[36] C. Howard, et al., Investigation of specimen size effects by in-situ microcompression of equal channel angular pressed copper, Mater. Sci. Eng.: A 649 (2016) 104–113.
[37] C. Peng, Y. Zhan, J. Lou, Size-dependent fracture mode transition in copper nanowires, Small 8 (12) (2012) 1889–1894.
[38] Y. Yue, et al., Approaching the theoretical elastic strain limit in copper nanowires, Nano Lett. 11 (8) (2011) 3151–3155.
[39] A.T. Jennings, J.R. Greer, Tensile deformation of electroplated copper nanopillars (91)Philos. Mag. 7–9 (2011) 1108–1120.
[40] A.T. Jennings, J.M. Burek, J.R. Greer, Microstructure versus size: mechanical properties of electroplated single crystalline Cu nanopillars, Phys. Rev. Lett. 104 (13) (2010) 135503.
[41] A.T. Jennings, et al., Higher compressive strengths and the Bauschinger effect in conformally passivated copper nanopillars, Acta Mater. 60 (8) (2012) 3444–3455.
[42] D. Jang, C. Cai, J.R. Greer, Influence of homogeneous interfaces on the strength of 500 nm diameter Cu nanopillars, Nano Lett. 11 (4) (2011) 1743–1746.
[43] A.T. Jennings, J. Li, J.R. Greer, Emergence of strain-rate sensitivity in Cu nanopillars: transition from dislocation multiplication to dislocation nucleation, Acta Mater. 59 (14) (2011) 5627–5637.
[44] J.Y. Zhang, G. Liu, J. Sun, Strain rate effects on the mechanical response in multi- and single-crystalline Cu micropillars: grain boundary effects, Int. J. Plast. 50 (2013) 1–17.
[45] B. Yang, et al., Yield stress influenced by the ratio of wire diameter to grain size–a competition between the effects of specimen microstructure and dimension in micro-sized polycrystalline copper wires (92)Philos. Mag. 25–27 (2012) 3243–3256.
[46] D. Kiener, et al., In situ nanocompression testing of irradiated copper, Nat. Mater. 10 (8) (2011) 608–613.
[47] Q. Guo, et al., Helium implantation effects on the compressive response of Cu nanopillars, Small 9 (5) (2013) 691–696.
[48] H. Höppel, M. Brunnbauer, H. Mughrabi, Cyclic deformation behaviour of ultrafine grain size copper produced by equal channel angular extrusion, Materials Week 2000, 25–28 September 2000, Werkstoffwoche-Partnerschaft (ed.), Frankfurt, (http://www.materialsweek.org/proceedings), 2001.
[49] H. Mughrabi, The cyclic hardening and saturation behaviour of copper single crystals, Mater. Sci. Eng. 33 (2) (1978) 207–223.
[50] S.R. Agnew, J.R. Weertman, Cyclic softening of ultrafine grain copper, Mater. Sci. Eng. A244 (1998) 145–153.
[51] H.W. Höppel, et al., Microstructural study of the parameters governing coarsening and cyclic softening in fatigued ultrafine-grained copper, Philos. Mag. A 82 (9) (2002) 1781–1794.
[52] R.Z. Valiev, et al., Deformation behaviour of ultra-fine-grained copper, Acta Metall. et Mater. 42 (7) (1994) 2467–2475.
[53] R.Z. Valiev, Structure and mechanical properties of ultrafine-grained metals, Mater. Sci. Eng.: A 234 (1997) 59–66.
[54] Y.T. Zhu, T.C. Lowe, Observations and issues on mechanisms of grain refinement during ECAP process, Mater. Sci. Eng.: A 291 (1) (2000) 46–53.
[55] Markus, Aicheler. Surface Phenomena Associated with Thermal Cycling of Copper and their Impact on the Service Life of Particle Accelerator Structures, Diss. Ruhr U., Bochum, 2010.
[56] G.R. Odette, M.J. Alinger, B.D. Wirth, Recent developments in irradiation-resistant steels, Annu. Rev. Mater. Res. 38 (2008) 471–503.
[57] J. Chen, W. Hoffelner, Irradiation creep of oxide dispersion strengthened (ODS) steels for advanced nuclear applications, J. Nucl. Mater. 392 (2) (2009) 360–363.
[58] R.L. Klueh, et al., Oxide dispersion-strengthened steels: a comparison of some commercial and experimental alloys, J. Nucl. Mater. 341 (2) (2005) 103–114.
[59] D. Kiener, et al., Overview on established and novel FIB based miniaturized mechanical testing using in-situ SEM, Int. J. Mater. Res. 100 (8) (2009) 1074–1087.
[60] G.V. Samsonov (Ed.)Handbook of the Physicochemical Properties of the Elements, IFI-Plenum, New York, USA, 1968.
[61] P. Schwarzkopf Plansee, Bar Grain Class 6 ODS Iron Alloy Sheet, material property datasheet, Material No.: 1.4768, Abbreviated DIN name: CrAl, 21(6), 2000.
[62] I. Kubena, et al., Fatigue behaviour of ODS ferritic-martensitic Eurofer steel, Procedia Eng. 2 (1) (2010) 717–724.
[63] S. Ukai, S. Ohtsuka, Low cycle fatigue properties of ODS ferritic-martensitic steels at high temperature, J. Nucl. Mater. 367–370 (2007) 234–238.

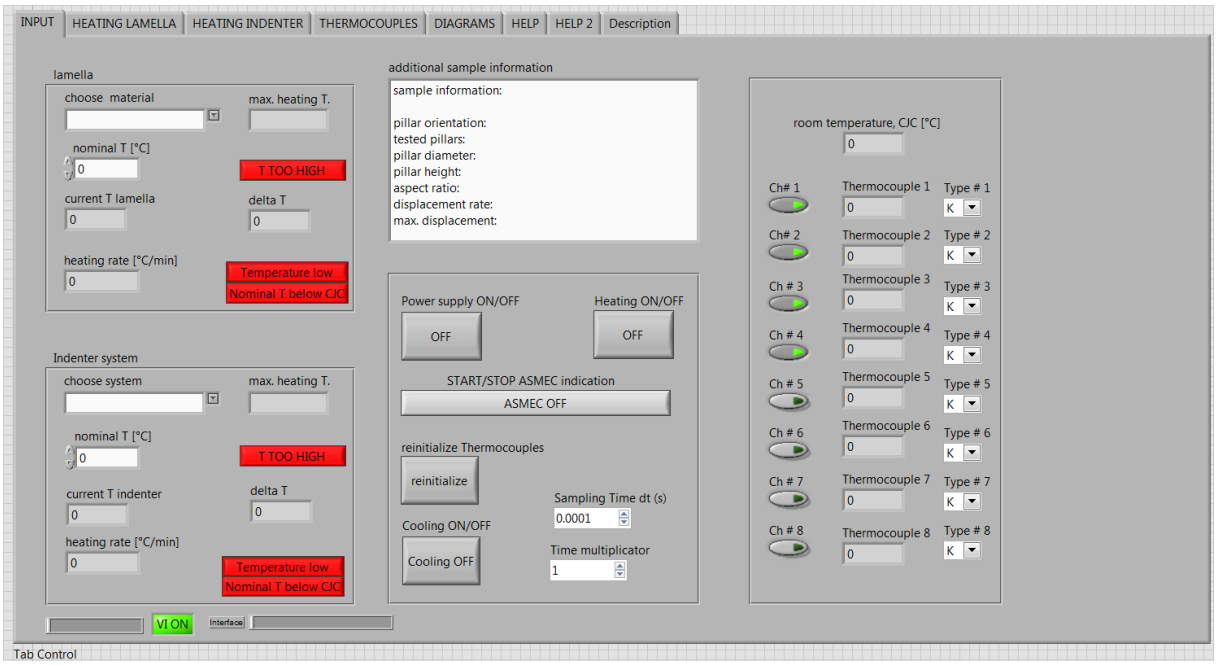
INPUT
HEATING LAMELLA
HEATING INDENTER
THERMOCOUPLES
DIAGRAMS
HELP
HELP 2
Description
lamella
choose material
max. heating T.
nominal T [°C]
T TOO HIGH
current T lamella
delta T
heating rate [°C/min]
Temperature low
Nominal T below CJC
Indenter system
choose system
max. heating T.
nominal T [°C]
T TOO HIGH
current T indenter
delta T
heating rate [°C/min]
Temperature low
Nominal T below CJC
VI ON
Interface
additional sample information
sample information:
pillar orientation:
tested pillars:
pillar diameter:
pillar height:
aspect ratio:
displacement rate:
max. displacement:
Power supply ON/OFF
OFF
Heating ON/OFF
OFF
START/STOP ASMEC indication
ASMEC OFF
reinitialize Thermocouples
reinitialize
Sampling Time dt (s)
0.0001
Cooling ON/OFF
Cooling OFF
Time multiplicator
1
room temperature, CJC [°C]
Ch# 1
Thermocouple 1
Type # 1
Ch# 2
Thermocouple 2
Type # 2
Ch # 3
Thermocouple 3
Type # 3
Ch # 4
Thermocouple 4
Type # 4
Ch # 5
Thermocouple 5
Type # 5
Ch # 6
Thermocouple 6
Type # 6
Ch # 7
Thermocouple 7
Type # 7
Ch # 8
Thermocouple 8
Type # 8
Tab Control

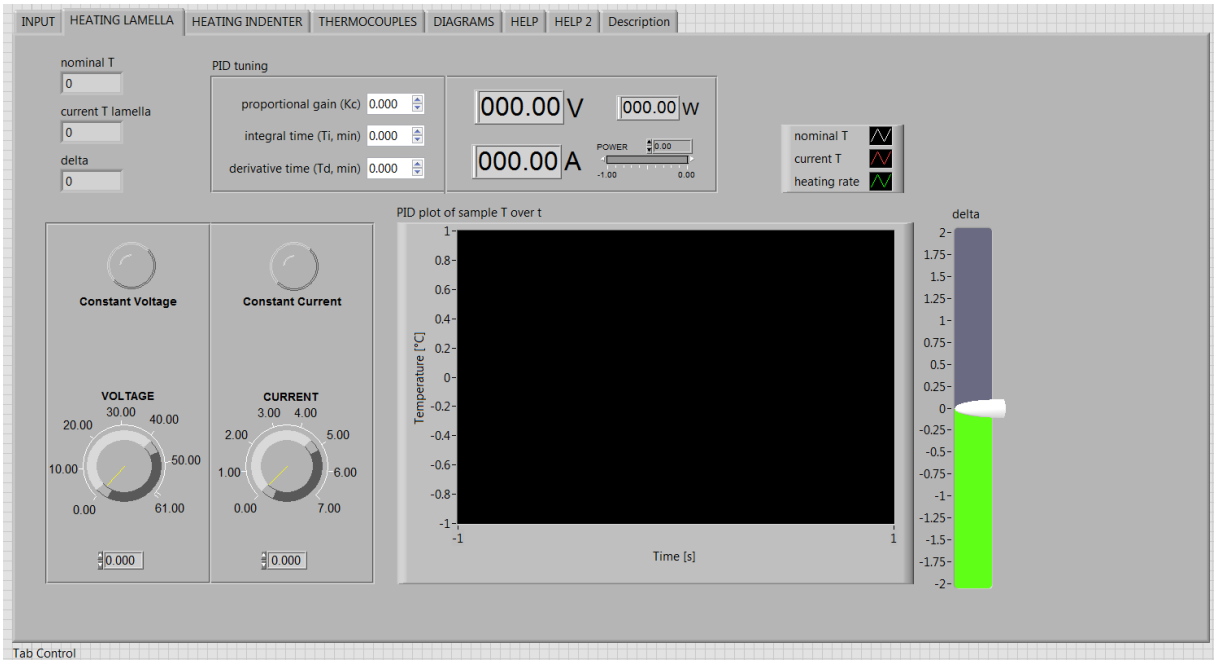
INPUT
HEATING LAMELLA
HEATING INDENTER
THERMOCOUPLES
DIAGRAMS
HELP
HELP 2
Description
nominal T
current T lamella
delta
PID tuning
proportional gain (Kc)
integral time (Ti, min)
derivative time (Td, min)
000.00 V
000.00 W
000.00 A
POWER
nominal T
current T
heating rate
Constant Voltage
Constant Current
VOLTAGE
CURRENT
PID plot of sample T over t
Temperature [°C]
Time [s]
delta
Tab Control

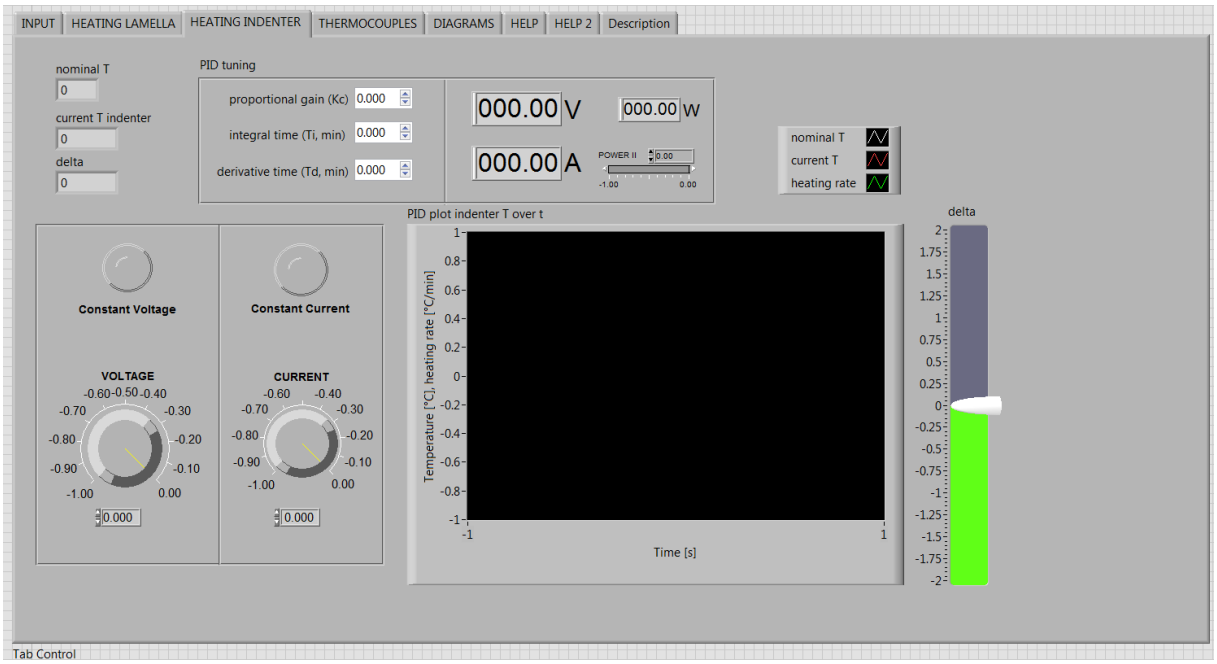
INPUT
HEATING LAMELLA
HEATING INDENTER
THERMOCOUPLES
DIAGRAMS
HELP
HELP 2
Description
nominal T
current T indenter
delta
PID tuning
proportional gain (Kc)
integral time (Ti, min)
derivative time (Td, min)
000.00 V
000.00 W
000.00 A
POWER II
nominal T
current T
heating rate
PID plot indenter T over t
Temperature [°C], heating rate [°C/min]
Time [s]
delta
Constant Voltage
Constant Current
VOLTAGE
CURRENT
Tab Control


INPUT
HEATING LAMELLA
HEATING INDENTER
THERMOCOUPLES
DIAGRAMS
HELP
HELP 2
Description
Units
Mains Frequency
Close and Exit
Amplitude
01:00:00.000
01.01.1904
01:00:05.000
01.01.1904
CJC
Ch 1
Ch 2
Ch 3
Ch 4
Ch 5
Ch 6
Ch 7
CH 8
Tab Control

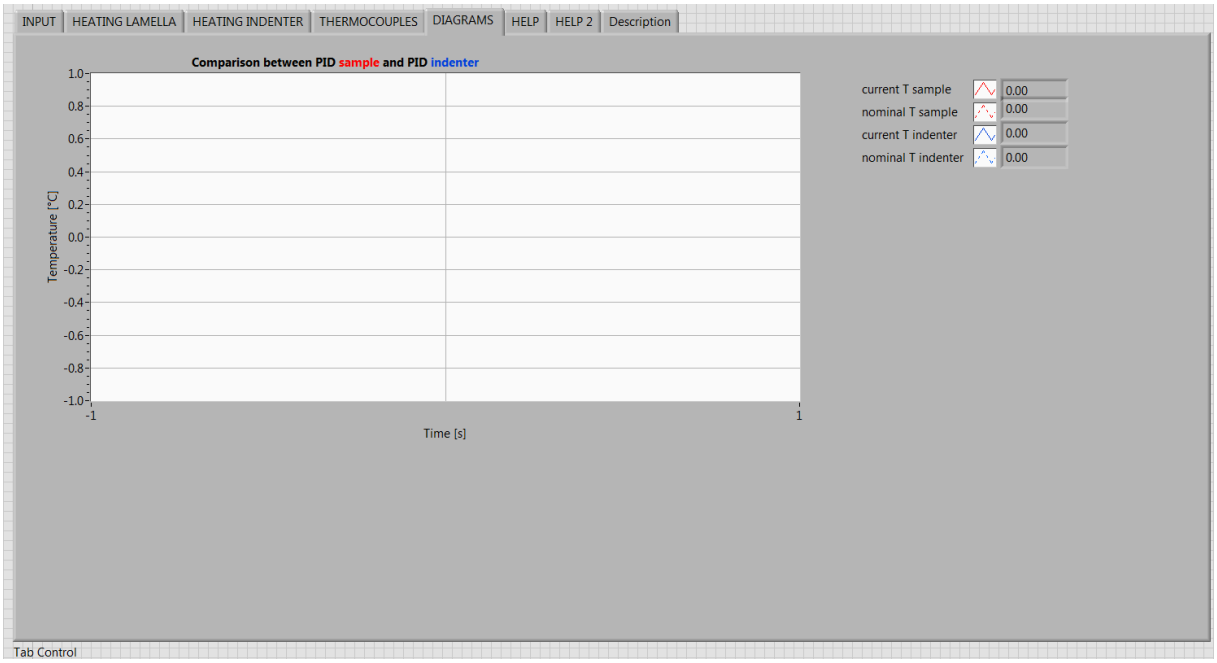
INPUT
HEATING LAMELLA
HEATING INDENTER
THERMOCOUPLES
DIAGRAMS
HELP
HELP 2
Description
Comparison between PID sample and PID indenter
Temperature [°C]
1.0
0.8
0.6
0.4
0.2
0.0
-0.2
-0.4
-0.6
-0.8
-1.0
-1
1
Time [s]
current T sample
nominal T sample
current T indenter
nominal T indenter
0.00
0.00
0.00
0.00
Tab Control